Strong-field driven dynamics
of metal and dielectric nanoparticles

by

Jeffrey Powell

B.S., Benedictine College, 2010

AN ABSTRACT OF A DISSERTATION

submitted in partial fulfillment of the requirements for the degree

DOCTOR OF PHILOSOPHY

Department of Physics
College of Arts and Sciences

KANSAS STATE UNIVERSITY
Manhattan, Kansas

2017

Abstract

The motion of electrons in atoms, molecules, and solids in the presence of intense electromagnetic radiation is an important research topic in physics and physical chemistry because of its fundamental nature and numerous practical applications, ranging from precise machining of materials to optical control of chemical reactions and light-driven electronic devices. Mechanisms of light-matter interactions critically depend on the dimensions of the irradiated system and evolve significantly from single atoms or molecules to the macroscopic bulk. Nanoparticles provide the link between these two extremes. In this thesis, I take advantage of this bridge to study light-matter interactions as a function of nanoparticle size, shape, and composition.

I present here three discrete, but interconnected, experiments contributing to our knowledge of nanoparticle properties and their response to intense, short-pulsed light fields. First, I investigate how individual nanoparticles interact with each other in solution, studying their temperature-dependent solubility. The interaction potential between 5.5nm gold nanoparticles, ligated by an alkanethiol was found to be -0.165eV, in reasonable agreement with a phenomenological model. The other two experiments explore ultrafast dynamics driven by intense femtosecond lasers in isolated, gas-phase metallic and dielectric nanoparticles. Photoelectron momentum imaging is applied to study the response of gold, silica, and gold-shell/silica-core nanoparticles (ranging from single to several hundred nanometers in size) with near-infrared (NIR), 25 fs laser pulses in the intensity range of 10^{11} - 10^{14} W/cm^2. These measurements, which constitute the bulk of my graduate work, reveal the complex interplay between the external optical field and the induced near-field of the nanoparticle, resulting in the emission of very energetic electrons that are much faster than those emitted from isolated atoms or molecules exposed to the same light pulses. The highest photoelectron energies ("cutoffs") were measured as a function of laser intensity, nanoparticle material and size. We found that the energy cutoffs increase monotonically with laser intensity and nanoparticle size, except for the gold/silica hybrid where the plasmon resonance response modifies this behavior at low intensities. The measured photoelectron spectra for metallic nanoparticles display a large energy enhancement over silica.

Finally, the last part of this thesis explores the possibility to apply time-resolved x-ray scattering as a probe of the ultrafast dynamics in isolated nanoparticles driven by very intense (~10^{15} W/cm^2) NIR laser radiation. To do this, I developed and built a nanoparticle source capable of injecting single, gas-phase nanoparticles with a narrow size distribution into the laser focus. We used femtosecond x-ray pulses from an x-ray free electron laser (XFEL) to map the evolution of the laser-irradiated nanoparticle. The ultrafast dynamics were observed in the single-shot x-ray diffraction patterns measured as a function of delay between the NIR and x-ray pulses, which allows for femtosecond temporal and nanometer spatial resolution. We found that the intense IR laser pulse rapidly ionizes the nanoparticle, effectively turning it into a nanoplasma within less than a picosecond, and observed signatures of the nanoparticle surface softening on a few hundred-femtosecond time scale.

Strong-field driven dynamics
of metal and dielectric nanoparticles

by

Jeffrey Powell

B.S., Benedictine College, 2010

A DISSERTATION

submitted in partial fulfillment of the requirements for the degree

DOCTOR OF PHILOSOPHY

Department of Physics
College of Arts and Sciences

KANSAS STATE UNIVERSITY
Manhattan, Kansas

2017

Approved by:

Co-Major Professor
Artem Rudenko

Approved by:

Co-Major Professor
Christopher Sorensen

Copyright

Abstract

The motion of electrons in atoms, molecules, and solids in the presence of intense electromagnetic radiation is an important research topic in physics and physical chemistry because of its fundamental nature and numerous practical applications, ranging from precise machining of materials to optical control of chemical reactions and light-driven electronic devices. Mechanisms of light-matter interactions critically depend on the dimensions of the irradiated system and evolve significantly from single atoms or molecules to the macroscopic bulk. Nanoparticles provide the link between these two extremes. In this thesis, I take advantage of this bridge to study light-matter interactions as a function of nanoparticle size, shape, and composition.

I present here three discrete, but interconnected, experiments contributing to our knowledge of nanoparticle properties and their response to intense, short-pulsed light fields. First, I investigate how individual nanoparticles interact with each other in solution, studying their temperature-dependent solubility. The interaction potential between 5.5nm gold nanoparticles, ligated by an alkanethiol was found to be -0.165 eV, in reasonable agreement with a phenomenological model. The other two experiments explore ultrafast dynamics driven by intense femtosecond lasers in isolated, gas-phase metallic and dielectric nanoparticles. Photoelectron momentum imaging is applied to study the response of gold, silica, and gold-shell/silica-core nanoparticles (ranging from single to several hundred nanometers in size) with near-infrared (NIR), 25 fs laser pulses in the intensity range of 10^{11} - 10^{14} W/cm^2. These measurements, which constitute the bulk of my graduate work, reveal the complex interplay between the external optical field and the induced near-field of the nanoparticle, resulting in the emission of very energetic electrons that are much faster than those emitted from isolated atoms or molecules exposed to the same light pulses. The highest photoelectron energies (“cutoffs”) were measured as a function of

laser intensity, nanoparticle material and size. We found that the energy cutoffs increase monotonically with laser intensity and nanoparticle size, except for the gold/silica hybrid where the plasmon resonance response modifies this behavior at low intensities. The measured photoelectron spectra for metallic nanoparticles display a large energy enhancement over silica.

Finally, the last part of this thesis explores the possibility to apply time-resolved x-ray scattering as a probe of the ultrafast dynamics in isolated nanoparticles driven by very intense (~10^{15} W/cm^2) NIR laser radiation. To do this, I developed and built a nanoparticle source capable of injecting single, gas-phase nanoparticles with a narrow size distribution into the laser focus. We used femtosecond x-ray pulses from an x-ray free electron laser (XFEL) to map the evolution of the laser-irradiated nanoparticle. The ultrafast dynamics were observed in the single-shot x-ray diffraction patterns measured as a function of delay between the NIR and x-ray pulses, which allows for femtosecond temporal and nanometer spatial resolution. We found that the intense IR laser pulse rapidly ionizes the nanoparticle, effectively turning it into a nanoplasma within less than a picosecond, and observed signatures of the nanoparticle surface softening on a few hundred-femtosecond time scale.

Table of Contents

List of Figures

List of Tables

Acknowledgements

My path to the completion of this thesis was not without a multitude of indispensable, devoted, and enthusiastic people. Though this list of acknowledgments is not comprehensive, recognizing the people around me, both past and present, provides a feel for the help and encouragement I have been given.

To my parents, who encouraged me from the beginning to strive to do more and set an example of hard-work and endurance.

To my siblings, the source of countless childhood stories and experiences and who helped form me into what I today.

To my wife, who has been my biggest fan throughout all of graduate school, enduring the many extended ups and downs married to a student. Her sanity was and is much-appreciated.

To my kids, who have not known anything other than their father going to 'school'. They are my greatest accomplishment and a source of immense pride.

My mentors at Benedictine College, Dr. Brothers and Dr. Beard who never stopped pushing and asking for more. Their encouragement opened the door of science to me which has continually whetted my appetite for building and learning.

My graduate school advisors here at Kansas State, Dr. Christopher Sorensen and Dr. Artem Rudenko. The quest for knowledge and passion to teach was a daily routine for Chris. It has been an honor to learn from you, including your open-door policy that I took full advantage of. Artem has never shied away from pushing me to strive to be a better scientist. The opportunity to have an excellent mentor is definitely a thing to be cherished. My future career has been momentously shaped by these two men.

To Matthias Kling, who first introduced me to strong-field nano-science and strongly influenced the overall flavor of this thesis.

To Daniel, who through our many joint group meetings and VMI expertise has become a go-to person for knowledge and assistance. And gardening chats.

To Carlos, who always had time to listen to my wild ideas where I always came away more excited about my work than when I came in. The openness you showed to an up-an-coming graduate student has shaped by future path in many different ways. It goes to show that you cannot always pick your (work) neighbors, but you can definitely make the best of them.

To the physics professors at KSU, including Vinod (and especially his group members Mac and Aram) who assisted in getting my JRML experiment off the ground with their LabView skills.

To the Fennel group, including Thomas, Christian, and Lennart who never hesitated to give excellent guidance and advice. Their collaboration, including an excellent visit to Rostock, helped influence the research and results in this thesis. A special acknowledgement to Christian (and those assisting) in the analysis of the LCLS X-ray scattering data where the data included in this thesis and future publications was an especially large undertaking.

To the Kling group, especially Philipp who have been close collaborators for most of my graduate career. Their advice and helpfulness has been a benefit for my own projects and our shared experiments. It has been a pleasure to work with Philipp (and ongoing) on these nanoparticle projects.

To all the support staff here at Kansas State University, especially in the Physics Department. To Al, Chris, Andy, Russ, Justin, Mike, Scott, and Jim who spent many hours helping design and build experimental apparatus, including the many ‘chats’ that occurred weekly.

To the Physics office staff, including Peggy, Deanna, Lindsay, Kim, and Kim who are always incredibly helpful for any and all questions.

To Jim who taught and guided my glassblowing skills which proved to be a critical assest. He is always a friendly face for a good chat, regardless of the topic.

To Ben from Cytodiagnostics, my "nano-guy" who truly went above and beyond. His helpfulness and knowledge was well-appreciated.

To those graduate students who I have known over the years, especially the Sorensen, Rudenko and Rolles group members (Javad, Jessy, Raiya, Yuli, Arjun, Balram, Xiang, Yuba, Shashank and Farzaneh) and others including Sean, Amy, Ben, Travis, Jason and Bethany. And to Adam and Derrek for those many late night JRM 'discussions' about 'work-related' topics. These are the memories that make graduate school an unforgettable experience.

Dedication

This thesis is dedicated to my children, Anthony, Oliver, and Sophia, and most especially to my wife, Jacqueline. She is the rock of our family and took the many late nights, long hours, and busy schedules over the years in stride. My accomplishments would not have been possible without her continued love and support.

Chapter 1 - Introduction and Background

- *Science progresses not only because it helps to explain newly discovered facts, but also because it teaches us over and over again what the word 'understanding' may mean"*

  - *Werner Heisenberg*

1.1 Motivation

Human ambition to grasp the universe we inhabit begins with an awareness of simple observations. These range from the childlike 'Why is the sky blue?' to the contemplative 'How many stars in the night sky?'. Each one of these questions is asking for an explanation of how our world interacts with itself. How sunlight scatters off the atmosphere determines our blue skies and fiery red sunsets [1] while astronomers estimate 10^{24} (a trillion trillion) [2] stars in our universe. Fundamental questions lead to great advances in humanity's collective knowledge and continuously open new frontiers of research.

Science observes the interactions of the physical world and uses mathematical constructs to describe them. Observations and patterns play a key role in exploring these interactions. The use of light to see and understand physical matter is a vital part to scientific research. Light can be used as a probe and a tool for investigating phenomena as wide-ranging as the study of subatomic particles to the history of the universe. Here, I utilize light to further understand matter-matter and light-matter interactions in nanoparticle systems.

1.1.1 Nanotechnology

Nanoparticles (and the aptly called nanotechnology) are a form of matter with a size dimension on the order of 10^{-9} meters (nanometer). They are a collection of atoms and/or molecules that are larger than their individual constituents but are not yet reaching macroscopic dimensions. For scale, a single gold atom has a radius of 0.135nm while a gold nanosphere with a 5nm diameter already has 4000 atoms. Nanoparticles (and, in general, any nano-scale systems) are a hybrid form of matter between a macroscopic solid and an atomic system which allows for the study of the transition between these two extremes. Their unique composition, size, and shape result in novel properties that have the potential to impact many areas of science. Nanoscience is truly an 'engineered' science in that every aspect of the nanosystem can be fabricated and manipulated to exploit specific characteristics.

Nanoparticles have been used by humanity for millennia dating back to the extraction and use of gold in the 5th Century B.C in Bulgaria, Egypt, and China [3]. Colloidal or 'soluble' gold was used for aesthetic and curative purposes such as coloring glass and ceramics, as seen in stained-glass windows. One of the most famous example is the 4th century B.C. Roman 'Lycurgus Cup' as seen in Figure 1.1 which is a glass cup infused with gold and silver colloids [4]. The presence of the gold-silver alloy nanoparticles imparts the cup's ability to look green in reflected light and ruby red in transmitted light.

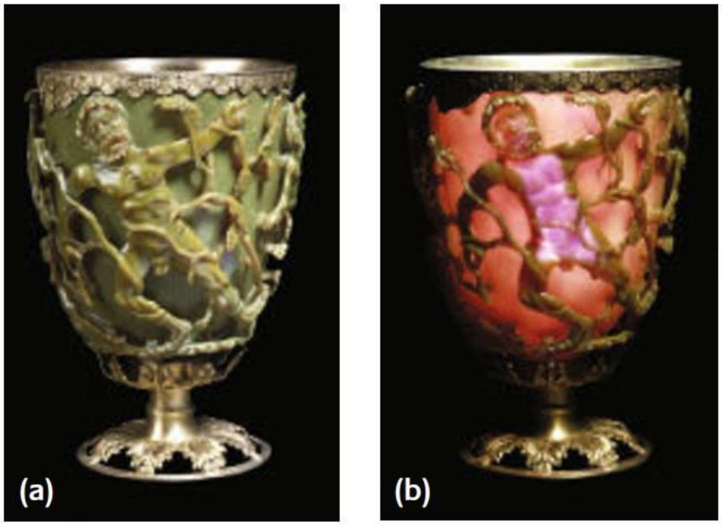

Figure 1.1 *4th century B.C. 'Lycurgus Cup'. The presence of a gold-silver colloid in the glass results in the **a)** reflected green light and **b)** transmitted red light. Image from [4].*

Michael Faraday conducted what could be considered the first scientific study on metal colloids, especially for gold [5]. A sample of his gold colloid (Figure 1.2) from can still be seen over 150 years later and is a testament to Faraday's work and the impressive stability of gold. Gustav Mie in 1908 explained the color of a gold colloid by applying Maxwell's electromagnetic theory to provide a theoretical basis for light absorption and scattering by a spherical object [6].

Figure 1.2 *Faraday's gold colloid solution stable after 150 years. Photo from Royal Institution's Faraday Museum.*

The last two decades of the 20th century opened the floodgates to the synthesis and quantification of nano-materials. Techniques such as transmission electron microscopy allow for the direct observation of nano-sized objects. Improved spectroscopic methods greatly increased the ability to observe minute nanoparticle properties. A beautiful example is that of quantum dots (QDs) which are single nanometer-sized semiconductor nanoparticles shown in Figure 1.3. These QDs usually range from 2-6nm in diameter and their emission wavelength is highly dependent on their dimensions. These particles exhibit quantum confinement and the particle in the box model can be used to predict their energy levels [7]. A small 'box' will emit shorter wavelengths than a longer 'box' which is seen in the QD fluorescence emission. Metallic nanoparticles are of great interest because of their optical properties, especially in the visual wavelength range. They can also support surface plasmons which show great potential in the field of nanoplasmonics [8–12].

Figure 1.3 *Different sized quantum dots. QDs emit different wavelengths as a function of their size (left to right = small to large diameter). Photo from Wikipedia.*

Nanotechnology is the application of nanoscience. There is a multitude of active research areas to use nanotechnology to better the world around us. A short, incomplete list include solar cells, cancer treatments, ultrafast electronics, environmental waste clean-up, and computing [12,13]. The use of nanoparticles has become ingrained into our everyday lives and will only continue to change the way we live.

1.2 Nanoparticle interactions

Nanoparticles present a new and unique scaffold for basic science research. They provide ample avenues to study their fundamental properties through interactions with themselves or with ultrafast, intense laser sources. My work ties together several promising research directions in both nanotechnology and ultrafast laser physics. On one hand, an immense interest in perfecting synthetic techniques has led to the ability to perform first-of-its kind fundamental experimental studies probing into the interaction between individual nanoparticles. On the other hand, the use of intense, femtosecond lasers in the optical and x-ray domains allows me to explore nanoparticle interactions with light on the femtosecond (10^{-15} sec) timescale and the natural nanometer length scale of isolated nanoparticles. These two ideas are the central theme of the thesis presented here.

1.2.1 Solubility of nanoparticles

Basic thermodynamic quantities such as chemical potential, entropy, and enthalpy are properties of a system that can be measured. These values describe the state of a physical system, be it atoms, molecules, gases or bulk matter. Entire handbooks are filled with such quantities (my 82nd edition of the CRC Handbook of Chemistry and Physics is over 8cm thick) of almost every material and their derivatives known to science. These valuable resources are the aggregate of many decades of work and countless amounts of laboratory research.

The field of nanoscience is rapidly synthesizing new and novel structures with incredible potential, yet basic thermodynamic properties for these systems is lacking. A centralized 'handbook' for nanoparticle properties would be an invaluable source for the large array of nanoparticle-themed research currently active. Once the basic building blocks of a nano-system are understood, new and exciting possibilities are bound to transpire.

Here, I advance the concept that a nanoparticle colloidal suspension is a solution with thermally reversible solubility phenomena [14]. A solution is traditionally seen as a single-phase homogeneous mixture of a solvent and a solute that cannot be separated. However, using the definition of a solution as simply a homogenous mixture [15,16] applies well to a nanoparticle suspension with a narrow size distribution. Observations by our group and others have shown that nanoparticle suspensions show behaviors common to many molecular and ionic solutions [17–21] including the thermal reversibility of aggregation and nucleation phenomena. These observations are dependent on having a monodisperse (narrow) size distribution which is precisely what digestive ripening is used for [22].

To quantify a thermodynamic property, it is useful that all the individual constituents (nanoparticle monomers) of the solute are almost the same. Digestive ripening is similar to Oswalt ripening except that large nanoparticles 'transfer' some of their atoms to the smaller particles until a size equilibrium is found [22]. Once these self-similar nanoparticles are synthesized, the ability to extract thermodynamic properties becomes an intriguing experiment.

A solution/suspension of monodisperse 5nm gold nanoparticles (AuNPs) dissolved in toluene exhibit thermally reversible solubility, show aggregation phenomena, and mimic molecular and ionic behaviors. Classical solution theory is extended to analyze the thermodynamic properties of a nanoparticle system.

1.3 Matter response to intense optical fields: from atoms to nanosystems

1.3.1 Merging nanotechnology and ultrafast laser science

Nanoparticles occupy a unique position in science because of their recent arrival and interesting properties. One of the most exciting areas for their application is the emerging field of ultrafast nanophotonics [100]. This rapidly developing branch of science is to a large extent based on the ability of modern nanotechnology to design and synthesize nanometer-sized structures with a tunable response to electromagnetic radiation, controllable on the femtosecond or sub-femtosecond time scale [11,12,92,101,102]. A range of particular applications includes ultrafast computation and information storage on the nanoscale [103], the generation of extreme ultraviolet (XUV) frequency combs [104], plasmon-enhanced photo-processes in femtosecond photochemistry, light detection, and solar energy conversion [105]. This has caused an increasing interest in different scientific communities to have a detailed understanding of the behavior of nano-objects irradiated by short, intense laser pulses. From the more fundamental point of view, nanoparticles bridge the gap between atomic/molecular and bulk matter and thus offers unique opportunities to study light interactions with complex systems as a function of their size, shape, composition, and electronic structure [23].

Experimental methods typically used to characterize the ultrafast response of nanoscale objects to intense laser radiation include techniques based on absorption measurements [106], detection of the fluorescent light emitted as a result of direct field-induced or secondary collisional excitations [107,108] or different types of charged particle spectroscopy [24-26,109-111]. The latter include ion time-of-flight mass-spectrometry, energy- and angle-resolved ion measurements, and various photoelectron spectroscopy and imaging techniques. Photoelectron spectroscopy in a single-photon regime ("weak field" limit) makes use of the photoelectric effect to probe intrinsic properties of solids, gases or liquids by measuring the emitted electrons and has long been one of the most important sources of our knowledge of the electronic structure of matter [112]. It was also successfully utilized to characterize the interaction of atoms and molecules with more intense external fields, typically generated by pulsed laser sources [113]. In this case, the emission of an electron requires more than one photon, and, depending on the laser parameters, can be better described either within the multiphoton or tunneling ionization picture. The extension of photoelectron spectroscopy and imaging techniques to isolated nanosystems exposed to intense laser pulses presents the prospect of probing nanoscale electron motion on a sub-laser cycle timescale and is currently an active area of research [24-26,114,115].

1.3.2 Ionization of atoms by intense laser pulses

Single electron emission from atoms exposed to intense short-pulse laser fields is one of the most fundamental and well-studied reaction channels in non-linear strong-field physics [113,116,117]. The intuitive view of such ionization processes for optical frequencies evolves from a "photon-based" picture at moderate laser intensities, to the interaction with an oscillating electromagnetic field in electron tunnelling or the complete suppression of its binding potential in

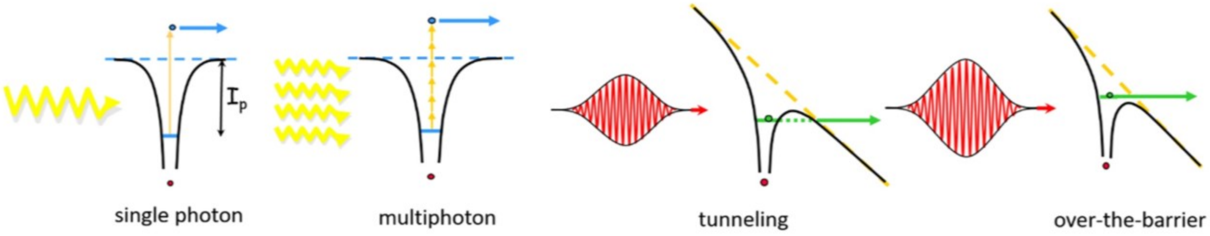

Figure 1.4 *Schematic representation of different ionization regimes*

the high-intensity regime (see Figure 1.4). Somewhat more quantitatively, ionization is often considered as either a “multiphoton” or “tunnelling” process depending on the value of the so-called Keldysh parameter γ [118]

$$\gamma = \sqrt{I_p/2U_P} \tag{1}$$

where U_P is the ponderomotive potential (wiggling-energy of a free electron in an oscillating laser field) and I_p is the ionization potential. Here, U_p is defined as

$$U_p\,[eV] = \frac{e^2E_0^2}{4m_e\omega^2} \approx 9.34\times10^{-20}\times(\lambda[nm])^2\times I\,[W\,cm^{-2}] \tag{2}$$

where e is the electron charge, E_o is the laser electric field, m_e is the electron mass, ω is the angular frequency of the laser, I is the intensity of the laser, and λ is the laser wavelength.

For a given wavelength, the Keldysh parameter describes the ionization regime. At high intensities where $\gamma < 1$, tunneling or classical over-the-barrier ionization is usually the dominant process. For lower intensities where $\gamma \gg 1$, multiphoton ionization provides a better simplified picture, where the absorption of n photons is required to overcome the binding potential ($n\hbar\omega > I_p$). Theoretically, ionization processes in this regime can be adequately described by low-order perturbation theory [116]. In the intermediate regime, where $\gamma \sim 1$, mixed “field” and “photon” language is often used. Of particular importance here is the concept of above-threshold ionization (ATI), which is the extension of a multiphoton picture implying that more photons than the minimum number needed to overcome the binding energy of the electron is absorbed. This results in a series of discrete peaks in the photoelectron spectrum spaced by one photon energy [119,120].

There are several theoretical approaches aimed at calculating absolute and differential ionization rates for high-order above-threshold and tunnel ionization. Most of them are based on the so-called "strong-field approximation", which assumes that the acceleration of the electron after it is released from the atom is dominated by the external laser field [118,121,122]. This approximation provides the framework for a very intuitive model describing laser-atom interactions, often referred to as "three-step model" or "simple man model" [123,124]. The essence of this approach is sketched in Figure 1.5 for a linearly polarized field. The electron initially tunnels from an atom (step 1) and is then driven by the oscillating field of the laser (step 2). Two general classes of electron trajectories in the field can be distinguished: those which return to the position of the atom, and those that leave the atom without return ("direct electrons"). The former group of trajectories results in the interaction between the electron and its parent ion known as "rescattering" or "recollision" (step 3). The "recolliding" electron can either **i)** recombine and emit a high-energy photon (step 3a), **ii)** scatter inelastically resulting in an impact ionization or excitation of a second electron, **iii)** or

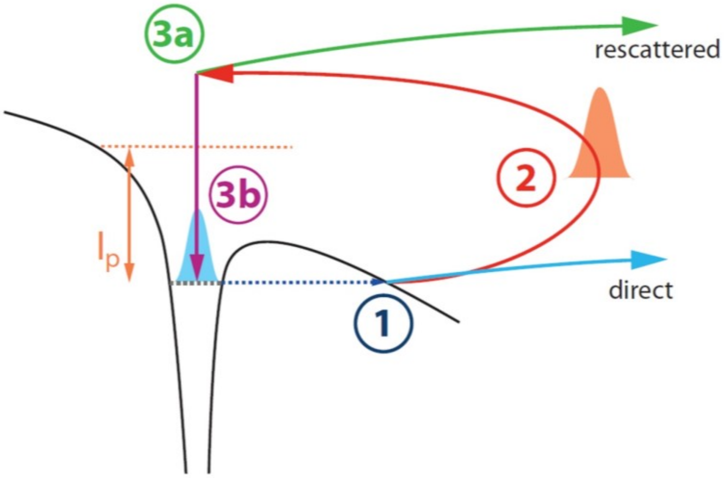

Figure 1.5 *Schematic of the 'three-step model' of laser-atom interaction. From [87]*

scatter elastically and gain additional energy from the laser field (step 3b). Within this oversimplified picture, each of the above classes of interaction was found to be responsible for such important strong-field phenomena as high-harmonic generation [125], non-sequential double ionization [126] and high-energy above-threshold ionization [127], respectively. Because of the sub-optical cycle synchronization between the electron liberation and "recollision", the latter process also provided the basis for modern attosecond science, in particular for attosecond light pulse generation [102,125].

Of importance for this work is the process of elastic rescattering, which allows an electron to gain energy from the field. Within the simple-man model outlined above, it can be easily shown that the maximum kinetic energy a "direct" electron can gain after a laser pulse (under the assumption that its envelope is considerably longer than one optical cycle), is equal to $2U_p$, where U_p is the ponderomotive potential introduced above [123,128]. However, if the electron experiences a rescattering event, which changes its phase with respect to the oscillating driving field, it can gain considerably higher energy [127]. Within the three-step model, the largest energy an electron can gain from the field occurs when the electron trajectory is exactly backscattered upon recollision and is approximately $10U_p$. A more precise expression, taking into account the effect of the atomic potential yields $E_{max} = 10.0007U_p + 0.538I_p$ [129].

1.3.3 Nanoparticles in intense laser pulses

Atomic ionization driven by strong external fields outlined in the previous section still represents a significant challenge for theory, with the exact *ab initio* treatment currently out of reach for systems larger then helium. However, countless exciting and novel applications involve interactions of such laser fields with much more complex systems involving thousands to millions of atoms [100]. Therefore, the development of theoretical methods and experimental techniques aimed to unveil the strong-field response of large objects ranging from clusters of a few atoms to nanoscale systems and to macroscopic solids currently attract plenty of attention. Considerable work in this direction was done on metal and rare-gas clusters, which represent complex systems tunable in size from a few atoms to tens of nanometers. The interplay of the individual atom response, buildup of large Coulombic potentials, distinction between “inner” and “outer” ionization and the role of collective effects have been studied as a function of cluster material and size as well as of driving laser parameters (wavelength, intensity, pulse duration etc.). Reviews of most important work on clusters in intense laser fields can be found in [96,130].

Experimentally, the most impressive observation is the possibility of efficient coupling of the optical laser energy into clusters, resulting in the production of very energetic ions and electrons as well as the emission of high energy x-rays [108,109,111]. From the experimental point of view, apart from material and shape restrictions, the main limitation of clusters as model systems for detailed quantitative understanding of the mechanisms of laser-matter interactions is their typically broad size distribution. This limitation can be significantly relaxed with advances of modern nanotechnology, allowing for the synthesis of nanosystems with precisely controlled sizes, shapes and properties. As a result, several recent studies focused on the response of well-defined spherical

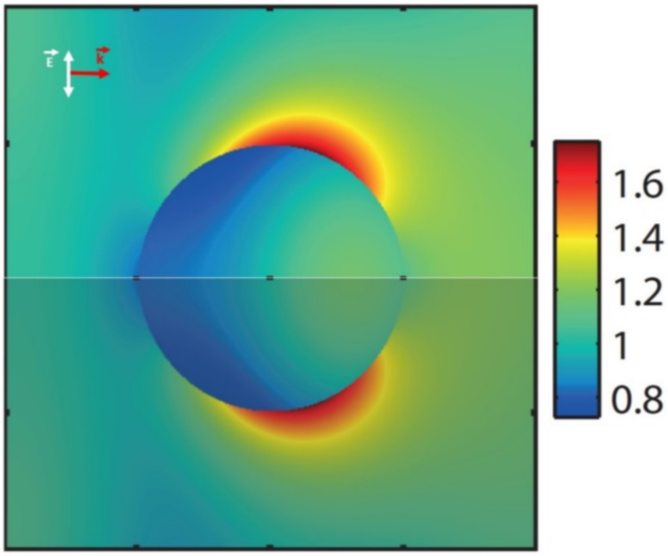

Figure 1.6 *Localized, near-field enhancement of 300nm SiO_2 nanoparticle relative to incident field. Image from [87]*

nanoparticles to intense, ultrashort laser pulses.

The main features defining the nanoparticle's response to a large external field are a local near-field enhancement (enhanced relative to incident field, see Figure 1.6) and related sub-wavelength localizations of the effective field driving the electrons in the nanoparticle. For metals, near-field enhancement is often described in terms of collective electronic excitations (plasmons). However, even dielectric particles without any pronounced dc-conductivity exhibit near-field enhancements at optical frequencies, quantitatively governed by the wavelength-dependent dielectric function [87,96,100]. For certain material properties, nanoparticles smaller than the incident wavelength can be imagined as an antenna for optical light, with its response leading to a pronounced near-field enhancement and resonant oscillations of the electronic polarization.

Several studies of the photoelectron emission from dielectric nanospheres irradiated with few-cycle laser pulses demonstrated a dramatic increase in electron energies compared to atoms exposed to the same fields. [24-26,86]. Combined experimental and theoretical analysis highlighted the ability to understand and control electron emission [24,25]. In particular, phase-stable few-cycle pulses incident on gas-phase SiO_2 spherical nanoparticles in vacuum were utilized for precise control of electron motion on the attosecond timescale. The dynamics of this interaction show some similarities to those of atoms and molecules under similar conditions but differ in noteworthy ways. The nanoparticle response to the electric field of the laser pulse produces a localized near-field, which can have a larger amplitude than the incident field (see Figure 1.6). The trajectory of a photoelectron is dictated by the convolution of all the fields present, which includes the laser field, nanoparticle's near-field, and the Coulomb interaction with other charges (ions and electrons) created in the nanoparticle. This results in the emission of electrons with energies much higher than those for individual atoms. The final photoelectron momentum and angular distribution are determined by the interplay between these forces described above. It was shown that the trajectories involving electron rescattering (discussed in the previous section for atoms), in such a combined effective field are responsible for the production of the electrons with highest energies [24-26,86].

Besides the phase-controlled emission of high-energy electrons, a deep insight into the dynamical evolution of the near-field enhancement in nanoparticles can be obtained by attosecond photoelectron streaking. This technique is based on the photoionization by an attosecond XUV pulse and the subsequent modulation of the electron energy by the oscillating laser field. Its application to isolated atoms allowed for the first direct visualization of a few-cycle light wave [132] and sparked heated discussion on the time delays in photoionization [133]. For nanosystems, this approach holds promise for the time-resolved imaging of the dielectric response and plasmonic fields. It was successfully applied to study the electron propagation and screening effect in solid-state samples. The applicability of attosecond streaking spectroscopy to the element-specific investigation of induced time-dependent electric fields near nanoparticle surfaces has also been recently demonstrated both, experimentally [135] and theoretically [89,90].

1.3.2 Size and material effects

Mechanisms of electron acceleration in isolated nanoparticles crucially depend on their size and composition. Size-dependent properties can be readily analyzed by varying the diameter of the nanoparticles where the number of emitted photoelectrons, their kinetic energies, and angular distributions are all related to the nanoparticle's dimensions. In [25], size dependent energy and angular photoelectron distributions are measured and clearly show an increased energy cutoff (highest electron energy detectable) along with a propagation-induced directionality. As the dipole approximation breaks down for large particles (the particle diameter becomes comparable to the incident wavelength), the maximum near-field enhancement shifts away from the particle poles and towards the laser propagation direction (see Figure 1.6). This shift becomes evident in the final photoelectron angular distribution.

Nanoparticle material dependence also plays a significant role in understanding the particle's response to intense laser light, electron emission mechanisms and final photoelectron spectra. Intrinsic nanoparticle properties such as binding energies, permittivity, and field enhancement all can affect the electron acceleration process [26]. Theoretical predictions for localized near-field enhancements vary significantly as a function of the particle material and size [89-91]. It should be noted that in an intense laser field, a clear distinction between dielectric, semiconductor and metal nanoparticles becomes somewhat problematic because of the significant "inner" ionization [96,130] resulting in the presence of quasi-free electrons for any material. Therefore, the role of material properties in the laser-induced electron dynamics in nanostructures might evolve as a function of laser parameters, and in particular, laser peak intensity. Understanding basic mechanisms of size-, material- and intensity-dependent dynamics in gas-phase nanoparticles is the central theme of the work presented in this thesis.

1.4 Time-resolved dynamics in nanoparticles using free electron lasers

1.4.1 X-ray free-electron lasers: novel probe of nanoscale structure and dynamics

Most of the experimental techniques studying light-driven dynamics in nanoscale objects, discussed in the previous section, rely on the detection of charged particles, either ions or electrons. These charged-particle spectroscopies are very efficient for weak fields and work reasonably well at moderate laser intensities. However, the large degree of ionization at high laser intensities results in the creation of an enormous amount of charges where the space-charge effects strongly influence the experimental observables. These difficulties caused significant interest in the development of photon-based techniques aimed to characterize light interactions such as high-harmonic generation [135] or measurements of high-energy x-ray emission [109] from nanoparticles. Another novel and promising approach for the direct imaging of light-driven nanoparticle dynamics is time-resolved scattering, enabled by the development of x-ray free-electron lasers (XFELs).

Many fundamental questions related to the structure of matter were answered with the use of x-rays. X-ray diffraction on crystal structures (x-ray crystallography) has allowed for three-dimensional reconstruction of biological objects with the resolution approaching the natural length scale of the atom. X-ray diagnostics is indispensable for numerous medical applications. Countless advances in science such as the determination of the full structure of DNA were also made possible. New sources of XFELs can deliver coherent x-ray bursts of femtosecond duration and unprecedentedly high intensities (containing 10^{12}-10^{14} photons per pulse) that significantly broaden the range of applications of x-ray diffraction techniques [136]. The central concept here is the so-called "diffract-before-destroy" approach, which utilizes very intense and short x-ray pulses to catch a snapshot of the target structure before it gets modified and eventually destroyed by radiation damage [137]. This technique can obtain single-shot diffraction patterns from much smaller objects compared to conventional x-ray sources. It makes it possible to use x-ray diffraction to study materials that were previously inaccessible. One important example is the so-called nanocrystallography, which allows for obtaining high-resolution structural information for objects for which large crystals cannot be grown [138]. Single-shot, single particle imaging of nanoscale objects also appears to be in reach [139,140].

Because of their femtosecond pulse durations, XFELs can be efficiently applied to study the evolving structure of matter with high temporal resolution. This was impressively demonstrated on a number of molecular systems excited by the synchronized optical laser and probed by different types of x-ray spectroscopies [136]. Very recently, this approach was extended to study laser-driven dynamics in nanoscale systems [28].

1.4.2 Rare gas clusters as model systems for time-resolved x-ray scattering

Similar to the optical domain (see Section 1.3), early experiments at XFELs made use of rare-gas clusters as model objects for bringing the studies of light-matter interactions to the nanoscale [27–29]. These mesoscopic systems are easy to generate, have an adjustable mean size, and a large scattering and absorption cross-sections which make them a powerful "nano-lab" for many proof-of-principle experiments. Nano-clusters in vacuum also provide a straightforward opportunity to study isolated systems, detached from any sort of substrate. Single-shot x-ray diffraction using the XFEL source makes it possible to image one cluster at a time. As this FEL pulse has a duration of femtoseconds, time-resolved experiments can also be performed. Figure 1.7 shows an x-ray diffraction image of a single Xe cluster which encodes information about the cluster size and scattering intensity. As was shown in [27], the latter information can be extracted from the total number of scattered photons, and the former from the observed diffraction fringe spacing.

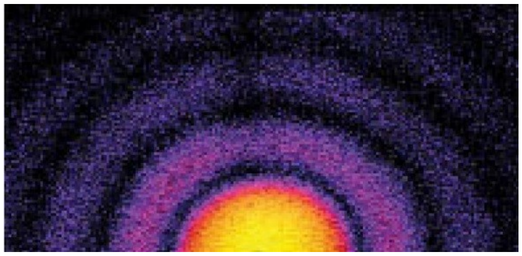

Figure 1.7 *X-ray scattering image from a 60nm Xe cluster. Image taken from [27].*

The ability to image isolated nano-clusters with a single shot enables the FEL beam to act as a camera ‘shutter’ to observe ultrafast dynamics. This can be exploited to resolve, in real-time, laser-driven dynamics in nanosystems at rather high intensities, where techniques based on electron or ion detection experience difficulties because of space-charge effects. A recent proof-of-principle experiment on Xe clusters demonstrated the feasibility of this approach [28]. The main idea of this study is sketched in Figure 1.8. Xe clusters of a few tens of nanometers in diameter were pumped with an intense (~10^{15} W/cm^2) femtosecond optical laser. Under these conditions, rapid ionization causes disintegration of the cluster, effectively turning it into expanding nanoplasma. The formation and evolution of the ion and electron densities in the created nanoplasma is deduced from a sequence of x-ray diffraction images created by an intense x-ray pulse arriving at variable, well-defined delays after the optical laser pulse. The process of x-ray diffraction relies on the elastic scattering off the individual atom’s electron cloud density. Any change in the arrangement of the electron density is seen in the small angle x-ray scattered image.

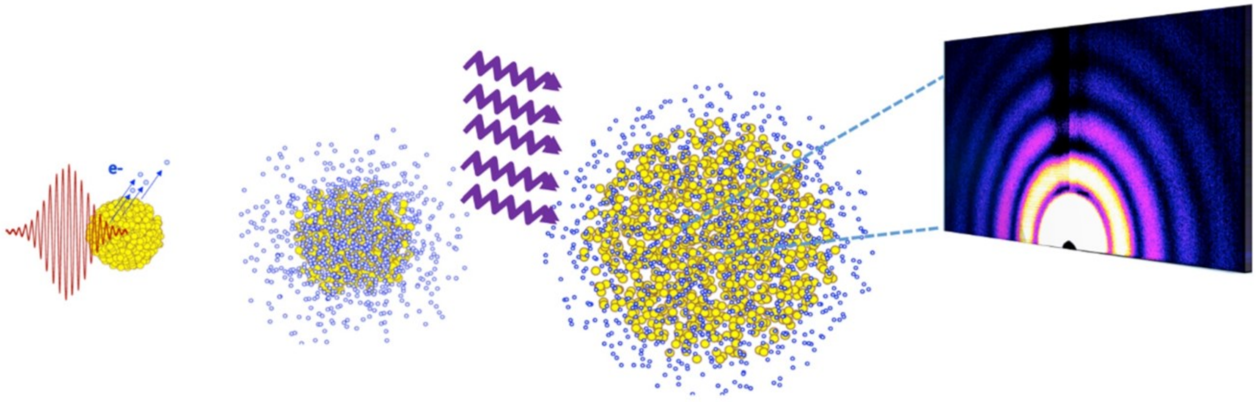

Figure 1.8 *Time-resolved x-ray scattering used to track the formation and evolution of a nanoplasma in a Xe nanocluster. An optical (red) pulse initiates the dynamics, while the x-ray (purple) comes at a set time-delay later. Image taken from [29].*

1.4.3 FEL Adaptable Nanoparticle Sources (FANS)

While the time-dependent dynamics of rare gas clusters is a milestone in the use of time-resolved single-particle imaging, the clusters as a target have severe limitations for this kind of experiment. First, the range of materials available for efficient cluster formation with a reasonable technical effort is rather limited. Second, more importantly, cluster sources typically yield very broad size distributions, resulting in the averaging of all the experimental observables over particles with significantly different size-dependent responses. In single-shot, x-ray only experiments using clusters, imaging is an elegant way to overcome this difficulty, as demonstrated in [27]. There, the measured data included x-ray scattering images, fluorescence spectra and ion charge state distributions that were sorted according to the spacing of the diffraction patterns and their total number of photons, allowing one to recover the results for single-size, single x-ray intensity conditions. However, this approach is not applicable to the studies of laser-driven dynamics since the spacing of the fringes might evolve as the cluster expands. This places a requirement for the development of monodisperse nanoparticle sources.

Several techniques were proposed to inject individual nanoscale objects into vacuum (see, e.g., [42-44]). Among them, some of the most successful techniques employed at XFEL facilities are based on aerodynamic-lens injectors [51,52, 141]. The development of such a FEL Adaptable Nanoparticle Source (FANS) [142] allows for a wide-ranging array of samples that that are potentially advantageous for many different FEL applications, including the injection of nanoparticle samples with a very narrow size distribution. The main advantage of FANS over a rare gas cluster source is the sample quality and selection. The samples to be studied are often prepared off-site and usually in a wet-synthetic method that can produce extremely pure and monodisperse particles. The ability to precisely tailor the samples before injection into vacuum and to maintain this narrow size distribution increases the reproducibility of the data and the amount of information which can be obtained from such an experiment.

Metal and dielectric nanoparticles (e.g., Au, Ag, SiO_2) can be synthesized with small size distributions (usually <10% dispersity) and with very defined surface features. In a single-shot x-ray imaging experiment, the diffraction fringes are the observable where the scattering information resides. Reproducibility lies in the ability for each nanoparticle interaction with the laser to be nearly identical to the previous one. A time-dependent 'movie' of the expansion of a nanoplasma on the surface of a nanoparticle can be made by performing an experiment where the conditions are all pre-optimized. The near-sphere-like particles also produce very clean, clear diffraction patterns. As statistics are crucial in following the time-dependent plasma evolution, FANS need to have the ability to produce a rather dense nanoparticle beam. Overall, a nanoparticle sample can be synthesized which precisely meets the size and shape requirements to ensure excellent signal to noise in the scattering signal.

1.5 Thesis outline

The overall theme of this thesis is understanding how nanoparticles interact with their surroundings, be it photons or matter. The thesis presents novel technical developments in nanotechnology and report three different, yet closely related studies enabled by these technical progresses. The results presented here were obtained at Kansas State University (KSU) and at the Linac Coherent Light Source (LCLS), the world's first hard x-ray free electron laser.

Beyond the motivation ideas and some background information presented above, the thesis is organized as follows: Chapter 2 describes experimental concepts and setups used for the studies of nanoparticle interactions. After a brief overview in Section 2.1, the tools needed for synthesis of nanoparticles and for the solubility studies are described in Section 2.2. Section 2.3 is devoted to the design, development and characterization of the nanoparticle sources used throughout this work. This is the main technical advance achieved in this work. The design and specific requirements for the nanoparticle source also provide an important practical link between the photoelectron spectroscopy experiments and the FEL-based x-ray imaging. Section 2.4 describes the detection setup used for photoelectron studies, centered around the so-called velocity map imaging (VMI) spectrometer. Section 2.5 outlines the main features of intense, near-infrared femtosecond laser systems used at KSU and at the LCLS. Finally, Section 2.6 provides an overview of main tools employed in the FEL-based study at the LCLS.

Chapter 3 presents the results of the nanoparticle solubility studies. A detailed and unique approach to measure and analyze the thermodynamic properties of nanoparticle systems provides first-of-its kind data. Self-similar nano-systems exhibit behaviors analogous to molecular or ionic solution and present a method of determining inter-nanoparticle interaction potentials. The temperature-dependent solubility of small gold nanoparticles provides experimental data to measure nanoparticle interactions.

Chapter 4 describes the outcome of the experiments aimed to determine basic formation mechanisms of the photoelectron spectra from nanoparticles irradiated by moderately intense ($\sim 10^{11} - 10^{14}$ W/cm^2), 25 fs NIR laser pulses. After the introduction of a novel technique allowing one to avoid focal volume averaging (Section 4.1), Sections 4.2 and 4.3 present the size-dependent photoelectron data obtained for SiO_2 and gold nanoparticles, respectively. The results for both materials are compared and the basic factors determining the outcome of these experiments are discussed. The last part of the photoelectron chapter (Section 4.4) reports on similar studies performed on silica core – Au shell nanoparticles tailored to have a resonant absorption peak at 800 nm, close to the central wavelength of the laser used in this work.

The results of the LCLS experiment on x-ray scattering imaging of the nanoparticles excited by intense (10^{15} W/cm^2) femtosecond, NIR laser pulses are presented and discussed in Chapter 5. Finally, Chapter 6 presents the summary of the work done and outlines some promising future directions.

Chapter 2 - Experimental Methods

- *Damn the torpedoes; Full steam ahead.*

- *David Glasgow Farrogut,*
as often repeated by
Christopher M. Sorensen

2.1 Experimental synopsis

The experiments described in this thesis present an amalgamation of my background in science. It is a mixing of physics and chemistry, a weave of condensed matter, physical chemistry and thermodynamics with ultrafast, strong field physics. It orbits around a central theme of understanding the nanoscale world, one nanoparticle at a time. A diverse set of apparatus was employed in my research, ranging from state-of-the art free electron lasers to the humble UV-Vis spectrometer.

Two discrete distinctions are made in how nanoparticles are investigated. The first method comes from the viewpoint of nanoparticles in their more customary form; in solution as an ensemble of particles. The second is a true single particle, gas-phase, in-vacuum study of how ultrafast, intense light interacts with nanoparticles. The first employs simple absorption measurements (Section 2.2) while the latter is a unique blend of particle sources (Section 2.3), velocity map imaging spectrometer (Section 2.4), ultrafast NIR lasers (Section 2.5), and Free Electron Lasers (Section 2.6)

2.2 Nanoparticle solubility

2.2.1 Monodisperse gold nanoparticles

To study a macroscopic property that is dependent on the nanoscopic properties of the system, a consistent synthetic method is required. Synthesizing monodisperse nanoparticles with a narrow size distribution (<15%) ensures that any bulk measurement can be extrapolated back to the single monomer entity of the system. The temperature-dependent solubility of an in-solution gold nanoparticle (AuNP) system is associated to its enthalpy of dissolution, an intrinsic property of the ensemble of individual nanoparticles. At the nanoscale, shape and size are fundamental properties.

Through a novel process developed at Kansas State by the Sorensen and Klabunde group, including Sorensen's previous student Xiao-Min Lin, called digestive ripening, a polydisperse gold nanoparticle system is transformed into a monodisperse solution [18,22]. The size and shape of all the nanoparticles become uniform, as seen in Figure 2.1. The exact mechanism is unknown, but it has become well-documented as a tool to produce particles of uniform dimensions [30–32]. An interest has been taken in understanding how digestive ripening differs from Oswalt ripening [33,34]. Once we can look at a single monomer (single nanoparticle) and with reasonable certainty say that its colloidal neighbors are nearly identical, macroscopic measurements can be performed that give insight into how nanoparticles of a given size interact with their environment.

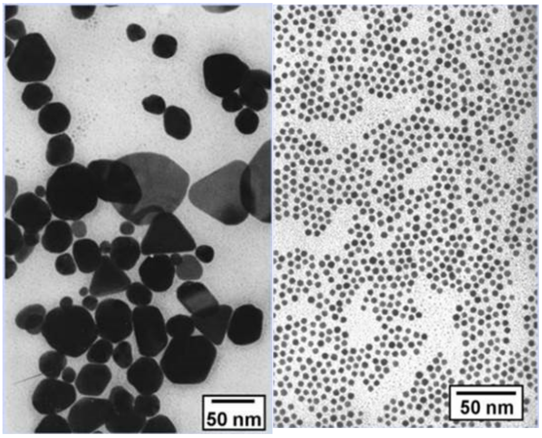

Figure 2.1 *AuNPs before (left) and after (right) digestive ripening. The polydisperse colloid becomes a uniform shape and size.*

2.2.2 Enthalpy of dissolution

A basic thermodynamic quantity is that of the enthalpy, H, of a system. Enthalpy has dimensions of energy or energy per mole and is defined as

$$\boldsymbol{H = U + pV} \tag{3}$$

where U is the internal energy of the system, p is the pressure, and V is the volume. Thus, enthalpy is equal to the internal energy of the system plus the product of pressure and volume. At constant pressure, the term $p\Delta V$ is the expansion work done by the system to make room for the changing volume, ΔV. Total enthalpy cannot be directly measured but only a change of energy within the system, ΔH [35]. As the laboratory is at constant pressure, this is the most straightforward measure to watch a process (in our case dissolution of nanoparticles) and determine if it is endothermic or exothermic. When one thinks of thermodynamic quantities, pictures of large ensembles of atoms and molecules interacting and reacting come to mind. Entire textbooks and handbooks are filled with such properties of every natural and synthetic chemical known to humanity. Everything from the simplest elements to the largest polymer is well-documented and analyzed. Science has opened a new door consisting of nanoparticles and nanostructures. These come in every size, composition, and shape imaginable [36–40] and each one with a diverse array of properties depending on said variables. Fundamental thermodynamic measurements have yet to be done on the simplest of systems, namely an ensemble of nano-sized spheres suspended in a solvent. This is where we can begin to understand the simplest of properties that can move science forward.

2.2.3 Temperature dependent solubility

The enthalpy of dissolution is the enthalpy gained or lost during the dissolution of a solute into a solvent, at constant pressure. The relative change in enthalpy can be found by measuring the change in solubility of the solute in the solvent by adjusting the temperature. The solubility of a system is a measure of the number of nanoparticles that can be dissolved in a given volume of solvent at saturation. Refer to Figure 2.2 as a representative nanoparticle phase diagram plotted as the total nanoparticle concentration vs temperature. Above the phase boundary, the system resides in a 1-phase regime where the solute is totally dissolved in the solvent at temperature $T=T_A$ and concentration $C=C_A$. The temperature is changed to T_B and the phase boundary is crossed. The concentration of the supernatant will follow the phase boundary line and thus have a concentration $C=C_B$, which is lower than C_A. The excess solute will precipitate (2-phase system) out of solution until a new equilibrium is reached with the supernatant. Another temperature adjustment to $T=T_C$ results in the supernatant concentration of $C=C_C$ and more solute will be precipitated. The concentration of the supernatant,

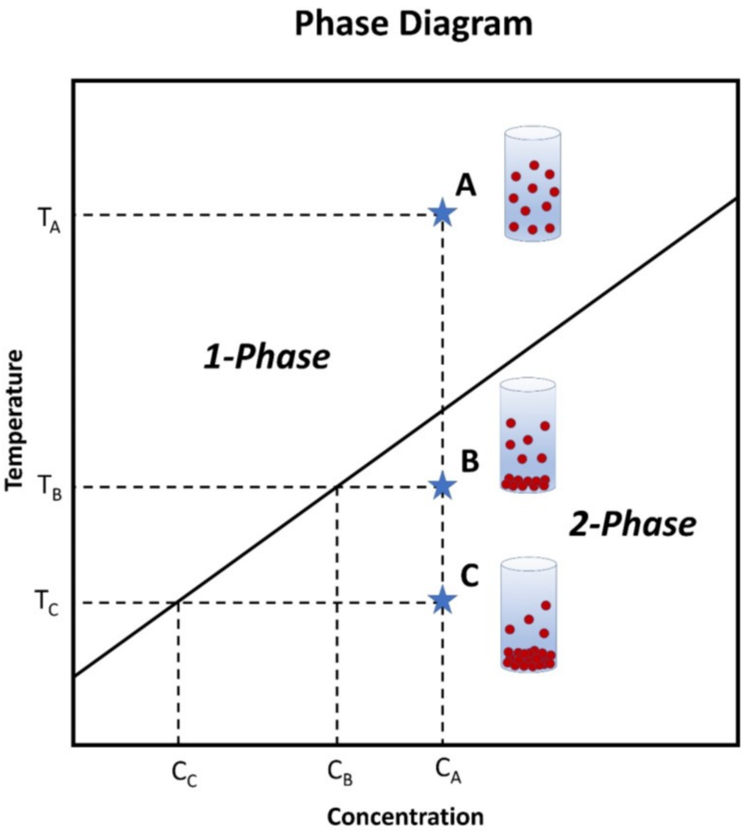

Figure 2.2 *Example phase-diagram. The sloped line is the phase boundary between 1-phase (totally dissolved) and 2-phase (solute in supernatant in equilibrium with precipitate).*

in this example, decrease for every temperature drop below the saturation line. The amount of energy it takes to transform the dissolved phase to solid phase, or vice-versa, in *B* and *C* can be measured as the enthalpy of dissolution.

2.2.4 UV-Vis spectrometer

The workhorse of this experiment was the UV-Vis spectrometer (Ocean Optics USB 4000+). As seen in Figure 2.3**a)**, this device produces a large spectrum of incoherent light ranging from 200nm to over 1000nm. The light is transmitted through the sample and detected using a charge-coupled device (CCD) along with a diffraction grating. The grating spatially spreads the 'white' spectrum into its spectral components across the CCD array. The primary function of this spectrometer is to measure the absorbance of a sample. The total amount of light going into the sample is compared with the amount of light exiting the sample as a function of wavelength. The absorbance spectrum is plotted as a function of wavelength where absorbance is defined as the log (base 10) of the ratio of the incident to transmitted power through a material, as seen in Figure 2.3**b)** for a solution of 5nm gold nanoparticles.

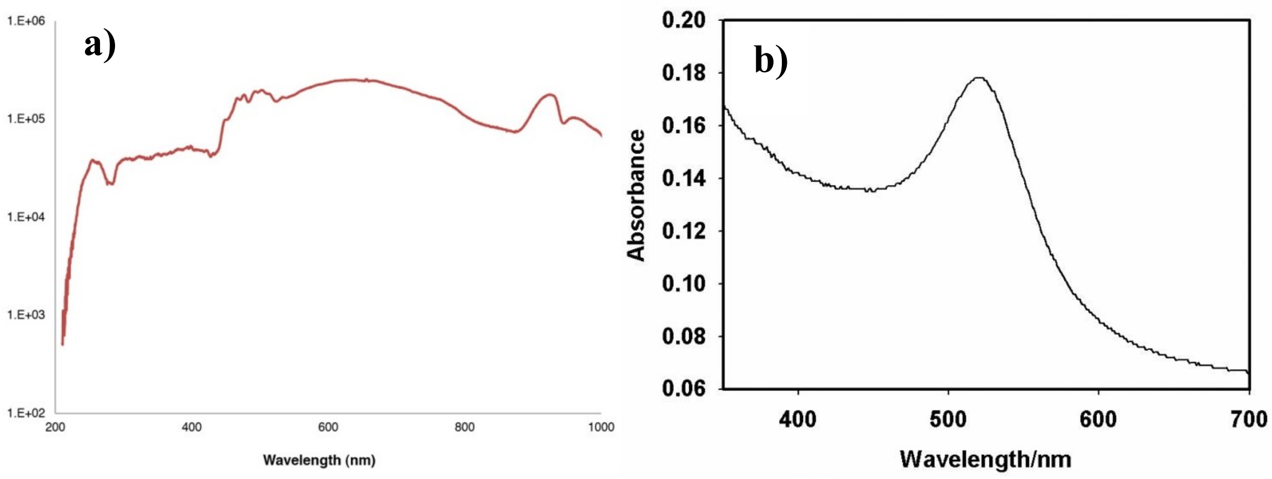

Figure 2.3 ***a)*** *UV-Vis spectrometer spectral output between 200-1000nm* ***b)*** *UV-Vis absorbance spectra from a 5nm AuNP solution in toluene.*

2.2.5 Experimental apparatus

To attain reliable temperature dependent solubility data from nanoparticles, a home-built device was constructed and subsequently modified throughout its lifetime, as shown in Figure 2.4. A commercial bench centrifuge (Eppendorf minispin+; 14500rpm/12000g) was transformed into a temperature controlled (-15°C to 100°C) centrifuge with a built-in UV-Vis spectrometer compatible rotor. Two laboratory heating/chilling units piped an ethylene glycol/water solution through copper tubing surrounding the centrifuge rotor (center). This allowed for precise temperature control over the entire experiment and greatly improved the reproducibility of the experiment. A UV-Vis spectrometer head (consisting of the light output and input fiber optic cables) was constructed to snugly fit over the custom-built centrifuge rotor. The rotor housed the nanoparticle sample and an absorbance reading could be taken without removing the sample from the centrifuge.

One challenge was the ability to reuse the same nanoparticle sample through multiple temperature scans. Toluene has a low vapor pressure and thus evaporates quickly. Losing solvent

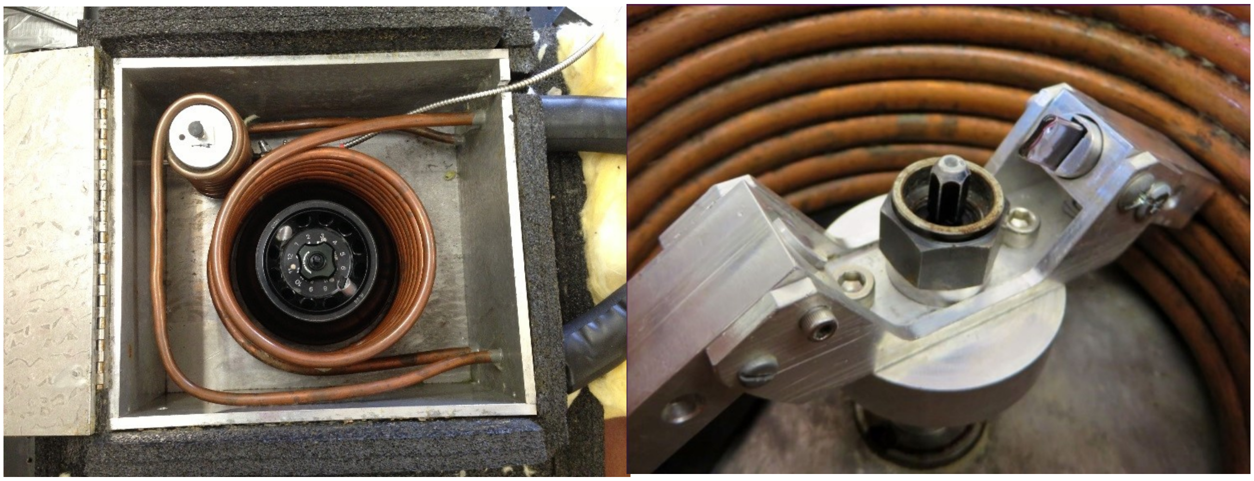

Figure 2.4 *Custom designed temperature-controlled centrifuge. On the left is an open-lid view of the system. On the right is the custom-made rotor designed for a fitting that connects to the spectrometer via optical fibers.*

means that the system concentration is changing as a function of time. To eliminate this problem, I developed a technique to flame seal each nanoparticle sample in a glass ampule (EMS #63831-10, borosilicate capillary micro glass slide). This allowed for a small path length (0.8mm), small sample volume (100-150μl), and a sealed environment. Each ampule was first flame sealed on the bottom, partially sealed on the top (leaving a small hole to add sample) and then oven annealed to relieve any heat-induced stress. The nanoparticle sample was syringed into the ampule and quickly sealed. This sealed nanoparticle sample is impervious to solvent loss and much more robust for multiple temperature scans.

2.2.6 Nanoparticle synthesis

Nanoparticle synthesis was done within the Sorensen group by a tried-and-true inverse micelle method. Coupled with the aforementioned digestive ripening, colloids of monodisperse gold nanoparticles are synthesized and quantified before use in the solubility experiments.

AuNP are synthesized using the toluene-water-dodecyldimethylammonium bromide inverse micelle method [22,41] followed by digestive ripening. Briefly, 34mg of gold(III) chloride was dissolved in 10ml of 0.02M solution of dodecyldimethylammonium bromide (DDAB) in toluene. The gold(III) was reduced by adding 40μl of an aqueous solution of 9.4M sodium borohydride followed by 30 minutes of stirring where a change in color is observed. 0.8ml of 1-dodecanethiol (DDT) was then added to the polydisperse colloid to displace the DDAB followed by 30 minutes of stirring. The molar ratio of DDT:Au was 30:1. A purification step of 30ml of ethanol precipitates the nanoparticles while the supernatant was removed. The AuNPs are reconstituted in 10ml of toluene and 30:1 DDT:Au ratio. The solution was digestively ripened (refluxed) under an argon atmosphere for 90 minutes. A typical before and after TEM image is shown in Figure 2.1, nicely illustrating the near-monodisperse size and shape of the AuNPs.

These as-prepared AuNPs are quite dilute, though they still strongly absorb light because of their plasmon resonance at ~525nm. To produce a system that can cross the phase boundary (a saturated system), the solution was concentrated by a factor of 10. The ligand (DDT) was also increased to 15% by volume as it was noted that the addition of excess ligand decreased the overall solubility of the AuNP. This observation still has not been explained as the surface of the AuNPs are coated with DDT and you would expect the AuNP:DDT particles to favor excess DDT. My previous work shows a general trend of 'like dissolves like', though not in all cases [19]. Visible inspection showed that the nanoparticle sample was in two-phase equilibrium at room temperature as the AuNP precipitate could be observed on the bottom of the ampule.

2.2.7 Solubility procedure

A specific procedure was developed over the course of many years that led to reproducible solubility data. Here is an outline of the steps taken.

- Sealed AuNP ampule is put in ultra-sonic bath for ~2 minutes to break up any precipitate and aggregates of the two-phase system and produce a homogenous suspension.
- Ampule is placed in centrifuge rotor inside the temperature-controlled box set to a desired temperature. The sample is left to 'rest' and come to an equilibrium for 15-30 minutes.
- While holding a set temperature, the sample is centrifuged at 7000rpm (3300g) for 12 minutes. This ensures that any suspended aggregates in solution have sufficient time to spin to the bottom of the ampule. Removal of the very fine precipitate (dimers, trimers, etc.) required a centrifuge.

- The sample is carefully removed from the rotor, inverted, and placed back into the holder. The inversion separates the precipitate from the supernatant.
- UV-Vis absorbance reading of the supernatant is taken and saved.
- Process repeats at another temperature setting.

The temperature range of the measurements were defined by both hardware limitations and sample hardiness. The chillers had a stable lower limit of -10°C while the AuNPs showed signs of damage beyond 35°C. The use of the centrifuge is required as the very fine precipitate (dimers, trimers, etc.) will not separate from the supernatant without additional help. The appearance of clusters in a nanoparticle sample shows up as a broadening and a red-shift in the plasmon resonance of the AuNP. The speed and time of the centrifugation ensured that only monomers are present in solution.

2.3 Nanoparticle injector for gas-phase experiments

To investigate how ultrafast, intense laser light interacts with a nanoparticle, a source that can supply such particles into vacuum was needed. It must be able to produce isolated, gas-phase, single monomer nanoparticles at a rate conducive to the constraints of the laser system. It must be able to have a nanoparticle flux that can maximize the probability of one nanoparticle in the focus per laser shot but minimize more than one. Synthetic methods such as sputtering [42], laser-ablation [43], or pyrolysis [44] can produce such gas-phase nanoparticles but they suffer from low yields and poor size and shape polydispersity. Wet synthetic methods have much finer control of yield, size, and shape [22,42,45,46]; every attribute desired for a nanosource.

To bring these nanoparticles to the gas-phase (i.e., inject into vacuum), a clever blend of aerosol technology and particle focusing is employed. The basic steps include **1)** atomization/aerosolization **2)** drying of aerosol and **3)** aerodynamic particle focusing.

2.3.1 Atomization

A nanoparticle aerosol is generated using a Collison-type commercial atomizer (TSI, Model 3076). Figure 2.5 shows a cross-sectional view of the internal workings of the atomizer. Compressed air expands through the orifice to create a high-velocity gas jet. This draws up the liquid sample into the gas stream where the sample is aerosolized by shear forces. The backing pressure and sample flow rate each have a moderate effect on the properties of the aerosol. Large micron-sized droplets are impacted out on the opposite wall while the finer mist exits the top with the carrier gas.

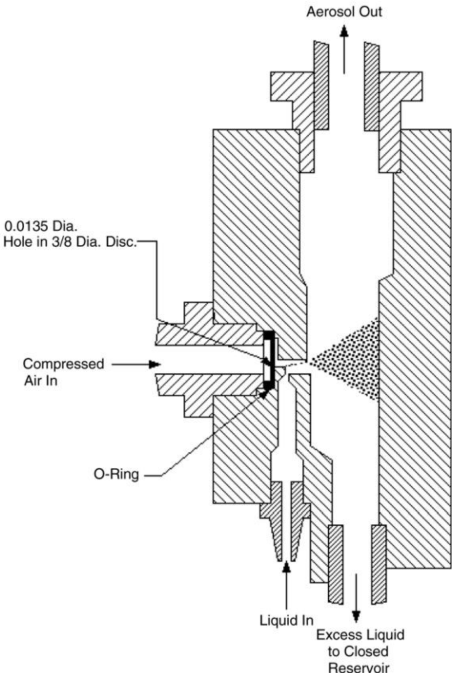

Figure 2.5 *Cross-section of Collison-type atomizer (picture courtesy of TSI, Inc)*

As mentioned above, the objective of the nanosource is to deliver one nanoparticle at a time to the laser focus at a practical rate. To minimize the probability that multiple nanoparticles are contained in each aerosol droplet, the initial sample concentration was adjusted to a value ~5x10^{10} particles/ml. A back of the envelope calculation $(5\times10^{10}NP/\text{cm}^3)^{-1/3}$ gives an average distance between nanoparticles of 3µm. A Poisson distribution analysis can also be used to calculate the probability of having 0,1, or 2 nanoparticles per droplet given the initial aerosol size distribution, though variables such as backing pressure and solvent directly affect the distribution. The sample concentration was empirically changed to ensure a dilute system. Figure 2.6 shows a histogram of aerosol droplet size exiting the atomizer and clearly displays that most of the droplets are less than 1µm in diameter. A TSI Optical Particle Counter (OPS Model 3330) was used which as a minimum sizing diameter of 500nm. With most droplet sizes less than 1 µm, the probability of having more than one nanoparticle per aerosol droplet in a homogenous sample was minimized.

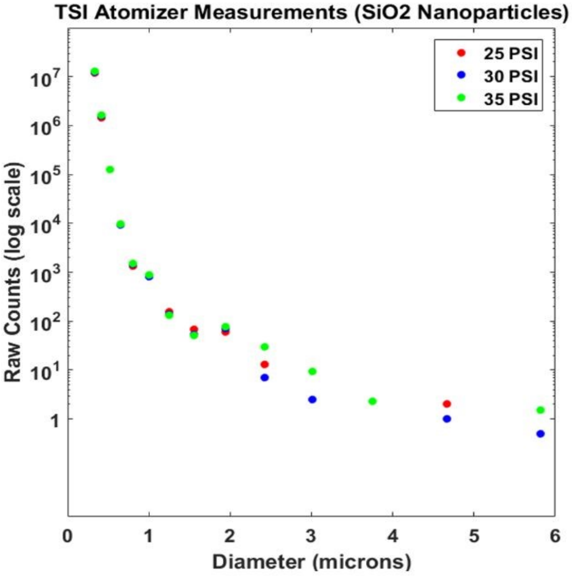

Figure 2.6 *Optical Particle Counter histogram of aerosol droplet size exiting TSI atomizer as a function of backing pressure. Note the log scale.*

2.3.2 Aerosol drying

The aerosol droplets must be dried to isolate the nanoparticles from the solvent and produce gas-phase nanoparticles suspended in its carrier gas. Initially, a diffusion dryer (TSI Model 3062) was used to dry the droplets. Silica beads surrounding the aerosol flow path provide a dry environment for the evaporation of the solvent, leaving behind any material that was suspended or dissolved in the droplet. This method was adequate but had some drawbacks. Once the silica beads became saturated with water, they had to be removed, baked to remove absorbed water, and then replaced again. This also means that the dry atmosphere inside the flow path gradually increased its relative humidity as the silica absorbed water. Silica also is inefficient at removing solvents such as alcohol (ethanol or methanol) which means that aerosol droplets of these solvents would enter the vacuum chamber not sufficiently dried.

The diffusion dryer was replaced by a far superior product called a Nafion™ dryer (MD-700 Large Diameter Nafion™ Dryer; Perma Pure, LLC). This innovation is a copolymer of tetrafluoroethylene (Teflon®) and perfluoro-3,6-dioxa-4-methyl-7-octene-sulfonic acid. This is extensively used in the gas industry to dry and monitor sample compositions [47]. Like Teflon®, it is highly resistant to chemical attack, but its inner sulfonic acid group network gives it beneficial properties. Sulfonic acid has a large waters-of-hydration where it can absorb 13 molecules of water for every sulfonic acid group or, equivalently, can absorb up to 22% of its weight in water [48,49].

Nafion™ dryers directly remove anything that acts like a base and/or contains a hydroxyl (-OH) group. This includes water, alcohols, and ammonia while leaving behind all hydrocarbons, gases such as nitrogen or oxygen, and most importantly, nanoparticles. The absorption of water or alcohol occurs rapidly as a first-rate kinetic reaction, driven by a difference in vapor pressure between the inside (high relative humidity) and the outside (low relative humidity) of the drying tube. This means that the aerosol droplets encounter a very dry atmosphere inside the dryer and evaporation and shrinkage of the droplet occurs. As there is nothing to become saturated, a Nafion™ dryer can run indefinitely, given a supply of dry purge gas. Another advantage over the diffusion dryer is its ability to also efficiently remove alcohol from the aerosol stream. On a side note, many synthetic methods to produce SiO_2 nanoparticles make use of ammonia, which can be effectively stripped from the aerosol stream to further reduce background contamination in vacuum.

Figure 2.7 is a plot comparing the performance of the diffusion dryer to the Nafion™ dryer. A constant flow of aerosolized water droplets was input into each of the individual dryers, similar to experimental conditions. A Testo 605-H2 Humidity Stick with Wet-Bulb Calculation was used

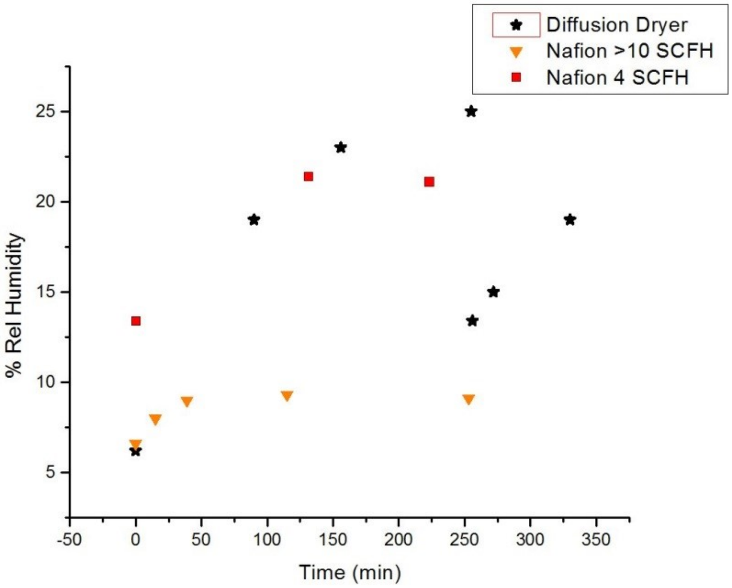

Figure 2.7 *Drying ability comparison of a diffusion dryer vs Nafion dryer. The diffusion dryer performance decrease as it absorbs more water. The Nafion dryer quickly reaches a steady-state and can run for extended periods of time.*

to measure the exit relative humidity of each dryer as a function of time. The newly dried silica in the diffusion dryer (black stars) initially starts off at 6% but quickly climbs into double digits and finally to 25% after 4 hours. At this point, the dryer was shaken to mix the saturated silica beads on the inner part of the dryer with the dry silica towards the outside. The humidity drops under 15% but starts to quickly increase. This shows that more water is being allowed through the diffusion dryer as a function of run time.

The Nafion™ dryer needs a supply of dry purge gas to properly function. Using 4 SCFH (standard cubic feet per minute) (red squares) of dry N_2 gas shows it is inadequately drying the aerosol flow. It begins at 13% and levels off at over 20%. Increasing the purge gas to >10 SCFH (orange triangles) shows the true potential of the system. Under the same conditions as the diffusion dryer, this dryer could achieve less than 10% relative humidity for over 4 hours of runtime. This dryer will consistently remove the same amount of water from the system continually, if there is sufficient flow of dry purge gas. This is a great advantage, especially if long scans are needed to account for low experimental statistics.

2.3.3 Aerodynamic lens

The current configuration of the aerodynamic lens was first developed in 1995 by a research group from the University of Minnesota [50,51] to produce highly collimated and tightly focused particle beams. An aerodynamic lens works on the principle of axi-symmetric flow contractions and expansions through a nozzle or aperture, driven by a difference in pressure. A series of progressively smaller apertures effectively drives the particles towards the center and increases the local particle density. The term ‘aerodynamic lensing’ comes from the use of multiple apertures to tighten and ‘focus’ the particle beam through aerodynamic forces. Figure 2.8 shows how the gas flow, including particles, behave when encountering an aperture [52]. This shows a single trajectory of a particle (solid line) vs the bulk gas flow (dashed line). Upon contraction through the aperture, the particle will stay closer to the center of the lens system because of its higher moment of inertia compared to the gas. The gas flow will again expand while the particle has gained momentum parallel to the lens. This is repeated multiple times through small openings, thus confining the particle beam tighter. Figure 2.9 shows a schematic of the inside of the aerodynamic lens. On the left is where the gas-phase aerosol enters the vacuum chamber through a 150µm glass orifice. This is called the ‘critical orifice’ as it regulates how much gas flow enters

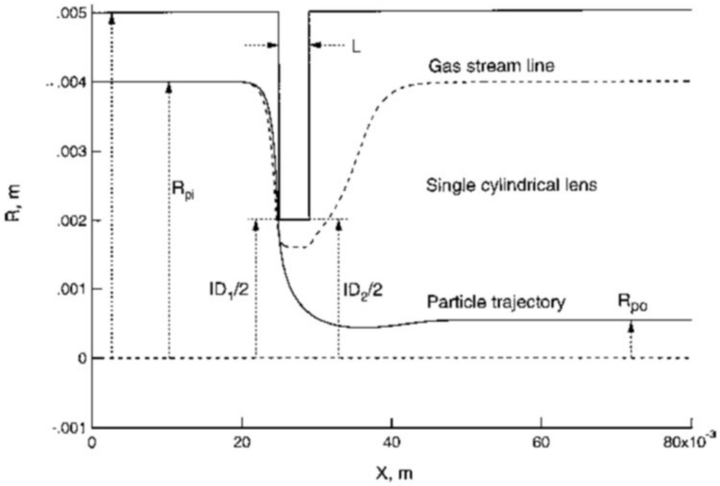

Figure 2.8 *Simulated working principle of an aerodynamic lens. A particle in the gas flow incident upon an aperture moves toward the middle while the gas again expands afterwards. Image taken from [52].*

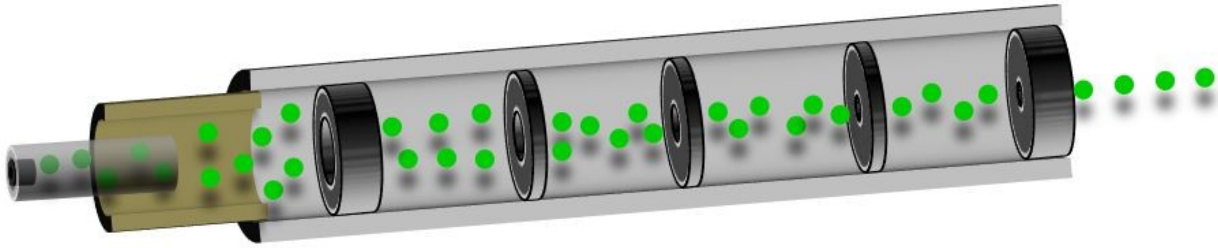

Figure 2.9 *Aerodynamic lens schematic. The nanoparticle aerosol (green spheres) enter from the left at atmosphere through a 150µm glass orifice under vacuum. It encounters a series of smaller lenses (apertures) which focus the particle beam. This is not to scale and is only a representation.*

the system which depends on the pressure difference between the two sides. The critical orifice allows a pressure drop from atmosphere to a few Torr which is a typical running condition for this lens design. This critical orifice was custom-made by a glassblower where a smooth inside taper was crafted, starting with an inner diameter of 3mm and having a smooth, funnel-like taper to 150µm. This helps the gas flow transition to an even, laminar flow more quickly inside the lens.

There are many variables that can affect how an aerodynamic lens systems functions. Complex computational fluid dynamics (CFD) have been used to analyze many different lens parameters including operating pressure, gas flow rate, particle size, and aperture size and spacing [53]. Table 2.1 shows the dimensions of the aerodynamic lens systems that was used for all the gas-phase nanoparticle experiments contained in this thesis. Experiments were performed on SiO_2, gold, and nanoshell nanoparticles ranging from 5nm to 750nm, all with the same lens system. Even though the lens was not optimized for all these sizes (resulting in different nanoparticle beam densities for different sizes), sufficient statistics could be accumulated for all sizes and materials. Further work to optimize focusing ability is currently in progress.

Table 2.1 *Dimensions of aerodynamic lens system*

Orifice	Orifice Diameter (mm)	Length between apertures (mm)
Critical orifice	0.150	
First aperture	5.3	49.5
Second aperture	5.0	50.5
Third aperture	4.7	50.5
Fourth aperture	4.4	50.5
Fifth aperture	4.24	60
Sixth aperture	4.0	75

2.3.4 Differential pumping

A sizeable volume of carrier gas is drawn through the critical orifice and used to focus the particle beam. To keep sufficient vacuum (at least low 10^{-5} Torr) for the VMI system to be safely operated, the aerodynamic lens must be differentially pumped to remove excess gas. This concept is relatively simple. The exit of the particle beam contains the collimated nanoparticles along with a quickly diverging gas stream. This enters a separate chamber that has its own roughing vacuum pump that is at relatively high pressure (~10^{-1} or 10^{-2} Torr) but can remove sufficient quantities of gas. A 'skimmer', consisting of a plate with a centered small hole, is placed between the first and second chamber. The skimmer is aligned to let the particle beam pass but limit the amount of gas entering the next chamber. The next chamber now has a turbomolecular pump operating at a lower pressure (10^{-3} Torr) to again remove more carrier gas. A third pumping chamber with another turbomolecular pump reduces the pressure to ~10^{-5} Torr before the particle beam exits through a last skimmer into the main experimental chamber. The main chamber can now sufficiently maintain high vacuum for the electron detector to safely run. Of note, the skimmer hole diameters used was 3mm, 4mm, and 3mm, from the first to the third pumping stage, respectively.

Figure 2.10 shows a cut-away view of the fully assembled NanoSource. The nanoparticle aerosol enters the aerodynamic lens from the right where it encounters the differential pumping stages. The nanoparticle beam enters the main VMI chamber on the far left and intersects the laser focus at the center of the spectrometer.

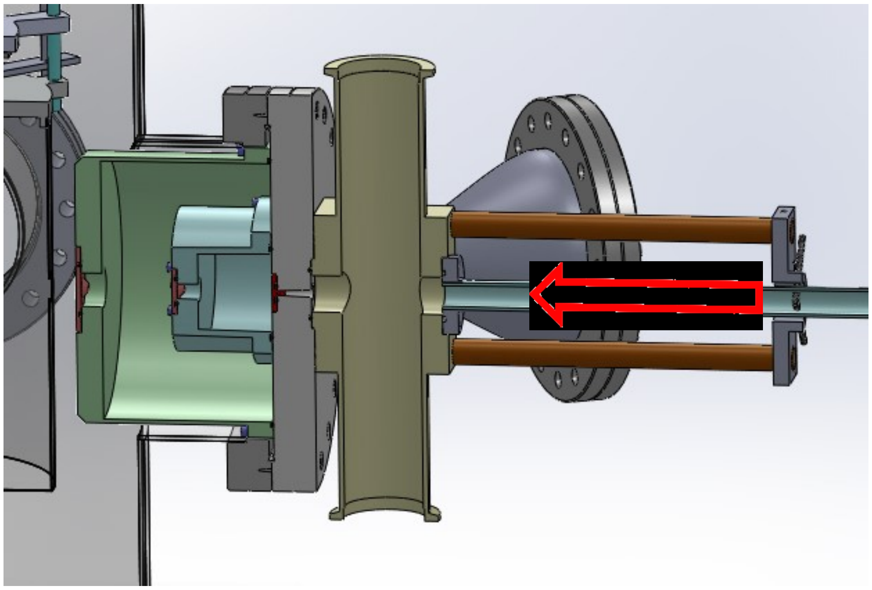

Figure 2.10 *Cut-away view of assembled NanoSource connected to VMI chamber. Nanoparticle aerosol enters from right into aerodynamic lens. Particle flow indicated by arrow.*

2.3.5 NanoSource sample characterization

Of upmost importance to gas-phase nanoparticles experiments is the purity of the sample. The aerosolization and subsequent drying of the nanoparticle sample inherently demands an extremely pure initial sample. Each aerosol droplet contains the solvent, nanosample, and any dissolved chemicals, usually leftover from the synthesis or added for particle stabilization. This could be salts, surfactants, or ligands that are not directly attached to the nanoparticle but are dissolved in solution. These materials will not evaporate with the solvent and therefore will deposit on or encapsulate the nanoparticle, thus 'contaminating' the pure nanosample. Assuming the initial contamination in the bulk sample is homogenous, every droplet with have the same concentration. The aerosol droplet size distribution (see Figure 2.6) is quite broad (and the droplet volume by extension) which means that the mass of contamination per droplet will widely vary. Instead of a clean gas-phase sample, the particle beam is awash with different ‘islands’ of leftover impurities. Depending on the actual amount, the contamination can be larger than the nanoparticle itself, especially for small sizes.

A few things can be done to ensure initial sample purity. Repeated washings of the samples, usually through centrifugation and removal of the leftover solvent, works well for very stable particles such as SiO_2 and polystyrene that can handle high g-forces without agglomeration. Metallic nanoparticles, on the other hand, are much more challenging to clean. These nanoparticles have a much larger Hamaker constant [54] than dielectric particles and thus are easily attracted to each other by a large van der Waals force. Surface modification by ligands provides enough steric and/or charge separation to prevent agglomeration, or sintering. The addition of a surfactant greatly increases the stability of metal nanoparticles to withstand centrifugation or large temperature swings. Some ligands, such as polyvinylpyrrolidone (PVP) are notoriously hard to remove from solution, a good reason to avoid them altogether [55].

The first indication that my particle beam was contaminated came while analyzing some early photoelectron data. A reference background scan of the pure solvent was always run but this was supplemented with a centrifuged sample background scan. Centrifuging the sample removed all of the nanoparticles but left behind anything dissolved in the solvent. When comparing the scans with nanoparticles present vs no-nanoparticles centrifuged sample, they were almost identical. Comparing this to a known clean sample of SiO_2, I could clearly see that the particle beam was contaminated.

To test this, I constructed a way to sample what the particle beam looked like in-vacuum at the interaction region. Figure 2.11 is a picture of the custom transmission electron microscopy (TEM) grid holder that allowed a detailed look at the non-irradiated particle beam where the laser focus would be located. The TEM grid (FCF300-Cu) is a small copper mesh coated with a layer of formvar resin and is the copper-color disk in the center of the nut. The grid holder is mounted on a manipulator perpendicular to the incident particle beam. A transmission electron microscope was used for precise analysis of the contents of the particle beam. Some concern has been noted that the particle beam will pass through the resin and thus I would not see a representative particle beam sample. I used a transmission electron microscope (Philips CM-100) with an accelerating voltage of 100kV capable of easily resolving less than 10nm. A tear or break in the formvar mesh is easily seen at the appropriate magnification and there is no evidence that the particle beam penetrates the mesh. The particles have a probability to also bounce off the grid and there was not a way to definitely rule this out.

Figure 2.11 *Custom TEM-grid jig to test particle beam in-vacuum. TEM grid (copper-colored) inside hole in holder.*

As mentioned above, metallic nanoparticles require a robust way to stabilize them in the form of strong ligands and the addition of surfactants. Standard commercial gold nanoparticles come with a surfactant, typically something like polysorbate 20 (Tween 20), added at the rate of 0.025% by volume for added stability. Now let's analyze a simple scenario. A 1µm size droplet of the nanoparticle/surfactant/water sample has been generated. Assuming a 100nm nanoparticle, the volume fraction taken up by the particle is 1:1000. The surfactant is 0.25 parts in 1,000. The droplet is dried completely, leaving only the nanoparticle and the surfactant. The diameter has decreased by a factor of 10, meaning the volume also decreased by 10^3. This means that the volume fraction of surfactant is now 1000 times greater, or 0.025% *1000=25%. This is exactly the reason that in-situ, in-vacuum testing is a much more accurate way to ensure a clean experiment. To verify this, the TEM grids were analyzed by looking at the particle beam with and without the surfactant added. The 70nm AuNP sample (Figure 2.12) with surfactant clearly shows the evidence of contamination. There are large 'islands' of surfactant (lighter colored material) which are most likely aggregates of smaller ones that coalesced upon impact with the TEM grid surface. The nanoparticles (dark circular spots) seem to have migrated to

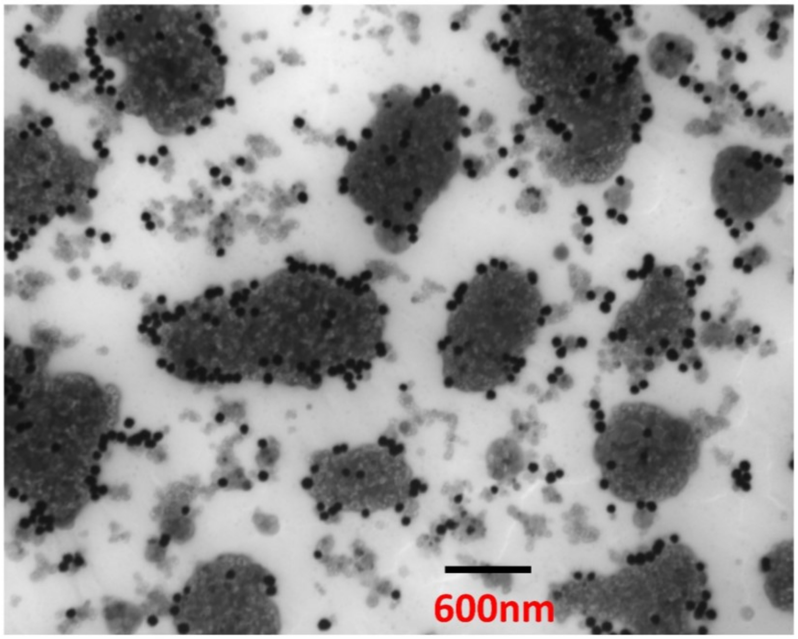

Figure 2.12 *TEM image of 70nm AuNP with surfactant. The scale bar is 600nm. The dark circles are the nanoparticles while the large, lighter colored islands are residual surfactant.*

the edges of the large ‘islands’. The handful of individual surfactant-free nanoparticles come from the droplets that were on the small end of the size distribution and therefore did not contain as much surfactant. This level of contamination in the particle beam is not acceptable for the study of isolated nanoparticles.

A sample of 120nm AuNPs was used that was verified to be 99% pure of residual reactants (later experiments were improved by another 10X purification step). Under the exact conditions of Figure 2.12, the cleaned 120nm AuNPs were also analyzed. The background of Figure 2.13 is mainly free from any surfactant or contamination and only contains nanoparticles. This is in stark contrast to the previous image where the background contribution dominated. The large nanoparticle in the upper left corner is a large SiO_2 nanoparticle from a previous run. The focusing of the aerodynamic lens also is affected by the size of particle, meaning a contaminated particle beam will focus differently than a clean one.

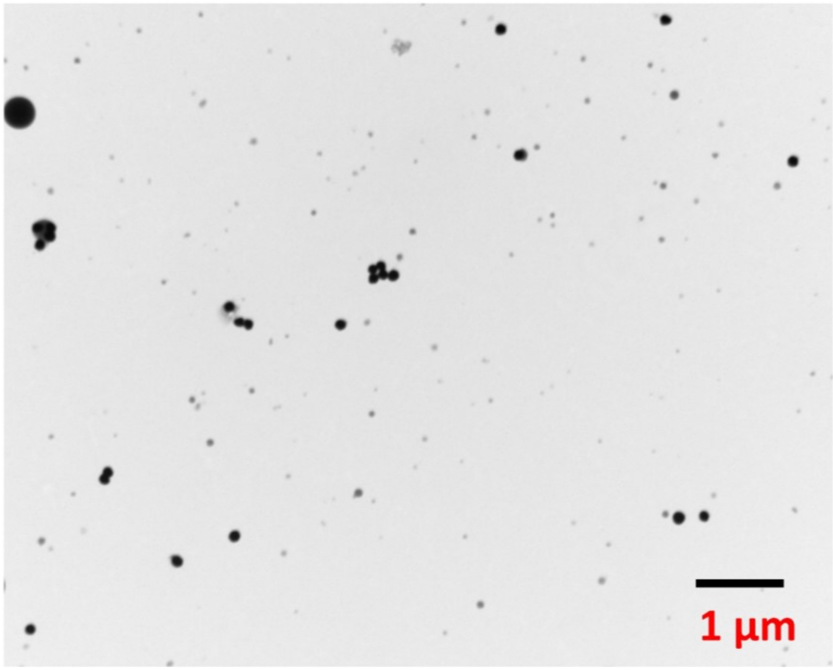

Figure 2.13 *TEM image of 120nm AuNP without surfactant. The scale bar is 1000nm. The largest dark figure (upper left) is source cross-contamination with the previous run of 600nm* SiO_2*. The lack of surfactant contamination shows a significantly cleaner sample.*

One side effect of using ultra-clean metallic nanoparticles is that they become much more fragile. Great care must be taken to avoid the nanoparticles from irreversibly aggregating. They cannot be put in an ultrasonic bath or centrifuged beyond a certain g-force limit. Over the course of a few months, even under optimal conditions, the nanoparticles will eventually aggregate and settle out of solution with no way to use them. A process as aggressive as atomization is not conducive to metallic nanoparticle stability. Within minutes, the use of the traditional atomizer in recirculation mode (the excess sample that is drawn up is recycled back into the bulk solution) causes the particles to irreversibly aggregate and the sample becomes unusable. This was the main reason that surfactant was initially added as this greatly improved their resilience during the atomization process. One solution made use of a syringe pump coupled with the atomizer in non-recirculation mode. The syringe pump meters in a fixed sample rate to the atomizer and any excess (non-aerosolized) sample is removed to a separate flask. The rate at which metallic nanoparticles are used (as they are not being recycled) was much greater than for SiO_2 but this ensures that the experiment was performed with an uncontaminated particle beam and allowing the dynamics of clean, gas-phase nanoparticles to be studied.

2.4 Velocity map imaging setup for photoelectron measurements

As discussed in Section 1.3, one of the most efficient ways to study light interaction with isolated nanosystems is the detection of the emitted electrons, along with the measurement of their energy and angular distributions. To obtain this information, this work utilizes the so-called velocity map imaging technique.

The entire experimental setup for the nanoparticle photoemission experiment is shown in Figure 2.14. The NanoSource aerosolizes and dries a nanoparticle colloid before injecting it into the high-energy VMI chamber. An aerodynamic lens in vacuum collimates and focuses the gas-phase nanoparticles for increased particle jet density. A laser beam is focused onto the nanoparticle beam by a 500mm focal length lens to the center of the VMI spectrometer. The created photoelectrons are projected onto the MCP detector equipped with a phosphor

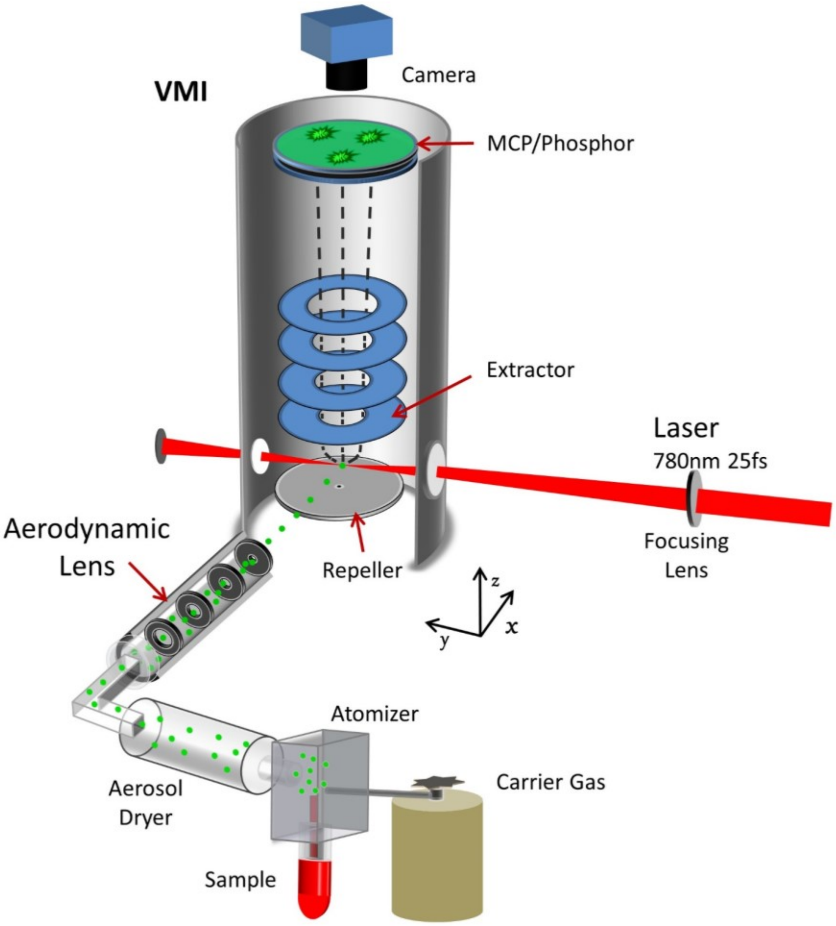

Figure 2.14 *Experimental setup for photoelectron spectroscopy on laser-irradiated nanoparticles. A nanoparticle colloid is aerosolized (green spheres) and dried before being injection into vacuum to be focused. The laser beam propagating perpendicular to the particle jet is focused to the center of the VMI spectrometer. The VMI projects all the created electrons onto a MCP/phosphor screen detector assembly, and the image is captured by a single-shot camera.*

screen. A single-shot camera captures the spatial distribution of the photoelectron on the phosphor ("VMI image") for individual laser shots. Below, the individual elements of this setup are described.

2.4.1 Velocity map imaging spectrometers

The concept and the design of a modern velocity map imaging (VMI) setup was presented by Eppink and Parker in 1997 [56], following some early work on photofragment imaging [143]. A charged particle (ion or electron) placed into an electrostatic field can be projected onto a position sensitive detector. A VMI technique usually relies on spatial information obtained from the measured 2D photoelectron image, which is essentially a 2D projection of the initial 3D momentum distribution. This is different from other photoelectron detection techniques which often rely on the time-of-flight information to calculate the kinetic energies of the detected electrons. VMI is typically capable of detecting charged particles emitted in a full solid angle of 4π and is well-suited for experiments based with a rather high count rate. The VMI is an efficient tool for gas-phase nanoparticle experiments based on its the ability to efficiently image hundreds of electrons per laser shot. A typical VMI spectrometer can be often driven as an ion TOF spectrometer if a somewhat different set of voltages (of opposite polarity) is used.

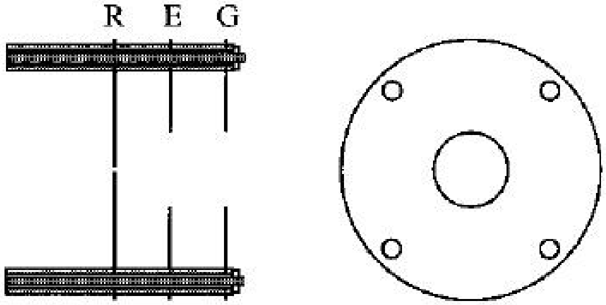

Figure 2.15 *Original VMI configuration. R=repeller, E=extractor, and G=ground. Schematic from [56]*

The central idea of a VMI is the use of an inhomogeneous electric field as a ‘lens’ to guide and focus charged particles. I will focus on electrons though only a change in electric field polarity is needed to switch to ion imaging. The first and simplest VMI setup consisted of 3 circular electrodes as seen in Figure 2.15. The source of the charged particles (cross-over of a particle beam with laser focus in the interaction region) is centered between the repeller and extractor plates which are held at a biased voltage, relative to the third plate at ground. The extractor and ground plates are flat plates with a hole in the middle for the charged particles to fly. By correctly choosing the voltages on the repeller and extractor, the non-uniform electric fields can be set to focus the particles to a detector surface. This voltage tuning changes how the VMI spectrometer focuses. The goal is to map all the charged particles with equal initial momentum to the same position on the detector. This is nicely shown in the groundbreaking initial publication describing the new ‘velocity map imaging’ device by Eppink and Park [56] seen in Figure 2.16. Irrespective of the starting position in a gas jet or laser focus, the VMI will map the charged particles with the same momentum to the same detector position, greatly increasing the resolution.

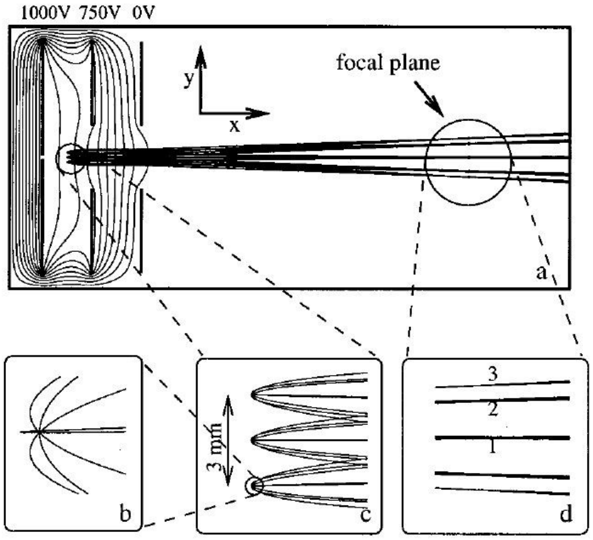

Figure 2.16 *Schematic of simple VMI spectrometer setup* ***a)*** *showing electric fields lines and electron trajectories while* ***b-d)*** *show close-up images of how the VMI maps any charged particle, regardless of initial position, to the same detector position, assuming equal initial momentum. Schematic from [56]*

By assuming that the initial kinetic energy of the particle is small compared to the energy imparted by the electric field of the spectrometer, the radial position of the charged particle on the detector is approximated by [57]

$$\boldsymbol{R \approx NL\sqrt{\frac{E_r}{qV}}}\ , \tag{4}$$

where E_r is the electron kinetic energy, N is the unique magnification factor of the spectrometer and repeller/extractor voltages, L is the length of the spectrometer, q is the charge of the particle, and V is the accelerating potential. Looking at only the terms coming from the initial charged particle production, their radial position can be expressed as

$$\boldsymbol{R \propto \sqrt{\frac{E_r}{Z}}}\ , \tag{5}$$

where Z is the charge number of the particle. Here we see that the radial position of the particle on the detector is proportional to the square root of its kinetic energy divided by charge, where the charge becomes important if looking at higher ionic charge states. For ion detection, care must be taken to distinguish which charge states are being collected which can be done easily using a time of flight gate on the detector to temporally separate different ionic charge states. Gating can also be useful for electron imaging by allowing one to reject stray electrons not synchronized to the laser pulse and improve the signal to noise ratio.

2.4.2 High energy VMI

The VMI used in this work was modified to make it conducive for the detection of high energy electrons and was aptly named the 'High Energy VMI'. In general, for a given set of voltages, the performance of the VMI-type spectrometer represents a compromise between achieving reasonable energy resolution and ensuring 4π collection efficiency for electrons with high kinetic energies. This VMI is a modified version of the one proposed by Kling et al. of a so-called ‘thick-lens’ design that makes use of numerous plates of different voltages in the extractor region [58]. The modifications aimed to ensure the 4π collection of the electrons up to 1keV in energy as the photoelectrons emitted from nanoparticles under intense laser fields are expected to be very energetic. High energy resolution is typically not needed for such experiments. Correspondingly, the spectrometer was designed for voltages up to 30kV. However, during this work the highest voltage used was restricted to 8kV which was sufficient to ensure collection of all electrons up to 400eV. At higher voltages, static-field ionization of the nanoparticle beam starts to contribute to the background signal.

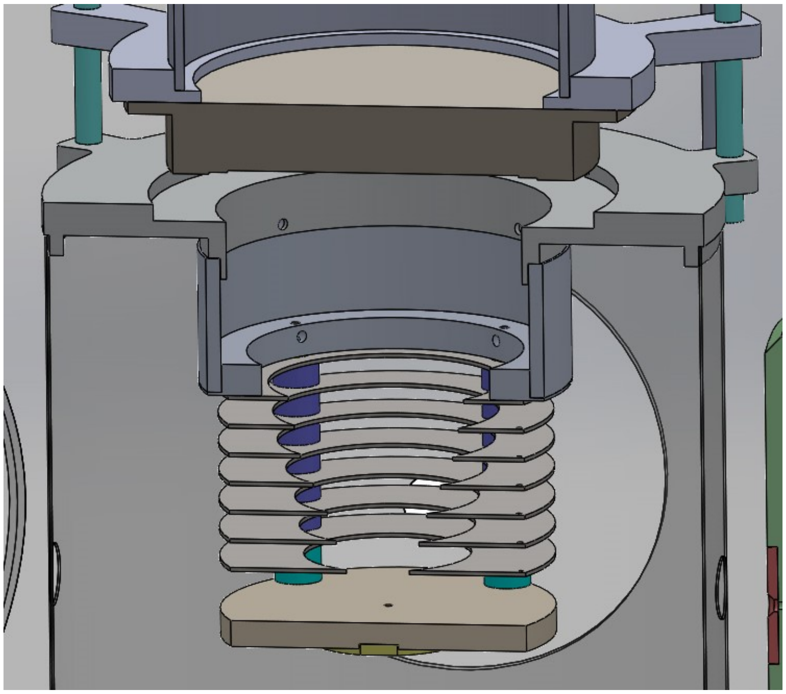

Figure 2.17 *Schematic of my VMI spectrometer configuration. Diffusive gas jet orifice is seen in the bottom (repeller) plate. The extractor and field-free region are shown below the MCP/phosphor detector at the top. The spectrometer is shielded from outside magnetic fields by the μ-metal shield.*

This high energy VMI (Figure 2.17) consists of a repeller plate with a diffusive jet in the center to allow for gas input as an effusive atomic beam, a 6-lens extractor along with a ground plate, and a field-free drift tube. The voltage on the extractor array was applied to the first plate nearest the repeller and each successive plate was linked by a chain of 10MΩ resistors which stepped the voltage gradually down to ground on the last plate. Voltage on the repeller was applied through the gas line attached to the diffusive jet. Each plate of the extractor is spaced 6mm apart and has a wider central hole than the previous plate to maximize the maximum acceptance energy of the electrons in the focusing field. The interaction region is placed halfway between the repeller and extractor (6mm away from each). The field-free flight region is 55mm. The entire spectrometer is surrounded by a μ-metal shield to block any outside fields from interfering with the electron flight path. All electrodes were constructed from stainless steel.

2.4.3 SIMION simulations

SIMION is a computer program that can simulate electron trajectories for specific spectrometer geometries and input parameters. Figure 2.18**a)** is a SIMION representation of the electric field lines using the geometry of my VMI spectrometer. Electrons will experience a force equal to the amplitude of the local field times their charge and thus be accelerated towards the detector. As SIMION can simulate electron trajectories using the input VMI geometry and voltages, it can be used as a tool to test design parameters, input voltages, and acceptance energies.

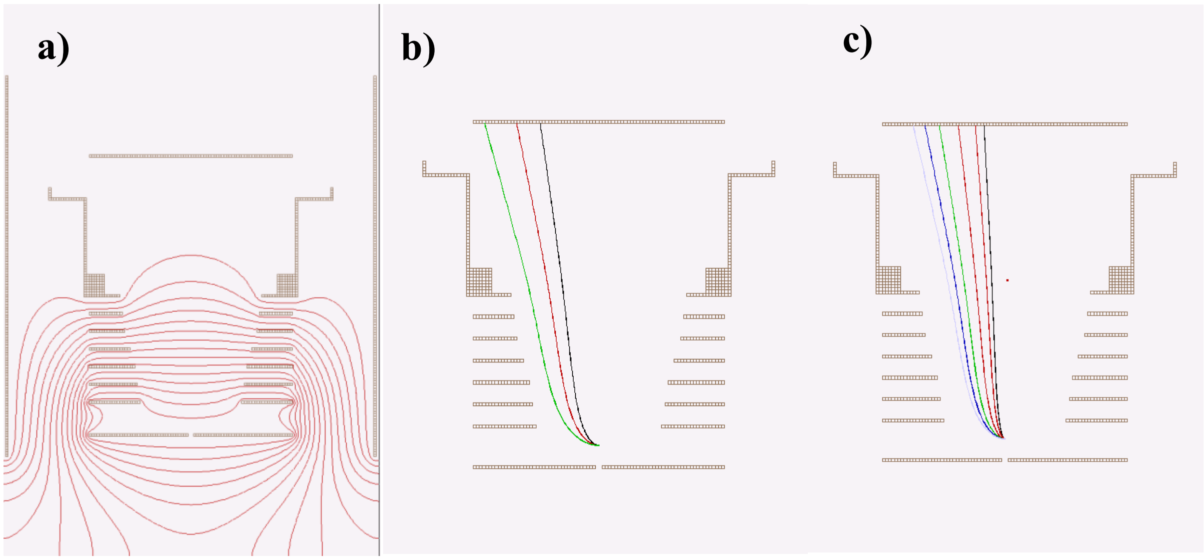

Figure 2.18 *SIMION simulation.* ***a)*** *SIMION simulation of electric field lines in my experimental VMI spectrometer. Bottom is the repeller and top is the detector.* ***b)*** *Trajectories of electrons with initial energy 50,100, and 200eV at repeller voltage -4kV* ***c)*** *Trajectories of electrons with initial energy 50,100, 250, 500, 750, and 1000eV at repeller voltage -30kV. Highest energy electrons will be impact the 'detector' on the outside, or largest radius. The detector diameter is 80mm.*

Figure 2.18**b-c)** show different electron trajectories of my VMI as a function of spectrometer voltage, up to 1keV electrons at a voltage of -30kV.

The typical mode of operation used voltages between (-)4kV to (-)8kV on the repeller and 97% of this value on the first extractor plate. Though SIMION can help approximate the voltage ratio between the repeller and extractor, this value was found empirically. To verify proper focusing conditions, xenon photoelectrons were imaged with a laser polarization perpendicular to the plane of the detector, ideally showing a projection of a sphere. If the projection is asymmetric, the voltage ratio is not optimized and needs to be fine-tuned. This VMI has an acceptance electron energy up to approximately 200eV at -4kV and up to 400eV at -8kV. The spectrometer voltage was chosen as a function of the sample going to be studied; primarily dielectric or metallic nanoparticles. A sufficient voltage was needed to ensure that the highest energy photoelectrons are well within the acceptance limit of the spectrometer.

This spectrometer was vacuum-tested with voltages up to 27kV. To achieve such high voltage, great care had to be taken to ensure that all components are extremely clean. Arcing will occur in high-vacuum first across the surface of contaminated elements in the spectrometer, mainly ceramic spacers where 'track' marks will be seen. All non-electrode elements were composed of ceramic, glass or plastic and cleaned in an ultra-sonic bath before assembly. Voltage connections to the electrodes were soldered and made to be as flat as possible to avoid any sharp peaks or edges. Though rated and tested up to 30kV, actual experiments used smaller voltages of no more than 8kV as the electron energies of the samples studied did not necessitate a higher acceptance value. Plans to use this VMI on electron energies up to 1keV photoelectrons are in the pipeline and will make use of this VMI's full potential.

2.4.4 Detector

All electrons are detected using a microchannel plate (MCP) connected to a phosphor screen. The MCP (Hammamatsu F2226-24P218) consists of two plates in a chevron configuration and biased up to 2.0kV on the rear while grounded on the front. An incident electron to the MCP front causes an exponential cascade of electrons with a gain up to 10^6. The back end of the MCP is coupled to a phosphor screen biased at 5.5kV to accelerate electrons from the MCP. The phosphor fluoresces in the visible spectrum at 510nm with a lifetime of about 300ns (P46 type). While a P43 type phosphor has three times the relative energy efficiency, it has a lifetime of 1ms which is too long for a 10kHz laser system. The location of a ‘bright’ spot on the phosphor is directly correlated to where the electron was incident on the MCP and thus contains momentum information.

A camera is used to gather the light emitted from the phosphor screen. The choice of camera depends on the sample being studied. For the study of photoelectrons or photo-ions from gases, a Peltier-cooled camera with high sensitivity but long exposures are best suited. This stems from the fact that the shot-to-shot dynamics of gases are consistent and the number of events per laser shot is steady. A gas-phase nanoparticle experiment requires a different approach that is a compromise of sensitivity and exposure time. A triggered, CMOS camera (Mikrotron EoSens 3CXP) is capable of 566 fps at 3Mpixels resolution with a 2 μs exposure time. At a resolution of 960x960 pixels, there is an increase to 1666 fps. With a 10kHz laser system, the frame rate of the camera had to be balanced versus the size of the phosphor screen image on the camera sensor. The addition of a large

Figure 2.19 *Single shot camera (top) along with collection lens (bottom)*

5” plano-convex lens with a 500mm focal length to the output vacuum window of the MCP/phosphor assembly increased the amount of light entering a fast f/0.95 (Schneider) camera lens as shown in Figure 2.19.

2.4.5 Hit finder

The MCP was gated (~200-400ns gate width; 1.2kV base MCP voltage, 700V gate increase) and synchronized to the laser while the camera was triggered with a 2μs exposure. This ensured that the MCP and camera were sensitive only in a short window during the laser pulse and effectively reduced background contributions from stray light and electronic noise. Moreover, this also reduced to a negligible level the residual ionization from the nanoparticle jet by the static VMI field, which does not correlate with the laser pulse.

The Mikrotron camera uses a 4-channel CoaxPress interface capable of 6.25 Gbit/s per channel in conjunction with a frame grabber (Bitflow Cyton Quad Channel CoaxPress). Even at the reduced resolution of 960x960 pixels, there is over 12 Gbit/s of camera data input. Therefore, storing full raw images for subsequent offline processing would significantly reduce the data acquisition rate. An online hit-finding solution which allows storing only the real events (charged particle hits) is therefore highly desirable. It also provides quick online feedback on the outcome of the experiment. In this work, an online hit-finding algorithm developed in [59,60] is implemented. This allows almost immediate feedback and decreases the stored file size by orders of magnitude.

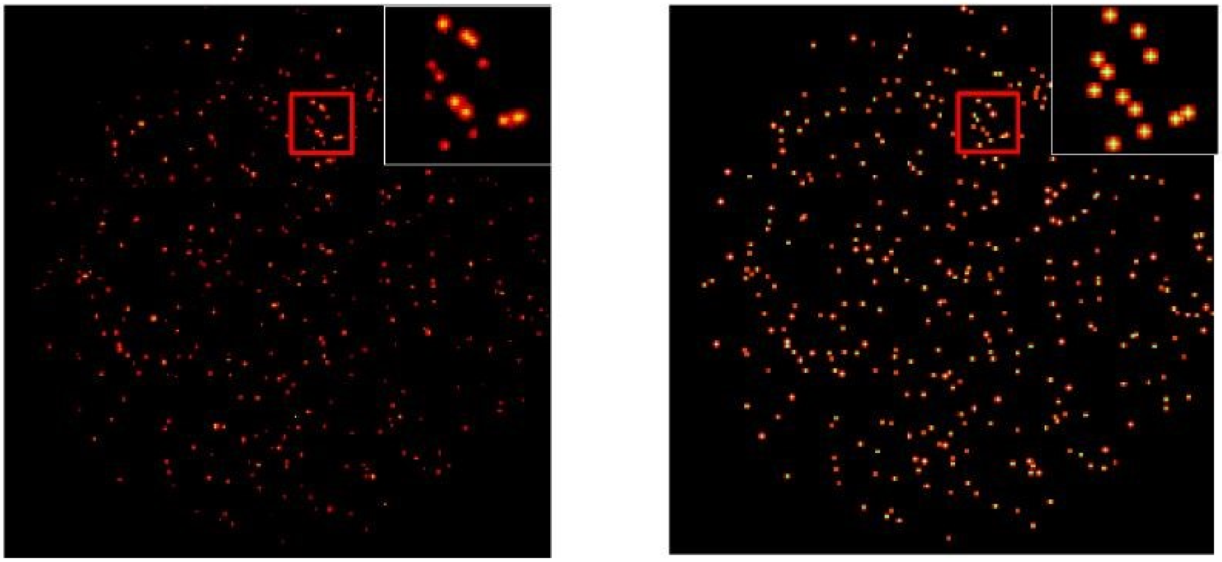

Image before analysis

Image after analysis

Figure 2.20 *Single camera frame of a VMI image before and after analysis by the hit-finder algorithm. Image on the right is reconstructed only from the saved locations where a 'hit' was detected. Each 'hit' in this case corresponds to a detected electron. Image from [59].*

Briefly, a LabView program was used that could distinguish individual events while discriminating from the background noise. A centroid-finding routine is used to analyze a raw camera image to look for pixel/s above a manually set threshold. Any event considered a 'hit' is indexed with its x and y coordinate values. The total 'hits' per camera image is saved while the raw image file is discarded. This process can be done very quickly with a sufficiently powerful desktop workstation (HP Z-820 with dual 12-core Xeon processors at 2.7GHz and 64GB of RAM). Each laser shot can be recalled and reconstructed using the indexed 'hit' coordinates. Figure 2.20 compares the raw camera image to the reconstructed image and only shows 'hit' locations that are above the set threshold. This allows for rapid feedback during the experiment and a complete shot-by-shot record for off-line analysis. Figure 2.21 illustrates the quality of images that can be produced with a single-shot camera and hit-finder routine. This is an integrated ($1\text{x}10^6$ laser shots) raw VMI image of Xe photoelectrons where an average of 10 electrons every laser shot were detected.

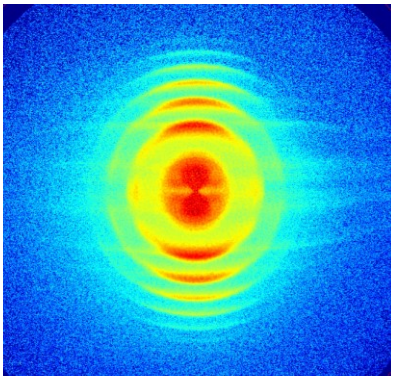

Figure 2.21 *Xe ATI image reconstructed from single-shot camera. 1x10^6 single-shot images are integrated in this non-inverted figure.*

For the gas-phase nanoparticle experiment, a low particle density means that less than 1% of the laser shots contain a nanoparticle in the focus. Most laser shots (and corresponding camera frames) will only contain background electrons from the carrier gas. A typical scan consists of 2.5 million laser shots of which ~99% are background only. Using an integrating camera (exposure times on the order of milliseconds and not synchronized to the laser) will produce an image dominated by the background. However, using a single-shot camera allows the analysis of each laser shot individually to determine if a nanoparticle was present. To determine this threshold, a simple hit histogram was used. On average, the number of photoelectrons counted by the algorithm when a nanoparticle is present is much higher than with only background gas. The number of emitted photoelectrons depend on the nanoparticle size and composition (SiO_2, Au, etc.) and incident laser intensity. Figure 2.22 is a hit histogram which shows how many camera frames (laser shots) with a given number of electrons were recorded. Overlapping this with a background scan of solvent only, it is clear where the deviation from the background occurs. The histogram is

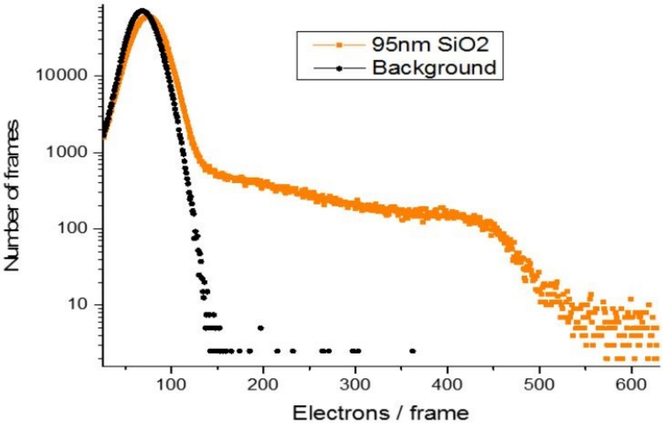

Figure 2.22 *Hit histogram of a single 95nm SiO_2 scan compared to background (solvent only). Notice the deviation from background indicating a nanoparticle was present.*

used to analyze only the camera frames that contain more than a background threshold (in this case ~150 electrons/frame.). Note the log-normal scale where the majority of the laser shots are contained within the background. The width of the histogram arises from the fact that the nanoparticle beam is much larger than the laser focus dimensions, thus the entire focal volume of the laser focus is sampled. Theoretically, the yield of photoelectrons from nanoparticles show nearly-linear behavior with intensity [61], so contributions from different focal regions lead to a different number of electrons emitted. The 'tail' where the histogram falls to single digit values is the region where the nanoparticles experienced the highest laser intensity, or equivalently the center of the laser focus. The center of a Gaussian-like focus contains the smallest volume and thus the smallest probability of a nanoparticle interaction.

2.4.6 Energy calibration

The energy spectra from above-threshold ionization of rare gas atoms such as Xe (see Figure 2.23) provides a practical way to calibrate the VMI spectrometer. The spectrometer focuses the photoelectrons as a function of the applied repeller and extractor voltages and thus small input voltage deviations result in different focusing conditions. By knowing that the spacing between consecutive ATI peaks in Figure 2.24 must correspond to the central incident photon energy, this information can be used to properly calibrate the raw VMI images. The VMI images

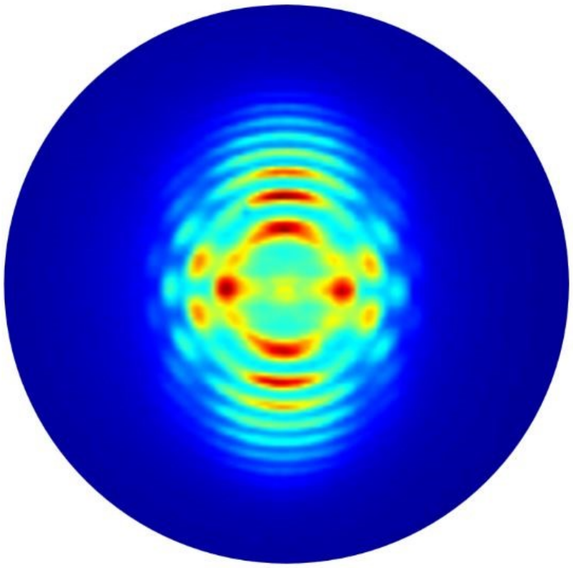

Figure 2.23 *Raw VMI image of Xe ATI. This is a sample image taken with an integrating camera for better resolution.*

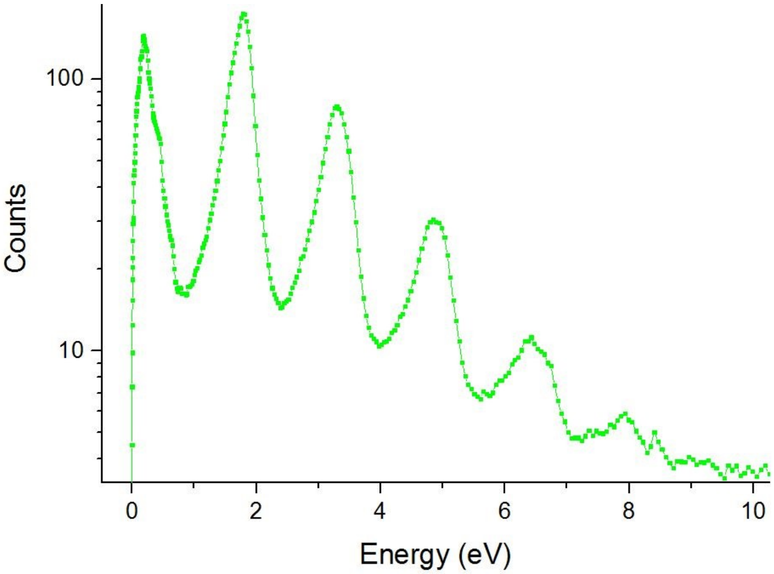

Figure 2.24 *Energy distribution of ATI from Xe.*

show velocity and angular dependent electron positions which need to be transformed into energy. Eqn. 3 shows how the radius of the images is related to the kinetic energy. The electron charge and spectrometer voltage are known while another factor, the 'calibration constant' is introduced to account for the magnification factor and electron flight length and was found empirically. The calibration constant is then used for subsequent analysis of scans from nanoparticles that do not have a defining feature such as ATI peaks for reference and allows for proper and consistent energy calibration.

2.4.7 Inversion of VMI images

The VMI records a 2D projection of the initial 3D photoelectron (or photo-ion) angular distribution (PAD). Several well-known techniques have been developed to recover either a slice or the full 3D PAD [57]. If VMI images exhibit cylindrical symmetry in the plane of the detector, usually along the laser polarization, an Abel transform can be applied. An Abel transform makes use of this cylindrical symmetry to reconstruct the full 3D momentum distribution. Other inversions methods include the so-called onion-peeling [144] and Fourier-Hankel algorithm [145]. The iterative inversion technique is a different approach that creates a trial 3D velocity distribution based on the 2D experimental radial and angular distributions without the introduction of noise [57,62]. The differences between the calculated and experimental projections are evaluated and a correction factor is applied for the next ‘iteration’. This is repeated until the differences between them are minimal. Finding the center of the experimental projection is critical before the inversion process. This inversion procedure was used if an inverted spectrum was required for proper analysis.

As cylindrical symmetry is required for the inversion procedure, this condition is in general not always met in the PAD from nanoparticles. Photoelectron images from spherical nanoparticles less than ~150nm diameter do appear to be symmetric with respect to the polarization axis. Larger particles begin to clearly exhibit asymmetric propagation effects as the particle diameter approaches the incident wavelength. The VMI images from small nanoparticles can thus be inverted to obtain the full 3D momentum distribution, whereas this approach is not valid for larger particles. As the primary focus of the photoelectron measurements performed in this work was determining and comparing the cutoff energies (i.e., the highest energies of the emitted electrons) for different nanoparticle sizes, non-inverted radial distributions had to be used. In accordance with the expectations based on the nature of the inversion procedure, tests confirmed that while inverting the nanoparticle VMI images did change the shape of the energy distribution compared to the spectrum reconstructed from the raw radial distribution, no change in electron cutoff energy was observed.

2.5 Near-infrared ultrafast lasers

In this work two different femtosecond systems were used: one used for the photoelectron spectroscopy studies at KSU, and another one employed as a “pump” for time-resolved x-ray scattering experiments at LCLS. Both of these lasers are chirped-pulse amplification-based

Ti:Sapphire system capable of delivering mJ level pulse energies. Such systems are a mainstay in countless laser labs around the world and the technology behind them is extensively covered in literature [63–66].

2.5.1 Ti:Sapphire laser system

The Prairie Ultrafast Light Source for Attosecond Research (PULSAR) used for the experiments performed in the James R. Macdonald Laboratory (JRML) at KSU is a customized version of the KMLabs "Red Dragon" design. It is based on the Kerr-lens mode-locked Ti:Sapphire oscillator generating pulses with central wavelength of 790nm with about 80 nm bandwidth at a repetition rate of 75.2 MHz and average power of about 300mW (which corresponds to 4 nJ pulse energy). Dispersion-compensating prisms in the oscillator reduce the pulse duration to 10 fs. Before amplification, the pulses are stretched to tens of ps by a pair of diffraction gratings to avoid amplifier crystal damage. After the stretcher, the repetition rate is reduced to 10 kHz using a Pockels cell. The PULSAR has two multi-pass amplification stages with a diode-laser pumped Ti:Sapphire gain medium, with the final output pulse energy of ~3 mJ. After the amplification, the pulses are sent through a grating-based compressor that reverses the stretching process, resulting in 21-23 fs pulses of ~2 mJ maximum pulse energy. The typical pulse duration in the interaction region was 25-27 fs.

The NIR laser in the AMO hutch at LCLS is a chirped-pulse regenerative amplified Ti:Sapphire system producing ~3 mJ, 35 nm bandwidth pulses. The still chirped but amplified output is relay-imaged through an evacuated tube to the experimental hutch, which is located on a different floor and split into two branches. The main branch containing nearly all of the pulse energy is compressed to ~40-50 fs and then used in the experiment. The secondary branch is independently compressed and used for direct, *in situ* cross-correlation measurement of the relative arrival time between the x-ray and the optical pulses [146] (see section 2.6). The system is running at 120Hz to match the repetition rate of the FEL [147].

2.5.2 Intensity calibration

In most experiments, especially in ultrafast, strong field physics, knowing the precise value of the incident peak laser intensity is critical. However, a precise determination of the absolute value of peak intensity from the optical beam parameters represents a significant challenge for intense femtosecond pulses, mainly because of the difficulties in the exact characterization of the spatial profile of the laser beam in the interaction region. If, however, the absolute value of the intensity is known for a given pulse energy (or power), it can be scaled for all measured values of the pulse energy (power). A power meter measures the optical power, which is a measure of the pulse energy of the laser (i.e. a 10kHz laser system with 20W of maximum power will have up to 2mJ per laser pulse). A change in input pulse energy is linear with intensity, meaning that by doubling the pulse energy, the intensity also doubles. This assumes that no other optical elements in the beam path have been changed. Therefore, the peak value of laser intensity is often determined "in-situ" from the experimental observables stemming from the interaction region, and then scaled according to the measured pulse power.

Several methods for such "in-situ" calibration of laser intensity have been proposed [148-151]. In my experiment, I make use of the photoelectron spectra resulting from above-threshold ionization (ATI) of Xe atoms, which evolve as a function of intensity. As discussed in Section 1.3.2, ATI is a highly non-linear process where an integer number of photons are absorbed (per atom/molecule) until the 'threshold', aka the ionization potential, is met and the atom/molecule is ionized. The same atom, however, can also absorb more photons than the minimum needed to be ionized, so it is 'above-threshold'. The emitted photoelectron, therefore, following energy conservation, will carry the energy corresponding to the number of photons absorbed. This gives rise to the very nice periodic peak structure in Figure 2.24 where the spacing between successive peaks must be the incident photon energy. Using 25fs pulses indicates that the laser pulse inherently has bandwidth, typically 70nm for PULSAR, with a center wavelength around 780nm. This gives photon energies between 1.5-1.65eV and is one reason for the width of the ATI peaks.

Once the electron is in the continuum, it will interact with the oscillating electric field of the laser pulse. The energy associated with this interaction is the ponderomotive potential, U_p, (see Eqn. 2) which is defined as the cycle-averaged quiver energy of the free electron in the laser field [67]. The ponderomotive potential grows linearly with increasing laser intensity. This essentially means that at higher intensities more energy needs to be provided from the field to release the electron. Correspondingly, the expression for the kinetic energy of the electron emitted after the absorption of *n* photons

$$\boldsymbol{E_{elect} = n\hbar\omega - I_p} \qquad \textbf{(6)}$$

needs to be modified to account for this change:

$$\boldsymbol{E_{elect} = n\hbar\omega - I_p - U_p} \qquad \textbf{(7)}$$

This results in a shift of a comb of photoelectron peaks towards lower energies as the intensity grows and is known as a "ponderomotive shift". This shift is evident in Figure 2.25, where the measured photoelectron spectra from the ATI of Xe are shown for three different values of the laser power. Notice how the peak position of the same ATI order shifts to lower energy as the input power increases. The absolute value of this shift is dependent on the difference in intensity between the two scans, all else being constant. Eqn. 7 can then be used to estimate the intensity needed to cause the measured ponderomotive shift.

The intensity can then be reconstructed either from the value of the ponderomotive shift, or from the absolute positions of the photoelectron peaks at a given intensity. The ionization potential (I_p) of Xe is 12.13eV, so at minimum 8 photons of 1.59eV each are needed (1.59eV/photon * 8 photons = 12.72eV). The excess kinetic energy (12.72eV-12.13eV=0.59eV) must also include the ponderomotive shift. Subtracting the absolute peak position from this excess energy then gives the ponderomotive energy at that particular input power and can be converted to intensity using Eqn. 7.

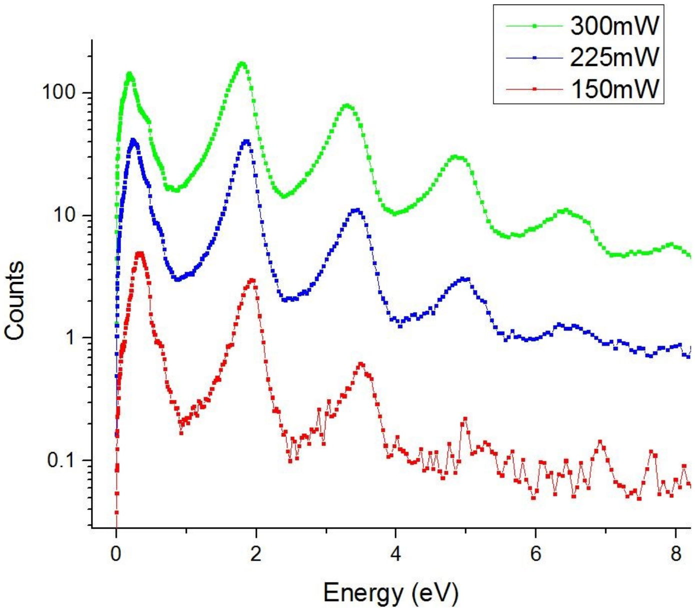

Figure 2.25 *Xe ATI energy distribution as a function of incident power.* $300mW = 5x10^{12}\ W/cm^2 \geq 0.28eV = U_p$

2.6 Free Electron Laser

2.6.1 Linac Coherent Light Source (LCLS)

The concept of a free electron laser (FEL) was introduced in 1971 by John Madey at Stanford University who predicted that this idea may be used to generate powerful coherent radiation from far infrared to the hard x-ray domain [152]. A few years later, Madey and coworkers reported the first functioning FEL device radiating in the mid-infrared [153]. The development of this concept paved a path to modern facilities such as the Linear Coherent Light Source (LCLS) at the SLAC National Accelerator Laboratory.

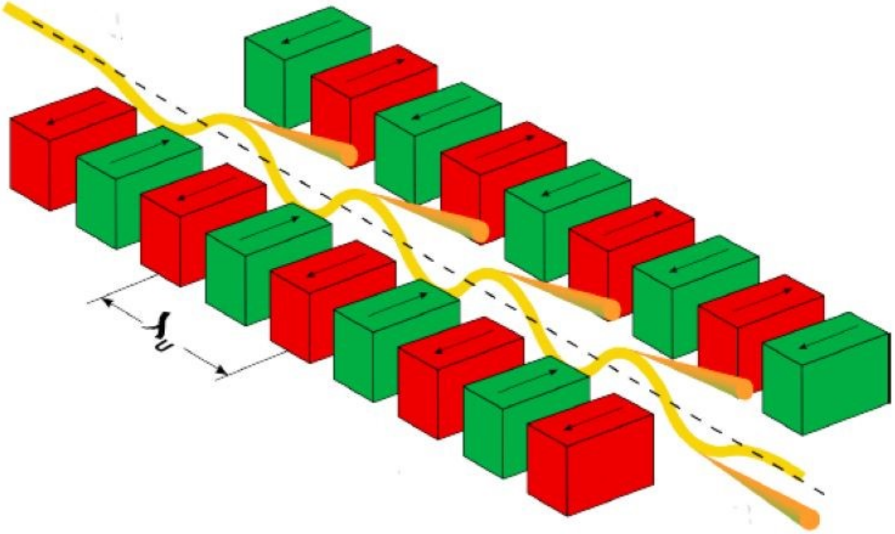

Figure 2.26 *Schematic of an undulator. This consists of a periodic arrangement of dipole magnets with a static magnetic field that alternate polarity (green and red). This spacing defines the undulator period, λ_u. A beam of electrons traveling into the magnetic field of the undulator will oscillate and emit radiation. Figure from [29].*

The basic principle of a free electron laser is the use of periodic magnetic structures to ‘wiggle’ electrons whereas the emitted radiation self-amplifies [154]. A linear accelerator is used to accelerate the electron produced by a photocathode radio frequency electron gun to relativistic velocities. These electrons then travel into an undulator as seen in Figure 2.26. The undulator is a periodic set of dipole magnets with a period λ_u that uses the Lorentz force to transversely wiggle the electrons. Because of this induced transverse acceleration, the electrons spontaneously emit so-called synchrotron radiation. As the electrons are traveling near the speed of light, relativistic contraction of λ_u along with the Doppler effect lead to light emission in the x-ray regime. As the spatial extension of the electron bunch is larger than the wavelength of the radiation, their interaction leads to modulations in the electron density called microbunching. The electrons become concentrated at the positions where the energy transfer to the radiation field has a maximum, which, in turn, enables the electrons to radiate in phase, thus drastically increasing the radiation power. This phenomenon is known as self-amplified spontaneous emission (SASE), which starts with initially incoherent (random phase) emission, and produces coherent (phases constructively interfere) radiation at the end of the undulator. As SASE is essentially a stochastic process, the parameters and the exact generation point of the SASE-FEL pulses can vary significantly shot-to-shot, and a robust single shot measurement of key parameters such as wavelengths, pulse energy and electron bunch length is mandatory.

While many of the important SASE-FEL concepts were tested at the Free Electron LASer in Hamburg (FLASH), which covered the range of photon energy from extreme ultraviolet (XUV) to soft x-ray domain (up to ~ 300 eV, i.e. ~4 nm wavelength) [155], the LCLS became the world's first FEL to produce ultrabright, coherent x-rays of sub-nm wavelengths [156]. The LCLS has a 132m undulator with a λ_u of 3cm that uses 3.5-15 GeV electrons to produce x-rays between 0.15 and 4 nm, pulse durations of a few to several hundred femtoseconds, and 10^{11} to 10^{13} photons per pulse running at 120Hz [68]. This outshines any synchrotron x-ray sources by up to ten orders of magnitude in peak brightness and enables three orders reduction in pulse duration. The LCLS radiation in the standard SASE mode has a very high degree of transverse coherence and is partially coherent longitudinally [156].

2.6.2 LAMP instrument

The experiments described here were performed at the Atomic, Molecular, and Optical (AMO) beamline of LCLS using the LAMP instrument [147,157,158]. LAMP is the second-generation multipurpose end station at the AMO-LCLS beamline, which is an advanced version of the CFEL ASG Multi-Purpose instrument (CAMP) [69]. The basic idea of both CAMP and LAMP setups is to make the most efficient use of limited and valuable XFEL machine time by

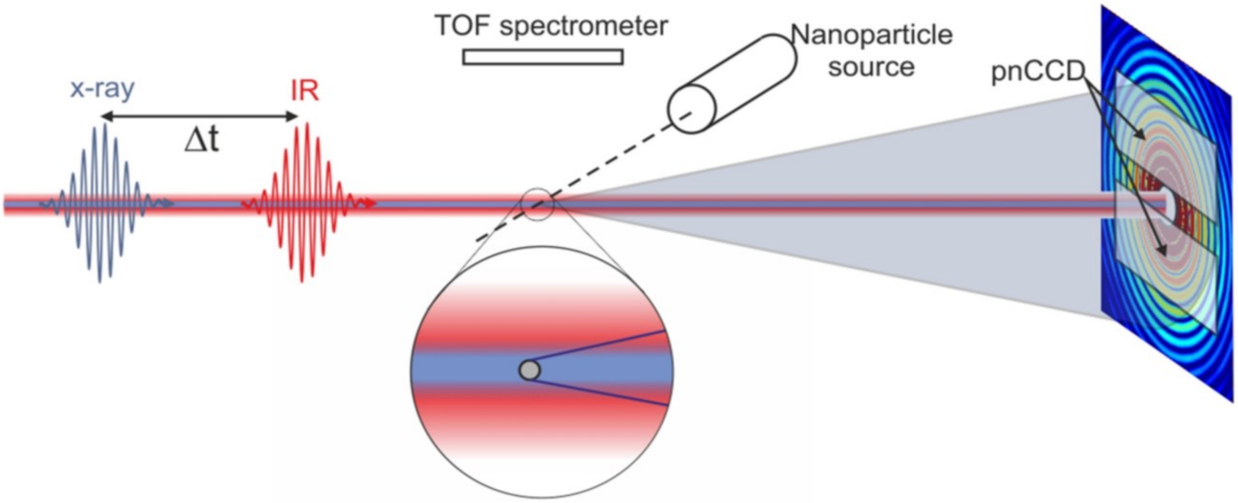

Figure 2.27 *Schematic of the configuration of the nanoparticle source in the LAMP endstation at LCLS. The x-ray and NIR beams are spatially and temporally overlapped and focused perpendicular to the nanoparticle beam. X-ray detectors gather small-angle scattered light in the forward direction. A time-of-flight (TOF) collected emitted ions from the interaction region.*

simultaneous detection of ions, electrons and photons. Figure 2.27 shows a schematic of the experimental configuration of the x-ray, NIR, and nanoparticle beams. The x-ray and NIR beams are spatially and temporally overlapped and focused perpendicular to the nanoparticle jet. The LCLS beam is focused onto the sample by two bendable parabolic-curved grazing incident Kirkpatrick-Baez (KB) silicon mirrors with a boron-carbide coating, resulting in a focal spot size of a few µm^2.

The setup used in this work is essentially similar to that used by Gorkhover et al. to study the dynamics of nanoplasma formation and expansion in laser-irradiated rare gas clusters [28]. To build on the results of that study, a transition from clusters to monodisperse nanoparticle samples is a natural next step, as was discussed in section 1.4.3. Therefore, a new particle source was needed. Its properties and implementation into the LAMP setup is discussed below. Because of its rather large dimensions, the new nanoparticle injector was not compatible with the standard LAMP imaging spectrometers for charged particles. Therefore, a compact time-of-flight (TOF) spectrometer for ions placed directly across from the particle source was employed in this work. The internal arrangement of the LAMP setup for this experiment is depicted in Figure 2.28. This spectrometer was used to distinguish when a nanoparticle was in the FEL focus, mainly by total signal yield. It also provided data for the NIR laser intensity calibration and helped to determine "time-zero" which is the position of exact temporal overlap of the NIR and x-ray beams extracted from the TOF spectra from two-color fragmentation of N_2 molecules [159]. Shot-to-shot fluctuations between the arrival times of both NIR and x-ray pulses were monitored and corrected for using an x-ray – optical cross-correlator described in [146].

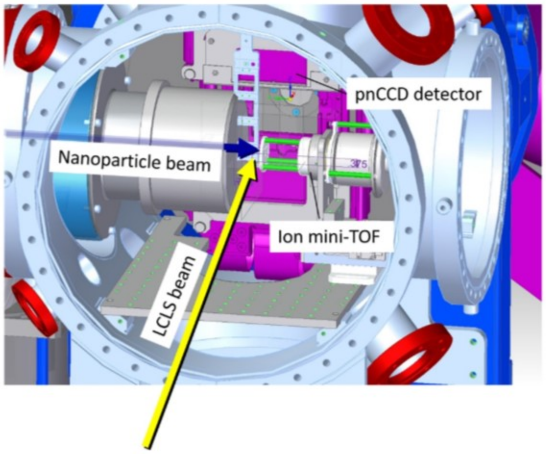

Figure 2.28 *Internal arrangement of the LAMP setup.*

2.6.3 pnCCD detectors

For the detection of scattered x-ray photons, LAMP uses pn-junction charge coupled devices (pnCCDs) similar to those employed in CAMP [69]. These detectors are based on those developed for the x-ray satellite mission XMM-Newton [69,70]. They are large-area pnCCDs with 8 x 8 cm^2 (1024 x 1024 pixels) with a pixel size of 75µm x 75µm. They are ideal for x-ray imaging at soft x-ray FELs as they have low signal noise allowing for single-photon detection, high quantum efficiency at these wavelengths, energy resolution to (at least, partly) distinguish scattered signal from the fluorescent signal, and a reasonably high dynamic range. They also can read-out on a shot by shot basis. They are separated into two halves on adjustable stages which allows for the laser beam to pass through the center. Extensive stray-light suppression techniques are used to prevent stray light from interfering with pnCCD images.

2.6.4 FEL Adaptable Nanoparticle Source (FANS) at LCLS

Building on my knowledge of designing and using nanoparticle sources, I was tasked with constructing a compatible NanoSource for LAMP. The initial requirements called for the ability to produce a nanoparticle beam of sufficient particle density capable of handling dielectric and metallic nanoparticles. As detailed in Section 2.3, a nanoparticle colloid is aerosolized, dried, and focused before entering the main vacuum chamber. One big advantage was the use of the Nafion aerosol dryer as the AMO end station cannot be occupied when the FEL beam ON and the dryer allowed for continuous source operation. Figure 2.29**a)** is a schematic of the newly designed NanoSource that is compatible with the LAMP end station. A negative flange was used to

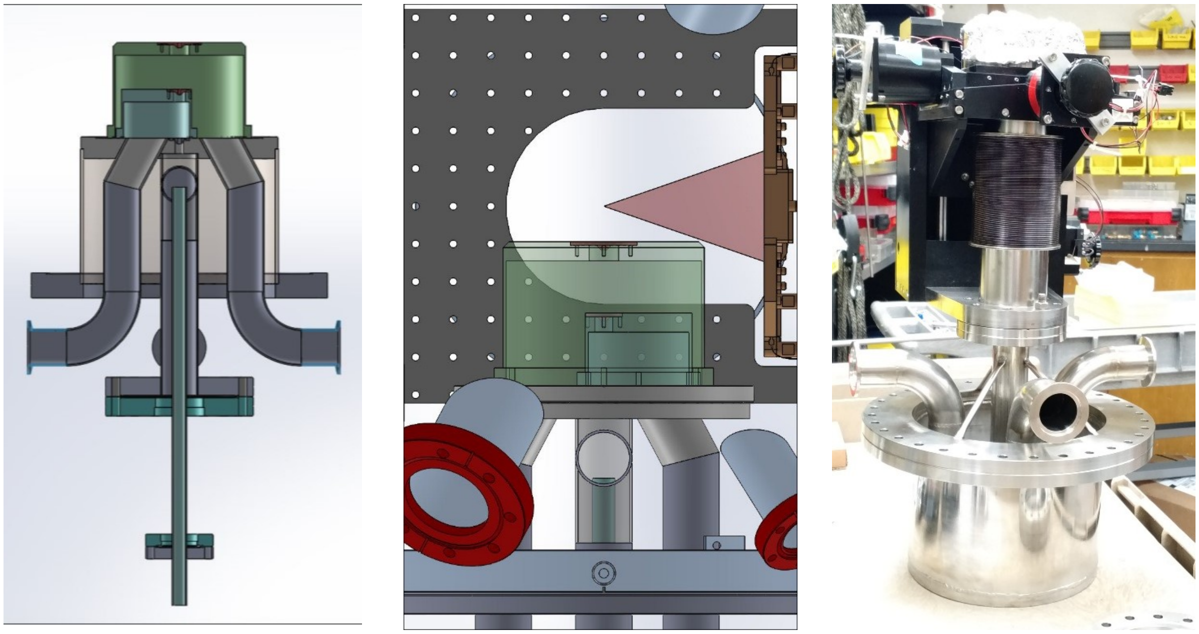

Figure 2.29 *LAMP-compatible NanoSource.* ***a)*** *NanoSource as designed to fit into LAMP to minimize distance to interaction region while having sufficient differential pumping* ***b)*** *Inserted NanoSource with differential pumping cans showing the maximum scattering angle possible (~8°). The pnCCD detectors are on the right* ***c)*** *Actual NanoSource used at LAMP at LCLS. On top is an XYZ manipulator to move nanoparticle jet relative to the fixed skimmers.*

minimize the distance between the nanoparticle jet and the interaction region. As this source needs to be differentially pumped to remove the excess carrier gas, the three stages are constructed to make use of the empty space in the negative flange. The first stage (roughing vacuum supplied by Roots blower) uses the aerodynamic lens outer vacuum housing. The second and third stages use turbomolecular pumps to remove additional carrier gas as the particle beam transits through the respective skimmers. Figure 2.29**b)** is a close-up of the source inside the LAMP chamber and inserted the maximum distance possible as to not obstruct any scattered x-rays incident on the x-ray detector on the right. The third image is the actual NanoSource used at LCLS with an XYZ manipulator on top that is used to move the particle jet relative to the fixed skimmers for optimum alignment in the NIR and x-ray beams.

As the facilities at LCLS included the use of a "FEL Simulator", our group tested the NanoSource before the beamtime started. This allowed for testing and troubleshooting of the source before time became a critical issue. An essential detail that was tested was the alignment of the particle jet with the skimmers. The use of gel paks (GelPak AD-22T-00-X0) allowed for the nanoparticle jet to be seen on a substrate. A single gel pak was mounted in vacuum at the same distance as the interaction region. By testing the nanoparticle throughput as a function of X, Y,

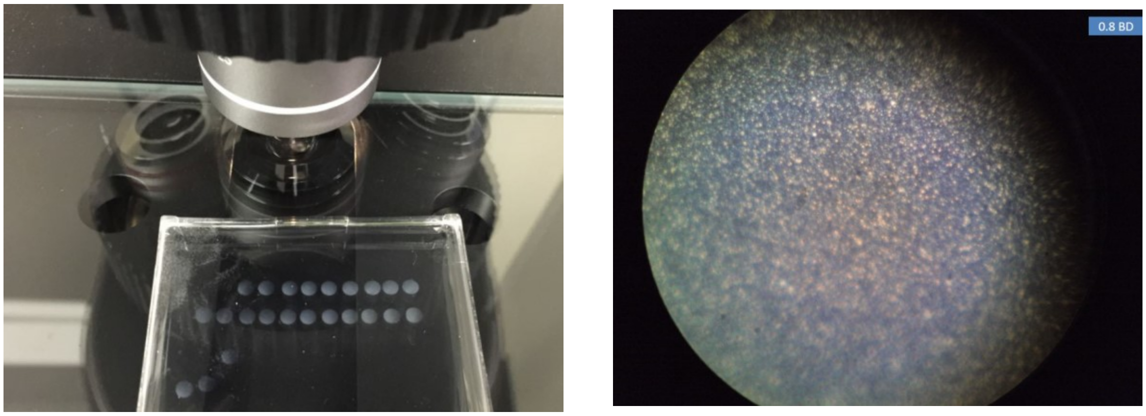

Figure 2.30 *SiO_2 nanoparticles incident on a gel pak slide. Each XYZ position of the manipulator was analyzed for total particle throughput to align the source with the skimmers. On the right is a magnified image of the individual scan on the gel pak. The circular aspect is the particle beam being cut by the last skimmer.*

and Z positions, the optimum location was found to maximize particle throughput. The three skimmer diameters used here that worked the best to balance particle throughput with carrier gas removal was 2mm, 2mm, and 2mm. Larger and smaller skimmers were tested. The circular nature of the particle profile on the gel pak (Figure 2.30) show that the jet was cut by the last skimmer. The diameter of the circles on the gel pak were about 3mm, indicating that the nanoparticle jet is diverging as the last skimmer only had a 2mm diameter.

2.6.5 Nanoparticle samples

To give ourselves the best chance of success, the nanoparticle sample with the smallest size distribution with a reasonable diameter was chosen. The primary sample was SiO_2 with a diameter of 127nm ±2% suspended in ethanol. Samples of polystyrene and gold nanoparticles of similar sizes were also available to be used. Silica (SiO_2) nanoparticles are more stable in a high concentration and prefer ethanol over water. Most gas-phase experiments dilute silica samples with excess ethanol before an experiment. The initial dilutions of the silica particles were done using ultrapure water while later scans used ethanol. During post-beamtime analysis, the scans where ethanol was used to dilute the silica particles showed a correlation to the lack of damage seen on scattering images in contrast to the scans where water was used. A working theory is that a layer of ethanol was left on the particles (the Nafion dryer more efficiently removes water than ethanol [48]) which acted as an ablation layer in the interaction region and therefore the particle was not destroyed. Therefore, only the data where water was the solvent was used for the final analysis of time-dependent x-ray images from SiO_2 nanoparticles.

A few short scans using gold nanoparticles were performed but the lack of sufficient scattering images forced the experiment back to silica. As explained in Section 2.3.5, the use of surfactants contaminates the particle jet. The supplied gold particles could not be used in the atomizer without the addition of surfactant as the particles would irreversibly aggregate within minutes. As clean, isolated nanoparticles are needed in this experiment, this contaminated particle jet was not suitable.

This source is designed to be a versatile piece of hardware. The work presented in this thesis limited the NanoSource to producing particle beams from SiO_2, AuNPs, and polystyrene to be used to study the time-resolved dynamics of an expanding nanoplasma. This source is capable of producing particle beams of almost any nano-sample that can be synthesized and delivering them for FEL studies. This is in slight contrast to rare-gas cluster studies which rely on a high-pressure, pulsed gas source to produce small, polydisperse clusters. Few modifications need to be done to quickly shift the size or composition of the nanoparticle samples. The density and quality of the particle beam is dictated mostly by the initial particle sample which is highly advantageous over cluster or sputtering sources.

Chapter 3 - Temperature Dependent Solubility of Gold Nanoparticle Suspensions/Solutions

> - *What do you get when you cut your gold wedding ring in half?*
>
> \- *Christopher M. Sorensen*

This chapter is adapted from the publication:

- J. A. Powell, R. M. Schwieters, K. W. Bayliff, E. N. Herman, N. J. Hotvedt, J. R. Changstrom, A. Chakrabarti, and C. M. Sorensen. Temperature dependent solubility of gold nanoparticle suspensions/solutions. *RSC Adv.*, 2016, **6**, 70638 DOI: 10.1039/c6ra15822f © The Royal Society of Chemistry 2016

3.1 Nanoparticles colloidal suspensions as solutions

Traditionally, a solution consisting of a solvent and a solute meant a homogenous, single-phase mixture [71]. Dissolving sodium chloride in water is a classic example. Interactions between the solute and solvent can be energetically favorable or unfavorable. As all solutions have a positive entropy of mixing, a saturated solution occurs when the energy penalty from the interactions outweighs the entropy gain of dissolving more solute into the solvent. This balance of entropy gain vs energy loss is dependent on thermodynamic parameters such as temperature, pressure, and volume and thus solubility will shift accordingly. A phase diagram is used to illustrate the co-existence curves of the dissolved solute with the precipitated solute.

Gold nanoparticle (AuNP) synthesis has progressed from the Turkevich method [72] to the Brust-Schriffin method [73] to digestive ripening [18,22,41] in terms of the ability to produce extremely narrow size distributions. This work proposes to consider a system of small 5nm diameter spherical gold nanoparticles dissolved in a solvent to be a solution, as it is a homogenous mixture [15,16]. There is debate as to call such a system a suspension or a solution mainly because of the nanoparticle's large size compared to atomic or molecular entities.

One characteristic that works in favor of a 'solution' description is the fact that this system of gold nanoparticles exhibits temperature dependent solubility. An analogy is best suited here. Think of sugar (long axis diameter ≈ 1nm [74]) dissolving in water as compared to dissolving 5nm gold nanoparticles in toluene, a solvent. Adding solid sugar to water causes the inter-molecular sucrose bonds to break and each molecule will be surrounded by water, aka dissolved. This will happen until saturation occurs, or more precisely a phase boundary (red line) has been crossed as shown in Figure 3.1. A saturated sugar solution resides in the two-phase regime where the dissolved sugar is in equilibrium with the solid sugar. A temperature change will shift the position (vertical) on the phase boundary line and a new equilibrium will be formed by either precipitation of sugar (cooling) or more solid dissolving into solution (heating). Our gold nanoparticles are the 'sugar' in this scenario and we find that they act very similar to that of the molecular sugar. Our gold nanoparticles dissolved in toluene show thermally reversibility where an increase in temperature dissolves more into solution while

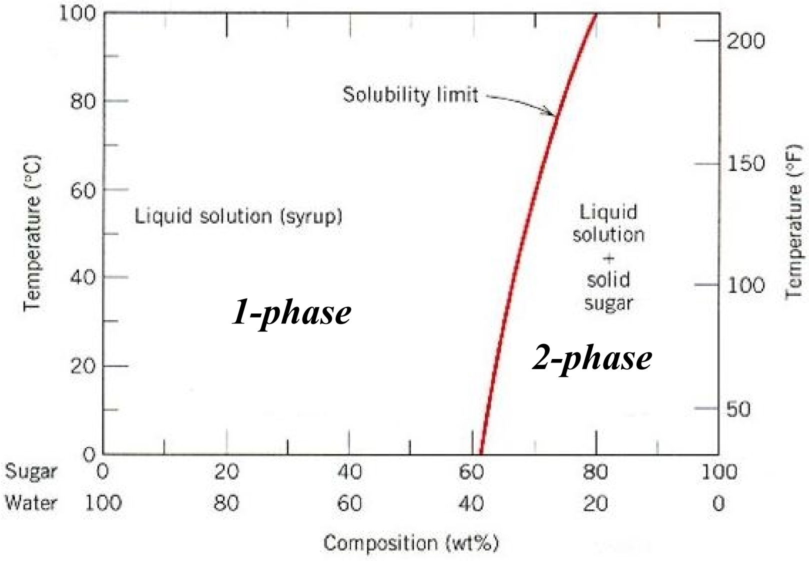

Figure 3.1 *Phase diagram of sucrose in water. Red line is the phase boundary.*

a decrease in temperature will cause precipitation. A similar phase diagram to Figure 3.1 can be constructed for gold nanoparticles with experimental data that map the dissolved (1-phase) with the dissolved + solid (2-phase).

A colloidal suspension of gold nanoparticle monomers is thermally reversible, show aggregation phenomena, and mimic common molecular and ionic behaviors. The extension of a nanoparticle colloid as a solution is therefore made.

3.2 Experimental methods

As described in detail in Section 2.2, a monodisperse 5.5nm AuNP sample is synthesized and digestively ripened. The particles are ligated with an alkane-thiol and dissolved in toluene. The size distribution is verified with the use of a TEM as seen in Figure 3.2. Analogous to traditional solutions, a two-phase system is produced by the addition of solid AuNPs to the solvent. The particles will dissolve into solution (and single monomers will not precipitate by themselves under earth's gravity because of their small size) until a solubility limit is reached and the solution is saturated. Any excess AuNPs added after this will not dissolve but settle to the bottom as a solid precipitate. This solubility limit is highly dependent on not only the outside environment such as temperature and solvent but by internal variables such as particle composition, size, and ligand shell. This experiment needed a high degree of reproducibility to get precise measurements for a specific nanoparticle system.

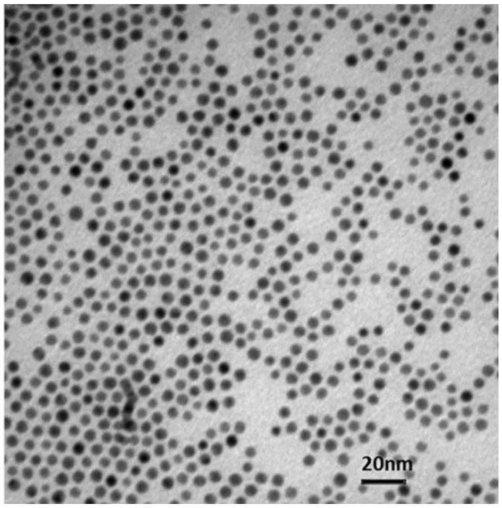

Figure 3.2 *Representative TEM micrograph of 5.5nm AuNPs. Scale bar is 20nm. Figure from [14].*

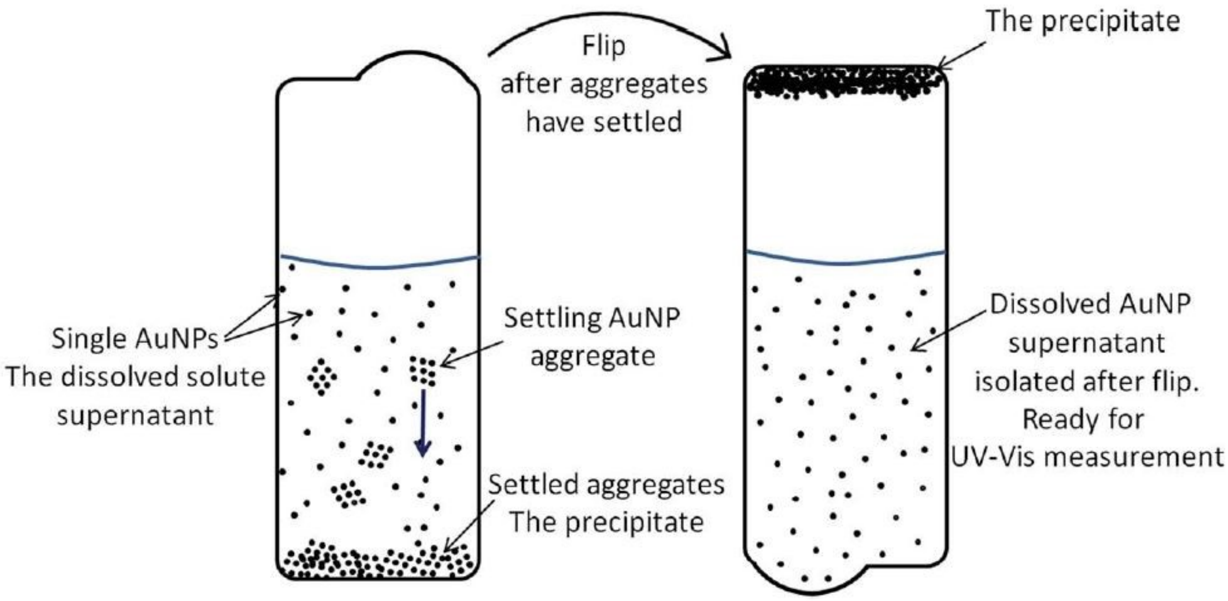

Figure 3.3 *Schematic of an AuNP sample in a sealed ampule. A two-phase system is evident with the single monomers in equilibrium with the precipitate (aggregated monomers). Centrifugation after aggregation speeds the process of separating the monomers from the aggregates. Photo taken from [14].*

This precision came from the use of sealed sample ampules. This isolates the AuNP solution from outside influences and allowed the same sample to be used for an entire temperature scan. Figure 3.3 is a simple but effective schematic showing a sealed AuNP sample. The two-phase system consists of single gold nanoparticles (monomers) and the precipitate (aggregates). An ultrasonic bath disperses the system by breaking up any large aggregates and producing a more homogenous starting point. The sample is inserted into the centrifuge rotor set to a fixed temperature. The sample quickly comes to thermal equilibrium because of its small volume during which time the two-phase system begins to relax to a new equilibrium. Equilibrium in this case is defined as the systems existing in a steady state with no net change between the dissolved state and the aggregated state. High-speed centrifugation is needed to accelerate the separation of the aggregates from the monomers. The absorbance of the supernatant is then measured with a UV-Vis spectrometer. As concentration is proportional to absorbance, the amount of AuNP dissolved in the supernatant was obtained. This process is repeated for temperature values ranging from -0°C to 35°C.

3.3 Absorption measurements

A key aspect in this experiment entails the ability to properly measure the dissolved concentration of AuNPs [19,75]. An absorption feature that is particularly useful in noble metal nanoparticles is the presence of a localized surface plasmon resonance at visible wavelengths. This is the origin of the beautiful array of colors seen in the coinage metal nanoparticles of gold, silver, and copper. The origin of the surface plasmon resonance is the resonant oscillation of the conduction electrons (in metals), oscillating relative to the ion lattice. The electric field of the incident light is the driving force of the conduction electrons [8] where the exact response of the nanoparticle is dictated mainly by its relative permittivity, shape and size. In metallic nanoparticles, this effect is highly localized to the particle surface and thus is very sensitive to any local changes. The precise resonance spectra are dependent on the nanoparticle composition, size, shape, and permittivity. A change in nanoparticle size will redshift the resonant wavelength for larger sizes while a change in shape (such as a nanorod) can lead to two independent plasmon resonances [76].

The obvious use of the plasmon resonance is to have a defining feature to find the relative absorbance changes between different temperature scans. The shape of the plasmon resonance also gives insight into the local aggregation state of the nanoparticles. For small 5nm AuNP dissolved in toluene, the plasmon resonance is centered at 524nm with a FWHM of 60nm. In a two-phase system, the monomers are in equilibrium with the monomer aggregates (precipitate). As these aggregates can be very fine (dimers, trimers, etc.), they will stay suspended in the solvent.

Figure 3.4 shows clear evidence of the sensitivity of the plasmon resonance to the shape and size of the AuNP sample. The red dashed line shows a quenched sample (temperature reduced) and the formation of aggregates. The ensemble absorbance measurement is now a summation of plasmon resonances from the monomers and their aggregates. The large aggregates redshift the peak and produce a 'shoulder'. The same sample is then centrifuged at 3300g to remove the aggregates from the supernatant. The black solid line shows the true monomer resonance without any influence from the precipitate. This is the spectrum that ensures that only the monomer absorbance is taken.

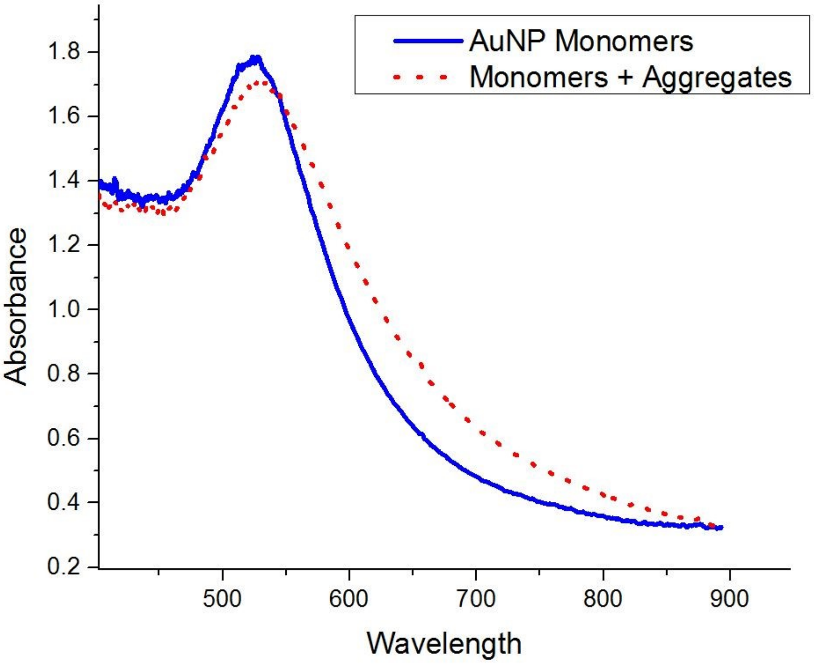

Figure 3.4 *UV-Vis absorbance spectra of 5nm AuNPs. The dashed line is the sample before centrifugation is done to remove any aggregates from the supernatant. The solid line is after centrifugation and only monomers are present.*

The plasmon can be used to verify that the supernatant phase contains only monomers and no aggregates and simultaneously measure the concentration of AuNP monomers. A UV-Vis spectrometer uses a bright, incoherent light source with wavelengths ranging from 180nm-900nm to measure the absorbance of the nanoparticle sample. Absorption is governed by the Beer-Lambert Law

$$\boldsymbol{I(z) = I(0)\exp(-\tau z)} \tag{8}$$

where $I(z)$ is the intensity of light after having passed through a distance z of the solution. The turbidity $\tau = C_{ext}*n$ where C_{ext} is the extinction cross section and n is the particle number concentration. C_{ext} is constant for a given average particle size and for small AuNPs is dominated by the absorption cross section, while scattered light becomes more important with larger-sized particles. The UV-Vis spectrometer measures $I(z)$ and $I(0)$ and calculates an absorbance A given by Eqn. 9

$$A = \log_{10}\left[\frac{I(0)}{I(z)}\right] = 0.43C_{ext}zn \tag{9}$$

This shows a direct proportionality to the absorbance measured by the UV-Vis and the supernatant concentration. AuNP samples of known absorbance were sent to Gailbraith Laboratories and analyzed for total gold content. Knowing the density of gold is 19.34 g/cm^3 and the average AuNP sphere diameter was 5.5nm verified by TEM, the number of nanoparticle monomers per unit volume was calculated. This allowed for a calibrated absorbance spectrum where the concentration of the AuNP supernatant could be found by measuring the plasmon peak absorption value. The mole fraction of AuNPs in the supernatant can then be calculated. The absorbance (and subsequently the concentration and mole fraction) of the AuNPs is measured as a function of

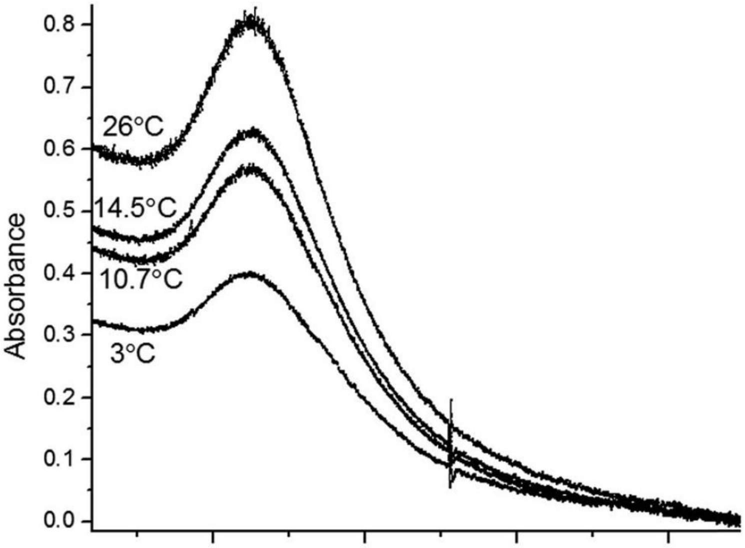

Figure 3.5 *Absorbance spectra of AuNPs as a function of temperature. A temperature change shifts the plasmon absorbance peak which is proportional to the number of dissolved nanoparticles. Feature at 660nm is a light source artifact. Figure taken from [14].*

temperature. Figure 3.5 is the absorbance spectrum of a single sample of AuNPs for four different temperatures. The peak and width of the plasmon resonance stays the same for each run indicating an aggregate-free supernatant. The height of the peak is proportional to the concentration of AuNPs dissolved in the solvent at the given temperature. It is clearly seen how the amount of AuNPs dissolved quickly decreases with temperature.

3.4 Results and analysis

3.4.1 Enthalpy of dissolution

Three different AuNP samples were synthesized by the same synthetic method and studied for completeness. Each one was separately made and analyzed for average particle diameter. Each separate sample vial was re-used throughout the entire temperature scan done over the course of approximately a week to avoid any possible long-term stability issues. The only variable changed in each of these scans (other than having three different samples) was the temperature. Each scan followed the precise procedure outlined in Section 2.2 which greatly increased the reproducibility of this experiment. Multiple, independent temperature scans were done to ensure an accurate representation of the temperature-dependent solubility of each sample.

Figure 3.6 is a plot of the actual experimental data with the three AuNP samples with average diameters of 5.2nm, 5.5nm, and 5.8nm. The absorbance data is converted to concentration and then to AuNP mole fraction *x* which is then plotted *ln(x)* vs *1/T*. According to thermodynamic theory [77], the solid phase – dissolved phase equilibrium solute mole fraction *x*

at a temperature *T* is given by Eqn. 10.

$$\boldsymbol{\ln x = \frac{-\Delta H^{d}}{R}\left(\frac{1}{T} - \frac{1}{T_m}\right) - \ln \gamma} \qquad \textbf{(10)}$$

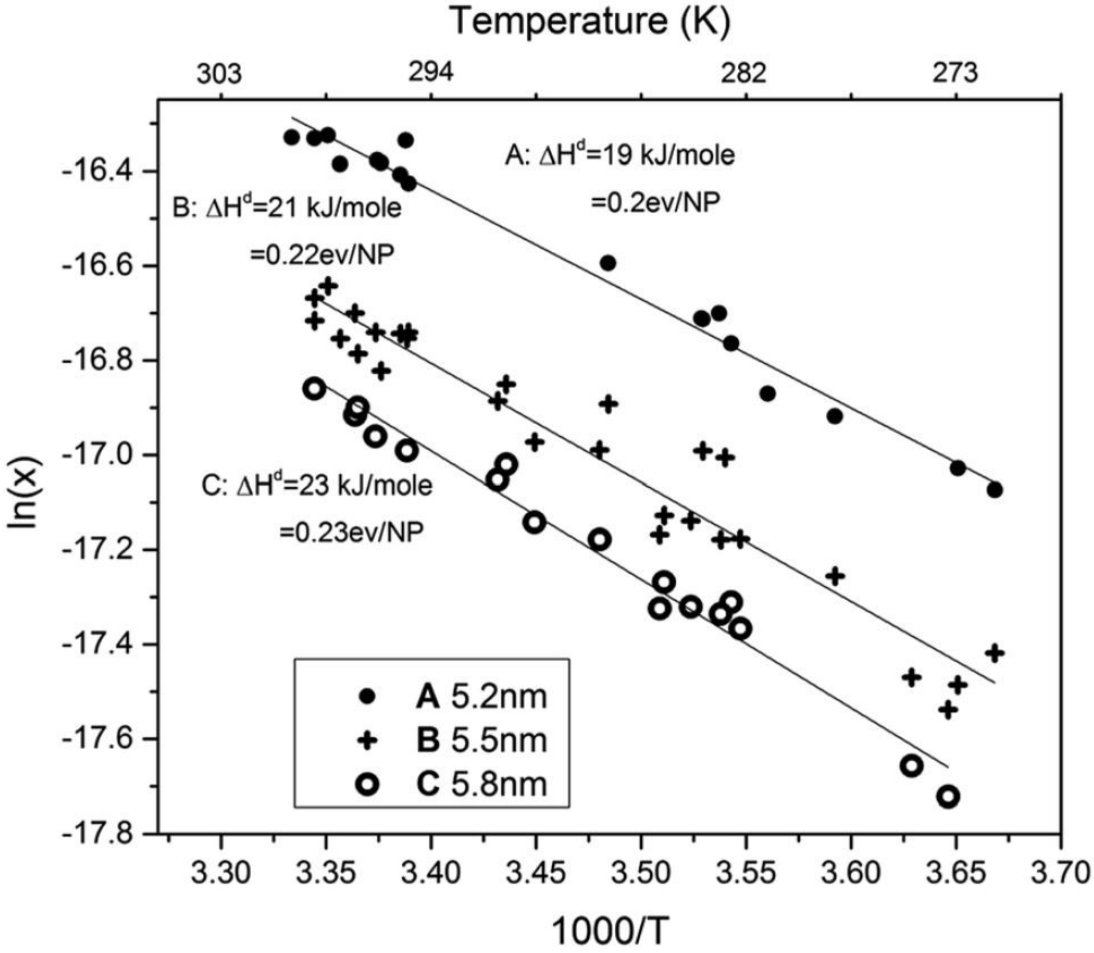

Figure 3.6 *Log mole fraction of dissolved AuNPs in the supernatant vs the inverse temperature. The slope of this graph gives the enthalpy of dissolution for each of the three samples. Photo taken from [14].*

where ΔH^d is the enthalpy of dissolution, T_m is the solid phase solute melting temperature, γ is the activity coefficient for the dissolved solute and R is the ideal gas constant. This also assumes that the enthalpy of dissolution is equal to the enthalpy of fusion, $\Delta H^d = \Delta H^f$, of the solute. The enthalpy of dissolution is the enthalpy change associated with the dissolution of the AuNPs in the solvent and the relevant quantity that this experiment measures.

Figure 3.6 is plotted as *ln(x)* vs *1/T* to use the form of Eqn. 10. The slope of this graph gives the enthalpy of dissolution for each sample, seen here to be endothermic (positive slope) with values of 19.1 kJ/mol, 21 kJ/mol, and 23 kJ/mol for the 5.2nm, 5.5nm, and 5.8nm samples, respectively. This is a measure of the amount of energy needed to dissolve a mole of nanoparticles in this solvent (toluene). Converting to eV/AuNP, an average value of 0.22 eV/AuNP is found. This is directly related to the potential well depth that each particle experiences in the nanoparticle solid and the amount of energy needed for each particle to be dissolved.

3.4.2 van der Waals solid

Due to the novelty of this measurement, there is a lack of empirical or theoretical support. Little is known about the formation of the nanoparticle solid as this precipitate is in dynamic equilibrium with the dissolved supernatant. The precipitate could be forming superlattices [22], fractal aggregates [54] or a combination of short-range lattices assembled in a large fractal pattern. The precipitate structure can give clues into the dynamics of such systems as the coordination number of the nanoparticle solid affects such values as the cohesive energy of the nanoparticle solid, hence the enthalpy of dissolution. As the exact morphology of the precipitate is unknown (a topic of future work), we make a reasonable model for the solid. Gold nanoparticle superlattices viewed on the surface of electron microscope grids has shown twelve-fold coordination [41]. With this said, and given the roughly spherical nature of these particles, their lack of significant charge if assumed to be identical, and the van der Waals force that exists when they are far apart, we propose that these AuNP solids can be visualized as a van der Waals solid similar to those formed by inert gases [78,79]. For argon, the lattice cohesive energy is a factor of 6.5 larger than the latent heat of fusion which is similar to other inert gases [80]. Following the analogy of a van der Waals solid, these 5.5nm AuNP solids have an average $\Delta H^d = 21\ kJ/mol$ and thus $U_{coh} = 6.5 \times \Delta H^d = 136\ kJ/mol$. The melting temperature of a van der Waals solid is empirically described by $T_m = U_{coh} / 103 (J\ mol^{-1}\ K^{-1})$ which yields a predicted $T_m = 1300\ K$ for a van der Waals solid of nanoparticles.

This melting temperature seems rather large as the melting point of bulk gold is 1337 K, implying that the extension of a van der Waals solid for nanoparticles is weak from this perspective.

Previous work by the Sorensen and Chakrabarti groups developed a phenomenological nanoparticle-nanoparticle pair potential model looking at alkane-thiol ligated AuNPs [54]. The model simulated the local environment where NP-NP interactions occur which includes the interactions between the gold cores, ligand-shell, and solvent. These all play a role in determining the overall local potential and dictate how NP solids are formed and dissolved in solution. Included in the potential was the van der Waals interaction between the gold cores with the ligands treated as elastic, flexible polymer chains. Figure 3.7 shows a diagram of how the ligand shell can be compressed and provides an additional free energy of mixing term in the potential. The ligand (in this case an alkane-thiol) are ligated to the AuNP surface and form a shell. This provides steric stability and prevents 'sintering' of two gold cores together. Another possible scenario is where the ligands between different AuNPs do not interpenetrate (mix) but are only compressed in a process known as 'denting' [81]. The comparison of the interaction potentials of these various scenarios allows for insight into experimental results.

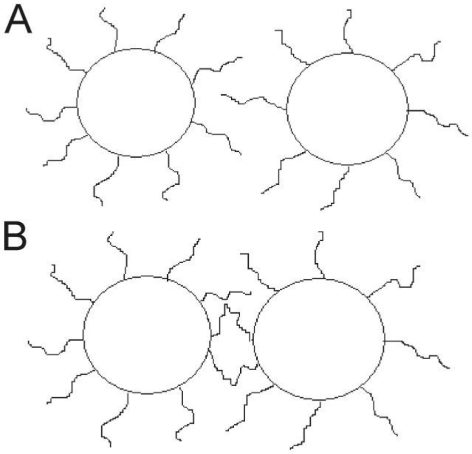

Figure 3.7 *Schematic drawing alkane ligands on the surface of 5nm AuNP.* ***a)*** *Two isolated NP with non-interacting ligand shells.* ***b)*** *Cartoon of interacting ligands showing interpenetration and compression. Figure taken from [54].*

This phenomenological model was successful at predicting the separation distance of nanoparticles at the potential minimum compared to experimental superlattice constants of various ligand lengths. The results of this model in Figure 3.8 plot the nanoparticle effective potential *V(x)* as a function of nanoparticle center to center separation *r* divided by the particle diameter *d* for *d = 5.5nm*. This shape is the familiar addition of attractive and repulsive forces including van der Waals, ligand mixing, and elastic compression. The two lines are different effective potentials which take into the account the different approach to how the ligands interact with each other. The 'denting' (black) potential is the situation where no mixing occurs but just ligand compression. The ligand mixing (red) potential lets the ligands inter-digitate while also compressing.

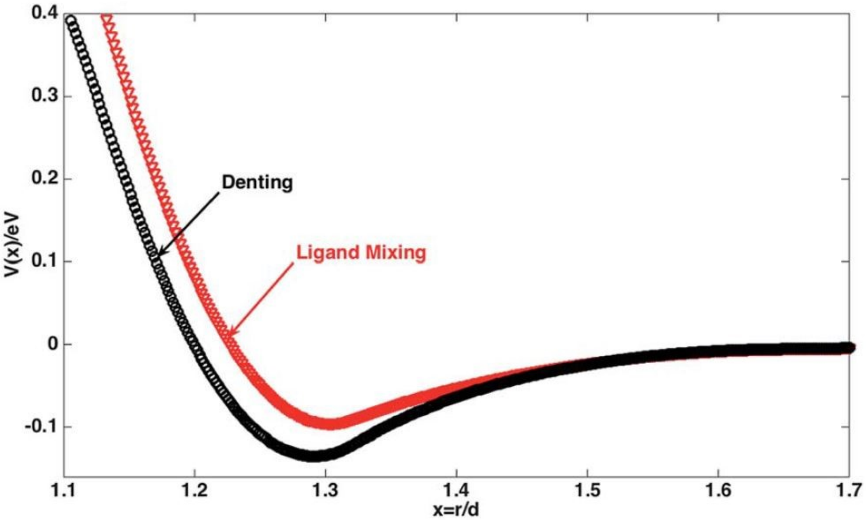

Figure 3.8 *Nanoparticle interparticle potential V(x) in eV vs nanoparticle center to center separation r divided by the NP diameter d for d = 5.5nm. Graph taken from [54].*

The minimum potentials found from Figure 3.8 show a potential well depth, ε, to be $\varepsilon = -0.10eV$ and $\varepsilon = -0.13eV$ for ligand mixing and ligand denting scenarios, respectively. The added free energy of mixing potential in the ligand denting situation clearly shifts the minimum effective potential to a shallower well depth and shows the effect even small changes in the ligand interactions can produce.

An interparticle potential minimum, ε, can also be found with the experimental results by again returning to the analogy of the van der Waals solid. The total lattice cohesive energy, U_{coh}

$= 8.6N\varepsilon$, where N is the total number of atoms or NPs [80], directly relates to the interparticle potential minimum. The NP superlattice energy, $U_{coh} = 136\ kJ/mol$ is derived from the calculated enthalpy of dissolution using the van der Waals solid assumption, and finds the experimental value of $\varepsilon = -0.165\ eV$. This compares favorably to the values found in the phenomenological model, even with the amount of assumptions made.

The use of the van der Waals solid model did not give a reasonable estimating for the melting point of the AuNP solid but did show modest agreement for the interparticle potential well minimum. More work is being done to investigate a more rigorous model to better understand the complex interactions in nanoparticles with each other, the ligands, and the solvent. This basic understanding will be key to the use of nanoparticles in real-world applications [82–84].

3.4.3 Activity coefficient

The activity coefficient is a measure of the deviation from ideal solution behavior when mixing substances. Two substances that are very similar chemically (methanol mixing in ethanol) will form an almost ideal mixture. Departure from this ideality makes the use of an activity coefficient factor, analogous to the fugacity coefficient for gases.

When the temperature-dependent solubility data is plotted as seen in Figure 3.6, the vertical shift is the measure of the deviation from an ideal solution, or the activity coefficient, γ. For an ideal solution, the $\ln x = 0$ intercept occurs at the solute melting temperature, T_m. Here, Figure 3.9 is the same experimental data as shown in Figure 3.6 but with expanded axes to extrapolate the slope. The collective data is shown in the lower right-hand corner. The extrapolated slope shows a negative x-intercept inferring a negative temperature for T_m. Looking back to Eqn. 10, the intercepts at $1/T = 0$ and $\ln x = 0$ yield the same relation between $\ln \gamma$ and T_m. This relation is roughly given as

$$\ln\gamma = 8 + \frac{2500}{T_m} \tag{11}$$

This is one equation with two unknowns which currently have no way of being measured independently. The value of T_m was attempted in the lab to look for the melting of the AuNP solid where the nanoparticle-nanoparticle bonds are breaking but not the gold core melting. The results were poorly reproduced as the ligand shell decomposed at high temperature but a reasonable guess of 400K is being made in this case. For a $T_m = 400\ K$, an activity coefficient of $\gamma = 1.5 \times 10^6$ is obtained which is a very large value. The van der Waals solid estimation of $T_m = 1300\ K$ gives $\gamma = 2 \times 10^5$. As $T \to \infty$, $\gamma = 3000$ which is still a very sizeable activity coefficient.

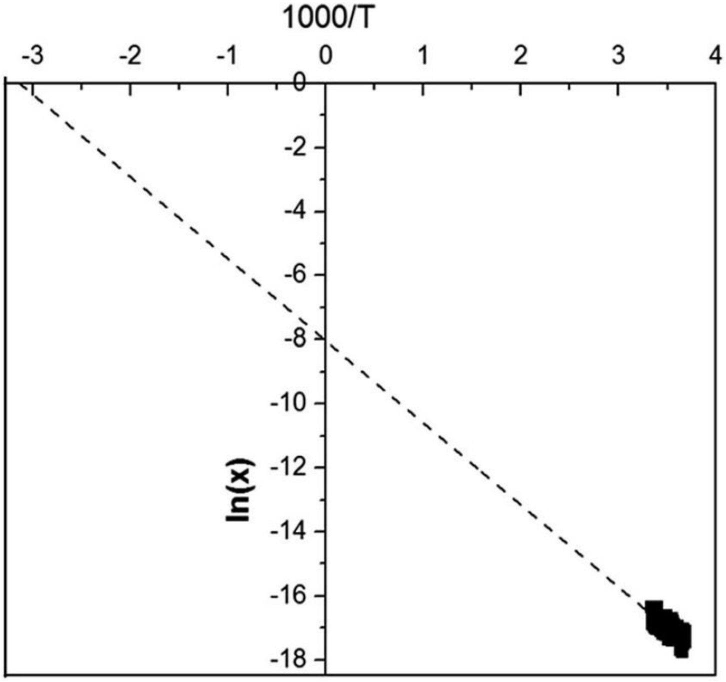

Figure 3.9 *Log mole fraction of AuNPs vs the inverse temperature on expanded scale. Lower right hand is the same data from Figure 3.6. Figure from [14].*

Another approach to gain insight to the activity coefficient of gold nanoparticle solutions uses Scatchard-Hildebrand theory [77]. The activity coefficient is calculated for regular solutions, defined as a solution for which there is no excess entropy of mixing. Regular solution theory applies when the solute and the solvent are similar. This is not exactly the case for small AuNPs dissolved in a molecular solvent, though the ligand shell which directly interacts with the solvent molecules (1-dodecanethiol and toluene) are relatively soluble in one another. As a solid theoretical framework is lacking, the Scatchard-Hildebrand approach is continued. The activity coefficient for the solute is predicted to be [77]

$$\boldsymbol{RT \ln \gamma = \nu \Phi_{solv}^{2} (\delta - \delta_{\mathrm{solv}})^{2}} \qquad \textbf{(12)}$$

where R is the gas constant, T is the temperature, ν is the molar volume of the solute, Φ_{solv} is the volume fraction of the solvent and δ and δ_{solv} represent the solubility parameters of the solute and solvent, respectively. The expected failure of the Scatchard-Hildebrand theory for AuNP solutions is seen when substituting Eqn. 12 into Eqn. 10 that a negative temperature is not possible. The experimental data clearly shows an extrapolation to a negative temperature.

Some insight is gained as Eqn. 12 does hint at the origin of a very large activity coefficient as the molar volume v for AuNPs is enormous, approximately 160 liters (assuming an Au core plus ligand shell of combined diameter of 8nm). An interesting question can be asked at this point. An equal molar solution consists of equal moles of solute and solvent. In the case of a AuNP solution dissolved in toluene, an equal molar solution will have approximately 160 liters of AuNPs and 0.1 liters of toluene. 100ml of toluene cannot possible dissolve that quantity of AuNPs and therefore it is not physically possible to have molar solutions close to unity. Equal volumes of toluene and AuNP gives a mole fraction of AuNP to be 6.6×10^{-4}. The large molar volume of nanoparticles inherently will lead to large activity coefficients.

3.5 Conclusion

I have presented what appears to be the first measurements of the temperature dependence of thermally reversible solubility for a nanoparticle suspension/solution. Extending standard thermodynamic solution theory to a 5.5nm AuNP solution yields an average enthalpy of dissolution of $\Delta H^{d} = 20.9$ *kJ/mol NP*. A lack of theoretical support to serve as a backbone of understanding complex nanoparticle-nanoparticle and nanoparticle-solvent interactions lead to various assumptions made to gain a better understanding of the experimental results. The extension of the concept of a van der Waals solid to a AuNP solid lead to unrealistically high melting temperatures. However, under the same assumption, the minimum of the interparticle potential derived from the data agreed fairly well with a phenomenological model of this same system. The dissolution of AuNPs in toluene is a non-ideal solution meaning it has an activity coefficient. The activity coefficient could not be determined due to a lack of a reliable known melting temperature for AuNP solids, though any finite temperature implied a very large activity. This is consistent with the thermodynamic measurement that extrapolates to a negative temperature at AuNP mole fraction equal to one. The application of Scatchard-Hildebrand theory gave some insight into the very large activity as a result of the very large molar volume of the AuNPs. It is clear that much work needs to be done to sufficiently interpret this novel experimental data.

Chapter 4 - Photoelectron Spectroscopy from Nanoparticles in Intense Fields

- *"The most exciting phrase to hear in science, the one that heralds new discoveries, is not 'Eureka!' but 'That's funny…"*

- *Isaac Asimov*

4.1 Photoelectron imaging avoiding focal volume averaging

The parameters of a nanoscale target can be well defined in a gas-phase experiment where no more than one particle contribute to the measured observables. A key factor in determining mechanisms and subtleties of the electron emission is the effective driving laser intensity. The spatial distribution of the target is usually non-negligible (and much larger) compared to the dimensions of the laser focus which causes the irradiated object to experience different intensities depending on its position in the focus. Therefore, the measured photoelectron energy and angular distributions are effectively averaged over the spatial intensity distribution of the laser field which can complicate their interpretation and comparison to theory.

In isolated atoms and molecules in a multiphoton or tunneling regime, the intensity distribution of the laser focus is often less critical because of the highly non-linear dependence of the ionization probability (and thus the photoelectron yield). The vast majority of the events contributing to the observed spectra originate from the small volume corresponding to the peak intensity value. In contrast, for a nanoscale system, the dependence of the number of emitted electrons on the laser intensity often might be nearly linear [26,27], and the resulting spectra might directly reflect the spatial profile of the laser focus, heavily favoring the regions with lower intensities which have a larger focal volume.

4.1.1 'Binning' technique for near-single intensity observables

Here we present an experimental technique aimed to study intensity- and size-dependent photoelectron emission patterns from gas-phase nanoparticles, while avoiding focal volume averaging. The method is based on using the number of emitted photoelectrons per laser shot for a given nanoparticle size as a relative measure of the local laser intensity (i.e. the particle's position within the laser focus). By sorting results according to this observable, accurate energy- and angle-resolved photoelectron spectra corresponding to a particular laser intensity range are obtained. This technique is used to study size-dependent electron emission from SiO_2 (silica) and gold nanoparticles (AuNPs) driven by an intense, femtosecond near-infrared laser field. Photoelectron energy cutoffs and angular distributions are obtained from the measured data.

A simple histogram plotting a nanoparticle scan vs a background scan (solvent only; no nanoparticles in solution) shows where an appropriate demarcation limit should be placed as the nanoparticle contribution diverges from the background. Figure 4.1 clearly shows the divergence of the nanoparticle contribution from the background scan. This sets the lower threshold to properly segregate the background from the nanoparticle contribution. By scanning the laser intensity from

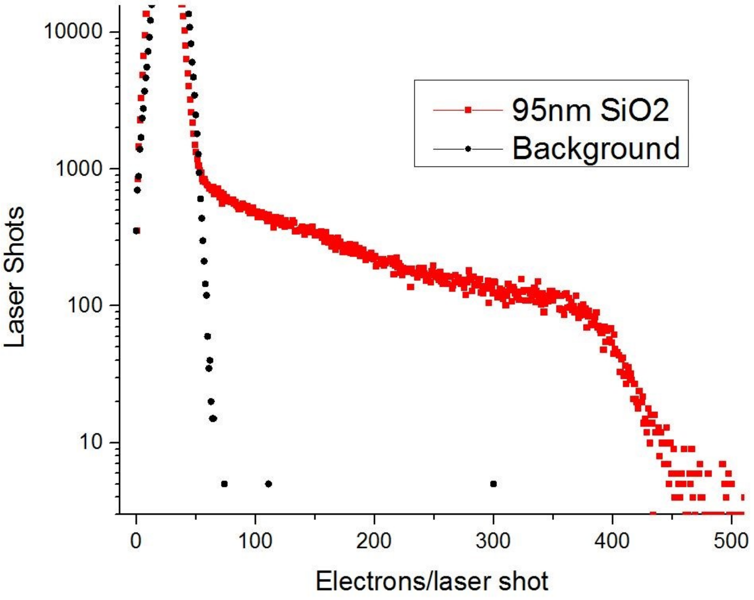

Figure 4.1 *Hit histogram from 95nm SiO_2 of number of photoelectrons per laser shot. Nanoparticle scan (red) compared vs solvent-only background scan (black). Here 2.5 x 10^6 laser shots were recorded at 6 x 10^{13} W/cm^2.*

2×10^{13} W/cm^2 to 8×10^{13} W/cm^2 for the same sample (Figure 4.2), the histogram shows a clear shift in the maximum number of electrons per laser shot observed.

The number of photoelectrons emitted from a single, isolated nanoparticle is determined by the nanoparticle composition, shape, and size while also sensitive to laser parameters such as wavelength and intensity [26,27]. Referring to the histogram in Figure 4.1, the above-background values between 75-450 electrons per laser shot are a microscopic probe of the focal volume of the laser. Each nanoparticle is incident on a random area of the laser focus as the nanoparticle beam is much larger than the laser focus. Thus, the intensity seen by that particular particle will be determined by its spatial position in the Gaussian-like distribution of the laser focus.

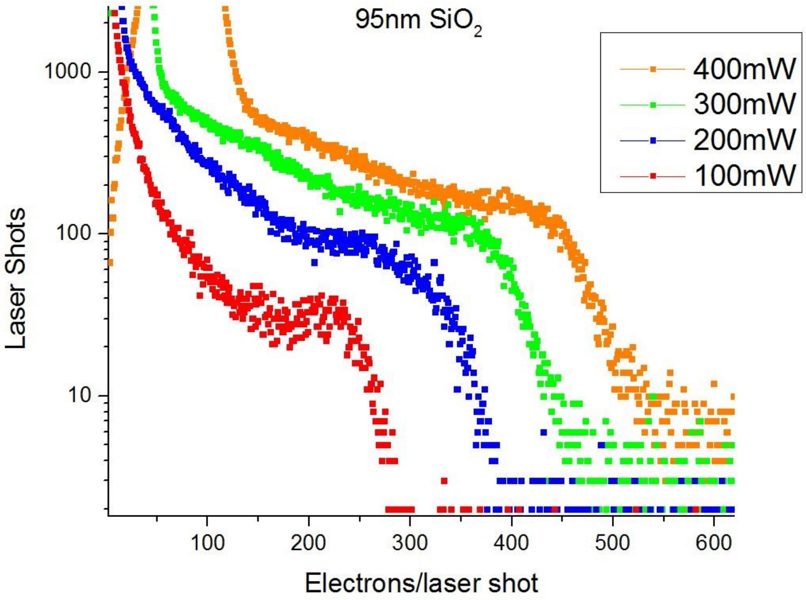

Figure 4.2 *Hit histogram of 95nm SiO$_2$ nanoparticles at different laser intensities. The largest number of electrons per laser shot shifts to larger values as the laser intensity increases. 100mW = 2×10^{13} W/cm^2.*

The width of the histogram arises from the nanoparticle contribution as a function of incident laser intensity. The limit where a nanoparticle only sees one laser intensity would transform this histogram into a delta function-like spectrum as there would be no convolution of laser intensities. As the predicted photoelectron yield is nearly linear as a function of intensity [61] (at least in the intensity range in this study), the number of electrons per laser shot can be used as a coarse guide for near-single intensity sampling of the nanoparticle interaction. In the actual experiment, detection efficiencies prevent a true representation of the total emitted electrons, especially at high intensity and/or large particle sizes. A 'bin' is defined as a portion of the hit histogram that corresponds to near-single intensity nanoparticle contributions as seen in the grey shaded regions of Figure 4.3. The upper-right corner of this figure is a cross-section schematic of a Gaussian laser focus. The laser intensity is maximum in the center and decreases as a function of distance away from the middle, while the focal volume is a minimum at the center and increases towards the focal 'wings'. The placement of the 'bins' **a)**, **b)**, and **c)** correspond to the lowest to highest intensity the nanoparticle sample experienced, respectively. Bin **c)** is defined as the maximum number of electrons per laser shot as it corresponds to the peak laser intensity.

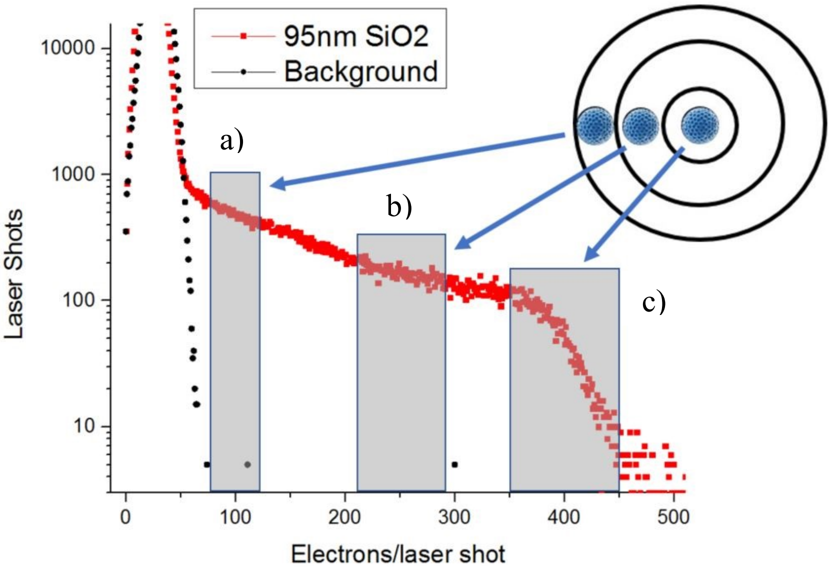

Figure 4.3 *Nanoparticle hit histogram with 'binning' technique. Only laser shots containing the number of electrons within a specified bin-width are analyzed to produce near-single intensity photoelectron VMI images. The upper-right corner is a simple cross-section representation of a Gaussian laser focus. The center has the highest intensity but smallest focal volume. Moving spatially outwards the intensity decreases but volume increases.* ***a)*** *Smallest 'bin' with the least number of electrons per laser shot and thus the smallest incident intensity.* ***b)*** *Intermediate laser intensity* ***c)*** *Largest number of electrons per laser shot and the peak laser intensity at center of focus.*

This 'binning' technique essentially avoids focal volume averaging, or volumetric weighting effects where the contribution from the low intensity 'wings' of the laser focus can dominate the overall nanoparticle angular and energy spectrum and allows accurate single-intensity analysis. This in in contrast to an integrated spectrum which include all the laser shots above the background level regardless of local laser intensity. As there are contributions from many different intensities, intensity-dependent features can be washed out, most notably angular distributions in VMI images.

The corresponding laser shots within each selected 'bin' are combined to produce a raw VMI photoelectron image. Figure 4.4 illustrates the 'binning' technique on several different peak

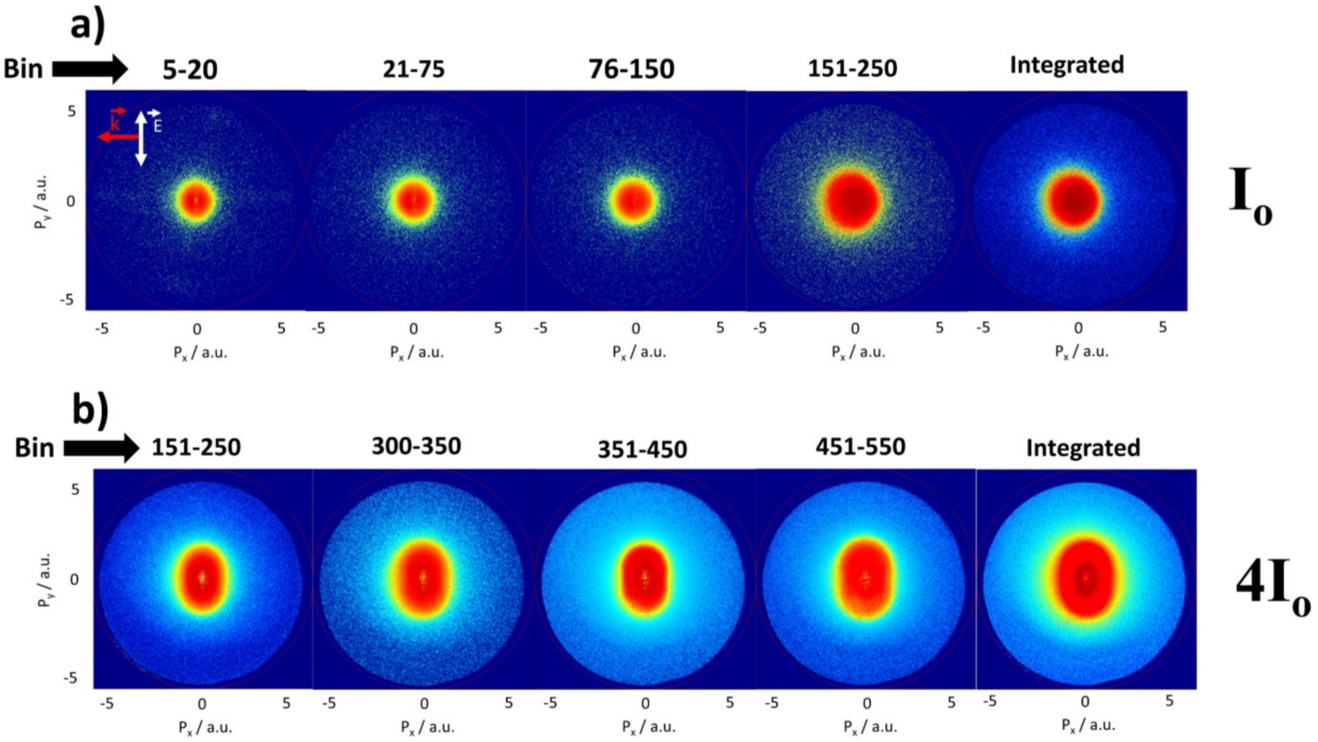

Figure 4.4 *VMI images sorted by their respective 'bins', defined as the number of electrons per laser shot. Each row is a scan at a fixed peak intensity. The progression from left to right on a row shows the different nanoparticle spectra resulting from different intensities within the laser focus, as compared to the integrated image (far right). The photoelectron momenta get larger as the number of electrons per laser shot ('bin') increases. The angular distribution also is clearly intensity dependent. These scans were done with 95nm* SiO_2 *with* $I_o = 2 \times 10^{13}$ *W/cm*^{2}*. The log color scale has red=max counts and blue=background level.*

laser intensities for the same sample. From left to right, there is an obvious difference between different 'bins' as the photoelectron spectra depend on the local laser intensity, including the elongation along the polarization axis and the increased photoelectron momenta. The far-right images show the integrated, focal volume-averaged, VMI images which are the sum of all possible bins from the background level to the maximum number of electrons per laser shot.

The advantages of having single-intensity photoelectron spectra include the ability to better resolve the angular distribution. Prominent features such as the elongation along the polarization axis can be seen in the integrated images but 'binning' can help distinguish minute changes. The near-single intensity images seen in Figure 4.4 shows the evolution of the angular distribution as a function of intensity. An isotropic, circular distribution at low intensities stretches along the polarization axis as the intensity increases. The spectra from 'bin 451-550' begins to show a figure-eight shape that is not seen in the 'binned' images at lower intensities or in the integrated spectra. Simulations of nanoparticle electron emission also show this characteristic shape at similar intensities [86] but experimental focal volume averaged images of the same data can wash out angular distribution features, as seen in the integrated image from Figure 4.4**b)**.

To analyze the photoelectron emission patterns more quantitatively, the radial distribution of a VMI image is rescaled to energy units. If an inversion of the 2D VMI projection would be done, a full energy distribution can be found. However, as discussed in Section 2.4.7, this relies on having an axis of symmetry and thus could not be applied to all of the samples studied in this work. Therefore, non-inverted radial distributions (in energy units) are used as a "replacement" for the true photoelectron kinetic energy spectra. This did not cause any substantial loss of information since determining the exact form of the energy or angular distributions was not the goal of this work. Direct comparison of inverted and non-inverted VMI data will be presented in the next section.

The radial distribution of each ‘bin’ is obtained by taking a 30° full-opening angle slice along the polarization direction of the VMI image. After calibration, the radial distribution displays the photoelectron spectra scaled in energy units. Figure 4.5 is the radial distribution of a single nanoparticle scan at a fixed peak intensity. The positive shift in energy as the ‘bin’ increases mimics what is seen in the raw VMI images from Figure 4.4 and quantitatively shows the different intensity regions with the laser focus. Notice how the integrated radial distribution (red curve) has a slightly lower energy (shifted to the left) than the largest ‘bin’ (cyan). As the integrated spectra has all laser intensity contributions present, it can wash out the small contribution from the peak intensity region (largest ‘bin’) and thus, slightly underestimate the actual peak photoelectron energy. The overall shape of the energy distribution also varies as a function of ‘bin’ or integrated spectra. The ‘binning’ technique successfully portrays the

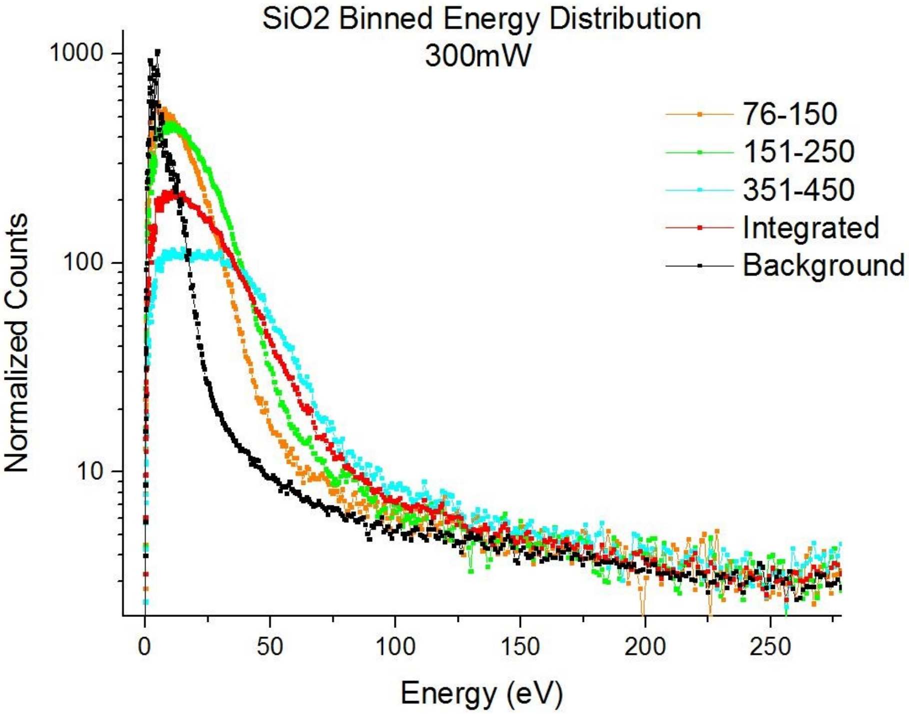

Figure 4.5 *Nanoparticle radial distribution as a function of ‘bin’. The radial distribution of each ‘bin’ in one nanoparticle scan at a fixed peak intensity. The increase in energy with bin size shows the different intensity regions within the laser focus.* 300mW ≈ $6x10^{13}$ W/cm^2 *in this plot.*

changing morphology of the intensity-dependent energy distribution that is convoluted in the integrated distribution.

It is important to realize that the hit histograms presented in Figure 4.1-Figure 4.3 do not provide the real number of the electrons emitted from a nanoparticle. First, the detection efficiency of the MCP detector/phosphor screen arrangement, i.e., the probability to register an electron hitting the MCP, is considerably smaller than unity (~0.4-0.5), therefore reducing the number of measured electrons. Under ideal conditions, this would provide a constant scaling factor for all data sets. However, a second, more critical issue stems from detector saturation effects. If a large number of electrons impinge on a particular area of the detector (most likely the center), the detection efficiency for this area is reduced and becomes negligibly small for certain threshold values of the electron hit density. This can be seen in the reduction of the low-energy photoelectron contributions in Figure 4.5 as the number of electrons per laser shot ('bin') increases. Therefore, for higher intensities and large particle sizes where more electrons are emitted, the detection efficiency decreases, and the measured number of electrons are less likely to reflect the actual number of emitted electrons. Accordingly, even if the exact relation between the local peak laser intensity and the number of emitted electrons would be known, the technique presented here is not capable of reconstructing the exact spatial profile of the laser focus and, thus, assigning the exact intensity value to each bin using the current detection technology. It can become capable of achieving this goal if detectors with larger dynamic ranges will become available. However, already now this technique can be efficiently used to separate low-intensity contributions to the photoelectron data and effectively approach single-intensity conditions.

4.1.2 Determination of photoelectron cutoff

A robust method for systematically finding experimental photoelectron cutoffs provides a way to systematize the role of different parameters such as nanoparticle size and laser intensity. A cutoff is defined as the maximum observed photoelectron energy. Each VMI image, either 'binned' or integrated, has a characteristic cutoff determined by the photoelectron spectra within each image. Such cutoffs are important observables for atomic ionization and have been used to determine peak laser intensities [148]. However, the cutoff determination is by far not a straightforward procedure since it strongly depends on signal to noise ratio. The VMI technique is not ideal for this purpose since the electronic noise and dark counts of a single shot camera are typically non-negligible compared to the rather low electron yield in the cutoff region. Two different empirical approaches are often used to find the highest energy for which the photoelectron yield is non-zero. The first one relies on a signal reduction to a given fraction (e.g., three orders of magnitude) compared to the energy of maximum abundance (which, for experiments with high intensities, corresponds to electrons with nearly zero energies). This technique implies certain knowledge of the shape of the spectrum and is hardly applicable if the low-energy region is saturated, which is often the case for the experiments on nanoparticles. Therefore, many recent experiments on nanosystems which utilized few-cycle laser pulses with stable carrier-envelope phase (CEP) relied on the evolution of the CEP-dependent asymmetries to determine the cutoff values [24,25,86]. Since longer, ~25 fs pulses without CEP stabilization were employed in this work, this approach could not be applied here.

To systematically quantify the energy cutoffs in nanoparticle data obtained in this work, a 'background matching' procedure was found to be the most effective. The use of a reference scan enables the comparison of a nanoparticle spectra to its corresponding background radial distribution. The hit histogram in Figure 4.3 illustrates how the background contributions is separated from the nanoparticles by comparison to the solvent-only scan. The background laser shots (all the laser shots in the red line that overlap the black, solvent-only scan) are designated as the reference distribution. As the reference scan are laser shots taken concurrently to the nanoparticle scan, it is a true representation of the background. It includes all the background contributions: the events coming from the ionization of residual gas, any stray laser light incident on the detector, and camera noise, all in the exact conditions of the obtained nanoparticle data.

Figure 4.6 shows a typical radial distribution using the 'background matching' method. The two spectra shown are taken from a single scan at a fixed peak intensity where the background (black) 'bin' is compared to the integrated signal. The nanoparticle integrated signal (red) is shifted vertically to overlap and 'match' the background spectra. The location where the two spectra intersect means that the nanoparticle signal has fallen into the background and thus has no photoelectron contribution from the particle itself past this crossover. This is defined as the photoelectron energy cutoff.

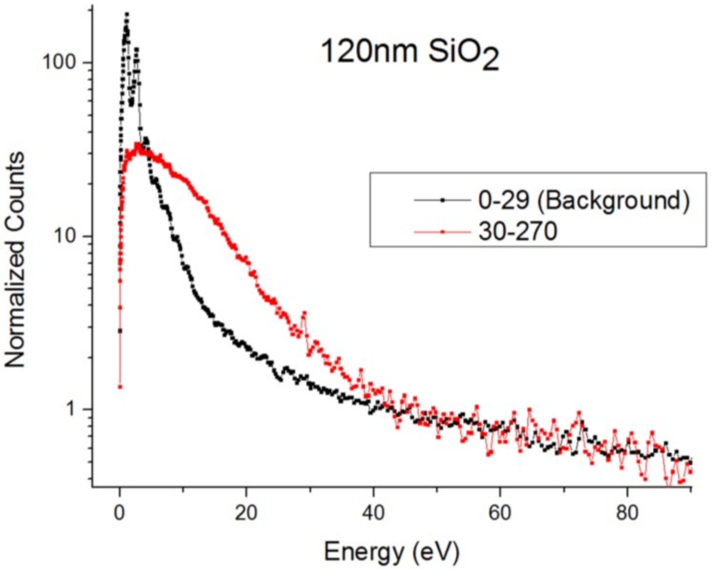

Figure 4.6 *Radial distribution of 120nm* SiO_2*. The integrated nanoparticle signal (red) has been shifted vertically to overlap the background signal (black). The legend is showing the number of electrons per laser shot to determine the background and nanoparticle signal. Data taken at* $1.3x10^{13}$ *W/cm*^{2}*.*

It is useful to make the comparison between a photoelectron radial distribution and an energy distribution. The radial distribution makes use of the 2D VMI projection to show a spectrum scaled in energy units while the energy distribution is calculated from the full 3D momentum components. An inversion procedure makes use of a symmetry axis to produce the energy distribution. As discussed in Section 2.4.7, this can be done for small nanoparticles such as those seen for 50nm SiO_2 in Figure 4.7 as their photoelectron distribution is symmetric along the polarization axis. The radial distribution (left) is compared to the energy distribution (right) to show that the cutoff is not significantly different between the two spectrums. There is a noticeable change in the overall shape of the energy distribution (seen between 10-40eV) where the full energy distribution of the inverted spectra more effectively depicts the initial 3D momentum distribution (Newton sphere [57]) of the nanoparticle photoelectrons. However, for the purpose of determining the energy cutoff, a non-inverted radial distribution is equivalent to the inverted energy spectrum. This essentially should be expected since the 2D projection on the detector

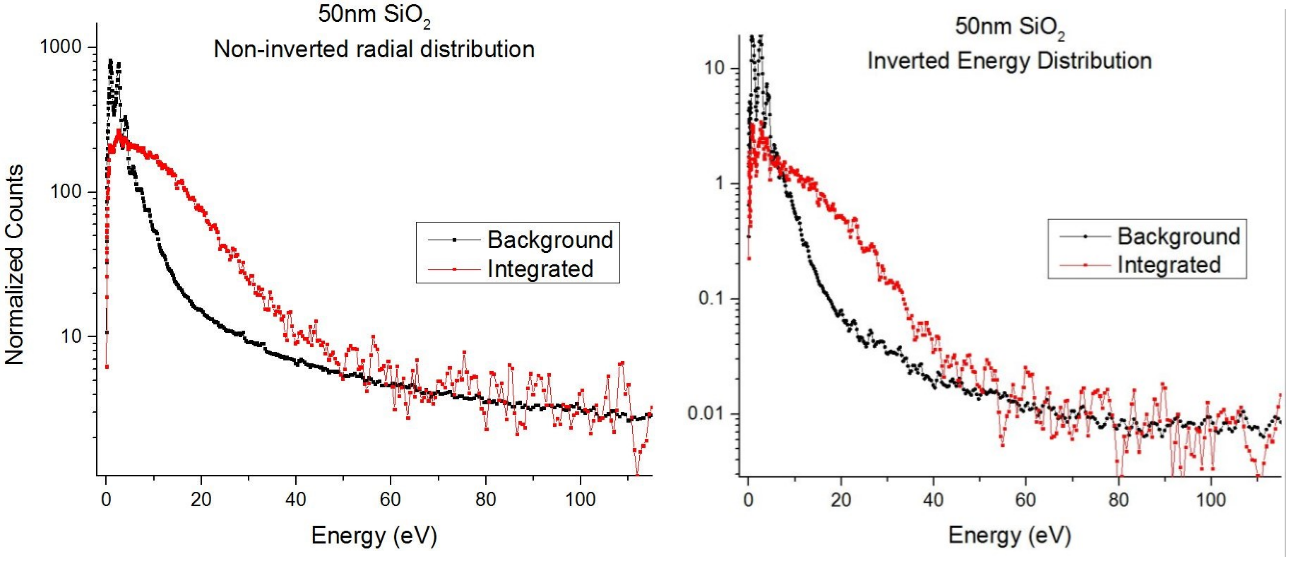

Figure 4.7 *Non-inverted radial distribution compared to inverted energy distribution from 50nm* SiO_2*. On left is the radial distribution (non-inverted) while on the right is the energy distribution (inverted). The energy cutoff between the two spectrums is not significantly different. Peak intensity = 1.8 x* 10^{13} *W/cm*^{2}*.*

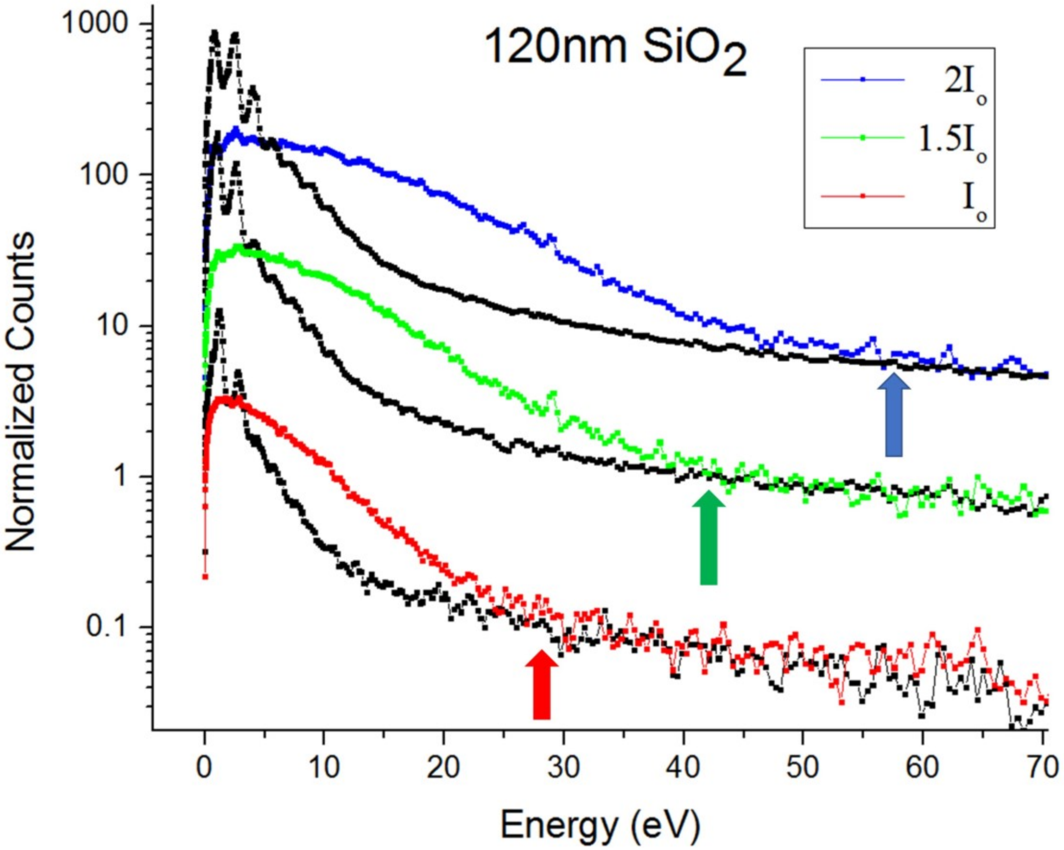

Figure 4.8 *Integrated photoelectron radial distributions as a function of intensity. The cutoff energy is found by overlapping the respective background (black) with the nanoparticle distribution. Arrows show the measured cutoff energy of each intensity scan for 120nm* SiO_2 *found to be 28, 43 and 58eV, for* I_o*, 1.5*I_o*, and 2*I_o*, respectively.* $I_o = 8.8 \times 10^{12}$ *W/cm*^{2}

plane, which is the non-inverted VMI image, should have the same upper boundaries as the full 3D momentum sphere.

The final test of the 'background matching' method for determining photoelectron cutoffs is shown in Figure 4.8 where the radial distributions of the integrated spectra is plotted as a function of laser intensity. The respective backgrounds (black) for each intensity scan overlaps the nanoparticle distribution where the cutoff value is found. Colored arrows indicate where the energy cutoff is placed for each of the scans. The increased momentum distribution of the integrated raw VMI images seen in Figure 4.4 can now be fully quantified and a cutoff value obtained.

4.2 Size- and intensity-dependent photoelectron spectra from SiO_2 nanoparticles

4.2.1 VMI images and radial distributions

SiO_2 nanoparticles with diameters of 20nm, 50nm, 80nm, 120nm, 200nm, 400nm, and 750nm (Nanocomposix, Inc) were studied with laser intensities ranging from 8.8 x 10^{12} W/cm^2 to 1.8 x 10^{13} W/cm^2. A 95nm SiO_2 sample was studied at higher intensities from 2 x 10^{13} W/cm^2 to 8 x 10^{13} W/cm^2. Each scan consisted of 2.5 million laser shots to ensure sufficient statistics for this 'binning' method in determining photoelectron energy and angular distributions.

Figure 4.9 illustrates size-dependent hit histograms at a constant laser intensity of 8.8 x 10^{12} W/cm^2. The trend clearly indicates a monotonic increase in the maximum electrons per laser shot as a function of increasing particle diameter. The smallest sample on the left figure emits considerably less electrons per laser shot than the largest on the right. Figure 4.2 is representative intensity-dependent histogram showing how the peak laser intensity shifts the maximum electrons per laser shot. Each of these size and intensity dependent scans have a corresponding integrated

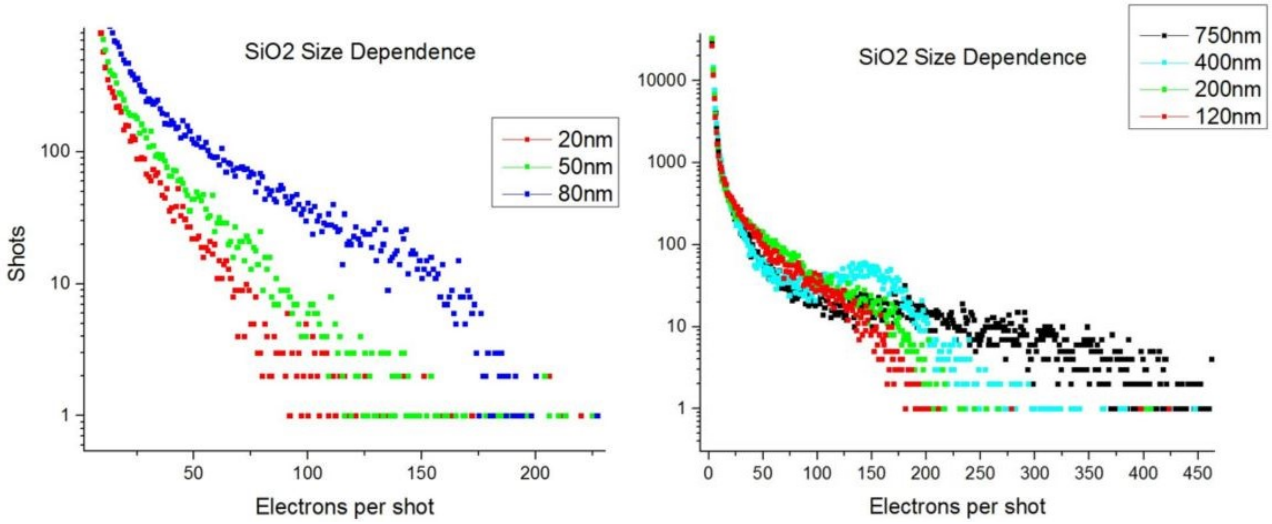

Figure 4.9 *Histogram of different sized SiO_2 nanoparticles at constant intensity of 8.8x10^{12} W/cm^2. On the left is for <100nm particles while on the right is for >100nm. The trend shows that for the same peak laser intensity of 8.8 x 10^{12} W/cm^2, the upper electrons per laser shot limit increasing as a function of particle size.*

raw VMI images showing the photoelectron energy and angular distribution, although focal-volume averaged. Raw, integrated VMI images give the first glimpse into how particle size and laser intensity effects the photoelectron distribution as seen in Figure 4.10. Rows **a)**, **b)**, and **c)** correspond to 20nm, 120nm, and 400nm SiO_2 samples, respectively, at three different peak intensity values. The influence of sample diameter and laser intensity can be seen in the increased

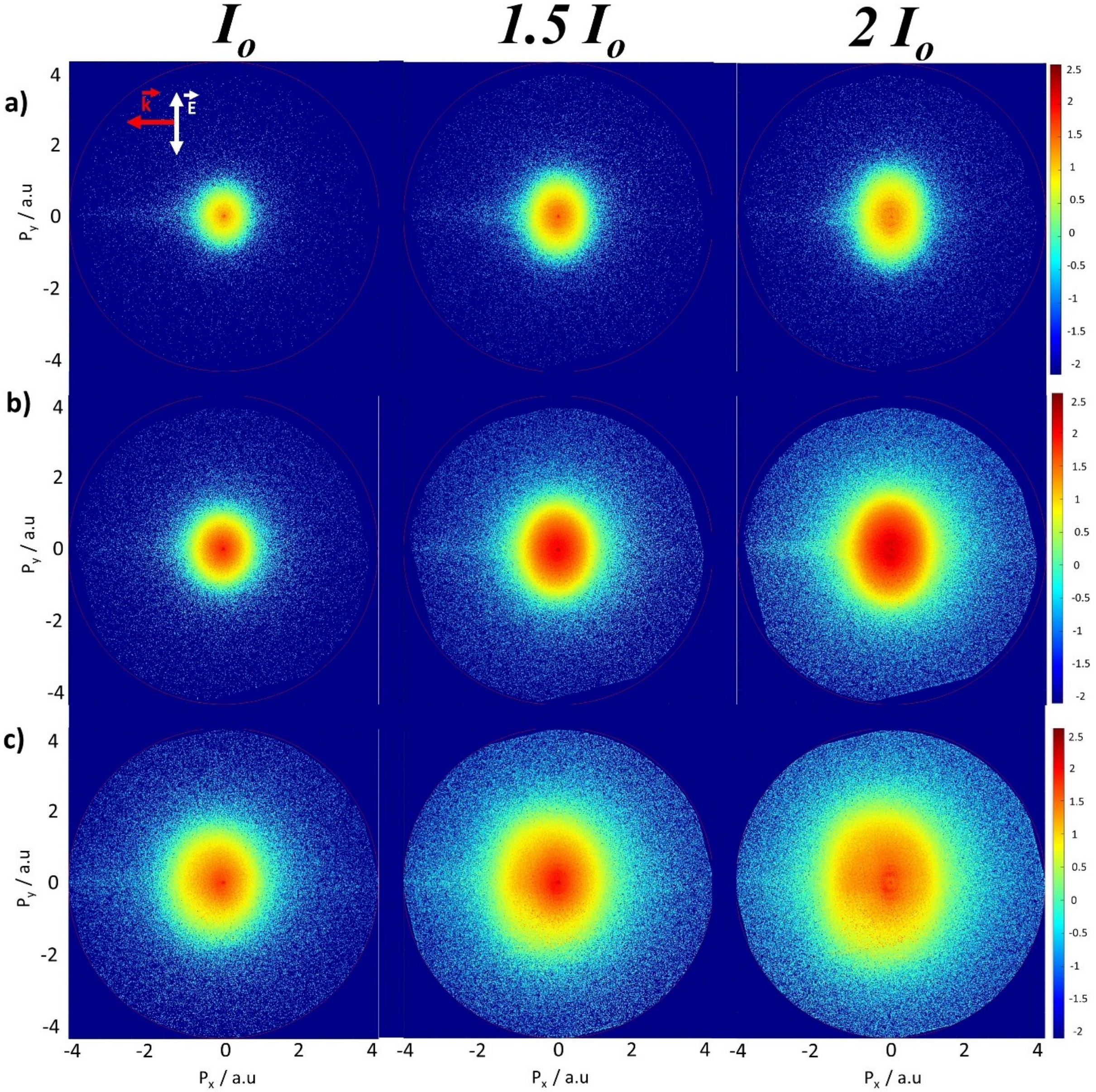

Figure 4.10 *Collection of integrated VMI images as a function of size and laser intensity. Units of momentum (a.u.) are shown.* $I_o = 8.8 \times 10^{12}\ W/cm^2$. *Horizontal rows are same nanoparticle diameter with increasing intensity.* ***a)*** *20nm* SiO_2 ***b)*** *120nm* SiO_2 ***c)*** *400nm* SiO_2 *Color bar in log scale.*

electron momentum cutoff and the changing angular distribution. The images elongate in the vertical direction as the photoelectrons are driven the strongest along the plane of polarization. A substantial asymmetry along the propagation direction is seen for the large nanoparticles as the particle diameter begins to approach the incident wavelength. The asymmetry is accurately described by the Mie solution where the excitation of higher order multipole modes leads to propagation-induced near-field deformation [85]. The vertical columns in Figure 4.10 are a size scan at a fixed intensity. This directly compares the photoemission from nanoparticles as a function of particle diameter and demonstrates the major role of the nanoparticle dimensions on the overall electron distribution.

As all the VMI images in Figure 4.10 are focal-volume averaged, the 'binning' technique described in the previous section is advantageous for purposes of probing near-single intensity angular and energy distributions. Figure 4.11 is a clear representation of the different intensity regions found with the laser focus of a 120nm particle at the peak intensity of 1.8 x 10^{13} W/cm^2. Figures **a-c)** are 'binned' images corresponding to intensity regions from the outer focal 'wings' to its center. This mimics the integrated intensity-dependent (rows) images seen in Figure 4.10,

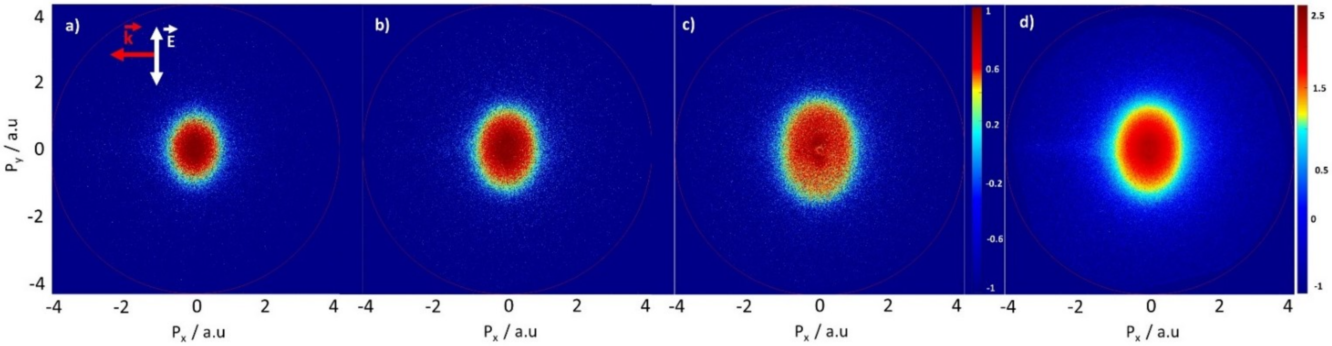

Figure 4.11 *'Binned' VMI images from 120nm SiO$_2$ at 1.8 x 10^{13} W/cm^2.* ***a)*** *125-135 electrons/shot* ***b)*** *175-190* ***c)*** *250-300* ***d)*** *101-360 (integrated image). 'Binned' images* ***a-c)*** *are contrasted to integrated image* ***d)*** *to show the contributions from different intensity regions within the focus. Color bar in log scale. Color bar for* ***d)*** *seen to its immediate right.*

except 'binning' produces a near-single intensity spectra. Using Figure 4.11**a)** as an example, the 'bin' was set between 125-135 electrons per laser shot. As total photoelectron emission from nanoparticles theoretically show a nearly-linear dependence on laser intensity, a 'bin' width of only 10 electrons necessitates that laser shots within that 'bin' had to be from a narrow region of laser intensities. The corresponding spectra from this bin therefore is an accurate representation of the photoelectron distribution originating from a single-intensity value.

Once the 'bins' are chosen for each nanoparticle scan, radial distributions for each are found. The radial distribution of an individual 'bin' provide single-intensity information on the shape of the distribution and its cutoff, both of which are size- and- intensity dependent properties. Figure 4.12 shows collection of different 'binned' radial distributions at a fixed peak intensity compared to the integrated (red dashed line) spectra. The 'bins' are chosen to show the characteristic focal regions from the minimum to the maximum intensity. The shape of the 'binned' distribution varies compared to the integrated, with the most prominent difference being in the largest 'bin' containing the peak intensity contributions. The integrated distribution also slightly underestimates the cutoff compared to the largest 'bin' (green).

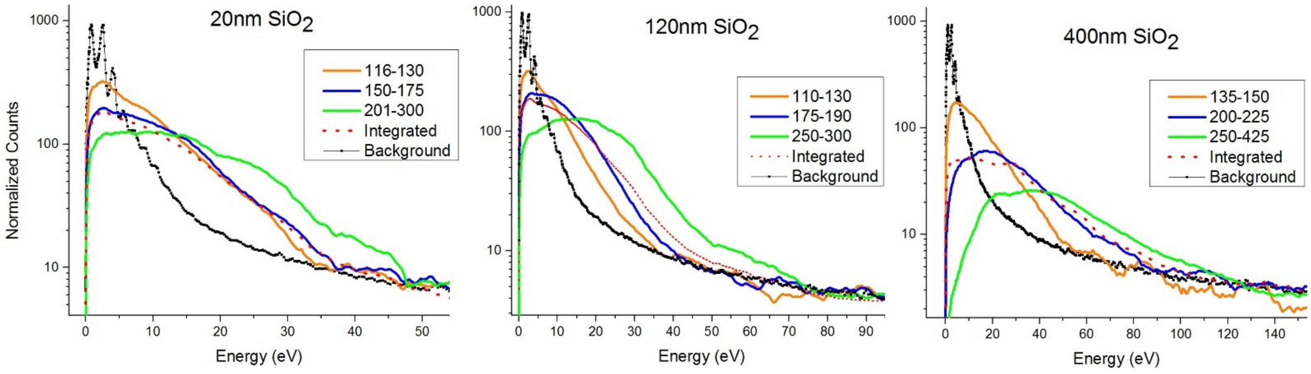

Figure 4.12 *Size-dependent 'binned' radial distribution. Colored lines indicate the radial distribution for that particular 'bin' (number of electrons per laser shot) as referenced to the background. Red dashed spectra are the integrated distribution. Data was smoothed for better comparison. Peak laser intensity = 1.8 x* 10^{13} *W/cm*^{2}.

4.2.2 Size-dependent photoelectron cutoffs for SiO_2

The determination of the size- and intensity-dependent photoelectron cutoffs gives insight into the underlying physics of the light/matter interaction. The photoelectrons contain a wealth of information about their excursion from the nanoparticle to the continuum, specifically their kinetic energy and angular distribution. Photoelectron spectroscopy of nanoparticles allows the electron to be a sensitive probe to the environment around the nanoparticle during its interaction with the ultrafast laser pulse. The measured photoelectron cutoff as a function of nanoparticle diameter is plotted in Figure 4.13, both in electron volts and scaled to the ponderomotive energy, U_p. The overall trend indicates a monotonic increase of absolute cutoff energy for both increasing diameter and incident laser intensity. Expressing the cutoff values in units of U_p allows one to eliminate intensity-dependence and focus on size-dependent effects as U_p scales linearly with intensity.

Beyond the physical dimensions of the particles, the interaction with the laser pulse dictates the physics of the emitted photoelectrons. The ultrafast intense laser pulse, which consists of an alternating electric field of ~10 cycles (25fs FWHM envelope / 2.6fs/cycle), encounters an isolated nanoparticle in vacuum. At sufficiently high intensities, ionization of the nanoparticle occurs, and the liberated electron propagates within the effective field of the laser pulse and dielectric response of the particle. As was discussed in Section 1.3, the important features controlling this process are the Coulomb potential of the ionized nanoparticle, near-field enhancement, and rescattering off the parent particle.

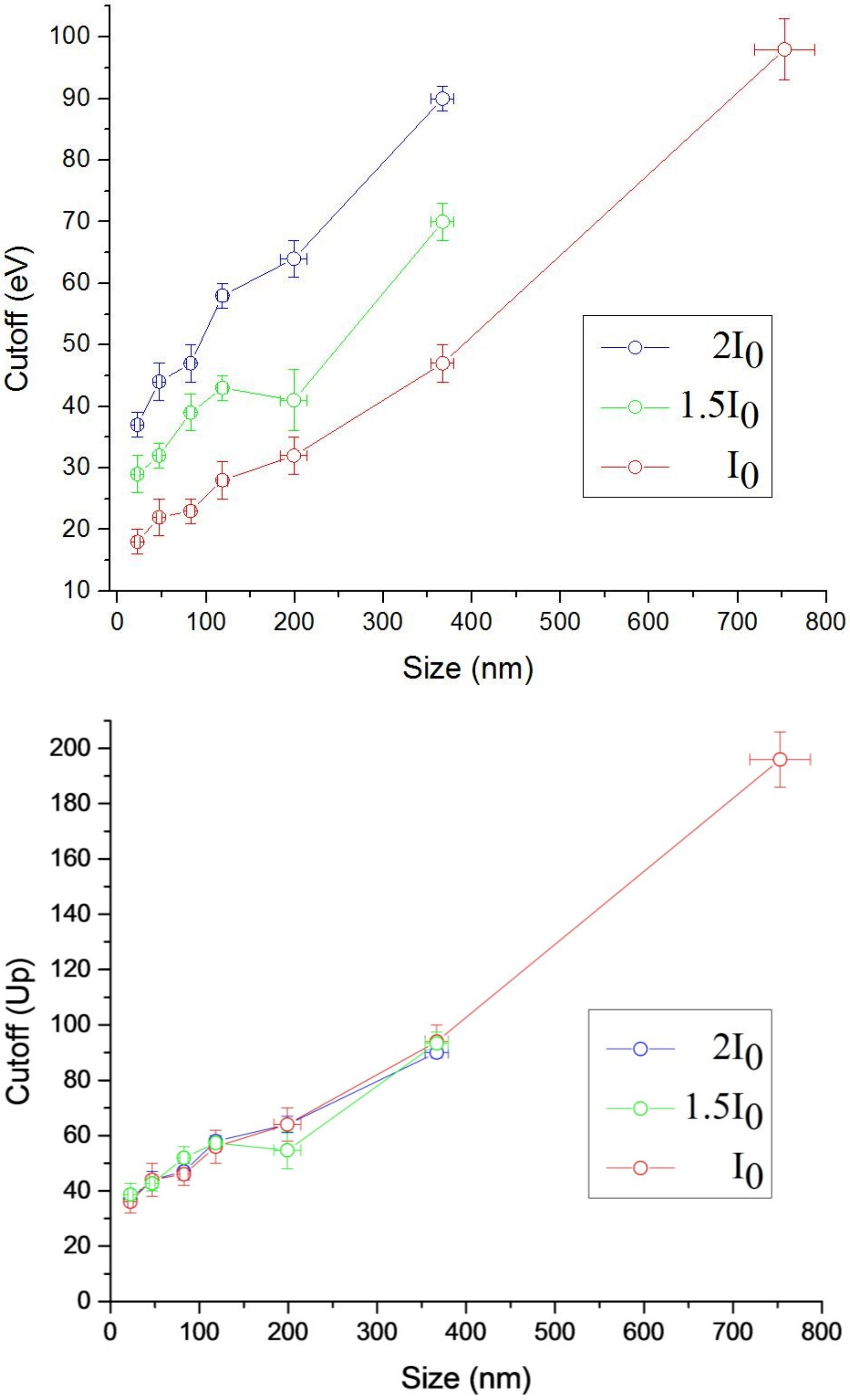

Figure 4.13 *SiO_2 nanoparticle size vs cutoff energy. Upper graph shows cutoff value in eV while the bottom graph is scaled to the ponderomotive energy, U_p. The cutoff increases with nanoparticle diameter. The normalization by U_p gives a constant cutoff value as U_p scales linearly with intensity. $I_o = 8.8 \times 10^{12}$ W/cm^2.*

According to the Keldysh parameter, the intensity regime (~10^{13} W/cm^2) at NIR wavelengths corresponds to the transition between multiphoton and tunneling ionization regimes (see Section 1.3). However, by taking into account the significant near-field enhancements, tunneling provides a more intuitive picture of the nanoparticle ionization at these intensities, with the greatest probability of ionization from the particle surface. Once the incident electric field is sufficiently strong enough to bend the potential barrier of the surface atoms, an electron can tunnel through the barrier into the continuum. Once ionization of the nanoparticle surface begins, a Coulomb potential is formed on the surface defined by the number of photoelectrons lost. Once a sufficient potential well depth is formed, subsequent ionization events require that the electron must have kinetic energy greater than this potential or they will be trapped and only ‘quasi-free’. This will efficiently dampen (quench) the ionization rate quickly, usually within a few laser cycles [26].

The photoelectrons that are in the continuum can be modeled as an electron propagating in a classical field. The total force acting on the electron is the sum of the local fields, consisting of the Coulomb field trapping potential and the near-field contributions generated by the laser field and the nanoparticle. As previously mentioned, the near-field of the nanoparticle is the dielectric response to the incident laser field and is calculated by Mie solutions to Maxwell’s equations that solve for the fields inside and outside the particle. Field enhancement occurs where the nanoparticle response is localized and is defined as the ratio of the induced field to the incident field. Figure 4.14**top)** shows the calculated fields of 100nm diameter dielectric and metallic nanoparticle where R<< λ with its characteristic dipolar shape. The bottom row is for a 300nm SiO_2 particle where R becomes none-negligible compared to λ and asymmetries caused by propagation effects are seen. Depending on the spatial and temporal ‘birth’ of the photoelectron relative to the laser pulse, the electron will feel this enhanced field and be influenced by it. For dielectrics, the maximum field enhancement reaches a limiting value of three when the permittivity of the nanoparticle becomes much larger than the medium, effectively shielding the interior of the nanoparticle from the incident field [87]. This enhancement can be higher for metals because of a negative relative permittivity stemming from a complex index of refraction.

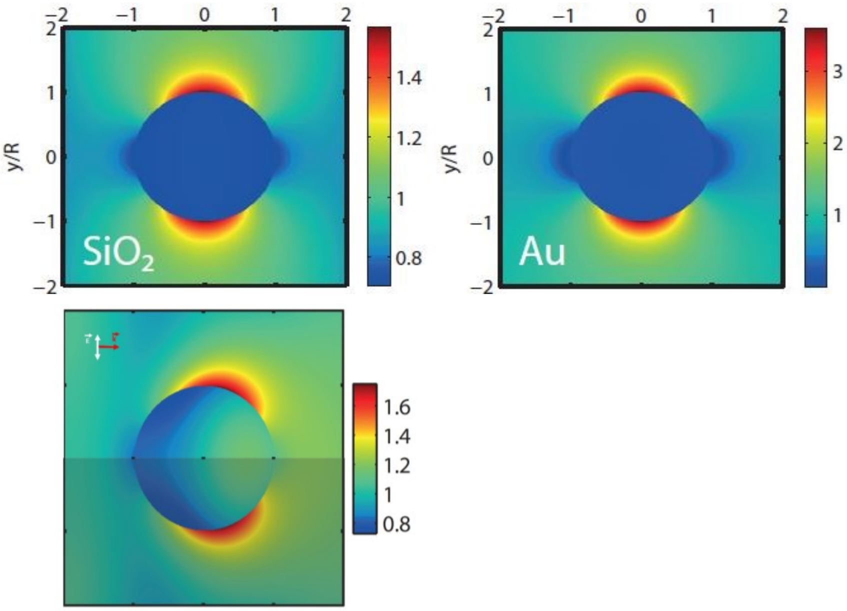

Figure 4.14 *Field distributions from nanoparticles in response to electromagnetic wave.* ***Top row)*** *Radius=50nm << λ showing dipolar shape of particles near field response.* ***Bottom row)*** *300nm diameter SiO_2 where R<< λ begins to not hold and propagation effects occur. Polarization is vertical, and propagation is to right. Image from [87].*

The free electron propagating in the field is driven by the alternating direction of the laser field. Analogous to the atomic case, photoelectrons from nanoparticles can return to the surface and be rescattered elastically or inelastically. The electron on this return trip will again be influenced by the effective field from the trapping potential, nanoparticle near-field, and the laser field. The highest energy electrons are what is defined as the cutoff in the VMI radial distributions.

These electrons are those that have been preferentially backscattered multiple times, gaining momentum from the effective field for each trip. This effective field will be at a maximum (and thus the largest momentum gain) where the field distribution of the nanoparticle is the greatest. This is a size-dependent property that can clearly be seen in Figure 4.10**c)** in the asymmetry in the propagation direction of the 400nm SiO_2.

Electron-electron Coulomb interactions also play a crucial role in the final momentum distribution of the photoelectron spectrum. The escaping electron 'bunch' consists of all the free photoelectrons that have left the nanoparticle, including direct emission and rescattered electrons. As seen in Figure 4.9, the number of detected electrons increases monotonically with nanoparticle size. For large particles, the total number is usually hundreds, up to a thousand, of electrons per laser shot, before factoring in the 40-50% detection efficiency of the MCP. The space-charge repulsion felt by this electron 'bunch' enhances the final photoelectron cutoff energy of the nanoparticles, especially for the larger sizes [25,86,87].

4.2.3 Comparison to earlier results obtained with few-cycle pulses

The joint experimental and theoretical work by Süßman et al. [25] used few-cycle (4fs) laser pulses along with stable carrier-envelope phase (CEP) to study and control photoemission from SiO_2 nanospheres. They demonstrate the propagation-induced directionality of electron emission and analyze how the measured photoelectron cutoffs and angular distributions are dictated by the size of the particle and nicely show the propagation induced asymmetry. As electron backscattering dominates the high-energy electron emission at these intensities (~10^{13} W/cm^2), a closer look at this process sheds light on the scattering process. In a few-cycle pulse,

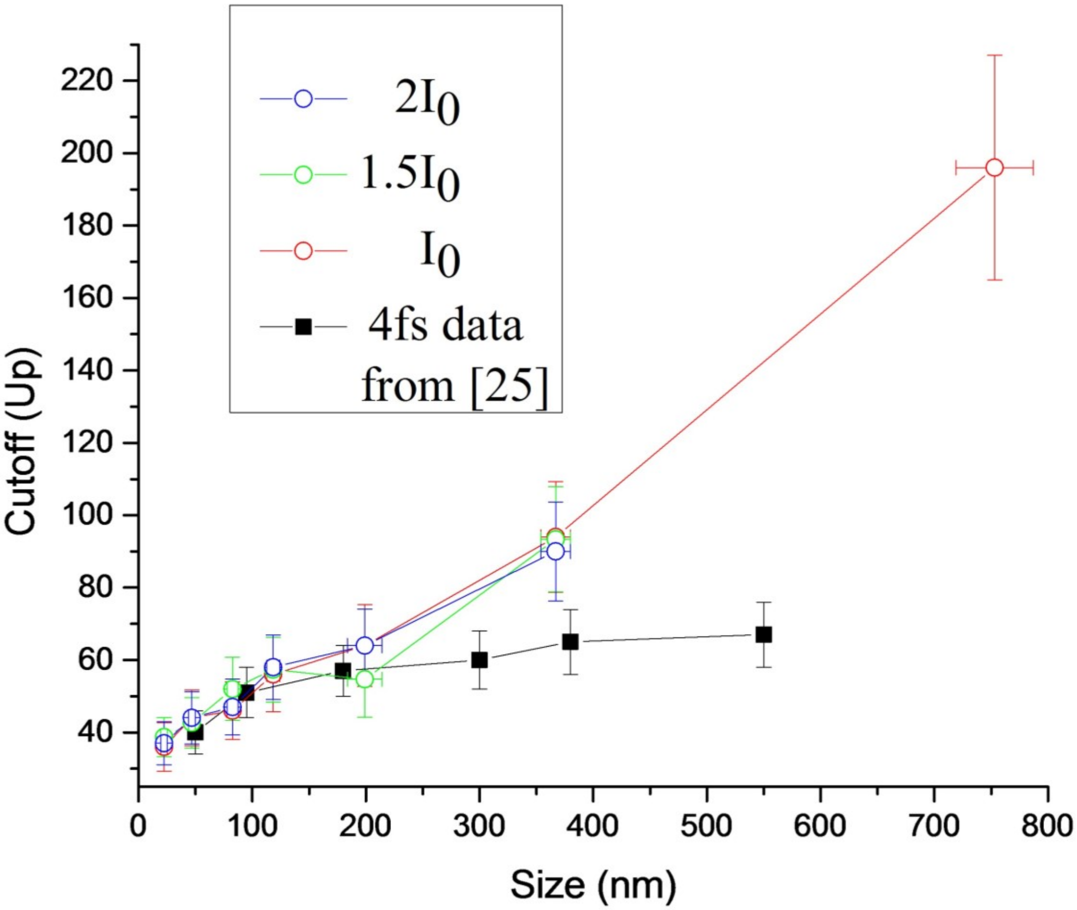

Figure 4.15 *Size dependent cutoff energy values from* SiO_2 *compared vs pulse duration. Cutoff values from 25fs pulses (colored) vs 4fs (black) as a function of particle diameter scaled to the free space ponderomotive potential,* U_p*.* $I_o = 8.8 \times 10^{12}$ *W/cm*^{2} *while 4fs data taken at* 3×10^{13} *W/cm*^{2}*. 4 fs data taken from [25].*

the first half-cycle produces most of the ionization before the growing Coulombic trapping potential effectively quenches further electron emission. The free electrons are subsequently propagated in the effective field dictated by the laser field and nanoparticle near-field, plus the surface trapping potential. A few-cycle pulse only has one or two more cycles to interact with the electrons, thus limiting the number opportunities to effectively backscatter any electrons. However, in the many-cycle, 25fs pulse duration case, an electron is much more likely to be rescattered multiple times, including backscattering where the electron gains the maximum momentum from the field.

Figure 4.15 shows a comparison of energy cutoffs as a function of SiO_2 particle size for my data (25fs) and from literature (4fs) [25]. The cutoff values are scaled to the free energy ponderomotive potential, U_p, to directly compare the cutoffs as a function of pulse duration. The few-cycle data (black squares) nicely matches the many-cycle data (colored circles) at particle sizes up to approximately 200nm. For larger sizes, the cutoffs for the 25fs data quickly diverge to much larger values.

An in-depth analysis of the role of single collisions (scattering) compared to double collisions show a fundamental difference in the scattering mechanism and on the overall contribution from each process [61]. The multiple scattering contribution increases as a function of nanoparticle size as shown in Figure 4.16, eventually becoming more energetic than the single scattering spectra. Here, electrons with n = 0,1, and 2 scattering events correspond to the direct, single, and double scattered events, respectively. At small sizes, the single scattered electrons dominate the high energy cutoff. As the particle size increases, the overall cutoff energy also

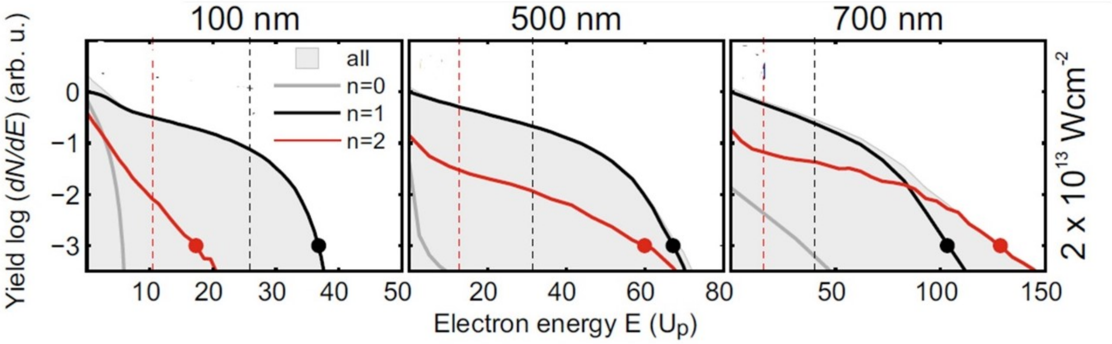

Figure 4.16 *Rescattered energy spectra as a function of size. The cutoff energy is calculated for each nanoparticle size as a function of the direct (grey), single scattering (black), and double (red) rescattered electrons. At small sizes, the single scattering electrons dominate the cutoff region. With large sizes, double rescattering becomes more prominent and are more energetic than the single scattered electrons. Figure taken and adapted from [61].*

increases but the contribution from the double rescattered electrons matches and even exceeds the maximum energy from the single-scattering events.

The trajectory of a single-scattered electron is ‘born’ at the classical tunnel exit, undergoes a large radial excursion and recollision (rescattering) with respect to the particle’s surface. The electron is accelerated while approaching the surface and increases velocity after elastic scattering, thus gaining a larger kinetic energy. This condition depends on the ‘birth’ time of the electron and its phase relative to the driving field. When an electron is scattered more than once from the particle’s surface, a different acceleration mechanism is seen. The trajectory has a smaller radial excursion compared to single scattering, but a much greater tangential component. The near-field is the particle’s dielectric response to the incident laser field. As seen in Figure 4.14 for the large SiO_2 particles, the near-field distribution cannot be approximated as a dipole and thus introduces a tangential component to the near-field. The doubly-scattered electrons take advantage of the tangential field components for large particle sizes and gain energy when its own tangential components are maximum, namely when it is first approaching the surface (first scattering event) and between the first and second collisions. The larger the near-field tangential components, the larger the energy gain for these multiple scattered electrons [61].

The mechanism for the enhanced energy cutoff from doubly-scattered electrons can be extended for more collisions. The near-field tangential fields are present for each cycle and presents another opportunity for an electron to rescatter off the nanoparticle surface many times while simultaneously gaining energy for each scattering event. The tangential components of the near-field only begin contributing significantly for large particles, so the cutoff enhancement from multiple-scattering in a many-cycle pulse can only be observed for rather large systems. This effect starts to be clearly seen for particles larger than 500nm as observed in the simulation in Figure

4.16 where only the first and second scattering events are considered. The cutoff deviation in Figure 4.15 is observed already for ~400nm particles where the contributions of later recollision events in a multicycle 25fs pulse are the most likely cause. The larger cutoff values observed for the 25fs pulse vs 4fs at large sizes thus appears to be a sensitive probe of the number of rescattering events contributing to the energy gain of the highest energy photoelectrons (in the cutoff region).

4.3 Size- and intensity-dependent photoelectron spectra from gold nanoparticles

Gold nanoparticles (AuNPs) with diameters of 5nm, 30nm, 70nm, 120nm, 200nm, and 400nm (Cytodiagnostics, Inc) were studied under laser fields ranging from 8.3 x 10^{12} W/cm^2 to 1.7 x 10^{13} W/cm^2. Since the data for the two largest particle sizes were hindered by space-charge effects and detector saturation, for 200nm AuNP an additional set of measurements at lower intensities of 2 x 10^{11} W/cm^2 to 2.5 x 10^{12} W/cm^2 has been performed. Analogous to the SiO_2 study, the photoelectron spectra from AuNPs was investigated as a function of size and laser intensity. To my knowledge, the successful study of *clean*, isolated, gas-phase gold nanoparticles has not been done, though attempts have been made [55,87]. The ability to properly prepare metallic nanoparticles to be free from contamination and at sufficient particle concentrations is a major roadblock to experiments. Untainted samples were the key to being able to distinguish gold nanoparticle-dependent properties such as photoelectron cutoffs and energy distributions.

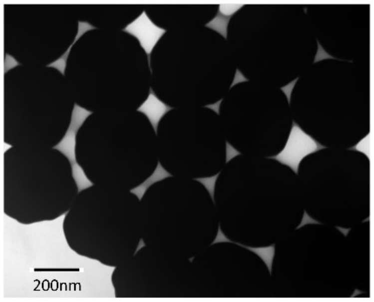

Figure 4.17 *TEM image of commercially available 400nm (±20nm) AuNPs. Scale bar is 200nm.*

AuNPs were chosen as the representative metallic nanoparticle sample because of their ability to be synthesized over a wide range of sizes and with a high degree of monodispersity. They are stable in water at room temperature for extended periods of time (months) and are not sensitive to light (unlike silver nanoparticles) or oxidation (unlike copper nanoparticles) and thus are the logical choice among the coinage metals. The smallest particle (5nm) contains only about 3900 gold atoms in contrast to a 400nm AuNP with over a billion atoms. This spans the size spectrum from the small cluster-like to the large bulk-like nanoparticles. The skin depth for AuNPs at optical and NIR wavelengths have been approximated between 15-25nm [11,160]. This is defined as where the incident electromagnetic field strength diminishes by a factor of 1/*e* inside the metal. Though the field can penetrate into the AuNP, the greatest probability of ionization still will occur where the field strength is the greatest, which is the surface. This means the number of atoms on the surface of the particle is also relevant, with only ~800 atoms for 5nm AuNP but 5 million for 400nm AuNP.

The properties of gold are fundamentally different than for a dielectric such as silica. Most notable is that as a metal and a conductor, its conduction band is already populated and can be modeled as a delocalized sea of electrons (free electron gas). Electrical conductivity in metals, both direct current (dc) and alternating current (ac), are a result of these delocalized electrons in the conduction band. The interaction of a metallic nanoparticle with optical wavelengths freely drives these electrons, moving them relative to a static ion core. A resonance occurs when the driving frequency matches the characteristic electron motion and is the cause for the striking colors due to light adsorption by the plasmon in metallic nanoparticles.

Metals have a complex index of refraction where the imaginary part takes into account extinction. This is related to the relative permittivity (dielectric constant) which, for the real part, is usually negative. The dielectric response of a metal nanoparticle to the incident radiation is different than for an insulator such as silica. This leads to larger field enhancements, along with the aforementioned plasmon resonances.

As mentioned in Section 1.3.2, when irradiated by sufficiently intense optical light, any material will have significant amounts of free electrons, effectively undergoing light-induced metallization through strong inner ionization [96]. In this regime, the difference between the response of metallic and dielectric particles is expected to be washed out. The determination of the conditions needed for this effect is one of the general goals of this work.

4.3.1 Photoelectron spectra

The method of analyzing the photoelectron spectra from gold nanoparticles was very similar to that of silica. Figure 4.18 is a hit histogram of AuNPs, again showing the number of electrons detected per laser shot for the entire scan. The background (~99% of laser shots with no nanoparticle present) are found at low values with a small number of electrons per laser shot. Figure 4.18**a)** shows the evolution of the hit histogram at a constant peak laser intensity, but with increasing AuNP diameter while **b)** presents a constant size but increasing peak intensity. Similar to SiO_2, the trends show a monotonic increase in the maximum number of electrons per laser shot with growing nanoparticle diameter and laser intensity. Overall statistics compared to SiO_2 are reduced as the AuNP particle concentrations are lower, though this also decreases the chance of particle clusters in the laser focus.

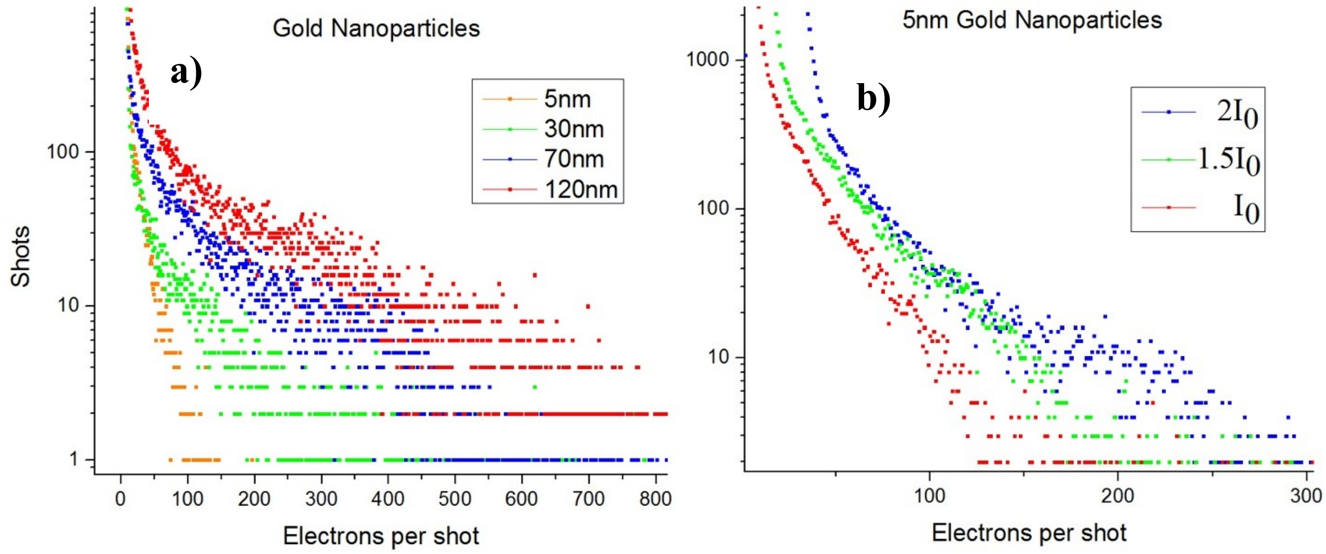

Figure 4.18 *Hit histograms of AuNPs.* ***a)*** *Size-dependent hit histogram showing the number of electrons detected per laser shot, as a function of AuNP size. Notice the increase of the maximum number of electrons with increasing size. 120nm (red) was multiplied by two for better contrast. Intensity = 8.3 x 10^{12} W/cm^2.* ***b)*** *Hit histogram of 5nm AuNPs as a function of peak intensity. The maximum total photoelectron emission increases as a function of peak laser intensity. I_o= 8.3 x 10^{12} W/cm^2.*

The 2D images of the photoelectron emission from AuNPs as a function of size and peak intensity is shown in Figure 4.19. These integrated images are again showing the focal volume averaged distribution and the momentum-space equivalent of the high-energy cutoff coming from the peak laser intensity is clearly seen increasing as a function of size and intensity. The AuNP sizes for rows **a-c)** are 5nm, 30nm, and 70nm, respectively. Each row shows a constant AuNP size with an increasing intensity while a vertical column portrays a constant intensity but changing diameter. As λ >> R for these AuNP sizes, the photoelectron spectra are symmetric about the polarization and propagation axis. Signatures of the characteristic elongation along the polarization axis is also seen.

To look at single-intensity spectra, each scan can again be 'binned' according to its respective hit histogram. Figure 4.20 shows a typical 'binned' photoelectron spectra as a function of the number of electrons per laser shot. Here, 120nm AuNP at 8.3 x 10^{12} W/cm^2 are shown in

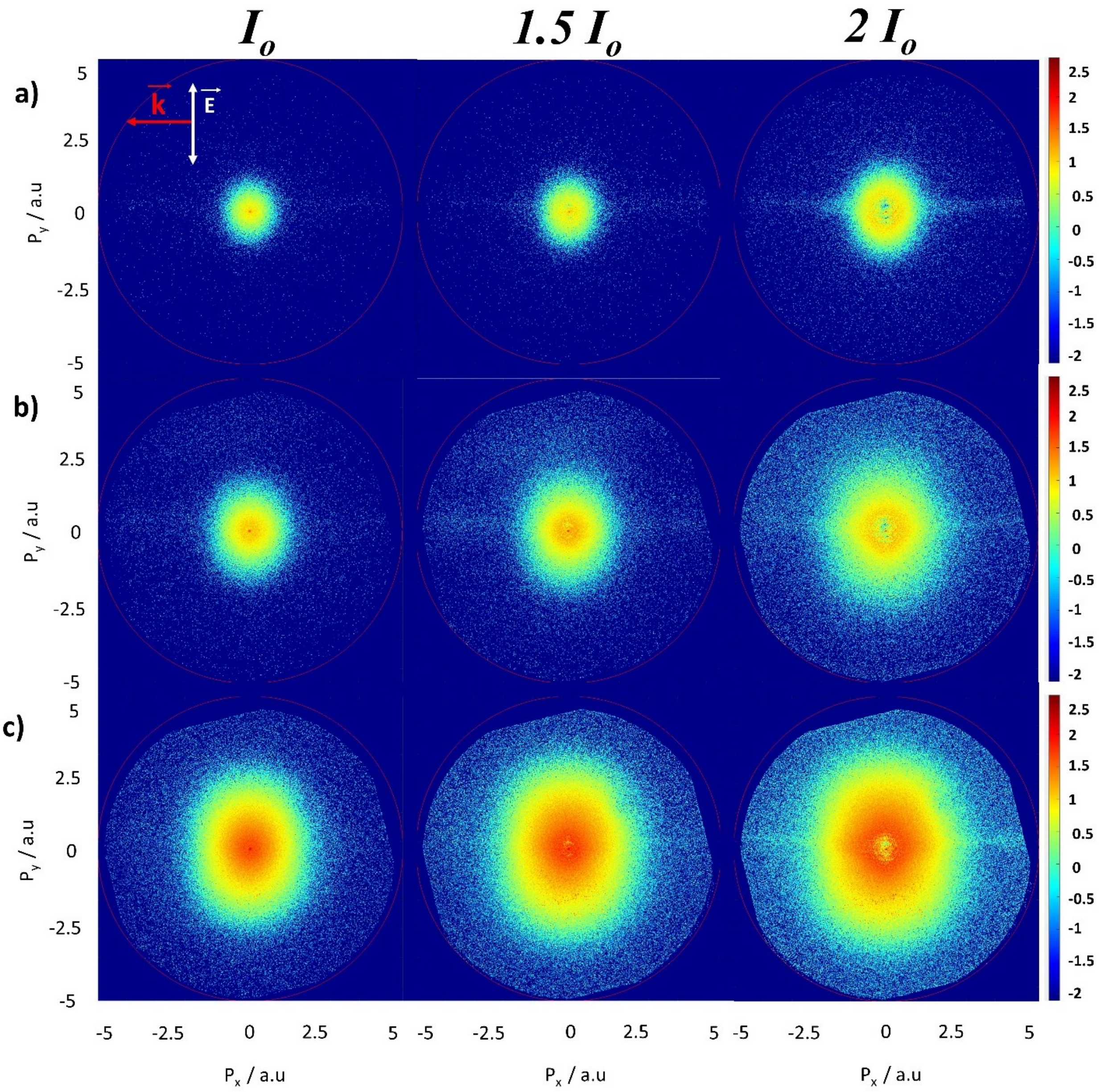

Figure 4.19 *Collection of AuNP integrated VMI images as a function of size and laser intensity. Units of momentum (a.u.) are shown.* $I_o = 8.3 \times 10^{12}$ *W/cm*^{2}*. Horizontal rows are same nanoparticle diameter with increasing intensity* ***a)*** *5nm AuNP* ***b)*** *30nm AuNP* ***c)*** *70nm AuNP* *Color bar in log scale.*

'bins' **a-c)** and compared to the integrated spectra, **d)**. The lack of signal in the center of **c)** is the result of detector saturation where a large density of photoelectrons saturated the MCP and reduced its detection efficiency nearly to zero. A 'hole' is not seen in **d)** as it is masked by the fact it is the sum of all the 'bins', i.e. integrated. The different intensity contributions in the 'binned' data clearly show the evolution of the angular and energy distribution of these spectra. The electron

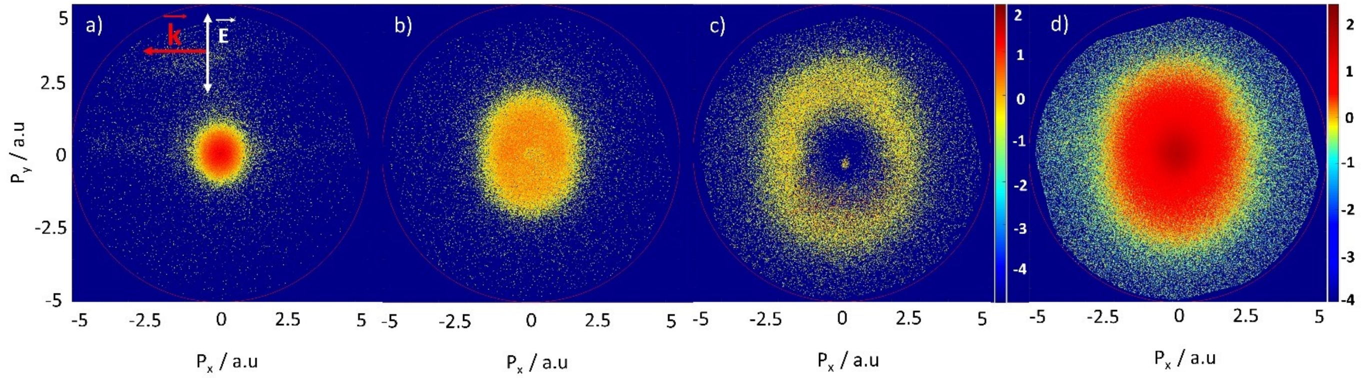

Figure 4.20 *'Binned' VMI images from 120nm AuNP at 8.3 x* 10^{12} *W/cm*^{2}*.* ***a)*** *20-50 electrons/shot* ***b)*** *250-300* ***c)*** *600-800* ***d)*** *13-800 (integrated image). 'Binned' images* ***a-c)*** *are contrasted to integrated image* ***d)*** *to show the contributions from different intensity regions within the focus. Color bar in log scale. Color bar for* ***d)*** *seen to its immediate right. Hole in* ***c)*** *due to detector saturation.*

radial energy distribution is obtained by angular integration over a 30° emission cone along the laser polarization axis for VMI spectra, such as those seen in Figure 4.19 and Figure 4.20. Plotting the radial distribution of the 'binned' versus integrated spectra in Figure 4.21 for AuNPs as a function of size allows for the comparison of their respective cutoff energy and energy profiles. These radial distribution plots show how near-single intensity properties of the AuNPs can be extracted from a single run.

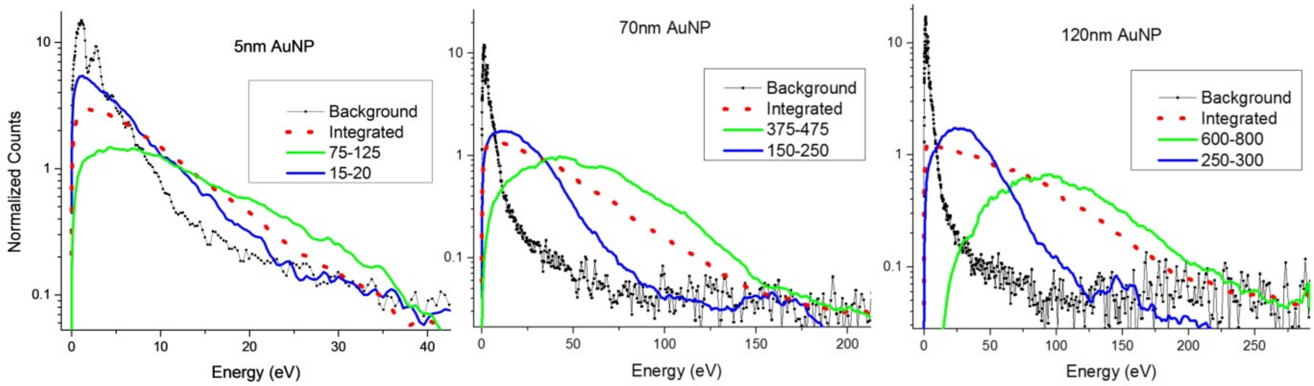

Figure 4.21 *Size-dependent 'binned' radial distribution. Colored lines indicate the radial distribution for that particular 'bin' (number of electrons per laser shot) as referenced to the background. Red dashed spectra are the integrated distribution. Blue line indicates a small (relative to green) 'bin' while green indicates the largest possible 'bin'. Data was smoothed for better comparison. Peak laser intensity = 8.3 x* 10^{12} *W/cm*^{2}*.*

Comparing the scaled radial distributions for the photoelectrons from SiO_2 and Au nanoparticles of the same size shown in Figure 4.22, one can see that the electrons emitted from AuNP are considerably more energetic. The photoelectron spectrum from AuNPs extend much beyond the cutoff value observed for SiO_2 particles. To quantify this huge energy enhancement and to shed light on the mechanisms behind it, the cutoff values measured for both materials as a function of nanoparticle size are systematically compared in the next section.

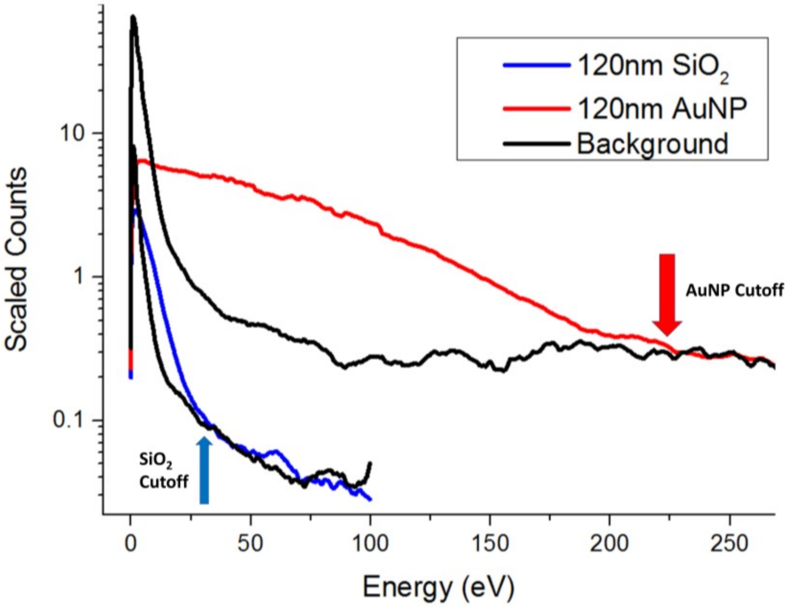

Figure 4.22 *Radial distribution of 120nm AuNP and 120nm SiO_2 at similar intensities around 8.5 x 10^{12} W/cm^2. The AuNP cutoff is ~8 times larger than silica. AuNP data and corresponding background shifted in vertical direction for visual clarity. Data smoothed for visual clarity.*

4.3.2 Photoelectron cutoffs

The gold nanoparticle data already shown has alluded to the fact that these AuNP samples emit considerably more photoelectrons and have much higher cutoff energies when compared to SiO_2. Comparing the hit histograms for AuNPs and silica (Figure 4.9 and Figure 4.18) at similar peak intensities, an 80nm SiO_2 particle emits no more than 200 electrons per shot while a 70nm AuNP has a maximum of almost 500 electrons. A cursory glance at the effective ionization potential is 9eV and 9.2ev for silica molecules and gold atoms, respectively. However, metal

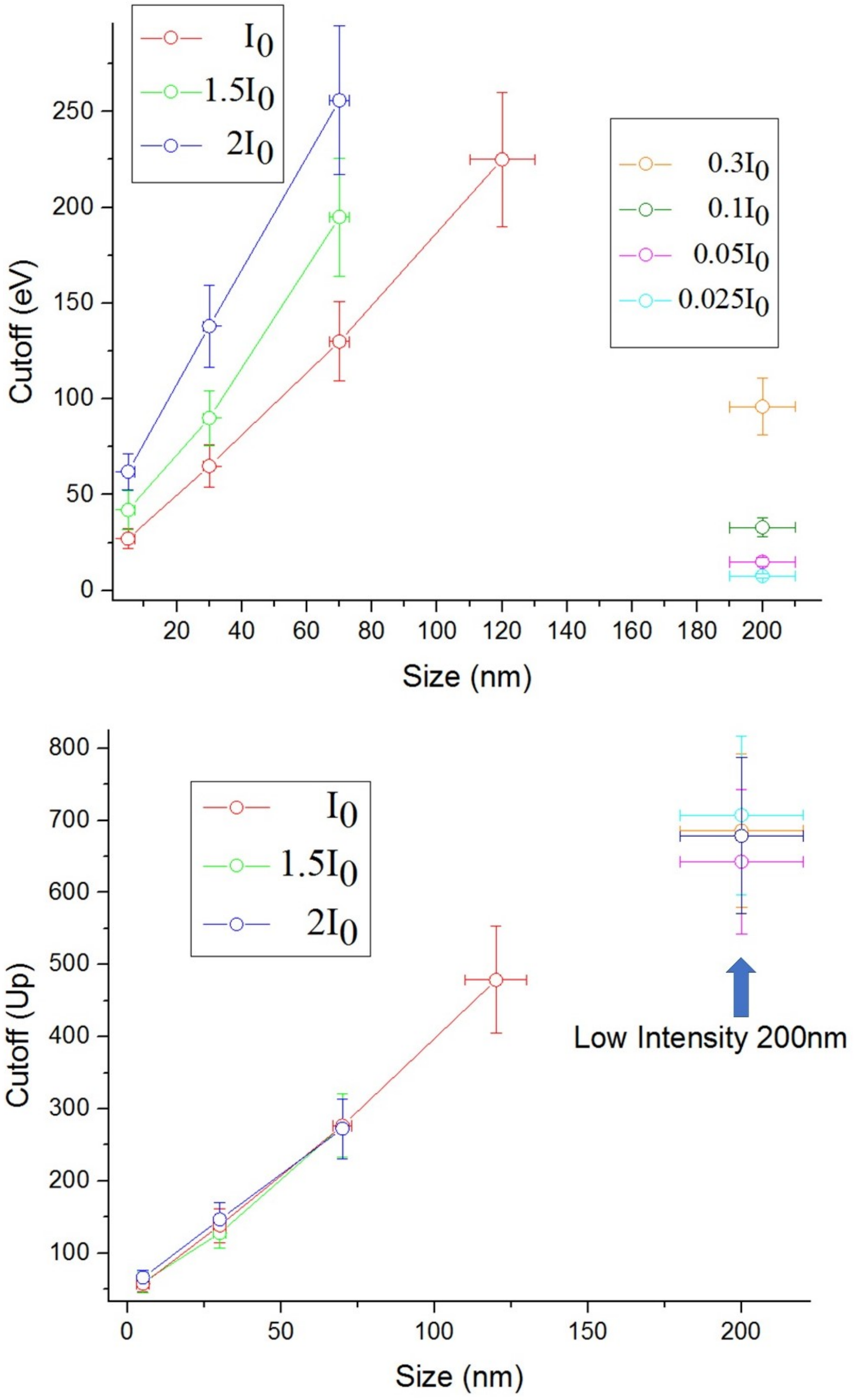

Figure 4.23 *AuNP size vs cutoff energy. Upper graph shows cutoff value in eV while the bottom graph is scaled to the ponderomotive energy, U_p. The normalization by U_p gives a constant cutoff value as U_p scales linearly with intensity. $I_o = 8.3 \times 10^{12}$ W/cm^2. 200nm AuNP was measured between 2×10^{11} W/cm^2 and 2.5×10^{12} W/cm^2 as the VMI acceptance energy was insufficient to measure the cutoff at the higher intensities.*

nanoparticles are a collection of thousands to billions of atoms and therefore, in the case of removing electrons from the particle, the work function of bulk gold instead of the ionization potential of an isolated atom is appropriate [88]. For SiO_2 nanoparticles, the binding energy was found to be 8.5eV [161]. The work function of bulk gold is 5.1eV which allows AuNPs to be ionized much easier than for SiO_2 nanoparticles and one explanation for the greater number of photoelectrons.

The photoelectron cutoffs are plotted in Figure 4.23 for all the AuNP scans. The cutoffs monotonically increase with particle size and laser intensity as also seen in the silica data. The upper plot is the AuNP size vs cutoff plotted in electron volts. The lower plot is normalized by the ponderomotive potential, U_p, for direct cutoff comparison independent of intensity. The cutoff energies of AuNPs are much higher than for silica, especially for larger sizes. The largest silica cutoff was less than $200U_p$ for a 750nm particle while a 70nm AuNP already has over $250U_p$. The large cutoff values and detector saturation for the AuNPs limited the ability of the VMI to detect the fastest photoelectrons, especially for 120nm, 200nm, and 400nm as the acceptance energy of the VMI under the conditions of the experiment was insufficient to focus them. One energy cutoff was measured for 120nm (see Figure 4.20) at 8.3 x 10^{12} W/cm^2 while none were resolved for 200nm or 400nm or 120nm at higher intensities. Both panels of Figure 4.23 include cutoff values for 200nm which were measured in a separate, low-intensity scan between 2 x 10^{11} W/cm^2 and 2.5 x 10^{12} W/cm^2.

A deeper look into the differences between SiO_2 and AuNP is needed to begin to understand the cutoff values. Section 4.2.1 outlines the trajectory of the cutoff photoelectrons in the local field of the nanoparticle and laser after nanoparticle ionization. This local field includes the trapping potential, linear dielectric particle response (near-field), and space-charge effects.

Each of these fields are affected by the change in nanoparticle properties and thus, the overall cutoff values. As seen in Figure 4.18, the maximum number of electrons emitted per laser shot increases for AuNP compared to SiO_2, if particle size and laser intensity are kept constant. The work function of gold (5.1 eV) is significantly lower than the binding energy of a SiO_2 nanoparticle (8.5eV) which allows more electrons to be emitted and a larger trapping potential on the particle's surface than for silica. A greater number of electrons in the escaping free electron bunch from the AuNP also increases the space-charge effects of the electron-electron interaction and enhance the final cutoff energy. However, a look at the effect of the near-field enhancement as a function of material and size also can shed light into the large cutoff disparity.

Figure 4.24 shows the cutoff values as a function of size plotted for AuNPs and SiO_2, scaled to the ponderomotive potential, U_p. For all sizes, the cutoff energies for the AuNPs are much larger than for SiO_2 of the same diameter, with the slope of the size-dependence line also much steeper. This reveals that a photoelectron emitted from a AuNP or silica particle experience

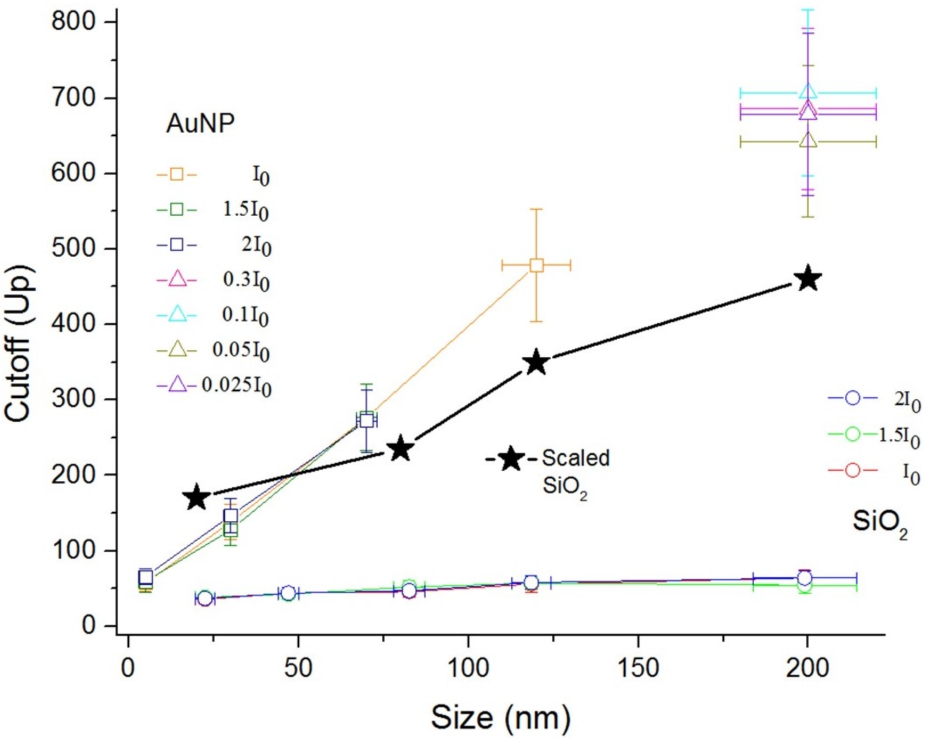

Figure 4.24 *Cutoff (U_p) comparison between SiO_2 and AuNP as a function of size. The scaled SiO_2 cutoff is shown in the black stars and is found by squaring the ratio of the field enhancements from similar-sized AuNP and SiO_2. I_o (AuNP) = 8.3 x 10^{12} W/cm^2 and I_o (SiO_2) = 8.8 x 10^{12} W/cm^2.*

extremely different field strengths. As the electrons gain most of their momentum from the local field after ionization, understanding the individual local field contributions can provide some understanding. Table 4.1 is a comparison of the cutoffs between AuNP and silica at similar sizes. The table also shows field enhancement factors, α, that are calculated by solving Mie's solution to Maxwell's equations for both AuNP and silica nanospheres of different sizes [87,89,90]. As the energy gain from the near-field is expected to depend on the intensity rather than the field strength, the field enhancement factor is squared to account for this. This ratio of α^2 thus indicates the ratio of local field intensities for AuNPs when compared to SiO_2 under the same incident light intensity. Figure 4.24 also shows the scaled SiO_2 energy cutoffs (black stars) which is found by multiplying the silica energy cutoff by the squared ratio of the field enhancements of AuNP and silica. If only the near-field enhancement of the nanoparticles played a role in determining photoelectron cutoffs, the scaled-cutoff values for SiO_2 should overlap those of the AuNPs. It could be seen that even though the SiO_2 values scaled with α^2 ratio now come much closer to the measured values for

Table 4.1 *Ratio of Cutoffs (Up) and field enhancements (α) between AuNP and SiO2 of similar size. Calculation of field enhancement factor used relative permittivity of (-22.6 + 1.35i) and 2.12 for AuNPs and SiO2, respectively.*

Nanoparticle/Size	Cutoff (Up)	Ratio Cutoff (AuNP/SiO_2)	Field Enhancement Factor (α)	$\left(\frac{\alpha_{AuNP}}{\alpha_{SiO_2}}\right)^2$
AuNP 30nm	138	3.7	3.3	4.6
SiO_2 20nm	37		1.54	
AuNP 70nm	275	5.7	3.5	4.9
SiO_2 80nm	48		1.58	
AuNP 120nm	478	8.4	4	6.14
SiO_2 120nm	57		1.6	
AuNP 200nm	678	11.1	4.7	7.55
SiO_2 200nm	61		1.7	

AuNPs, they do not perfectly coincide, and the slope of the AuNP curve is still steeper. This most likely reflects different scaling of the charge interaction with size for both types of materials resulting from significantly larger number of emitted electrons for AuNPs.

A recent study by Rupp, et al [26] looked at the electron emission from isolated nanoparticles as a function of different materials. They showed that the permittivity and binding energy of the material were the main parameters that determine the material's contribution to the electron acceleration process. The relative permittivity of a material determines the dielectric response (near-field) to the incident field and is much different for silica and AuNPs because of the complex index of refraction for gold. This gives the real part of the relative permittivity for AuNPs to have a large, negative value and subsequently a bigger field enhancement versus silica. The binding energy influences the electron tunneling process, especially the 'birth' time at the tunnel exit. This dictates the trajectory of the electron and its overall propagation pathway. A lower binding energy directly effects the ionization rate, leading to more photoelectrons and a larger space-charge effect, but this same situation can also lead to a faster 'quenching' of the ionization rate by the large trapping potential of the

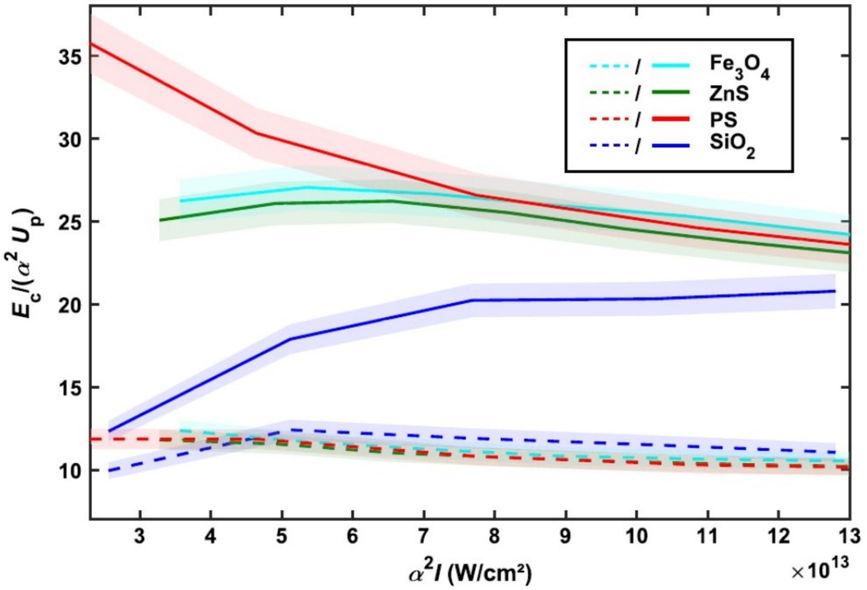

Figure 4.25 *Scaled cutoff energies (simulation) for different nanoparticle materials of approximately the same size. Here $\alpha^2 I$ is the dielectrically enhanced surface intensity. Dashed lines are with the mean field turned 'off' meaning no charge interactions between electrons or ions. Solid lines include all charge interactions. Figure taken from [26].*

surface ions. Figure 4.25 plots the scaled cutoff energies for different nanoparticles of approximately the same size to compare the contributions from the mean field. The dashed lines show the cutoff energies when the mean field is turned 'off' meaning that there are no charge interactions between any photoelectrons or ions. This leaves only the contribution from the field enhancement, α, which is normalized by the dielectrically enhanced surface intensity, $\alpha^2 I$. With no charge interaction, very little difference in cutoff energies is seen. The solid lines show the full simulation with the charge interaction 'on' and shows the significant contribution it can have. Each material has a different binding energy, and therefore the increase in the scaled-cutoff is dependent on this property.

As mentioned, the binding energy for AuNPs (gold work function) is considerable lower than for silica particles. The hit histograms showed that for the same size and intensity, more photoelectrons from gold are detected. This can enhance the cutoff because of charge interactions, specifically electron-electron. The maximum number of detected electrons per laser shot for both AuNPs and SiO_2 is shown in Figure 4.26. As discussed before, this plot does not show the real electron yields as the probability to detect an electron is determined by multiple factors,

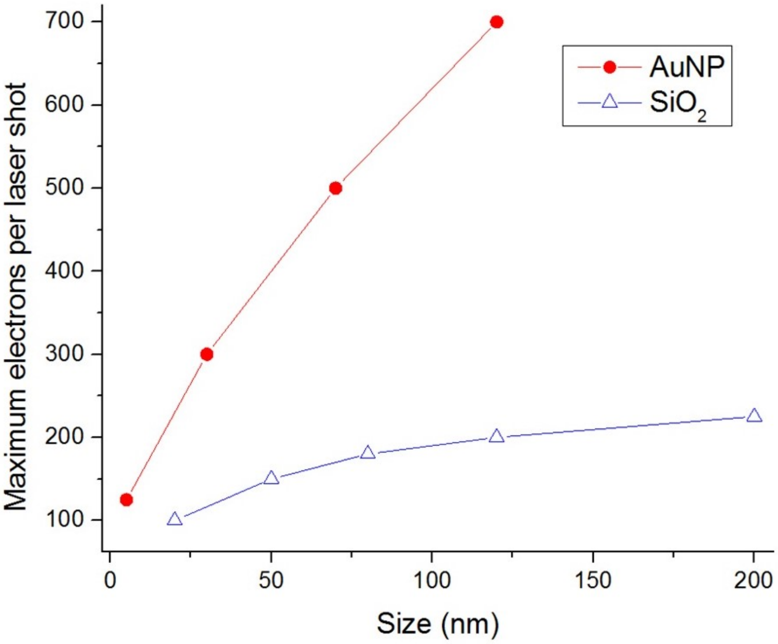

Figure 4.26 *Maximum number of detected electrons per laser shot for AuNPs and SiO_2 as a function of diameter. Intensity for SiO_2 = 8.8 x 10^{12} W/cm^2 and AuNP = 8.3 x 10^{12} W/cm^2.*

including the MCP (~40-50% detection efficiency), single-shot camera response, and detector saturation (see Figure 4.20c), especially at large sizes and high intensities. Theoretically, in our parameter range, the total yield of emitted electrons is expected to be roughly linear as a function of both size and laser intensity, but the slopes for different materials might be largely different [61]. Here the number of emitted electrons for AuNPs increases much more rapidly than for silica, thus the charge interaction for large AuNP will be greater than for an equivalent sized silica. The scaled SiO_2 energy cutoffs (black stars) in Figure 4.24 show an increasing separation to the measured values for gold for larger particle sizes, which likely indicates the increasing contribution of the charge interactions for large AuNPs.

4.4 Photoelectron spectra from resonant gold nanoparticles

The ability to synthesize and manipulate nanoparticles, especially metallic particles, leads to many useful novel properties [36]. Of particular interest are core-shell nanoparticles consisting of two different materials that are grown in layers, such as a dielectric (silica) core with a shell of gold on the surface. These nanoshells have unique, geometrically tunable optical resonances, dictated by the collective electronic motion, or plasmon resonance. Compared to solid metallic nanoparticles, the optical resonance of a nanoshell is extraordinarily sensitive to the inner and outer dimensions of the metallic shell [91,92]. This attractive property has the advantage of tuning the plasmon resonance to any optical wavelength, for example that of the

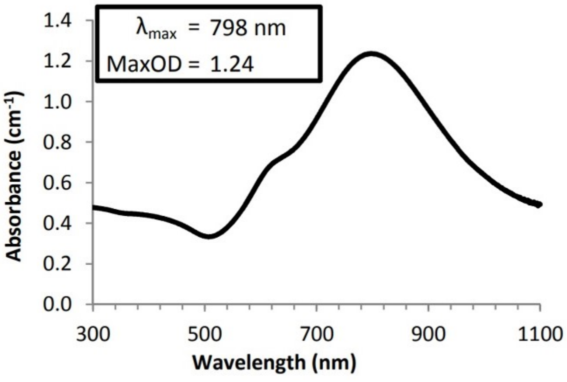

Figure 4.27 *Absorbance spectra of 800nm resonant gold nanoshells. Spectra courtesy of Nanocomposix, Inc.*

laser light from a Ti:Sapphire laser at 800nm. To study the role of resonant optical excitations in strong-field interactions with nanosystems, experiments on laser-induced photoemission from such Au shell – silica core nanoparticles tuned to have a resonant absorption peak at ~ 800 nm have been performed.

Commercial nanoshells (Nanocomposix, Inc) were purchased consisting of a 120nm diameter silica core and a 16nm thick gold shell for a total diameter of 152nm. The absorption of these particles peaks at 800nm, as seen in Figure 4.27 which gives the colloid a beautiful blue tinge. Solid spherical AuNPs of the same diameter do not have a defined resonance peak and have a broad absorption spectrum in the near-IR region. All the previous photoelectron spectra with nanoparticles have used off-resonant incident wavelengths but the unique nanoshell geometry allows a particle with similar shape and outer composition to simultaneously be resonant with the NIR Ti:Sapphire laser. Solid spherical AuNPs essentially have a fixed frequency resonance with only relatively small shifts to longer wavelengths with increasing size. Nanoshells, on the other hand, are an example of *plasmon hybridization* where the overall resonance is based on the interaction of plasmons (Figure 4.28) supported by basic elementary shapes, such as a sphere and a cavity [93]. The tuning of the ratio between the geometric dimensions, coupled to their overall size, allows for precise tuning of the optical absorbance.

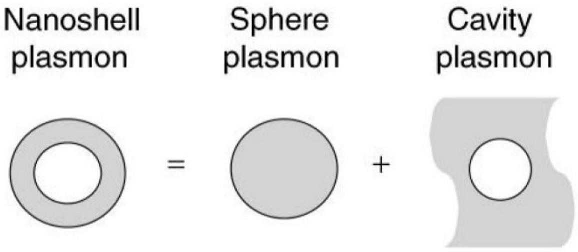

Figure 4.28 *Example of plasmon hybridization for a nanoshell. Figure taken from [93].*

800nm resonant gold nanoshells were studied using the same 25fs Ti:Sapphire laser pulses with a central wavelength at 780nm as in the previous sections, but with intensities ranging from 5.5 x 10^{11} W/cm^2 to 2.2 x 10^{12} W/cm^2. Like in the experiments on 200nm AuNPs described in the previous section, the choice of these comparatively low intensities was dictated by large electron yields and cutoff energies. Such measurements at higher intensities would suffer from saturation effects and insufficient energy acceptance of the VMI spectrometer. The photoelectron spectra were measured to assess the role that a plasmon resonance may have in the overall nanoparticle electron emission and final cutoff energy, compared to its solid gold counterpart. The histogram in Figure 4.29 shows the number of detected electrons per laser shot as a function of laser intensity. An intensity scan was done up to 8.8 x 10^{12} W/cm^2 but the cutoff electron energies were beyond the acceptance energy of the VMI. The corresponding integrated VMI images as a function of intensity are shown in Figure 4.31. Electron emission is isotropic at these relatively low intensities and do not show the elongation along the polarization axis as seen in SiO₂ and AuNPs at higher intensities. No propagation effects are noticed as the overall diameter (152nm) is still small compared to the wavelength of light.

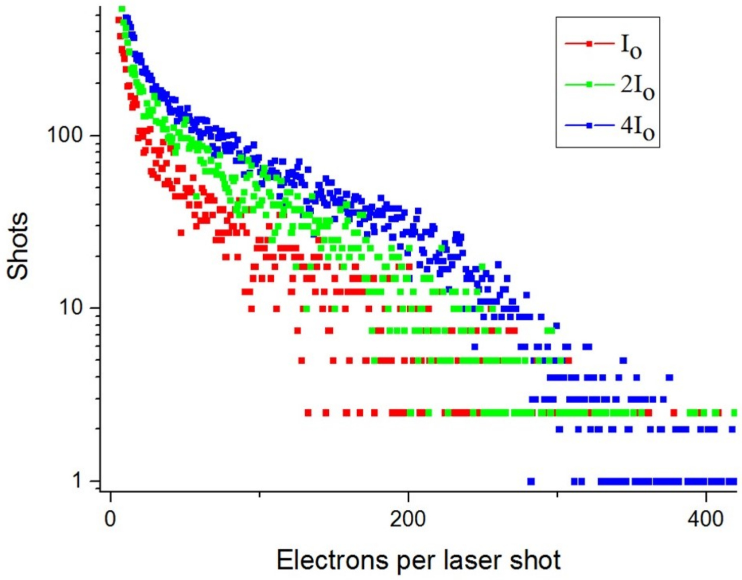

Figure 4.29 *Hit histogram of gold nanoshell particles. Total diameter = 152nm; Gold shell thickness = 16nm; Silica core = 120nm.* I_o *= 5.5 x* 10^{11} *W/cm*^{2}*.*

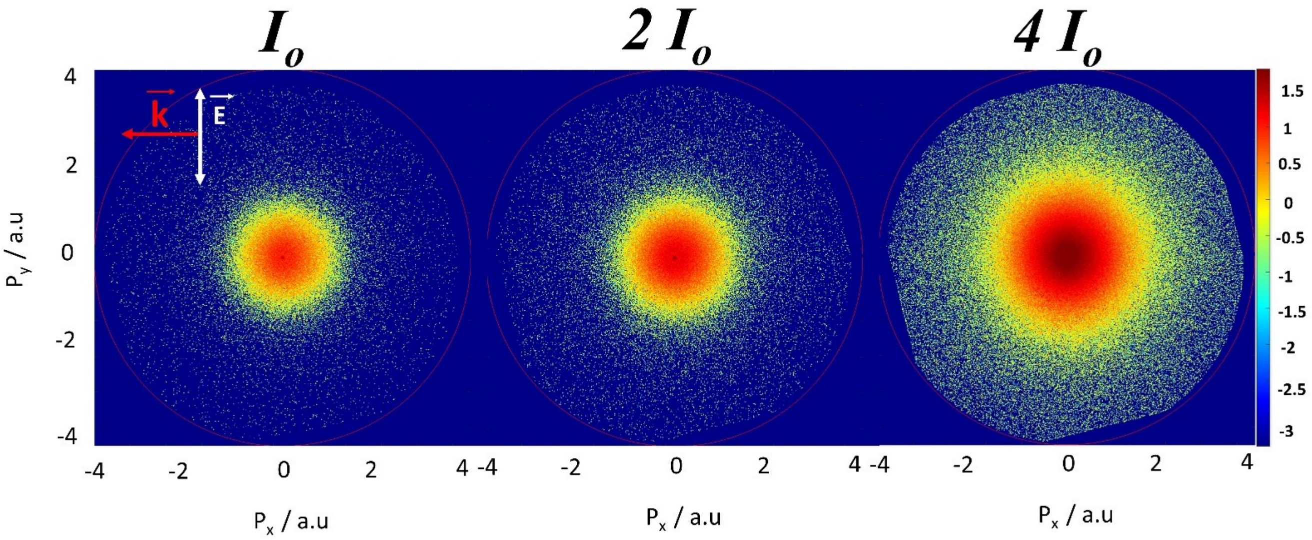

Figure 4.31 *Integrated VMI photoelectron spectra from 800nm resonant gold nanoshells. Electron emission is isotropic at these intensities.* $I_o = 5.5 \times 10^{11}$ *W/cm*^{2}.

Scaling these integrated VMI images to energy units gives the radial distribution shown in Figure 4.30. The background contribution at these low intensities is minimal and therefore not plotted in this figure. The energy cutoffs are plotted in Figure 4.32 as a function of peak laser intensity, in both energy units (eV) and in units of the ponderomotive potential, U_p. The laser intensity decreases by a factor of four, while the cutoff only decreases by a factor of two, indicating a qualitative difference from what has been seen in all the previous nanoparticle data presented. The energy cutoffs are

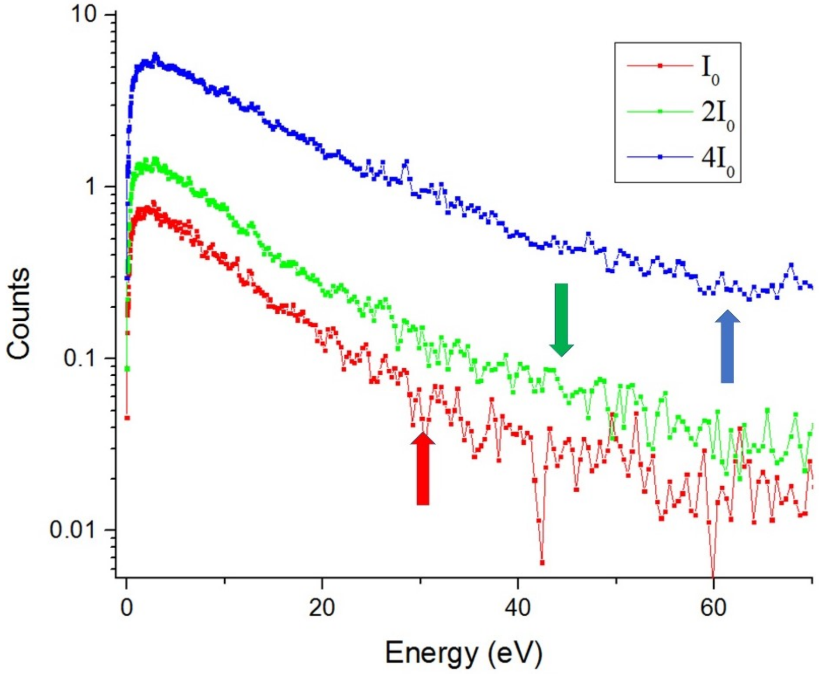

Figure 4.30 *Radial distribution of gold nanoshells as a function of intensity. Colored arrows indicate where the energy cutoff was measured using the 'background matching' method. The background contribution was excluded in this figure for the sake of readability.* $I_o = 5.5 \times 10^{11}$ *W/cm*^{2}

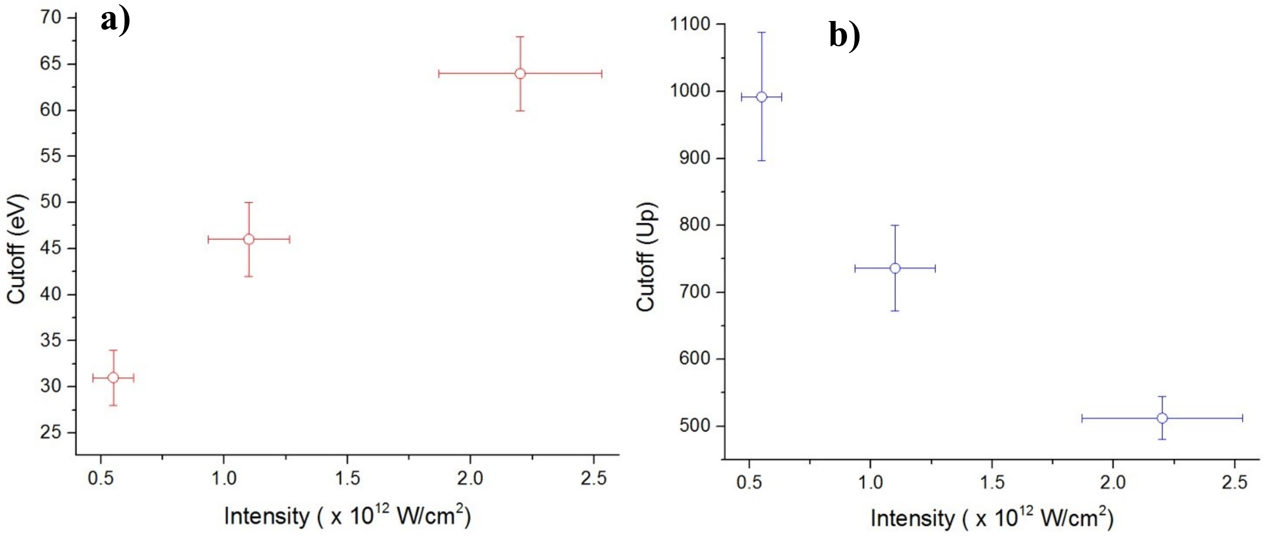

Figure 4.32 *Laser intensity vs nanoshell energy cutoff.* ***a)*** *Cutoff plotted in energy units.* ***b)*** *Cutoff scaled by ponderomotive potential. Notice the cutoff in U_p is not constant in this intensity range.*

again scaled by U_p as it is linear with intensity and therefore an intuitive way to compare nanoparticle cutoffs, independent of the incident intensity. The cutoffs for silica and AuNPs show an approximately constant cutoff for a specific diameter, regardless of the laser intensity, as shown in Figure 4.33. This figure shows a representative sample of nanoparticle cutoffs, scaled by U_p, and exhibiting a cutoff value independent of intensity. This is not the case, however, for the gold-silica nanoshells as a non-constant cutoff in units of U_p is measured as a function of intensity. This

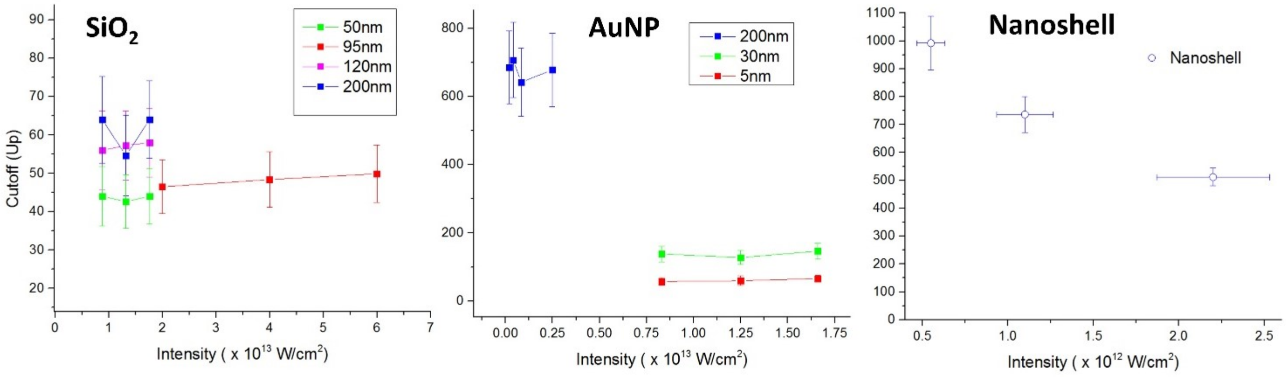

Figure 4.33 *Representative sample of cutoff energy (Up) vs laser intensity. All the SiO_2 and AuNP cutoff show a constant cutoff value when scaled by U_p. In contrast, the nanoshell cutoff does not stay constant with laser intensity. Note different y-axis (cutoff) ranges.*

is an indication that another mechanism is influencing the photoelectron emission for the resonant particles under our experimental conditions, resulting in deviations from the usual linear ponderomotive scaling seen for pure SiO_2 and AuNPs.

Figure 4.34 compares the cutoff values, in units of U_p, of the nanoshells to the solid AuNPs. The diameter of the spherical gold nanoshells used here is approximately 150nm with a 16nm thick gold shell. Even though we did not perform the measurement for 150 nm pure AuNPs, we can roughly extrapolate its approximate cutoff value from the measured nearly-linear size dependence. At 2.2 x 10^{12} W/cm^2, the cutoff value for nanoshell particles is comparable to where a cutoff for 150nm pure AuNP would reside. However, the values obtained for lower intensities expressed in units of U_p are significantly higher. This is an indication that a new mechanism in the photoelectron spectrum formation plays an important role only at low intensities.

Because the gold-shell thickness is similar to the skin depth (15-25nm) for AuNPs [11,160], it is reasonable to assume that the total number of emitted photoelectrons for a pure AuNP and a gold nanoshell of the same diameter should be comparable.

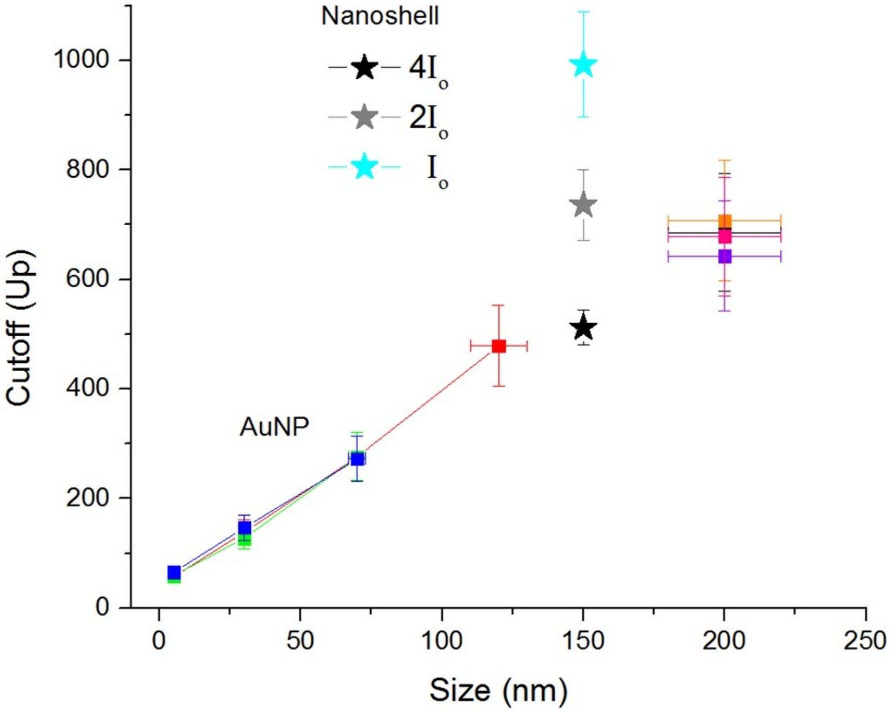

Figure 4.34 *Cutoff energy (Up) for pure AuNPs (colored squares) and nanoshells (stars). At the lowest intensity, the cutoff for the nanoshells dramatically increases while at four times this value, the cutoff matches where a pure AuNP of the same size would predicted to be.* $I_0 = 5.5 \times 10^{11}$ *W/cm*^{2}.

Figure 4.35 shows histograms of 200nm AuNP and the 150nm gold nanoshells at low intensities. The maximum number of detected electrons per laser shot is similar when looking at comparable intensities. Thus, the cutoff enhancement difference because of charge interaction must be minimal between the pure AuNP and the gold-nanoshell as this depends on the total number of photoelectrons and photoions created.

As seen in the comparison between the silica and AuNP cutoffs, the field enhancement factor, α, plays a significant role in determining the final cutoff energy. Scaling the silica data using this field enhancement factor showed how important this material- and size-dependent factor is in influencing the photoelectron spectra. Though the nanoshell surface is gold, the layered geometry, coupled with a dielectric core, greatly changes the overall relative permittivity of the nanoparticle for a given wavelength. Mie theory is the solution of Maxwell's equations in spherical coordinates with the appropriate boundary conditions and only relies on inputting the dielectric function of the particle and its surrounding medium to accurately calculate the absorbance spectra. For a nanoshell, the boundary conditions are specified so that there is an

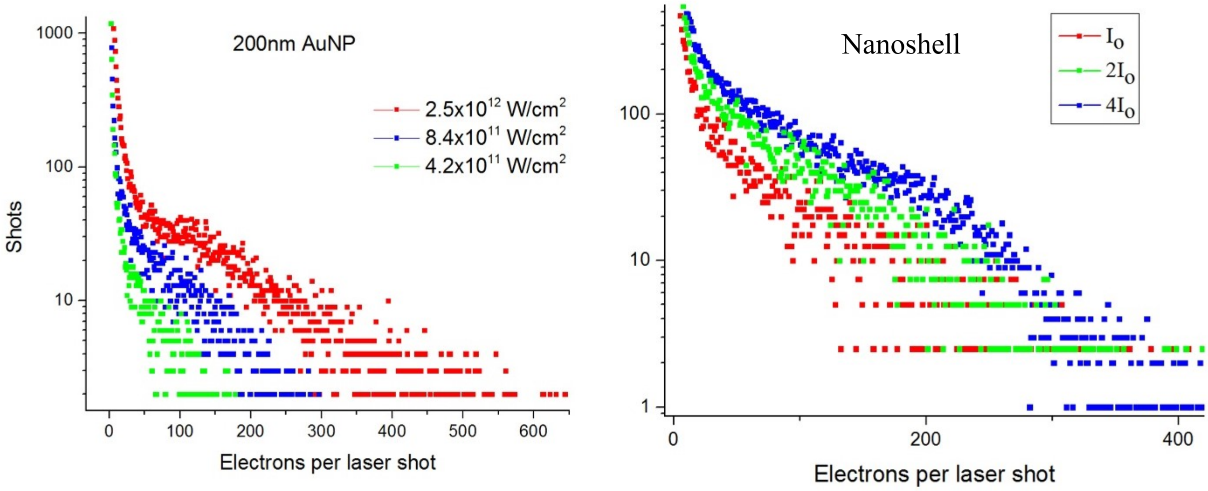

Figure 4.35 *Comparison of histograms for 200nm AuNP (left) and 150nm gold nanoshell (right). The overall maximum number of detected electrons per laser shot for similar intensities are comparable.* I_o *(nanoshell) = 5.5 x* 10^{11} *W/cm*^{2}.

additional interface, with the appropriate dielectric constant, $\varepsilon(\omega,r)$. This is responsible for changes in the electronic and optical properties as a function of wavelength and size [94].

While highly dependent on exact dimensions, material, and excitation wavelength, nanoshells have been shown to have large field enhancements for resonant conditions, much greater than solid AuNPs alone [91,94,95]. The nanoshell particles used here have maximum light absorbance at 800nm (see the spectrum in Figure 4.27), close to the central laser wavelength. The exact decomposition of different factors contributing to the observed cutoff enhancement for resonant nanoshells requires a detailed theoretical analysis beyond the scope of this work. It is reasonable, though, to assume that the plasmonically-enhanced light absorption is the main contributing factor to the significant wavelength-dependent increase of the near-field enhancement.

The natural question here is why the resonant response plays a role only at the lowest intensities studied, whereas at sufficiently high intensities, the nanoshell behaves similar to a solid AuNP of the same size. While a rigorous answer to this question again requires detailed theoretical modelling, a plausible qualitative explanation might be suggested based on the data shown in this section. While the nanoshell structures can be efficiently designed to meet the resonant condition for light absorption (e.g., at 800 nm, as seen in Figure 4.27), this response does not necessarily remain the same in the presence of a strong external field. One possible (though not the only) way in which the latter can modify the dielectric function of the nanoparticle is “inner” ionization by creating additional free charges. As described above, a rough estimate of the skin depth for gold at NIR wavelengths yields in the range of 15-25nm [11,160]. This means that in nanoshell with a 16nm gold shell, significant inner ionization might occur near the Au-SiO_2 interface, significantly changing the optical properties of the particle and “destroying” a resonance at high intensities. It should be noted that the hit histograms shown in Figure 4.35 cannot be used as a measure of this effect since they represent only the electrons emitted in the continuum, i.e., “outer” and not “inner” ionization. Even though this simplified picture is only one possible explanation, which could not be rigorously verified in the framework of this thesis, the data in Figure 4.34 and Figure 4.35 strongly suggest that at high intensities the resonant properties of the core-shell nanoparticles are significantly altered.

Following the discussion of photoelectron spectra, their formation mechanisms and cutoff energies for different materials presented above, one general remark should be made. As can be seen from Figure 4.24, Figure 4.32, and Figure 4.34, the cutoff values expressed in units of U_p yield extremely high values for all nanoparticles, approaching 1000 U_p for gold nanoshell particles at very low intensity. These results might be extremely misleading if one interprets them in usual terms of strong-field physics, where U_p is often considered as a direct measure of the electron acceleration by the field (either just the driving laser field for atoms or combined laser and near-field for nanosystems). It should be clearly understood that the lowest intensities used in this work clearly correspond to the multiphoton regime, where such view is definitely not appropriate. Indeed, at 10^{12} W/cm^2 at 800 nm, U_p (0.06eV) is a tiny fraction of the photon energy (1.55eV) and just the second-order peak for ATI of atoms would mean the energy of ~ 25 -50 U_p, in drastic disagreement with the predictions of a simple-man model derived for much higher intensities. Therefore, the representation of the cutoff energies in units of U_p discussed here for low-intensity regime should be considered merely as a practical tool to visualize the linearity of the intensity dependence and not as a basis for simplified model pictures.

Chapter 5 - Real-time X-ray Imaging of Femtosecond Nanoplasma Dynamics

> - *"Progress is made by trial and failure; the failures are generally a hundred times more numerous than the successes; yet they are usually left unchronicled."*
>
> - *William Ramsay*

Subjected to intense femtosecond laser pulses, solid-density materials exhibit ultrafast collective and collisional electron dynamics, transform into highly ionized plasmas, and explode on the sub-picosecond timescale [96]. As shown in the previous chapter, the utilization of isolated, gas-phase nanoparticles offers a fundamental path to infer the physics of laser-driven many-particle excitation and relaxation processes.

As seen in chapter 4, photoelectron spectroscopy of IR driven nanoparticles begins to become difficult already at mid- to high 10^{13} W/cm^2 because of the large electron kinetic energy coupled to the total amount of electrons per interaction. Other methods such as ion imaging and spectroscopy [97] and electron stereo TOF [98] do offer some advantages but are still using final photo-ion or electron emission to infer the interaction dynamics, where effects such as space-charge interactions can play a large role. Thus, laser-driven processes in nanosystems at higher intensities, which showcase an even more extreme case of light-matter interaction, are difficult to access experimentally.

The last part of my thesis describes an experiment designed to explore the ultrafast dynamics in isolated silica nanoparticles driven by very intense NIR laser radiation (~10^{15} W/cm^2) using time-resolved, single-particle x-ray scattering as a probe. These experiments became feasible with the advent of x-ray free electron lasers (XFELs). As discussed in Section 2.6.1, XFELs deliver intense x-ray pulses of femtosecond duration that allow real-time, single-shot, x-ray imaging using small-angle scattering. This is a new way to characterize strong-field driven nanosystems where the femtosecond dynamics are imprinted in the x-ray scattering images that are sensitive to the changes in the particle's evolving electron density. The x-ray probe can give a 'snapshot' of the local electronic density of the nanoparticle at a given time delay after the initial IR pulse. This photon-based technique, which does not rely on final ion or electron spectra, is not influenced by any post-interaction effects and thus enables direct measurements of the real-time processes. Previous work has successfully demonstrated the feasibility of this novel approach in nanoscale samples – Xe clusters of 60nm diameter [27]. There, xenon clusters were subjected to an intense NIR pulse and then imaged by x-ray scattering after a set time delay. However, as discussed in Section 1.4.3, the interpretation of the results of this impressive proof-of-principles experiment was hindered by a rather broad size distribution of the Xe cluster beam. Moreover, the time resolution of this study was limited to 200 fs by the inherent jitter between the SASE LCLS pulse and the synchronized NIR laser.

In this work, a novel nanoparticle source described in Section 2.6.4 was applied to perform NIR pump / x-ray probe experiment on spherical 120 nm SiO_2 nanoparticles with very narrow (±2%) size distribution. The use of such a monodisperse sample ensures the delivery of a pristine and nearly identical nanoparticle for each individual laser interaction. This significant improvement in size dispersity over the Xe cluster source allowed one to distinguish the diffraction fringe pattern evolving as a result of laser-nanoparticle interaction not effected by different initial sample sizes. The use of an x-ray – optical cross-correlator for shot-to-shot correction of the arrival times of the x-ray and NIR pulses [154] enabled time-delays scans to improve the time- and length-scale resolution of the experiment.

Any sample, either xenon or silica, will initially rapidly ionize in the presence of such large intensities (~10^{15} W/cm^2), either through tunneling or over-the-barrier processes. In nanoscale objects, electron recollision is a dominant mechanism, as shown in chapter four. The large electron kinetic energy at such high intensities also drives subsequent electron impact avalanching. The result of this nanoparticle interaction leads to the formation of a nanoplasma at the surface consisting of the 'free' photoelectrons and corresponding photo-ions. The large Coulomb potential at the surface efficiently traps and confines most of the electrons to the surface. At this point, the particle can be seen as a quasi-metal as it consists of 'free' electrons on the surface and the initial nanoparticle properties are not as important. The Coulomb repulsion of the surface ions, coupled with the continuing electron impact avalanching, creates and propagates the plasma. This entire process is initiated and driven by the IR pulse.

The ability to perform x-ray single shot imaging also gives the advantage of characterizing the nanoparticle sample for each interaction if no pump laser is used [27]. Though the silica nanoparticles have a small size dispersity, it will still contain a small number of non-spherical particles along with a range of ±2% in diameter. As discussed in section 2.3, there is also a finite probability that the nanoparticle source (FANS) will also produce cluster/s of individual nanoparticles. In nanoparticle photoelectron experiments, there is no direct measurement of the shot-by-shot size and dimension of the sample and care must be taken to prevent nanoparticle clustering (by dilution of the sample). In contrast, the use of x-ray scattering gives direct access to the physical size and shape of each nanoparticle being imaged by its unique diffraction pattern. As the scattering image of a spherical nanoparticle is very different than that of a cluster, the diffraction pattern can be used as a powerful tool for sorting data. This sensitivity

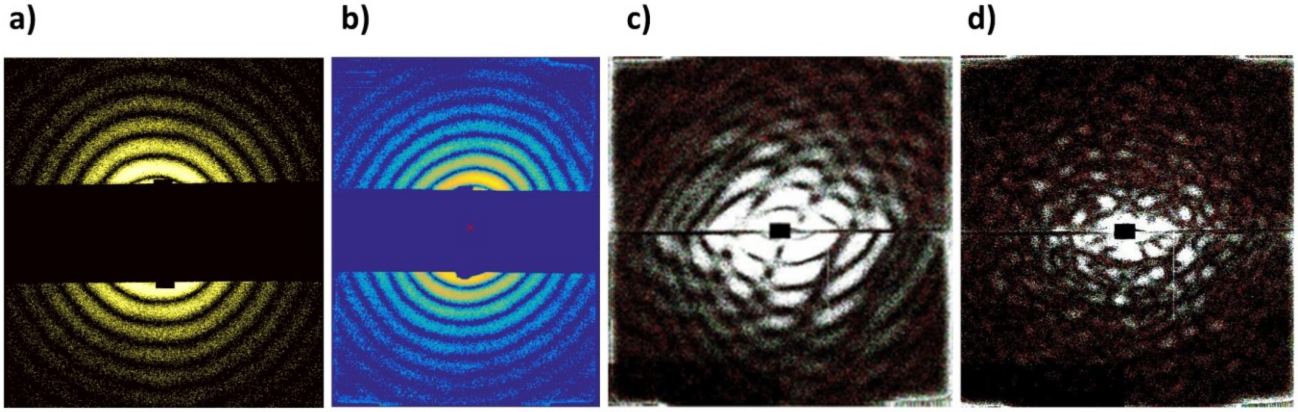

Figure 5.1 *Single-shot x-ray scattering images of silica nanoparticles. The x-ray is sensitive to nanoparticle size and shape, along with clustering.* ***a)*** *Single 120nm SiO_2 particle* ***b)*** *Non-spherical ellipsoid nanoparticle* ***c)*** *Interference pattern from two simultaneous, offset nanoparticles in x-ray focus* ***d)*** *Diffraction from a cluster of silica nanoparticles. All scattering images are x-ray only.*

is seen in Figure 5.1 where **a)** is a single, spherical 120nm SiO_2 nanoparticle with its characteristics hard-sphere diffraction pattern while a non-spherical ellipsoid seen in **b)** shows a left/right asymmetry. The interference pattern in **c)** is most likely the result of a twin, i.e., two attached nanoparticles that were simultaneously imaged in the laser focus while **d)** is an aggregate (cluster) of at least a few nanoparticles. A monodisperse nanoparticle sample coupled with a robust method of sorting monomer scattering images is the key to gathering sufficient statistics for each time step in this pump/probe experiment.

To elucidate the time-dependent laser-driven nanoparticle dynamics, the SiO_2 nanoparticles were irradiated by ~50 fs, 10^{15} W/cm^2 pulses from the LCLS NIR laser followed by ~60 fs, ~ 10^{17} W/cm^2 LCLS pulses at 800 eV photon energy (wavelength 1.55 nm). In order to produce a sequence of snapshots revealing of the state of the nanoparticle as a function of time, a series of delay scans were performed. The exact position of the time-overlap between the NIR and x-ray pulses was determined using the ionic spectra from N_2 fragmentation as described in [159].

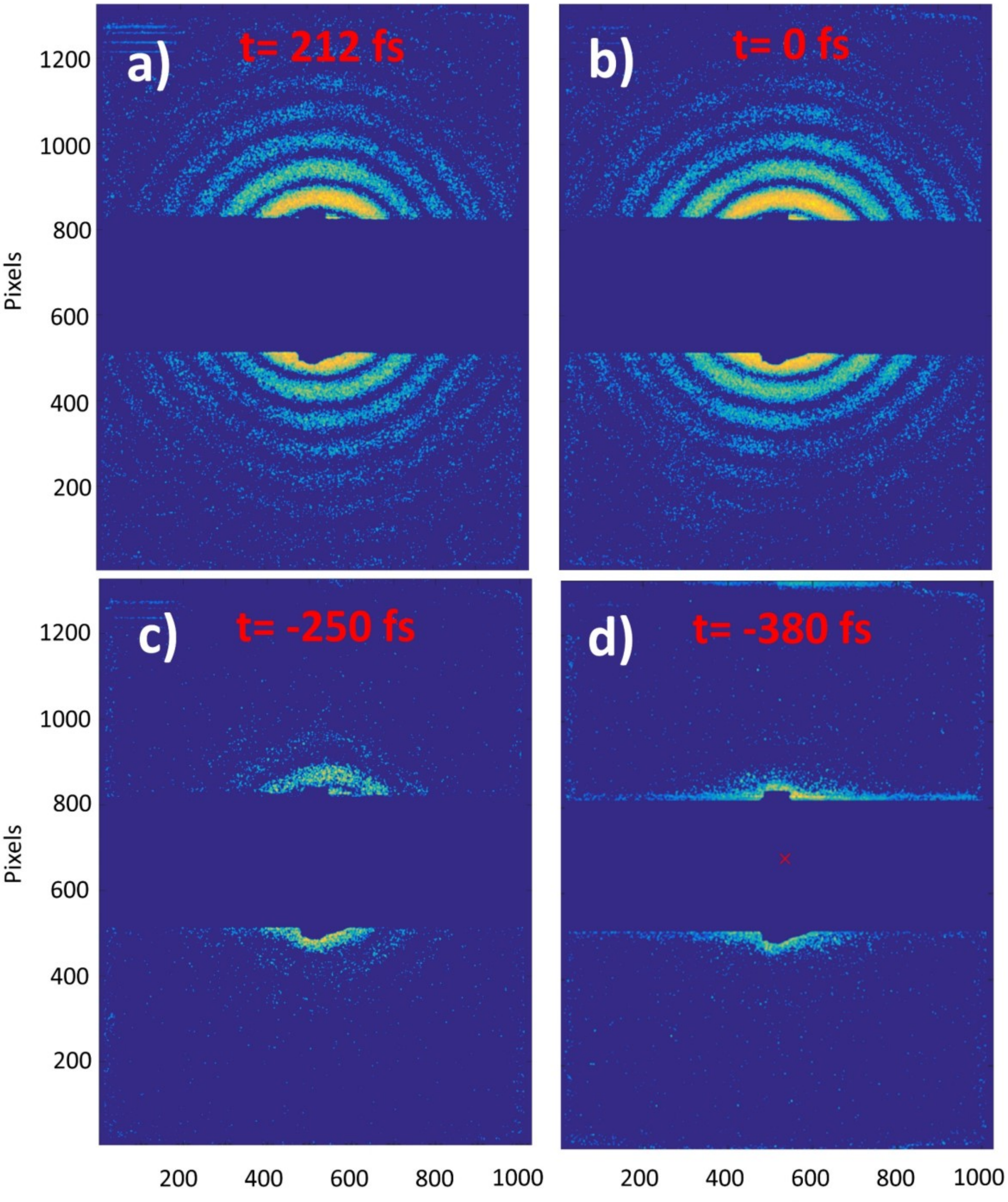

Figure 5.2 *X-ray scattering images of 120nm SiO_2 for various delay times between the IR pump and x-ray probe pulses.* ***a)*** *Unpumped image where x-ray pulse arrived first.* ***b)*** *IR and x-ray pulse arrive simultaneously* ***c)*** *IR pulse arrived 250fs before x-ray and have dramatically changed the scattering signal.* ***d)*** *At much longer times, the scattering signal cannot be resolved enough to extract information about the scatterer Positive delays correspond to x-ray pulse arrive first while negative means that NIR pulse arrives earlier. Blank stripe is result of pnCCD detector being opened to allow laser pulses to pass. Images courtesy of Christian Peltz.*

After this calibration, shot-to-shot variations of the relative NIR / x-ray arrival times were measured and corrected for by the cross-correlator setup described in [146] such that the temporal resolution of the experiment was mainly limited by both pulse durations.

Figure 5.2 displays three representative x-ray scattering images at different time-delay steps showcasing the ability of the scattering images to resolve local nanoparticle changes. Positive delays indicate that the x-ray pulse preceded the NIR pulse while negative delays have the NIR pulse initiating the dynamics before being probed by the x-ray. Here, **a)** is an example of a typical hard-sphere diffraction pattern from a single 120nm SiO_2 nanoparticle that has not interacted with the NIR pulse and therefore is 'unpumped'. Next, **b)** shows both the IR and x-ray pulse arriving simultaneously at time *t=0* while **c)** has the NIR pulse interacting with the nanoparticle 250fs before being imaged by the x-ray, therefore a 'pumped' particle. The first two images look similar where the NIR pulse either has not interacted or has not been given sufficient time to initiate any dynamics. Given sufficient time after the NIR pulse, the scattering image displays a very different picture of the nanoparticle.

Analysis of the full delay scan is ongoing to fully understand the creation and evolution of the IR interaction, with particular focus on the delay region between *t=0* to *-250fs*. The fine-step time delays in this region along with the corrections from the cross-correlator data will provide detailed information of the nanoplasma formation and propagation through the nanoparticle with high temporal resolution. Figure 5.2**d)** shows a scattering image at the even longer delay of 380fs after the initial IR pulse. Here, there are no discernible features to allow a reliable determination of the scattering body that produced this image. This gives a limit on the length of time that the dynamics of the nanoparticle can be followed.

The data shown in Figure 5.2 are plotted as a radial integral of each scattering image. Figure 5.3 shows a log-normal scattering plot of the scattering wave vector, *q*, vs total signal

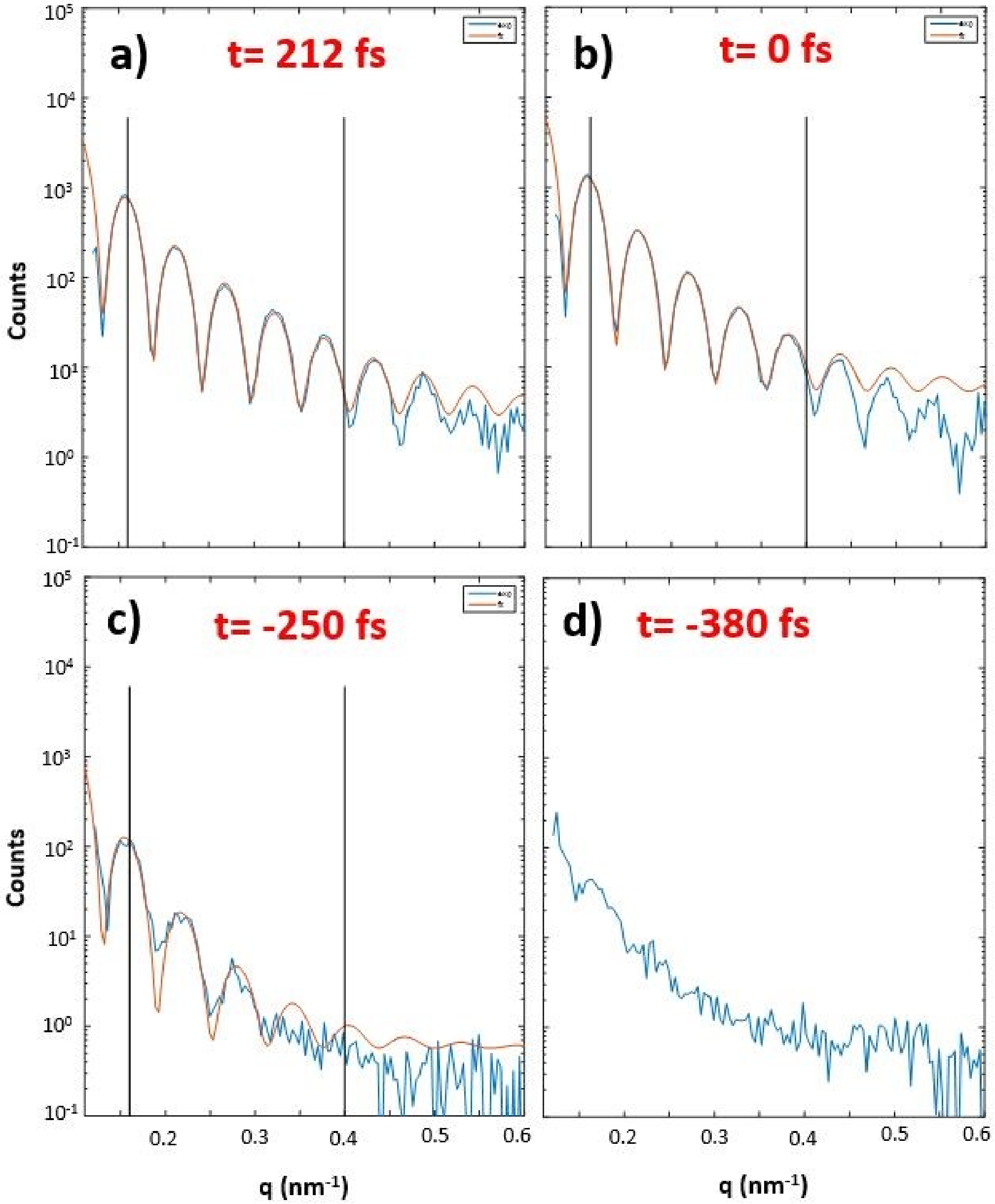

Figure 5.3 *Radial integral of time-delayed scattering images plotted vs q, the scattering wave vector. The experimental data (blue spectra) and best fit curve (red) are both plotted. Here,* ***a)*** *is unpumped,* ***b)*** *is IR and x-ray overlap and* ***c)*** *is pumped by IR at t=250fs.* ***d)*** *The loss of sufficient detected scattering signal at long delays limits the useful information extracted. Again, positive delays correspond to x-ray first and negative delays is IR first. Plotted as lognormal with vertical lines showing data where best fit parameters are taken from.*

intensity (determined from the radial integral of the corresponding panels of Figure 5.2). This allows for the fringe spacing to be determined as well as the characteristic slope for each delay. As the silica nanoparticles are well characterized in size, the fringe spacing is determined by the wavelength of the x-ray and the distance from the scattering body to the detector. The radial integral of a scattering image, at a particular time-delay, can immediately be used to determine the fringe spacing and how fast the scattering signal decreases (slope). X-ray scattering is sensitive to any laser-induced change in the nanoparticle that will be seen in the fringe spacing and/or the slope of the log-normal scattering intensity. The experimental data (blue spectra) is overlapped with a best fit curve (red) using a sharpened Fermi distribution [99].

Figure 5.3**d)** does not show enough features to give information on the scattering entity. This image and corresponding radial integral most likely come from a pumped monomer, but there is also a chance it comes from an aggregate. At this long time-delay, the pumped nanoparticle no longer can be quantitatively measured and thus gives an upper time limit to the tracking of the dynamics of the system.

The most noticeable difference in the time-dependent scattering images is the loss the higher order diffraction fringes at large negative delays. This is seen in the radial integral where the slope becomes steeper as compared to the unpumped or overlap-region spectra. After the initial NIR interaction, rapid ionization and subsequent trapping of the electrons leads to the formation of a plasma at the nanoparticle surface consisting of the ‘free’ photoelectrons and corresponding photo-ions. This “nanoplamsa” begins to expand and dilute the outer electron density. This is the so-called *surface softening* where the electron density profile at the particle surface spreads as the plasma wave propagates. The x-ray scattering image are sensitive to this change in electron density and can be used to trace the evolution of the expanding plasma as a function of time.

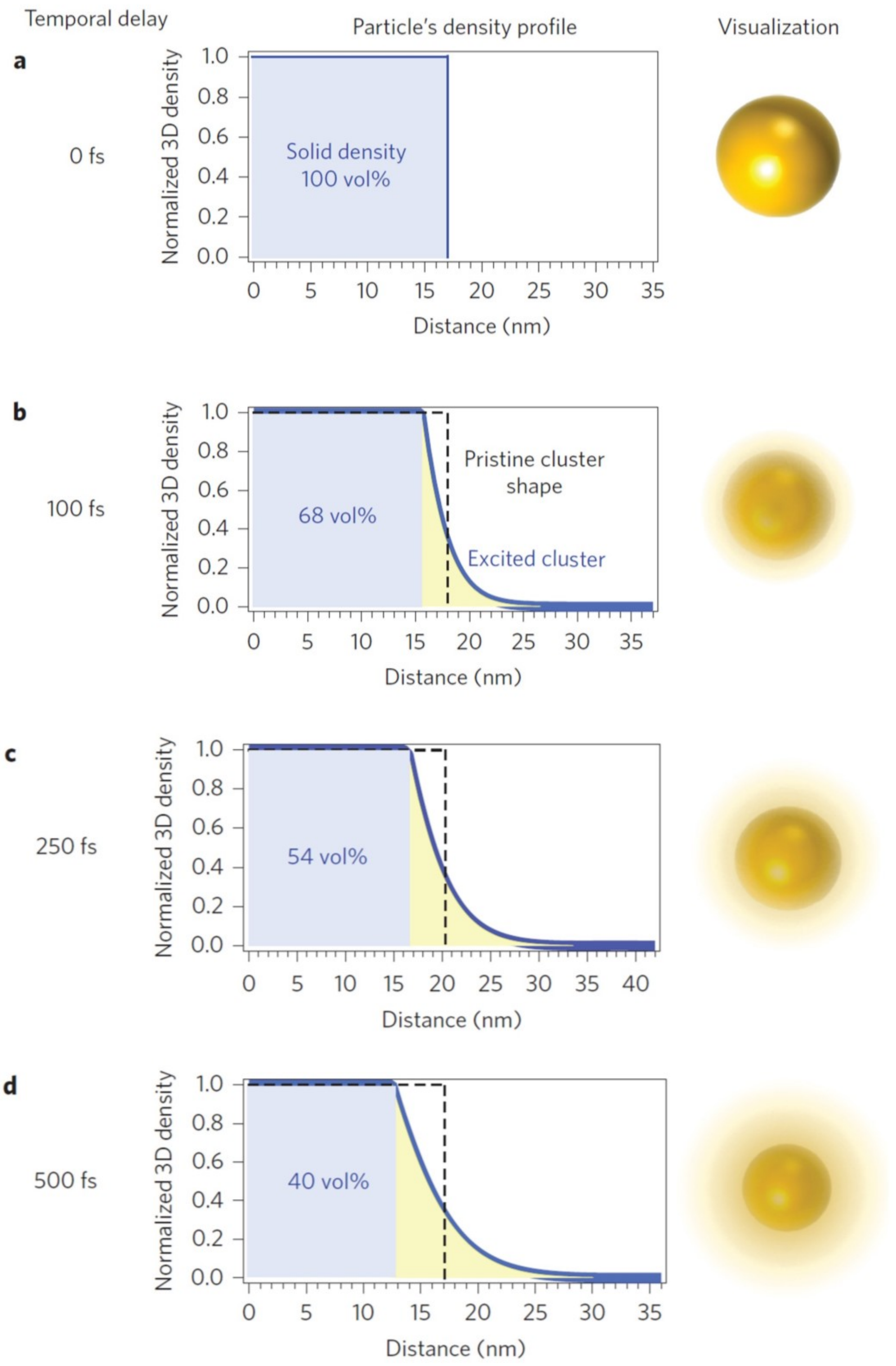

Figure 5.4 *Nanoplasma evolution in xenon nanoclusters as function of time after initial IR pulse.* ***a-d)*** *show the respective density profile of the cluster at the delay time indicated. As the nanoplasma propagates, more of the inner solid core is diluted by the expansion of the cluster as seen in* ***b-d)****. The corresponding x-ray scattering images show the evidence of the changing electronic density. Figure taken from [28].*

These dynamics could be better understood by considering the nanoplasma evolution reconstructed for laser-driven Xe nanoclusters in [28]. Figure 5.4 illustrates the nanoplasma formation as a function of time after the initial IR pulse. The assumed density profile models the particle as a hard sphere before the interaction occurs. For positive time delays (same as negative delays for my work), the structural dynamics are beginning to be seen. As previously said, the initial ionization induces a surface plasma to form consisting of the trapped photoelectrons and surface ions. The ions begin to Coulomb explode, therefore driving the expansion outward and diluting the outer cluster density profile but keeping much of the core intact. With increasing time, the evolution of the nanoplasma is seen in the decreasing size of the solid core density.

X-ray scattering provides a novel approach to studying the ultrafast dynamics in isolated nanoparticles driven by intense laser radiation. The ability to track and resolve, both on the femtosecond- and nanometer scale, provide a powerful tool for studies of the interaction of intense NIR pulses with silica nanoparticles at high intensities. The formation and propagation of a nanoplasma created on the nanoparticle was observed in the time-resolved x-ray scattering images. The loss of higher order diffraction rings visualizes how the expanding nanoplasma dilutes the surface electron density at large time delays after the NIR pulse where *surface softening* plays a dominant role. The use of a well-characterized sample coupled with x-ray imaging gives direct access to the spatiotemporal dynamical evolution of the IR-nanoparticle interaction. A more detailed analysis of the data from 0-250 fs delay region is underway and gives excellent prospects to infer the light-driven dynamics in SiO_2 nanoparticles on a sub-100 fs time scale.

Chapter 6 - Conclusion and Outlook

- *"What the hell is this?"*

- *Artem Rudenko*

6.1 Conclusion

The work presented in this thesis focused on several intriguing aspects of nanoscience and nanotechnology, with the common theme of nanoparticle interactions. In the first part presented in Chapter 3, the solubility properties of gold nanoparticles have been studied. Small nanoparticles that contain only a few thousand atoms, mostly residing on the surface, provide a transition from molecules to a small(ish) collection of atoms. They were shown to have solution-like properties such as thermally reversible, temperature-dependent solubility and aggregation phenomena that are behaviors common to many molecular and ionic solutions. The extension of solution theory to nanoparticle systems was done to extract thermodynamic quantities such as the enthalpy of dissolution from the experimental data. Measured thermodynamic values showed reasonable agreement to a phenomenological model, though more comprehensive theoretical work is needed. This experiment can be repeated for numerous nanoparticle systems to begin to develop an intuitive understanding of the solution properties of nanoparticles and the role multiple parameters play. Preliminary results from a system of 3nm spherical ZnS nanoparticles already have shown unusual behavior where the solubility of the system increases with decreasing temperature, opposite the trend seen in gold nanoparticles.

In the second, most extensive part presented in Chapter 4, photoelectron spectroscopy was used to investigate the ultrafast dynamics in isolated, gas-phase nanoparticle driven by intense, femtosecond lasers. These experiments are based on the optimized nanoparticle injector design and new sample purification procedure to avoid contamination and excessive aggregation of metallic nanoparticles. The highest photoelectron energies ("cutoffs") were measured from silica, gold, and gold-shell/silica core nanoparticles as a function of particle size and laser intensity. The cutoff values found were dependent on nanoparticle composition and size, as well as laser intensity and pulse duration. Gold nanoparticles exhibited an enhanced energy cutoff when compared to silica. This was attributed to the considerably larger near-field enhancement combined with stronger charge-interaction effects resulting from greater ionization yields, which, in turn, is due to the smaller electron binding energy for AuNPs as compared to SiO_2. The resonant core-shell nanoparticles manifested an even larger enhancement but only at low intensities, which is tentatively explained by the importance of resonant absorption and deterioration of the resonant conditions at higher intensities. All the nanoparticles cutoff values were found to be much larger than those from atoms under similar conditions. For large silica nanoparticles (above 200nm in diameter), the effects of multiple rescattering from a many-cycle (25fs) laser pulse are shown to increase the cutoff over a few-cycle (4fs) pulse at the same intensity.

Finally, to probe a nanoparticle driven at a much higher laser intensity, an alternative technique to photoelectron spectroscopy was needed. X-ray scattering provided a way to probe the femtosecond- and nanometer dynamics of a hard-driven isolated, gas-phase nanoparticle described in Chapter 5. Using femtosecond x-ray pulses from an FEL, single-shot x-ray scattering was a much more versatile probe for the high-intensity regime than photoelectron spectroscopy. The formation and evolution of a nanoplasma initiated by the intense NIR pulse was tracked using delay scans in a NIR pump / x-ray probe technique. The use of well-characterized nanoparticles injected by a source adapted, designed and built by me, coupled with the single-shot x-ray scattering, allowed for this precision. Analysis of this data is ongoing but promising. The effects of surface softening on the laser-driven nanoparticle was clearly seen while other, more discrete phenomena are being investigated.

6.2 Outlook

The use of XFEL light to probe IR driven dynamics in nanoparticles is now well-established. Future experiments include the use of FLASH at DESY (German Electron Synchrotron) which is another FEL located in Hamburg, Germany. Though similar to LCLS, FLASH has 1/12th repetition rate and longer wavelengths (XUV). For imaging nanoparticles, the longer wavelength means more scattering per unit area and a larger diffraction fringe spacing, as seen in Figure 6.1. The pnCCD detectors only have a finite acceptance angle which means that the shorter the wavelength, the more fringes will be seen, but the faster the signal will fall. At FLASH, the scattering signal will be able to be seen for longer delay scans and with increased signal compared to LCLS.

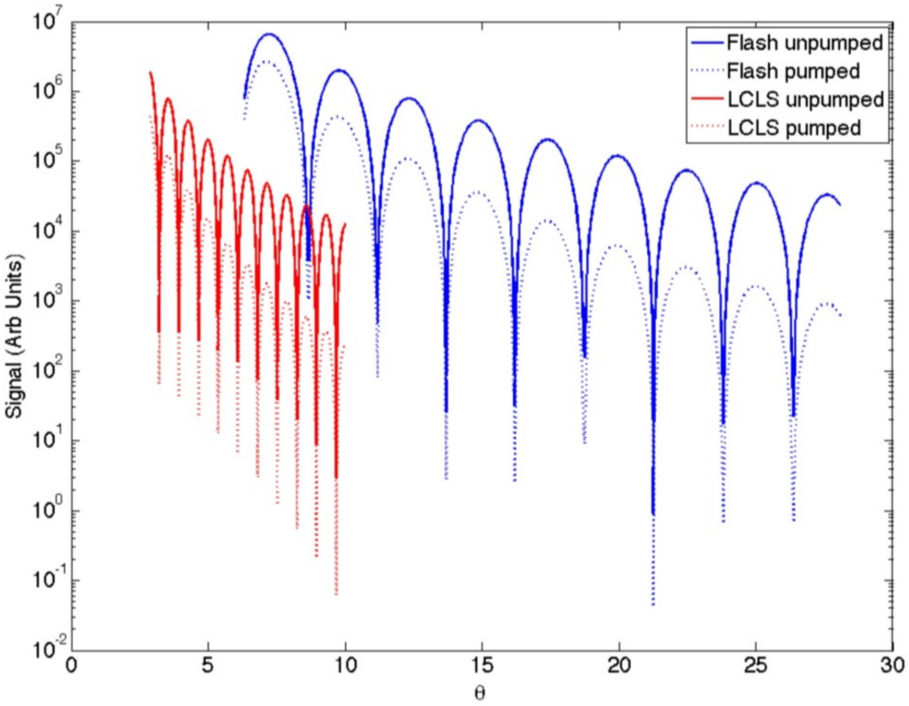

Figure 6.1 *Calculated scattering signal from 120nm SiO_2 nanoparticle from LCLS (red) and FLASH (blue). The longer wavelength at FLASH causes larger fringe spacing but less loss of signal over the same solid angle compared to LCLS. The dotted lines show the decrease in signal strength after a particle has been pumped by an IR pulse.*

Upcoming work at FLASH consists of looking at the ultrafast dynamics of NIR and / or visible light-driven metallic nanoparticles. As seen in the photoelectron spectroscopy experiments reported in Chapter 4, the electron recollision and near-field enhancements of metallic particles are much different than for silica. A comparison of these fundamentally different types of nanoparticles will study the impacts of material type, material density, ion mass, and nanoplasma formation.

As metallic nanoparticles can support surface plasmon resonances, time-resolved x-ray (or XUV) scattering is a unique way to investigate how a nanoparticle driven at its plasmon resonance frequency will influence the overall ultrafast dynamics. The second harmonic of the 800nm IR laser overlaps the plasmon resonance for 60nm spherical silver nanoparticles. Delay scans at optical wavelengths on and off the resonance will allow the influence of the plasmon on the overall nanoplasma formation and propagation. This couples nicely to the work in Chapter 4 showing how driving a metallic nanoparticle at its plasmon resonant frequency can enhance electron cutoffs.

Single-shot x-ray scattering can also be coupled with ion spectroscopy. Each laser interaction can be tagged with the appropriate x-ray scattering image along with the corresponding ion spectra. This dual-mode analysis can be beneficial for many different applications. In fact, ion spectra were recorded during the measurement described in Chapter 5; however, since the operation of the ion spectrometer was not given high priority during the beamtime, the data quality for nanoparticle runs was rather low.

Future photoelectron spectroscopy experiments might receive a new boost from technological developments. Employing detectors with larger dynamic range (currently under development in several laboratories world-wide) will reduce the problems related to the saturation effects and allow one to extend the studies reported here to higher intensities, bridging the gap towards the LCLS experiment. It would also significantly extend the range of materials and sizes, in particular the ability to make large, nearly NIR-wavelength scale metal particles experimentally accessible. Furthermore, if combined with the latest developments of tunable, intense, femtosecond laser sources at mid- and far-infrared wavelengths (already available at JRML / KSU), the study, control and "design" of electron emission patterns over a very broad energy range can be investigated. The key parameter of the present photoelectron analyses, the ponderomotive potential, scales quadratically with the laser wavelength and can provide a crosslink to different aspects of the rapidly developing ultrafast nanoplasmonics. Finally, many of the results obtained in this work might be linked to the outcome of attosecond streaking experiments and simulations, revealing different aspects of near-field configuration and charge dynamics in nanoscale systems.

Bibliography

1. Strutt, J. W. (1871). XV. On the light from the sky, its polarization and colour. *The London, Edinburgh, and Dublin Philosophical Magazine and Journal of Science*, *41*(271), 1. http://doi.org/10.1080/14786447108640452

2. Conselice, C. J., Wilkinson, A., Duncan, K., & Mortlock, A. (2016). The evolution of galaxy number density at z<8 and its implications. *The Astrophysical Journal*, *830*(2), 83. http://doi.org/10.3847/0004-637X/830/2/83

3. Daniel, M. C., & Astruc, D. (2004). Gold nanoparticles: Assembly,supramolecular chemistry, quantum-size-related properties, and applications toward biology, catalysis, and nanotechnology. *Chem. Rev.*, *104*, 293–346. http://doi.org/10.1021/cr030698+

4. Freestone, I., Meeks, N., Sax, M., & Higgitt, C. (2007). The Lycurgus Cup — A Roman nanotechnology. *Gold Bulletin*, *40*(4), 270–277. http://doi.org/10.1007/BF03215599

5. Faraday, M. (1857). The Bakerian Lecture: Experimental Relations of Gold (and Other Metals) to Light. *Philosophical Transactions of the Royal Society of London*, *147*(0), 145–181. http://doi.org/10.1098/rstl.1857.0011

6. Mie, G. (1908). Contributions to the optics of turbid media, particularly of colloidal metal solutions. *Ann. Phys.*, *25*(3), 377–445. http://doi.org/10.1002/andp.19083300302

7. Borovitskaya, E., & Shur, M. S. (2002). Quantum Dots. http://doi.org/10.1038/scientificamerican0193-118

8. Maier, S. A. (2007). Plasmonics: Fundamentals and Applications. http://doi.org/10.1007/0-387-37825-1

9. Atwater, H. A. (2007). The promise of plasmonics. *ACM SIGDA Newsletter*, *37*(9), 1–1. http://doi.org/10.1145/1859855.1859856

10. Atwater, H. A., & Polman, A. (2010). Plasmonics for improved photovoltaic devices. *Nature Materials*, *9*(10), 865–865. http://doi.org/10.1038/nmat2866

11. Stockman, M. I. (2011). Nanoplasmonics: past, present, and glimpse into future. *Optics Express*, *19*(22), 22029. http://doi.org/10.1364/OE.19.022029

12. Stockman, M. I. (2011). Nanoplasmonics: The physics behind the applications. *Physics Today*, *64*(2), 39–44. http://doi.org/10.1063/1.3554315

13. Karn, B., Kuiken, T., & Otto, M. (2015). A Review and in Situ Remediation: of the Benefits and Potential, *117*(12), 1823–1831. http://doi.org/10.1289/ehp.0900793

14. Powell, J. A., Schwieters, R. M., Bayliff, K. W., Herman, E. N., Hotvedt, N. J., Changstrom, J. R., … Sorensen, C. M. (2016). Temperature dependent solubility of gold nanoparticle suspension/solutions. *Rsc Adv*, *6*(74), 70638–70643. http://doi.org/10.1039/c6ra15822f

15. L. Pauling, *General Chemistry* (Dover, 1970).

16. E. A. Moelwyn-Hughes, *Physical Chemistry* (Pergamon, 1961).

17. Lin, X. M., Wang, G. M., Sorensen, C. M., & Klabunde, K. J. (1999). Formation and Dissolution of Gold Nanocrystal Superlattices in a Colloidal Solution. *The Journal of Physical Chemistry B*, *103*(26), 5488–5492. http://doi.org/10.1021/jp990729y

18. Prasad, B. L. V., Stoeva, S. I., Sorensen, C. M., & Klabunde, K. J. (2002). Digestive Ripening of Thiolated Gold Nanoparticles: The Effect of Alkyl Chain Length. *Langmuir*, *18*(20), 7515–7520. http://doi.org/10.1021/la020181d

19. Lohman, B. C., Powell, J. A., Cingarapu, S., Aakeroy, C. B., Chakrabarti, A., Klabunde, K. J., … Sorensen, C. M. (2012). Solubility of gold nanoparticles as a function of ligand shell and alkane solvent. *Physical Chemistry Chemical Physics*, *14*(18), 6509. http://doi.org/10.1039/c2cp40645d

20. Uzun, O., Hu, Y., Verma, A., Chen, S., Centrone, A., & Stellacci, F. (2008). Water-soluble amphiphilic gold nanoparticles with structured ligand shells. *Chem. Commun.*, (2), 196–198. http://doi.org/10.1039/B713143G

21. Centrone, A., Penzo, E., Sharma, M., Myerson, J. W., Jackson, A. M., Marzari, N., & Stellacci, F. (2007). The role of nanostructure in the wetting behavior of mixed-monolayer-protected metal nanoparticles. *Proceedings Of The National Academy Of Sciences Of The United States Of America*, *105*(29), 9886–9891. http://doi.org/DOI 10.1073/pnas.0803929105

22. Lin, X., Sorensen, C., & Klabunde, K. J. (2000). Digestive Ripening, Nanophase Segregation and Superlattice Formation in Gold Nanocrystal Colloids. *Journal of Nanoparticle Research*, *2*(2), 157–164. http://doi.org/10.1023/A:1010078521951

23. J. Powell, S. Robatjazi, A. Vajdi, V. Makhija, X. Li, Y. Malakar, W. L. Pearson, C. Sorensen, M. F. Kling, and A. Rudenko, "Intensity-dependent photoelectron spectroscopy of gas-phase nanoparticles without focal volume averaging," Conference on Lasers and Electro-Optics, OSA Technical Digest (2016). http://doi.org/10.1364/CLEO_QELS.2016.FTh4M.3

24. Zherebtsov, S., Fennel, T., Plenge, J., Antonsson, E., Znakovskaya, I., Wirth, A., … Kling, M. F. (2011). Controlled near-field enhanced electron acceleration from dielectric nanospheres with intense few-cycle laser fields. *Nature Physics*, *7*(8), 656–662. http://doi.org/10.1038/nphys1983

25. Süßmann, F., Seiffert, L., Zherebtsov, S., Mondes, V., Stierle, J., Arbeiter, M., … Fennel, T. (2015). Field propagation-induced directionality of carrier-envelope phase-controlled photoemission from nanospheres. *Nature Communications*, *6*, 7944. http://doi.org/10.1038/ncomms8944

26. Rupp, P., Seiffert, L., Liu, Q., Süßmann, F., Ahn, B., Förg, B., … Zherebtsov, S. (2016). Quenching of material dependence in few-cycle driven electron acceleration from nanoparticles under many-particle charge interaction. *Journal of Modern Optics*, 1–9. http://doi.org/10.1080/09500340.2016.1267272

27. Gorkhover, T., Adolph, M., Rupp, D., Schorb, S., Epp, S. W., Erk, B., … Bostedt, C. (2012). Nanoplasma dynamics of single large xenon clusters irradiated with superintense X-ray pulses from the linac coherent light source free-electron laser. *Physical Review Letters*, *108*(24), 245005. http://doi.org/10.1103/PhysRevLett.108.245005

28. Gorkhover, T., Schorb, S., Coffee, R., Adolph, M., Foucar, L., Rupp, D., … Bostedt, C. (2016). Femtosecond and nanometre visualization of structural dynamics in superheated nanoparticles. *Nature Photonics*, *10*(2), 93–97. http://doi.org/10.1038/nphoton.2015.264

29. Gorkhover, T. Ph.D. thesis. Ultrafast light induced dynamics of Xe nanoparticles studied with a combination of intense infrared and x-ray pulses. (2014)

30. Kalidindi, S. B., & Jagirdar, B. R. (2009). Highly monodisperse colloidal magnesium nanoparticles by room temperature digestive ripening. *Inorganic Chemistry*, *48*(10), 4524–4529. http://doi.org/10.1021/ic9003577

31. Sidhaye, D. S., & Prasad, B. L. V. (2011). Many manifestations of digestive ripening: monodispersity, superlattices and nanomachining. *New J. Chem.*, *35*(4), 755–763. http://doi.org/10.1039/C0NJ00359J

32. Bhaskar, S. P., & Jagirdar, B. R. (2017). A journey from bulk brass to nanobrass: A comprehensive study showing structural evolution of various Cu/Zn bimetallic nanophases from the vaporization of brass. *Journal of Alloys and Compounds*, *694*, 581–595. http://doi.org/10.1016/j.jallcom.2016.09.318

33. Manzanares, J. A., Peljo, P., & Girault, H. H. (2017). Understanding Digestive Ripening of Ligand-Stabilized, Charged Metal Nanoparticles. *Journal of Physical Chemistry C*, *121*(24), 13405–13411. http://doi.org/10.1021/acs.jpcc.7b04234

34. Irzhak, V. I. (2017). Digestive ripening of nanoparticles. *Russian Journal of Physical Chemistry A*, *91*(8), 1502–1506. http://doi.org/10.1134/S0036024417080131

35. Peter Atkins & Julio de Paula. (2006). *Physical Chemistry* (8th ed.).

36. Chateau, D., Liotta, A., Vadcard, F., Navarro, J. R. G., Chaput, F., Lermé, J., … Parola, S. (2015). From gold nanobipyramids to nanojavelins for a precise tuning of the plasmon resonance to the infrared wavelengths: experimental and theoretical aspects. *Nanoscale*, *7*(5), 1934–1943. http://doi.org/10.1039/C4NR06323F

37. Sau, T. K., & Murphy, C. J. (2004). Seeded high yield synthesis of short Au nanorods in aqueous solution. *Langmuir*, *20*(15), 6414–6420. http://doi.org/10.1021/la049463z

38. Jana, N. R., Gearheart, L., & Murphy, C. J. (2001). Seeding growth for size control of 5-40 nm diameter gold nanoparticles. *Langmuir*, *17*(22), 6782–6786. http://doi.org/10.1021/la0104323

39. Nyström, G., Fernández-Ronco, M. P., Bolisetty, S., Mazzotti, M., & Mezzenga, R. (2016). Amyloid Templated Gold Aerogels. *Advanced Materials*, *28*(3), 472–478. http://doi.org/10.1002/adma.201503465

40. Grzelczak, M., Pérez-Juste, J., Mulvaney, P., & Liz-Marzán, L. M. (2008). Shape control in gold nanoparticle synthesis. *Chemical Society Reviews*, *37*(9), 1783. http://doi.org/10.1039/b711490g

41. Prasad, B. L. V., Sorensen, C. M., & Klabunde, K. J. (2008). Gold nanoparticle superlattices. *Chemical Society Reviews*, *37*(9), 1871. http://doi.org/10.1039/b712175j

42. Kruis, F. E., Fissan, H., & Peled, a. (1998). Synthesis of nanoparticles in the gas phase for electronic, optical and magnetic applications - A review. *Journal of Aerosol Science*, *29*(5–6), 511–535. http://doi.org/10.1016/s0021-8502(97)10032-5

43. Amendola, V., & Meneghetti, M. (2009). Laser ablation synthesis in solution and size manipulation of noble metal nanoparticles. *Physical Chemistry Chemical Physics*, *11*(20), 3805. http://doi.org/10.1039/b900654k

44. Teoh, W. Y., Amal, R., & Mädler, L. (2010). Flame spray pyrolysis: An enabling technology for nanoparticles design and fabrication. *Nanoscale*, *2*(8), 1324. http://doi.org/10.1039/c0nr00017e

45. Hiramatsu, H., & Osterloh, F. E. (2004). A simple large-scale synthesis of nearly monodisperse gold and silver nanoparticles with adjustable sizes and with exchangeable surfactants. *Chemistry of Materials*, *16*(13), 2509–2511. http://doi.org/10.1021/cm049532v

46. Kimling, J., Maier, M., Okenve, B., Kotaidis, V., Ballot, H., & Plech, A. (2006). Turkevich method for gold nanoparticle synthesis revisited. *Journal of Physical Chemistry B*, *110*(32), 15700–15707. http://doi.org/10.1021/jp061667w

47. San, C., & Jolla, L. (2013). Design and performance of a Nafion dryer for continuous operation at CO 2 and CH 4 air monitoring sites, 1217–1226. http://doi.org/10.5194/amt-6-1217-2013

48. Pure, P. (2014). All About Nafion | Perma Pure LLC. Retrieved from http://www.permapure.com/resources/all-about-nafion-and-faq/

49. Permapure. (2013). *The Complete Guide to Gas Sample Drying*.

50. Liu, P., Ziemann, P. J., Kittelson, D. B., & McMurry, P. H. (1995). Generating particle beams of controlled dimensions and divergence: I. Theory of particle motion in aerodynamic lenses and nozzle expansions. *Aerosol Science and Technology*, *22*(3), 293–313. http://doi.org/10.1080/02786829408959748

51. Liu, P., Ziemann, P. J., Kittelson, D. B., & McMurry, P. H. (1995). Generating particle beams of controlled dimensions and divergence: II. Theory of particle motion in aerodynamic lenses and nozzle expansions. *Aerosol Science and Technology*, *22*(3), 314–324.

52. Zhang, X., Smith, K. A., Worsnop, D. R., Jimenez, J., Jayne, J. T., & Kolb, C. E. (2002). A numerical characterization of particle beam collimation by an aerodynamic lens-nozzle system: Part I. An individual lens or nozzle. *Aerosol Science and Technology*, *36*(5), 617–631. http://doi.org/10.1080/02786820252883856

53. Liu, P. S. K., Deng, R., Smith, K. A., Williams, L. R., Jayne, J. T., Canagaratna, M. R., … Deshler, T. (2007). Transmission efficiency of an aerodynamic focusing lens system:

Comparison of model calculations and laboratory measurements for the aerodyne aerosol mass spectrometer. *Aerosol Science and Technology*, *41*(8), 721–733. http://doi.org/10.1080/02786820701422278

54. Khan, S. J., Pierce, F., Sorensen, C. M., & Chakrabarti, A. (2009). Self-assembly of ligated gold nanoparticles: Phenomenological modeling and computer simulations. *Langmuir*, *25*(24), 13861–13868. http://doi.org/10.1021/la9008202

55. Hickstein, D. D., Ph.D. thesis, University of Colorado (2014). Photoelectron and photoion spectroscopy of atoms, nanoparticles, and nanoplasmas irradiated with strong femtosecond laser fields.

56. Eppink, A. T. J. B., & Parker, D. H. (1997). Velocity map imaging of ions and electrons using electrostatic lenses: Application in photoelectron and photofragment ion imaging of molecular oxygen. *Review of Scientific Instruments*, *68*(9), 3477–3484. http://doi.org/10.1063/1.1148310

57. Whitaker, B. J. (2003). Imaging in Molecular Dynamics: Technology and Applications.

58. Kling, N. G., Paul, D., Gura, A., Laurent, G., De, S., Li, H., … Kling, M. F. (2014). Thick-lens velocity-map imaging spectrometer with high resolution for high-energy charged particles. *Journal of Instrumentation*, *9*(5), P05005–P05005. http://doi.org/10.1088/1748-0221/9/05/P05005

59. Ren, X., Ph.D. thesis (2013). Laser-Driven Rotational Dynamics of Gas-phase Molecules: Control and Applications.

60. Makhija, V., Ph.D. thesis (2014). Laser-Induced Rotational Dynamics As a Route To Molecular Frame Measurements.

61. Seiffert, L., Süßmann, F., Zherebtsov, S., Rupp, P., Peltz, C., Rühl, E., … Fennel, T. (2016). Competition of single and double rescattering in the strong-field photoemission from dielectric nanospheres. *Applied Physics B: Lasers and Optics*, *122*(4). http://doi.org/10.1007/s00340-016-6369-0

62. Vrakking, M. J. J. (2001). An iterative procedure for the inversion of two-dimensional ion/photoelectron imaging experiments. *Review of Scientific Instruments*, *72*(11), 4084. http://doi.org/10.1063/1.1406923

63. Brabec, T., & Krausz, F. (2000). Intense few-cycle laser fields: Frontiers of nonlinear optics. *Reviews of Modern Physics*, *72*(2), 545–591. http://doi.org/10.1103/RevModPhys.72.545

64. Diels, J. C., & Rudolph, W. (2006). Ultrashort laser pulse phenomena (Second Edition).

65. Chang, Z. (2014). Fundamentals of Attosecond Optics. *Katalog BPS*, *XXXIII*(2), 81–87. http://doi.org/10.1007/s13398-014-0173-7.2

66. Posthumus, J. H. (2004). The dynamics of small molecules in intense laser fields. *Reports on Progress in Physics*, *67*(5), 623–665. http://doi.org/10.1088/0034-4885/67/5/R01

67. Andrews, D. L., & Demidov, A. A. (1996). An Introduction to Laser Spectroscopy, 240. http://doi.org/10.1007/978-1-4615-0727-7

68. Pellegrini, C. (2012). The history of X-ray free-electron lasers. *European Physical Journal H*, *37*(5), 659–708. http://doi.org/10.1140/epjh/e2012-20064-5

69. Stüder, L., Epp, S., Rolles, D., Hartmann, R., Holl, P., Lutz, G., … Ullrich, J. (2010). Large-format, high-speed, X-ray pnCCDs combined with electron and ion imaging spectrometers in a multipurpose chamber for experiments at 4th generation light sources. *Nuclear Instruments and Methods in Physics Research, Section A: Accelerators, Spectrometers, Detectors and Associated Equipment*, *614*(3), 483–496. http://doi.org/10.1016/j.nima.2009.12.053

70. Strüder, L. (2001). The European Photon Imaging Camera on XMM-Newton: The pn-CCD camera. *a&Al*, *365*, 18–26. http://doi.org/10.1051/0004-6361

71. Chang, R., & Chang, R. (2003). *General chemistry : the essential concepts* (5th ed.). McGraw-Hill. http://doi.org/10.1038/159590b0

72. Turkevich, J., Stevenson, P. C., & Hillier, J. (1951). A study of the nucleation and growth processes in the synthesis of colloidal gold. *Discuss. Faraday Soc.* Vol 11, 0–55.

73. Brust, M., Walker, M., Bethell, D., Schiffrin, D. J., & Whyman, R. (1994). Synthesis of thiol-derivatised gold nanoparticles in a two-phase Liquid–Liquid system. *J. Chem. Soc., Chem. Commun.*, *0*(7), 801–802. http://doi.org/10.1039/C39940000801

74. Kaszuba, M., McKnight, D., Connah, M. T., McNeil-Watson, F. K., & Nobbmann, U. (2008). Measuring sub nanometre sizes using dynamic light scattering. *Journal of Nanoparticle Research*, *10*(5), 823–829. http://doi.org/10.1007/s11051-007-9317-4

75. Lohman, B., Master thesis (2009). Solubility of ligated gold nanoparticles at room temperature in various hydrocarbon solvents.

76. Yi, G.-C., Wang, C., & Park, W. Il. (2005). ZnO nanorods: synthesis, characterization and applications. *Semiconductor Science and Technology*, *20*(4), S22–S34. http://doi.org/10.1088/0268-1242/20/4/003

77. Prausnitz, J. M., Lichtenthaler, R., & Gomes de Azevedo, E. (1999). Molecular Thermodynamics of Fluid-Phase Equilibria, 261,262,290.

78. Hall, G. (1991). Molecular solid state physics. *Springer-Verlag.*

79. Fahlman, B. D. (2007). *Materials Chemistry*. http://doi.org/10.1007/978-1-4020-6120-2

80. Kittel, C. (2005). Introduction to solid state physics. *Wiley*, New York.

81. Smitham, J. B., Evans, R., & Napper, D. H. (1975). Analytical theories of the steric stabilization of colloidal dispersions. *Journal of the Chemical Society, Faraday Transactions 1: Physical Chemistry in Condensed Phases*, *71*(0), 285. http://doi.org/10.1039/f19757100285

82. Li, M., Schnablegger, H., & Mann, S. (1999). Coupled synthesis and self-assembly of nanoparticles to give structures with controlled organization. *Nature*, *402*(6760), 393–395. http://doi.org/10.1038/46509

83. Liu, Y., Lin, X. M., Sun, Y., & Rajh, T. (2013). In situ visualization of self-assembly of charged gold nanoparticles. *Journal of the American Chemical Society*, *135*(10), 3764–3767. http://doi.org/10.1021/ja312620e

84. Xue, X., Wang, J., & Furlani, E. P. (2015). Self-Assembly of Crystalline Structures of Magnetic Core-Shell Nanoparticles for Fabrication of Nanostructured Materials. *ACS Applied Materials and Interfaces*, *7*(40), 22515–22524. http://doi.org/10.1021/acsami.5b08310

85. Mie, "Beiträge zur Optik trüber Medien, speziell kolloidaler Metallösungen," (1908).

86. Zherebtsov, S., Süßmann, F., Peltz, C., Plenge, J., Betsch, K. J., Znakovskaya, I., … Kling, M. F. (2012). Carrier-envelope phase-tagged imaging of the controlled electron acceleration from SiO 2 nanospheres in intense few-cycle laser fields. *New Journal of Physics*, *14*(7), 75010. http://doi.org/10.1088/1367-2630/14/7/075010

87. Süßmann, F., Ph.D. thesis, LMU Munich (2013). Attosecond dynamics of nano-localized fields probed by photoelectron spectroscopy.

88. Batista, R. J., Mazzoni, M. S., & Chacham, H. (2010). First-principles investigation of electrochemical properties of gold nanoparticles. *Nanotechnology*, *21*(6), 65705. http://doi.org/10.1088/0957-4484/21/6/065705

89. Saydanzad, E., Li, J., & Thumm, U. (2017). Characterization of induced nanoplasmonic fields in time-resolved photoemission: A classical trajectory approach applied to gold nanospheres. *Physical Review A*, *95*(5). http://doi.org/10.1103/PhysRevA.95.053406

90. Li, J., Saydanzad, E., & Thumm, U. (2016). Retrieving plasmonic near-field information: A quantum-mechanical model for streaking photoelectron spectroscopy of gold nanospheres. *Physical Review A*, *94*(5), 51401. http://doi.org/10.1103/PhysRevA.94.051401

91. Tanabe, K. (2008). Field enhancement around metal nanoparticles and nanoshells: A systematic investigation. *Journal of Physical Chemistry C*, *112*(40), 15721–15728. http://doi.org/10.1021/jp8060009

92. Halas, N. (2005). Playing with Plasmons: Tuning the Optical Resonant Properties of Metallic Nanoshells. *MRS Bulletin*, *30*(5), 362–367. http://doi.org/10.1557/mrs2005.99

93. Prodan, E. (2003). A Hybridization Model for the Plasmon Response of Complex Nanostructures. *Science*, *302*(5644), 419–422. http://doi.org/10.1126/science.1089171

94. Averitt, R. D., Westcott, S. L., & Halas, N. J. (1999). Linear optical properties of gold nanoshells. *Journal of the Optical Society of America B*, *16*(10), 1824. http://doi.org/10.1364/JOSAB.16.001824

95. Bardhan, R., Grady, N. K., Ali, T., & Halas, N. J. (2010). Metallic nanoshells with semiconductor cores: Optical characteristics modified by core medium properties. *ACS Nano*, *4*(10), 6169–6179. http://doi.org/10.1021/nn102035q

96. Fennel, T., Meiwes-Broer, K. H., Tiggesbäumker, J., Reinhard, P. G., Dinh, P. M., & Suraud, E. (2010). Laser-driven nonlinear cluster dynamics. *Reviews of Modern Physics*, *82*(2), 1793–1842. http://doi.org/10.1103/RevModPhys.82.1793

97. Hickstein, D. D., Dollar, F., Ellis, J. L., Schnitzenbaumer, K. J., Keister, K. E., Petrov, G. M., … Xiong, W. (2014). Mapping Nanoscale Absorption of Femtosecond Laser Pulses Using Plasma Explosion Imaging. *ACS Nano*, *8*(9), 8810–8818. http://doi.org/10.1021/nn503199v

98. Liu, Rupp, Förg, Schötz, Süßmann, Okell, Passig, Tiggesbäumker, Meiwes-Broer, Seiffert, Fennel, Rühl, Förster, Hommelhoff, Zherebtsov, and Kling, "Nano-Optics: Principles Enabling Basic Research and Applications," Springer 283–299 (2017).

99. Peltz, C., Varin, C., Brabec, T., & Fennel, T. (2014). Time-resolved x-ray imaging of anisotropic nanoplasma expansion. *Physical Review Letters*, *113*(3), 133401. http://doi.org/10.1103/PhysRevLett.113.133401

100. Hommelhoff, P., & Kling, M. F. (2015). *Attosecond Nanophysics: From Basic Science to Applications*. *Attosecond Nanophysics: From Basic Science to Applications*. http://doi.org/10.1002/9783527665624

101. Lin, L., & Yi, Y. (2014). Lattice plasmon resonance in core-shell SiO_2/Au nanocylinder arrays. *Optics Letters*, *39*(16), 4823–6. http://doi.org/10.1364/OE.23.000130

102. Krausz, F., & Ivanov, M. (2009). Attosecond physics. *Reviews of Modern Physics*, *81*(1), 163–234. http://doi.org/10.1103/RevModPhys.81.163

103. Sukharev, M., & Seideman, T. (2006). Coherent control approaches to light guidance in the nanoscale. *Journal of Chemical Physics*, *124*(14). http://doi.org/10.1063/1.2177651

104. Kim, S., Jin, J., Kim, Y.-J., Park, I.-Y., Kim, Y., & Kim, S.-W. (2008). High-harmonic generation by resonant plasmon field enhancement. *Nature*, *453*(7196), 757–760. http://doi.org/10.1038/nature07012

105. Furube, A., Du, L., Hara, K., Katoh, R., & Tachiya, M. (2007). Ultrafast plasmon-induced electron transfer from gold nanodots into TiO2 nanoparticles. *Journal of the American Chemical Society*, *129*(48), 14852–14853. http://doi.org/10.1021/ja076134v

106. Gaál, A., Bugár, I., Capek, I., Fialová, L., Pálszegi, T., Szöcs, V., … Uherek, F. (2009). Femtosecond multicolor transient absorption spectroscopy of colloidal silver nanoparticles. *Laser Physics*, *19*(5), 961–968. http://doi.org/10.1134/S1054660X09050120

107. Ashenfelter, B. A., Desireddy, A., Yau, S. H., Goodson, T., & Bigioni, T. P. (2015). Fluorescence from Molecular Silver Nanoparticles. *The Journal of Physical Chemistry C*, *119*(35), 20728–20734. http://doi.org/10.1021/acs.jpcc.5b05735

108. Ditmire, T., Donnelly, T., Falcone, R. W., & Perry, M. D. (1995). Strong x-ray emission from high-temperature plasmas produced by intense irradiation of clusters. *Physical Review Letters*, *75*(17), 3122–3125. http://doi.org/10.1103/PhysRevLett.75.3122

109. Ditmire, T., Tisch, J. W. G., Springate, E., Mason, M. B., Hay, N., Smith, R. A., … Hutchinson, M. H. R. (1997). High-energy ions produced in explosions of superheated atomic clusters. *Nature*, *386*(6620), 54–56. http://doi.org/10.1038/386054a0

110. Zamith, S., Martchenko, T., Ni, Y., Aseyev, S. A., Muller, H. G., & Vrakking, M. J. J. (2004). Control of the production of highly charged ions in femtosecond-laser cluster fragmentation. *Physical Review A*, *70*(1), 11201. http://doi.org/10.1103/PhysRevA.70.011201

111. Jha, J., & Krishnamurthy, M. (2008). Hotter electron generation in doped clusters. *Journal of Physics B: Atomic, Molecular and Optical Physics*, *41*(4), 41002. http://doi.org/10.1088/0953-4075/41/4/041002

112. Siegbahn, K. M. (1981). Electron spectroscopy for atoms, molecules and condensed matter. *Nobel Lecture-Physics*, 63–92. http://doi.org/10.1126/science.217.4555.111

113. Dimauro, L. F., & Agostini, P. (1995). Ionization dynamics in strong laser fields. *Advances in Atomic, Molecular and Optical Physics*, *35*(C), 79–120. http://doi.org/10.1016/S1049-250X(08)60161-5

114. Dombi, P., Hörl, A., Rácz, P., Márton, I., Trügler, A., Krenn, J. R., & Hohenester, U. (2013). Ultrafast strong-field photoemission from plasmonic nanoparticles. *Nano Letters*, *13*(2), 674–678. http://doi.org/10.1021/nl304365e

115. Herink, G., Solli, D. R., Gulde, M., & Ropers, C. (2012). Field-driven photoemission from nanostructures quenches the quiver motion. *Nature*, *483*(7388), 190–193. http://doi.org/10.1038/nature10878

116. Eberly, J. H., & Javanainen, J. (1988). Above-threshold ionisation. *Eur. J. Phys.*, *9*, 265. http://doi.org/http://dx.doi.org/10.1088/0143-0807/9/4/004

117. Protopapas, M., Keitel, C. H., & Knight, P. L. (1997). Atomic physics with super-high intensity lasers. *Reports on Progress in Physics*, *60*(4), 389–486. http://doi.org/10.1088/0034-4885/60/4/001

118. Keldysh, L. V. (1965). Ionization in the field of a strong electromagnetic wave. *Soviet Physics JETP*, *20*(5), 1307–1314. http://doi.org/10.1234/12345678

119. Agostini, P., Fabre, F., Mainfray, G., Petite, G., & Rahman, N. K. (1979). Free-free transitions following six-photon ionization of xenon atoms. *Physical Review Letters*, *42*(17), 1127–1130. http://doi.org/10.1103/PhysRevLett.42.1127

120. Cormier, E., Garzella, D., Breger, P., Agostini, P., Chériaux, G., & Leblanc, C. (2001). Above-threshold ionization contrast and channel closure in argon. *Journal of Physics B: Atomic, Molecular and Optical Physics*, *34*(2), L9–L17. http://doi.org/10.1088/0953-4075/34/2/101

121. Faisal, F. H. M. (1973). Multiple absorption of laser photons by atoms. *Journal of Physics B: Atomic and Molecular Physics*, *6*(4), L89–L92. http://doi.org/10.1088/0022-3700/6/4/011

122. Reiss, H. R. (1980). Effect of an intense electromagnetic field on a weakly bound system. *Physical Review A*, *22*(5), 1786–1813. http://doi.org/10.1103/PhysRevA.22.1786

123. Corkum, P. B. (1993). Plasma perspective on strong field multiphoton ionization. *Physical Review Letters*, *71*(13), 1994–1997. http://doi.org/10.1103/PhysRevLett.71.1994

124. Lewenstein, M., Balcou, P., Ivanov, M. Y., L'Huillier, A., & Corkum, P. B. (1994). Theory of high-harmonic generation by low-frequency laser fields. *Physical Review A*, *49*(3), 2117–2132. http://doi.org/10.1103/PhysRevA.49.2117

125. Agostini, P., & DiMauro, L. F. (2004). The physics of attosecond light pulses. *Reports on Progress in Physics*, *67*(8), 1563–1563. http://doi.org/10.1088/0034-4885/67/8/C01

126. Becker, A., Dörner, R., & Moshammer, R. (2005). Multiple fragmentation of atoms in femtosecond laser pulses. *Journal of Physics B: Atomic, Molecular and Optical Physics*, *38*(9), S753–S772. http://doi.org/10.1088/0953-4075/38/9/021

127. Paulus, G. G., Becker, W., Nicklich, W., & Walther, H. (1994). Rescattering effects in above-threshold ionization: a classical model. *Journal of Physics B: Atomic, Molecular and Optical Physics*, *27*(21), L703–L708. http://doi.org/10.1088/0953-4075/27/21/003

128. Feuerstein, B., Moshammer, R., Ullrich, J., Search, H., Journals, C., Contact, A., … Address, I. P. (2000). Nonsequential multiple ionization in intense laser pulses : interpretation of ion momentum distributions within the classical "rescattering" model. *Journal of Physics B: Atomic, Molecular and Optical Physics*, *33*(21), 823–830. http://doi.org/10.1088/0953-4075/33/21/105

129. Busuladžić, M., Gazibegović-Busuladžić, A., & Milošević, D. B. (2006). High-order above-threshold ionization in a laser field: Influence of the ionization potential on the high-energy cutoff. *Laser Physics*, *16*(2), 289–293. http://doi.org/10.1134/S1054660X06020149

130. Saalmann, U., Siedschlag, C., & Rost, J. M. (2006). Mechanisms of cluster ionization in strong laser pulses. *Journal of Physics B: Atomic, Molecular and Optical Physics*, *39*(4), R39–R77. http://doi.org/10.1088/0953-4075/39/4/R01

131. Fennel, T., Meiwes-Broer, K. H., Tiggesbäumker, J., Reinhard, P. G., Dinh, P. M., & Suraud, E. (2010). Laser-driven nonlinear cluster dynamics. *Reviews of Modern Physics*, *82*(2), 1793–1842. http://doi.org/10.1103/RevModPhys.82.1793

132. Goulielmakis, E., Uiberacker, M., Kienberger, R., Baltuska, A., Yakovlev, V., Scrinzi, A., … Krausz, F. (2004). Direct Measurement of Light Waves. *Science*, *305*(5688), 1267–1269. http://doi.org/10.1126/science.1100866

133. Schultze, M., Fiess, M., Karpowicz, N., Gagnon, J., Korbman, M., Hofstetter, M., … Yakovlev, V. S. (2010). Delay in Photoemission. *Science*, *328*(5986), 1658–1662. http://doi.org/10.1126/science.1189401

134. Seiffert, L., Liu, Q., Zherebtsov, S., Trabattoni, A., Rupp, P., Castrovilli, M. C., … Kling, M. F. (2017). Attosecond chronoscopy of electron scattering in dielectric nanoparticles. *Nature Physics*, *13*(8), 766–770. http://doi.org/10.1038/nphys4129

135. Singhal, H., Ganeev, R. A., Naik, P. A., Srivastava, A. K., Singh, A., Chari, R., … Gupta, P. D. (2010). Study of high-order harmonic generation from nanoparticles. *Journal of Physics B: Atomic, Molecular and Optical Physics*, *43*(2), 25603. http://doi.org/10.1088/0953-4075/43/2/025603

136. Bostedt, C., Boutet, S., Fritz, D. M., Huang, Z., Lee, H. J., Lemke, H. T., … Williams, G. J. (2016). Linac Coherent Light Source: The first five years. *Reviews of Modern Physics*, *88*(1). http://doi.org/10.1103/RevModPhys.88.015007

137. Neutze, R., Wouts, R., van der Spoel, D., Weckert, E., & Hajdu, J. (2000). Potential for biomolecular imaging with femtosecond X-ray pulses. *Nature*, *406*(6797), 752–757. http://doi.org/10.1038/35021099

138. Chapman, H. N., Fromme, P., Barty, A., White, T. A., Kirian, R. A., Aquila, A., … Spence, J. C. H. (2011). Femtosecond X-ray protein nanocrystallography. *Nature*, *470*(7332), 73–77. http://doi.org/10.1038/nature09750

139. Loh, N. D., Hampton, C. Y., Martin, A. V., Starodub, D., Sierra, R. G., Barty, A., … Bogan, M. J. (2012). Fractal morphology, imaging and mass spectrometry of single aerosol particles in flight. *Nature*, *486*(7404), 513–517. http://doi.org/10.1038/nature11222

140. Ekeberg, T., Svenda, M., Abergel, C., Maia, F. R. N. C., Seltzer, V., Claverie, J. M., … Hajdu, J. (2015). Three-dimensional reconstruction of the giant mimivirus particle with an X-ray free-electron laser. *Physical Review Letters*, *114*(9). http://doi.org/10.1103/PhysRevLett.114.098102

141. Bresch, H., Wassermann, B., Langer, B., Graf, C., Flesch, R., Becker, U., … Rühl, E. (2008). Elastic light scattering from free sub-micron particles in the soft X-ray regime. *Faraday Discussions*, *137*, 389-402-424. http://doi.org/10.1039/b702630g

142. Bogan, M. J., Benner, W. H., Boulet, S., Rohner, U., Frank, M., Barty, A., … Chapman, H. N. (2008). Single particle X-ray diffractive imaging. *Nano Letters*, *8*(1), 310–316. http://doi.org/10.1021/nl072728k

143. Chandler, D. W., & Houston, P. L. (1987). Two-dimensional imaging of state-selected photodissociation products detected by multiphoton ionization. *The Journal of Chemical Physics*, *87*(2), 1445–1447. http://doi.org/10.1063/1.453276

144. Manzhos, S., & Loock, H. P. (2003). Photofragment image analysis using the Onion-Peeling Algorithm. *Computer Physics Communications*, *154*(1), 76–87. http://doi.org/10.1016/S0010-4655(03)00277-7

145. Ma, S., Gao, H., & Wu, L. (2008). Modified Fourier-Hankel method based on analysis of errors in Abel inversion using Fourier transform techniques. *Applied Optics*, *47*, 1350–1357. http://doi.org/10.1364/AO.47.001350

146. Harmand, M., Coffee, R., Bionta, M. R., Chollet, M., French, D., Zhu, D., … Cammarata, M. (2013). Achieving few-femtosecond time-sorting at hard X-ray free-electron lasers. *Nature Photonics*, *7*(3), 215–218. http://doi.org/10.1038/nphoton.2013.11

147. Bostedt, C., Bozek, J. D., Bucksbaum, P. H., Coffee, R. N., Hastings, J. B., Huang, Z., … DiMauro, L. F. (2013). Ultra-fast and ultra-intense x-ray sciences: first results from the Linac Coherent Light Source free-electron laser. *Journal of Physics B: Atomic, Molecular and Optical Physics*, *46*(16), 164003. http://doi.org/10.1088/0953-4075/46/16/164003

148. Grasbon, F., Paulus, G. G., Walther, H., Villoresi, P., Sansone, G., Stagira, S., … De Silvestri, S. (2003). Above-threshold ionization at the few-cycle limit. *Physical Review Letters*, *91*(17), 173003. http://doi.org/10.1103/PhysRevLett.91.173003

149. Alnaser, A. S., Tong, X. M., Osipov, T., Voss, S., Maharjan, C. M., Shan, B., … Cocke, C. L. (2004). Laser-peak-intensity calibration using recoil-ion momentum imaging. *Physical Review A - Atomic, Molecular, and Optical Physics*, *70*(2). http://doi.org/10.1103/PhysRevA.70.023413

150. Jesus, V. L. B. De, Feuerstein, B., Zrost, K., Fischer, D., Rudenko, a, Afaneh, F., … Ullrich, J. (2004). Atomic structure dependence of nonsequential double ionization of He, Ne and Ar in strong laser pulses. *Journal of Physics B: Atomic, Molecular and Optical Physics*, *37*(8), L161–L167. http://doi.org/10.1088/0953-4075/37/8/L03

151. Wiehle, R., Witzel, B., Helm, H., & Cormier, E. (2003). Dynamics of strong-field above-threshold ionization of argon: Comparison between experiment and theory. *Physical Review A*, *67*, 1–7. http://doi.org/10.1103/PhysRevA.67.063405

152. Madey, J. M. J. (1971). Stimulated emission of bremsstrahlung in a periodic magnetic field. *Journal of Applied Physics*, *42*(5), 1906–1913. http://doi.org/10.1063/1.1660466

153. Deacon, D. A. G., Elias, L. R., Madey, J. M. J., Ramian, G. J., Schwettman, H. A., & Smith, T. I. (1977). First operation of a free-electron laser. *Physical Review Letters*, *38*(16), 892–894. http://doi.org/10.1103/PhysRevLett.38.892

154. Schmüser, P., Dohlus, M., Rossbach, J., & Behrens, C. (2014). Free-Electron lasers in the ultraviolet and x-ray regime: Physical principles, experimental results, technical realization. *Springer Tracts in Modern Physics*, *258*, 3–5. http://doi.org/10.1007/978-3-319-04081-3

155. Ackermann, W., Asova, G., Ayvazyan, V., Azima, A., Baboi, N., Bähr, J., … Zapfe, K. (2007). Operation of a free-electron laser from the extreme ultraviolet to the water window. *Nature Photonics*, *1*(6), 336–342. http://doi.org/10.1038/nphoton.2007.76

156. Emma, P., Akre, R., Arthur, J., Bionta, R., Bostedt, C., Bozek, J., … Galayda, J. (2010). First lasing and operation of an ångstrom-wavelength free-electron laser. *Nature Photonics*, *4*(9), 641–647. http://doi.org/10.1038/nphoton.2010.176

157. Ferguson, K. R., Bucher, M., Bozek, J. D., Carron, S., Castagna, J. C., Coffee, R., … Bostedt, C. (2015). The Atomic, Molecular and Optical Science instrument at the Linac Coherent Light Source. *Journal of Synchrotron Radiation*, *22*, 492–497. http://doi.org/10.1107/S1600577515004646

158. T Osipov, C Bostedt, J-C Castagna K R Ferguson M Bucher S C Montero M L Swiggers , R Obaid, D Rolles, A Rudenko and N Berrah· The LAMP Instrument at the Linac Coherent Light Source Free-Electron Laser, to be published.

159. Glownia, J. M., Cryan, J., Andreasson, J., Belkacem, a, Berrah, N., Blaga, C. I., … Bucksbaum, P. H. (2010). Time-resolved pump-probe experiments at the LCLS. *Optics Express*, *18*(17), 17620–30. http://doi.org/10.1364/OE.18.017620

160. Myroshnychenko, V., Rodríguez-Fernández, J., Pastoriza-Santos, I., Funston, A. M., Novo, C., Mulvaney, P., … García de Abajo, F. J. (2008). Modelling the optical response of gold nanoparticles. *Chemical Society Reviews*, *37*(9), 1792. http://doi.org/10.1039/b711486a

161. Antonsson, E., Ph.D. thesis (2011). Photoexcitation, Photoionization, and X-Ray Scattering of Free Nanoparticles Prepared in a Beam.

162. E.C. Le Ru and P.G. Etchegoin, Principles of Surface-Enhanced Raman Spectroscopy and Related Plasmonic Effects (Elsevier, Amsterday, 2009).

Appendix A - Nanoparticle Characterization

The ability to synthesize large, monodisperse nanoparticles is a requirement to perform a size-dependent experiment as described in Chapter 4. As previously explained in Section 2.3.5, the nanoparticle jet was characterized for contamination and was shown to be very sensitive to any dissolved substances in the initial nanoparticle colloid. This characterization also showed evidence that under certain conditions clustering of the nanoparticles in the particle beam occurred. By diluting the initial nanoparticle concentration, the probability of cluster formation was decreased. Table A.1 shows all the nanoparticle samples used along with the sample properties, including the dilution factor which was obtained immediately before the experiment was performed. SiO_2 and the gold nanoshell particles were purchased from Nanocomposix, Inc. and used as purchased, except for the final dilution. AuNPs were purchased from Cytodiagnostics, Inc. from their 'Reactant Free' stock, verified to be 99% free of residual reactants from manufacturing. These particles were custom ordered for the smallest available dispersity, no added pH stabilizing buffer, and purified an extra 10X. It was this combination of exceptional purity and monodispersity of the sample, coupled to the source modifications, that allowed these particles to be studied.

Surface chemistry is the term used to define the molecules present on the surface of the nanoparticle. These molecules are usually present for stability purposes (either steric or charge stabilized) and to prevent irreversible aggregation of the nanoparticles. Figure A.1 shows the molecular structure of the nanoparticle surfaces as given in Table A.1. The surface of the silica nanoparticles was silanol, consisting mainly of hydroxyl groups and gives a very 'clean' surface. Silica is generally stable in ethanol and water

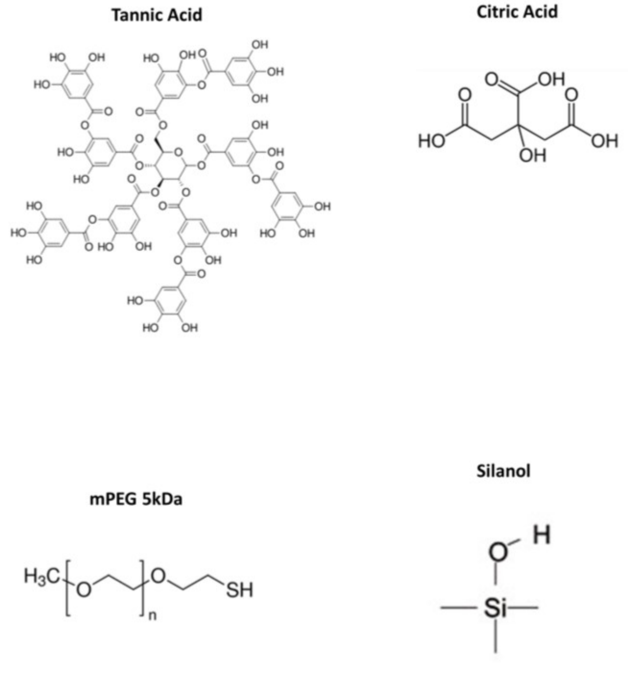
Tannic Acid

Citric Acid

mPEG 5kDa

Silanol

Figure A.1 *Molecular structures of the surface of the nanoparticles outlined in Table A.1.*

with limited contamination in solution. For the AuNPs and gold nanoshells, the metallic surface needs different and usually larger molecules, generally called ligands to prevent aggregation. For the nanoshells, the polymer ‘mPEG’ is used to make the particles water soluble and provide a robust surface bond to the gold surface with the thiol group. These were also extensively washed by the manufacturer. For 5nm AuNPs, tannic acid was used as it is a slighter stronger reducing agent and produces a stable colloid. All the larger AuNPs used citric acid as the surface ligand. The hydroxyl groups on tannic and citric acid provide a relatively weak bond to the gold surface as compared to the thiol in the nanoshell. This was one reason for the need to modify the nanosource to prevent aggregation of these gold nanoparticles.

Table A.1 *Nanoparticle samples used in the experiments outlined in Chapter 4. These are properties of the individual nanoparticles along with as delivered concentrations. The dilution factor (relative to the initial concentration) is the final concentration used for each sample.*

Material	*Size (nm)*	*Dispersity (±nm)*	*Surface Chemistry*	*Concentration (NP/ml)*	*Dilution factor*
AuNP	*5*	*2*	*Tannic acid*	*5.5x1013*	*1/100*
AuNP	*30*	*2*	*Citric acid*	*1.8x1011*	*1/10*
AuNP	*70*	*3*	*Citric acid*	*1.2x1010*	*1*
AuNP	*120*	*10*	*Citric acid*	*4.0x109*	*1*
AuNP	*200*	*20*	*Citric acid*	*1.9x109*	*1*
AuNP	*400*	*20*	*Citric acid*	*1.9x108*	*1*
Au shell/silica core	*151.3* *119.7 core/16 shell*	*5.1 (total)* *7.4 (core)*	*mPEG 5kDa*	*3.0x109*	*1*
SiO2	*22.5*	*2.8*	*Silanol*	*4.0x1014*	*1/1000*
SiO2	*47*	*3*	*Silanol*	*9.1x1013*	*1/1000*
SiO2	*82.6*	*4.7*	*Silanol*	*1.5x1013*	*1/100*
SiO2	*118.5*	*5.7*	*Silanol*	*5.6x1012*	*1/100*
SiO2	*199*	*15.2*	*Silanol*	*1.1x1012*	*1/50*
SiO2	*367*	*13*	*Silanol*	*1.9x109*	*1/10*
SiO2	*753*	*34*	*Silanol*	*2.1x1010*	*1/10*

The use of a transmission electron microscope gives details on the dimensions and surface features of nanoparticles. Silica nanoparticles are amorphous and easier to synthesize as a sphere. Gold nanoparticles tend to grow along preferential facets and therefore are less spherical, on average, than for silica. Figures A.2 and A.3 are TEM pictographs of the actual nanoparticles used in the experiments outlined in Chapter 4. As the nanoparticles were assumed to be spherical in the analysis and discussion, these images give a sense of how spherical they actual were. These images are only a very small subset of the entire ensemble of nanoparticles in a sample and should only be used to make rough observations.

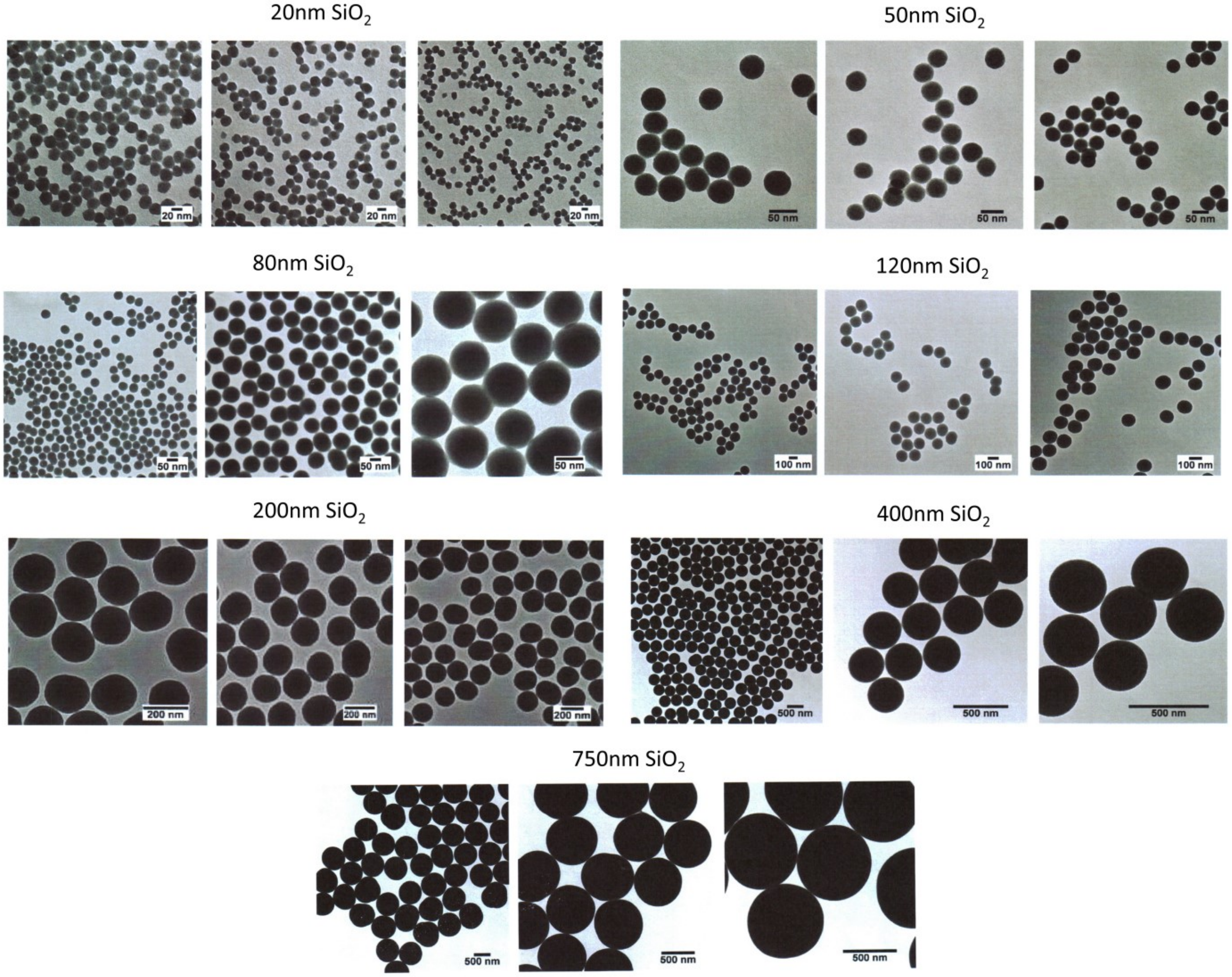

Figure A.2 *Transmission electron microscope images of SiO_2 nanoparticles used in the Chapter 4 experiment. Scale bars are on each picture. TEM pictures provided here by Nanocomposix, Inc where each nanoparticle sample is analyzed after synthesis.*

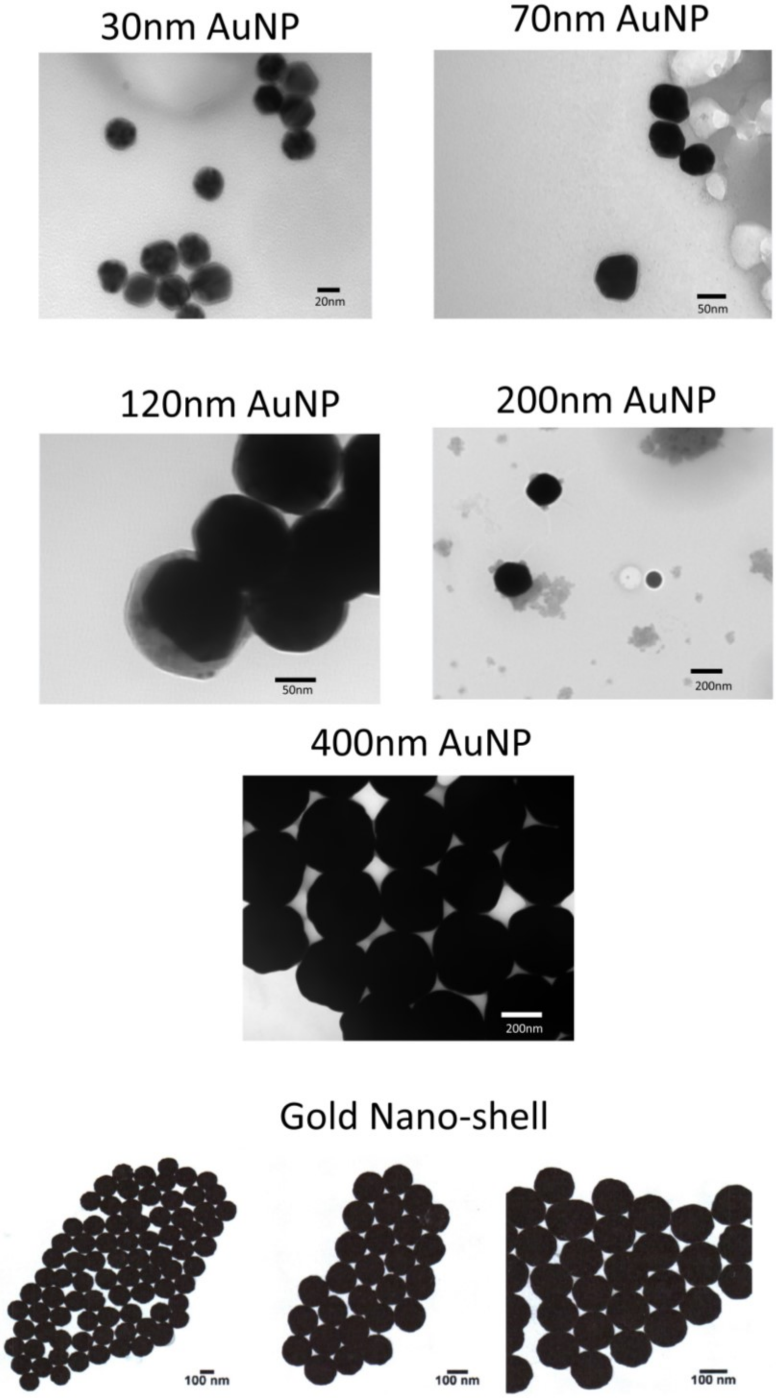

Figure A.3 *TEM images of AuNPs and gold nanoshells. Scale bars included in images.*

Appendix B - Photoelectron Spectroscopy

Pixels to Energy Mapping

The use of a Velocity Map Imaging (VMI) apparatus dictates that the velocity (proportional to momentum) of the photoelectron needs to be mapped energy. The spectrometer focuses the electrons as a function of repeller and extractor voltages as described in Section 2.4. An energy calibration needs to be performed for each different voltage. The MCP/phosphor screen image is captured by the single-shot camera where the CCD image in pixels needs to be calibrated into units of energy. Using the spacing of the ATI fringes allows for the determination of the calibration constant. Shown in Figure B.1 are the plots of the camera pixels mapped to energy for a specific

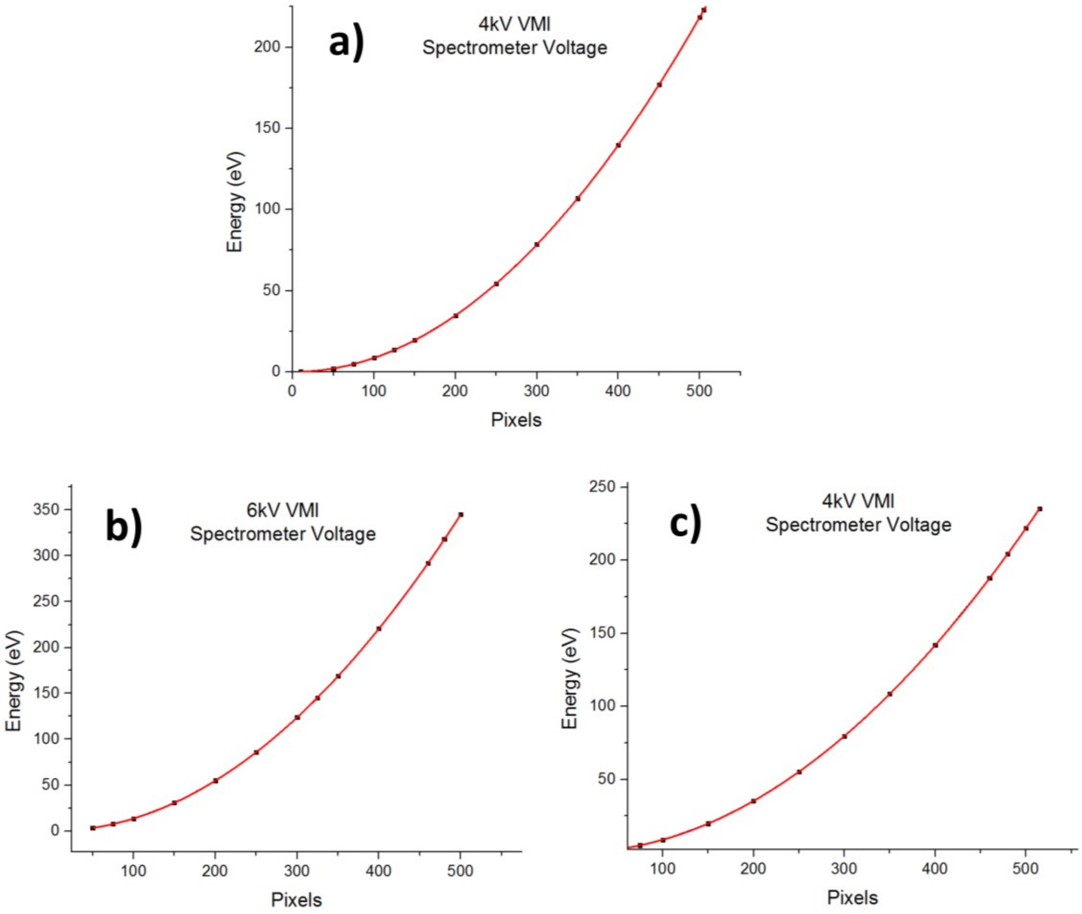

Figure B.1 *Plots mapping camera pixels to electron energy.* ***a)*** *Repeller voltage at -4kV and extractor at 97% of this value. Corresponds to all* SiO_2 *and gold nanoshell data.* ***b)*** *Repeller voltage of -6kV used for AuNP experiments, except for 200nm.* ***c)*** *Repeller voltage of -4kV used for low intensity 200nm AuNP scan.*

set of VMI spectrometer voltages and camera settings during the SiO_2 and AuNP experimental scans.

Inversion of the VMI Data

The raw VMI images are 2D projections of the full 3D momentum distribution of the photoelectrons. Various techniques are used to retrieve the full distribution if cylindrical symmetry is satisfied. Large nanoparticles have an asymmetric angular distribution and therefore will not satisfy symmetry requirements. Thus, as discussed in Section 2.4.7, all the data presented in Chapter 4 were non-inverted results. It was also shown that the highest energy photoelectrons, the 'cutoff' was the same for non-inverted and inverted data. Shown in Figure B.2 is an example of raw and inverted VMI images, using the iterative inversion approach. On top is the image from Xe at -500V on the spectrometer (hence the large size relative to the SiO_2 image) and a moderately low intensity. The image next to it is the same data after the inversion procedure to show the full energy and angular electron distribution. This same procedure was done for a 50nm SiO_2 nanoparticle for which the photoelectron emission patterns manifest cylindrical symmetry. The overall shape and cutoff do not appear to be dramatically changed, as was also shown in Figure 4.7 comparing the radial distribution of the non-inverted 50nm SiO_2 to the energy distribution of the same, but inverted, data.

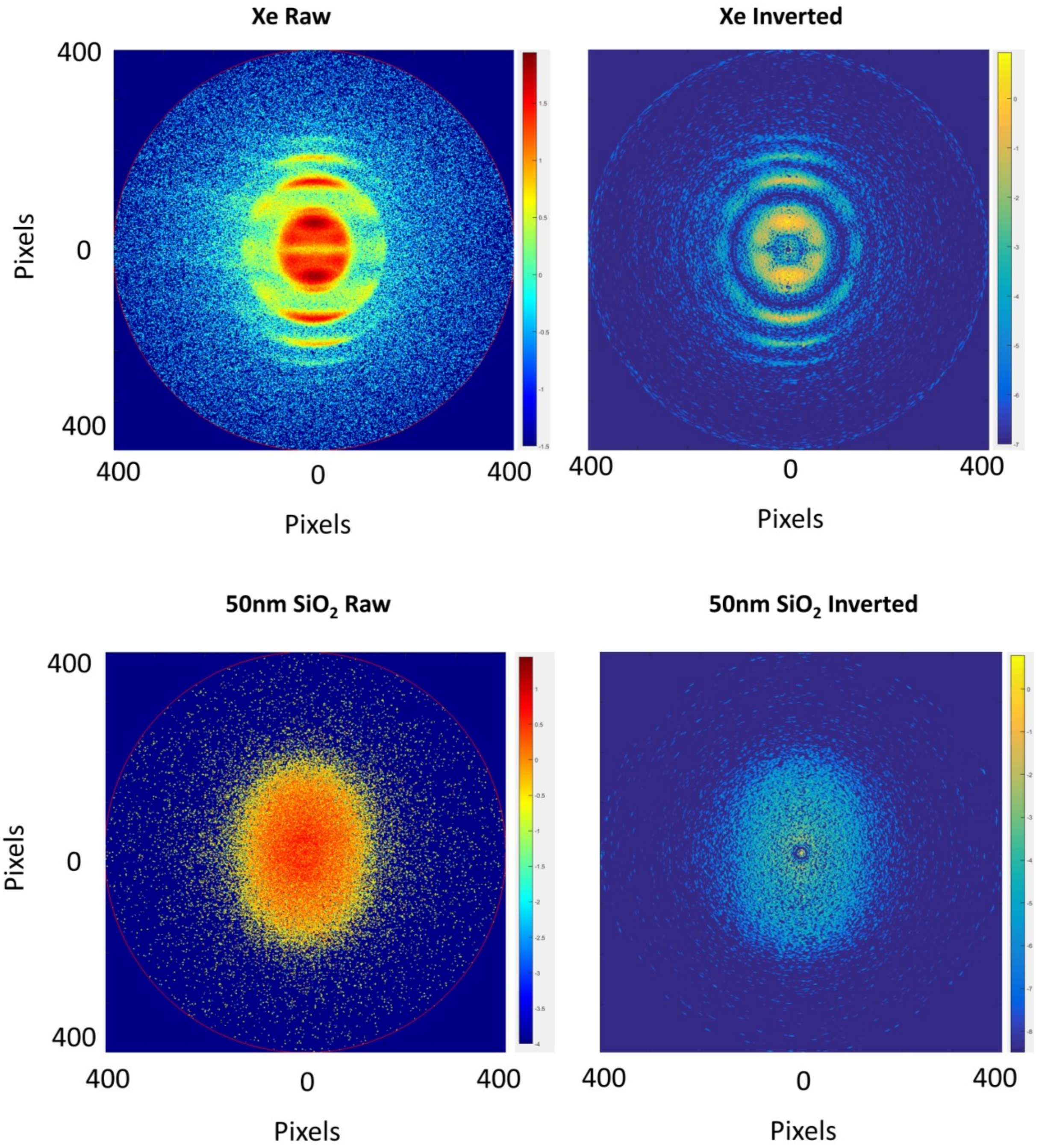

Figure B.2 *Comparison of raw VMI 2D projections to the inverted spectra. On top is atomic Xe at 4.4 x 10^{12} W/cm^2 and spectrometer voltage of -500V. On bottom is the spectra from 50nm SiO$_2$ nanoparticle, bin 200-300 (representing the largest bin and thus the peak intensity) at an intensity of 1.8 x 10^{13} W/cm^2 and spectrometer voltage of -4kV. The raw VMI images were inverted using the iterative approach.*

Hit Histograms

Hit histograms provide a look at the number of detected photoelectrons per laser shot as a function of laser intensity, nanoparticle size, and composition. The detection efficiency for a MCP/phosphor detector is at most 40-50%. This is also coupled with saturation issues where ta large local electron density incident upon the MCP will render the light output on the phosphor screen below the detection limit of the single-shot camera, thus producing the ‘hole’ as seen in Figure 4.20. However, trends can still be established with these relative electron counts seen in the hit histograms. Figure B.3 is the collection of hit histograms from all the nanoparticle scans obtained in Chapter 4. This gives a more detailed look at how the number of electrons emitted varies with the experimental parameters.

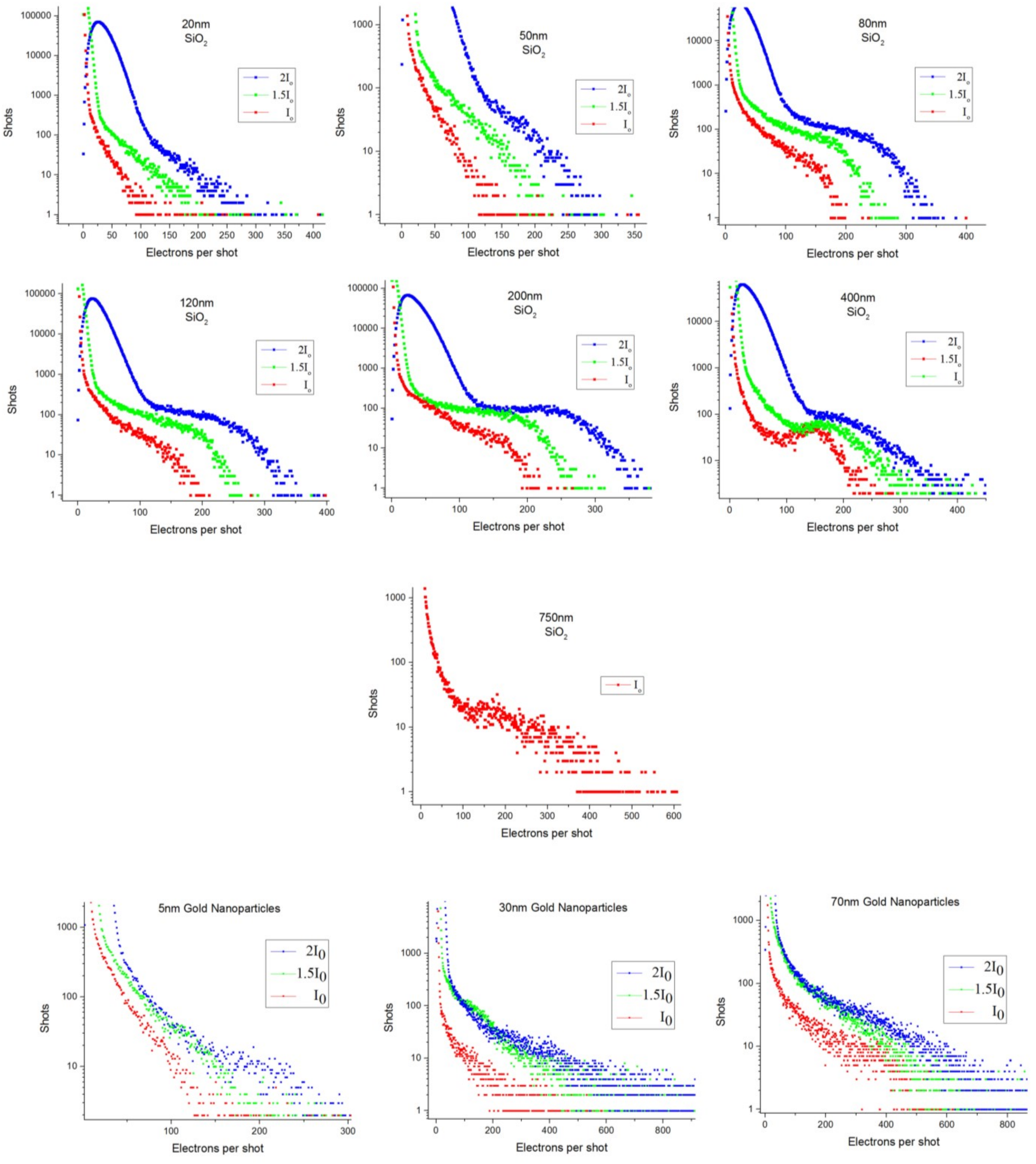

Figure B.3 *Hit histograms of SiO_2 and AuNPs as a function of laser intensity and nanoparticle diameter. $I_o = 8.8 \times 10^{12}$ W/cm^2 for SiO_2 and 8.3×10^{12} W/cm^2 for AuNPs.*

Raw VMI Images

The raw VMI images shown in Chapter 4 were a selection of all the actual images acquired. All images consist of a vertical polarization direction with the laser propagation going from right to left. To provide a more complete picture of the photoelectron momentum and angular distribution, Figure B.4 shows the raw VMI images from the entire SiO_2 size range from 20nm to 750nm. The first two columns show a sample of the 'binning' technique where the different intensity regions of the focus have much different spectra. The first column consists of a small 'bin' that was chosen to be just above the background level and representative of the outer fringes of the focus. It should be noted though that direct comparison between the small 'bins' as a function of size does not denote the same incident laser intensity. The largest 'bin' in column two does come from the peak laser intensity as the largest number of electrons per laser shot corresponds to the center of the focus. This column can be qualitatively compared between the different nanoparticle sizes. The two right columns are the integrated images from I_o and 2 I_o that is useful to compare the overall change in electron momentum and shape of the distribution. These images are in units of momentum as explicitly shown in Figure 4.10.

Figure B.5 are the raw VMI images from the size dependent AuNPs shown in the same manner as for the SiO_2 images. The AuNP images are done at a higher spectrometer voltage of -6kV which corresponds to the momentum values shown in Figure 4.19.

Figure B.6 are the raw VMI images from the low intensity scans. The cutoff energy from these nanoparticles were beyond the acceptance range of the VMI at the normally used intensity range. The intensity values are specified in the captions. The low intensity scans were done for 200nm AuNP and the gold nanoshells.

Figure B.7 is a VMI image from 400nm AuNP. This large size was not included in the thesis data as the cutoff electrons from all intensities were beyond the range of the VMI settings. However, as the nanoparticle probes the focal volume, there was some contribution from lower incident intensities. This image is to highlight the propagation-direction asymmetry due to its large size, similar to that of large SiO_2. The images for 200nm AuNPs do not show an obvious asymmetry yet but it can be clearly seen for 400nm. The crosshairs through the center of the image indicates the left/right asymmetry. This feature also helps to underscore the cleanliness of the particle beam. It is reasonable to assume that only a sufficiently clean nanoparticle would allow this asymmetry to be seen.

SiO$_2$

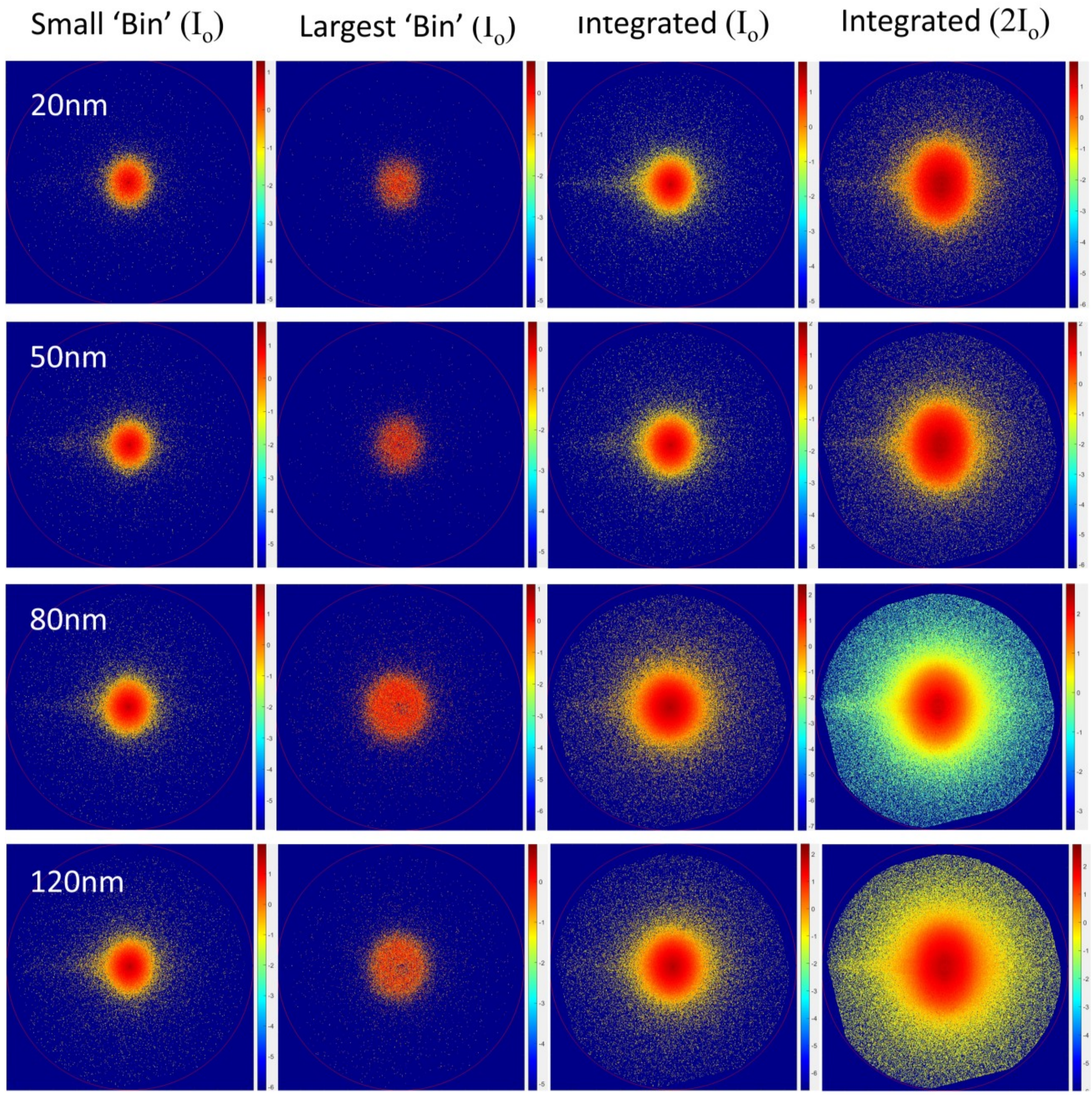
Small 'Bin' (I$_o$)
Largest 'Bin' (I$_o$)
Integrated (I$_o$)
Integrated (2I$_o$)
20nm
50nm
80nm
120nm

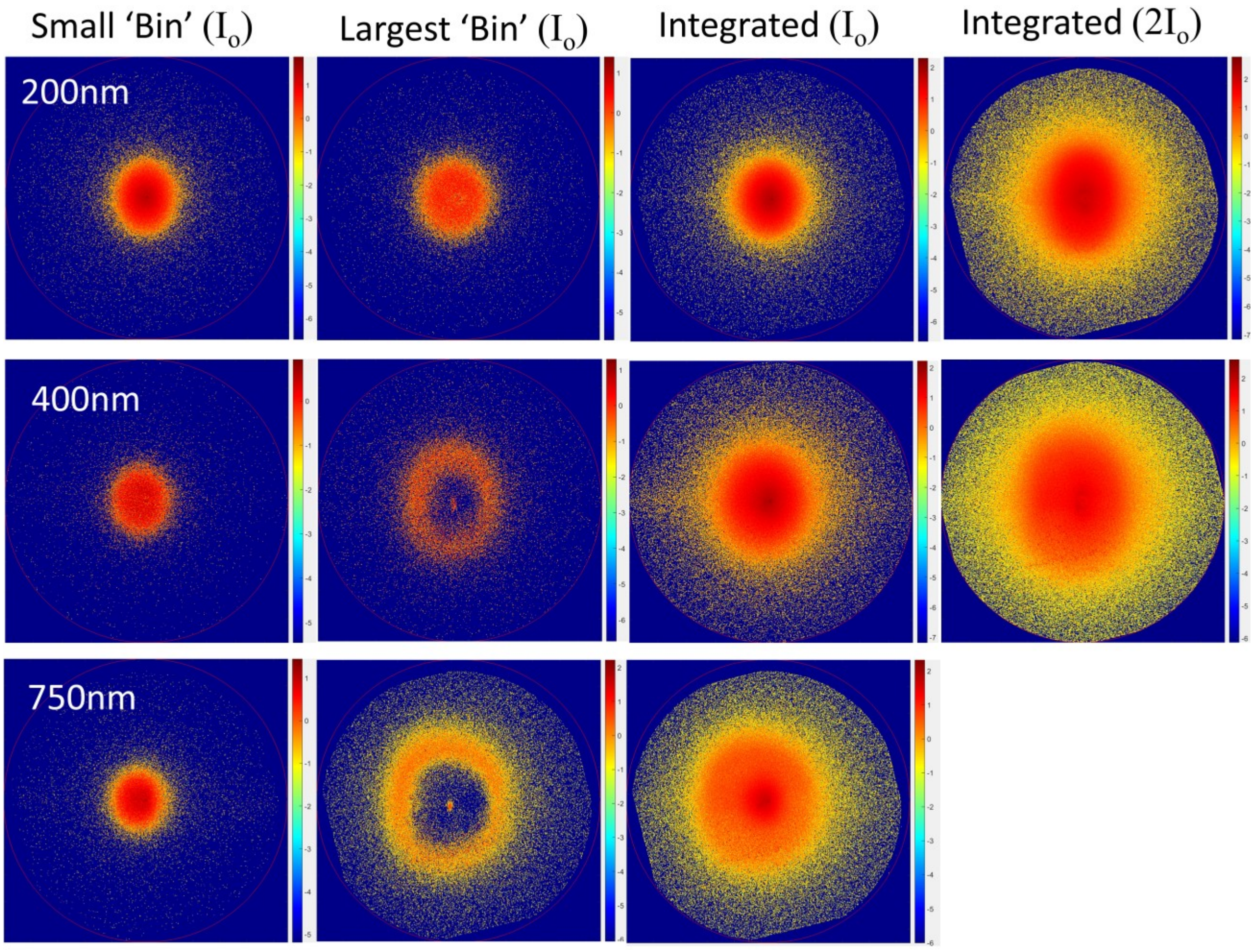

Figure B.4 *Collection of SiO_2 raw VMI images. Smallest 'bin' column is first 'bin' above the background level but not necessarily at the same incident intensity for each size. The largest 'bin' is chosen from the maximum number of electrons per laser shot and corresponds to the peak laser intensity. The right columns are the integrated images from I_o and $2I_o$ where $I_o=8.8x10^{12}$ W/cm^2. The images are in units of momentum as seen in Figure 4.10 where the outside of the detector corresponds to ~4 a.u. The color bar is in log scale.*

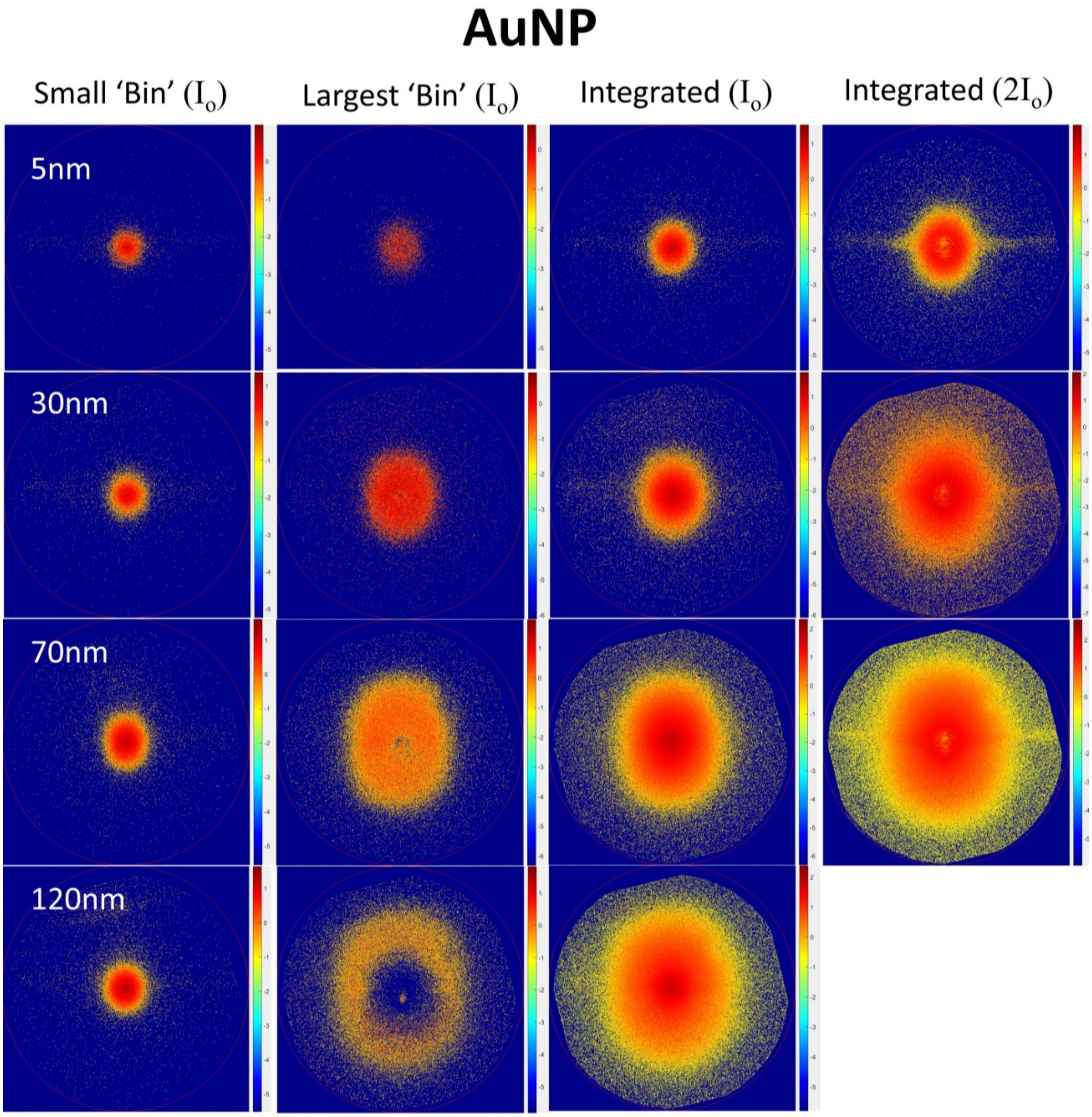

Figure B.5 *Collection of raw AuNP VMI images. Same configuration as in Figure B.4 except with AuNPs. Spectrometer voltage at -6kV and I_o=8.3x10^{12} W/cm^2. The images with no signal in the center is because of MCP saturation from too many incident electrons. Color bar is log scale.*

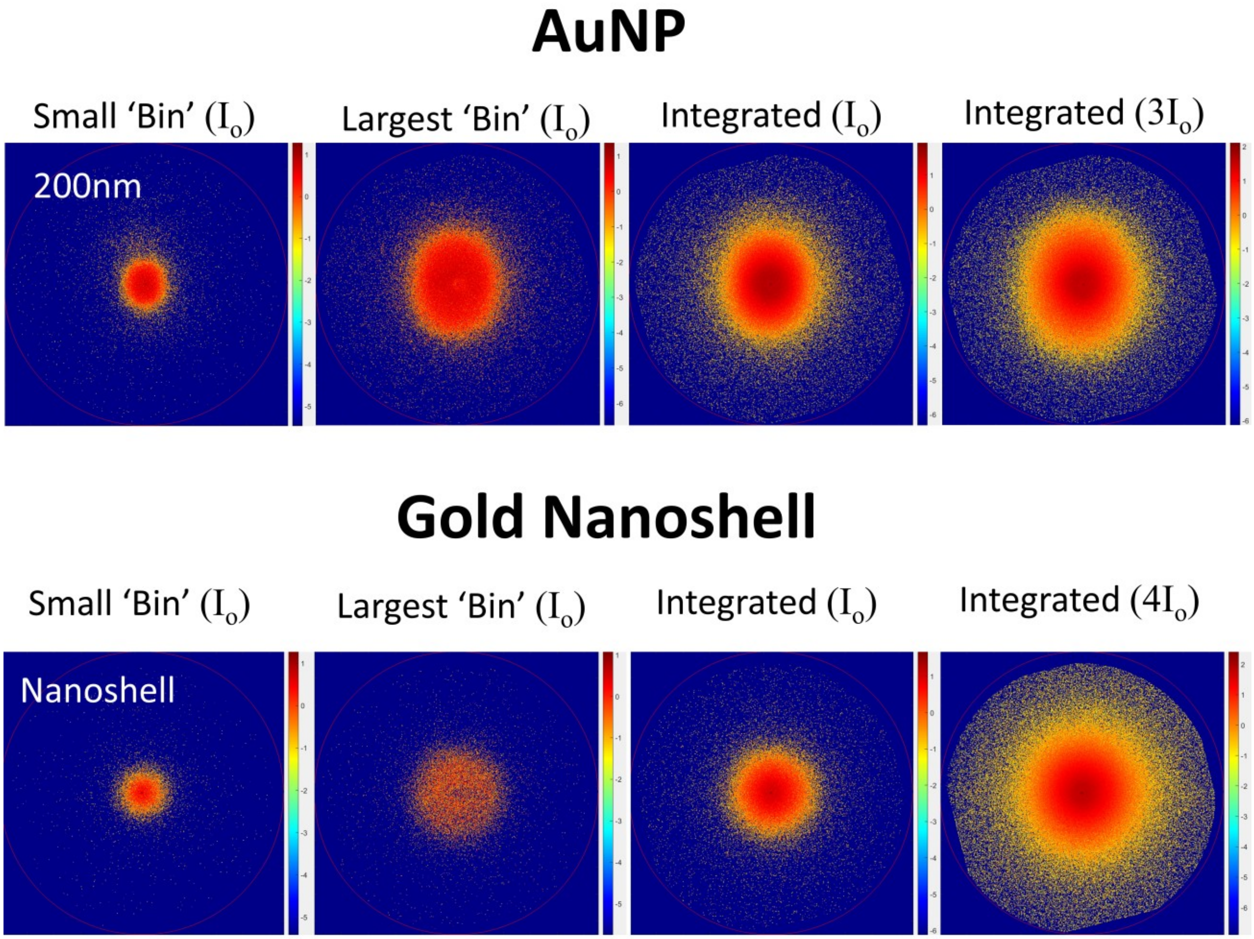

Figure B.6 *Collection of raw VMI images for low intensity scans. The 200nm AuNP was done with a spectrometer voltage of -4kV and* $I_o=8.3x10^{11}$ *W/cm*^{2}*. The gold nanoshell data was taken at -4kV with* $I_o=5.5x10^{11}$ *W/cm*^{2}*. The momentum axes are explicitly shown in Figure 4.31 that will apply to these scans. Color bar is log scale.*

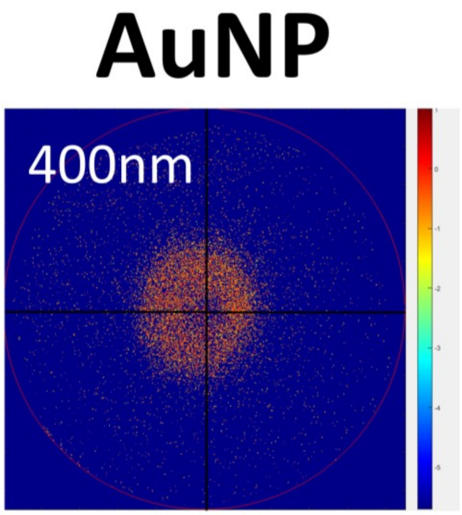

Figure B.7 *Raw VMI image from 400nm AuNP. The crosshairs show the center of the image and highlight that asymmetry from the large nanoparticle. This scan was not included in the cutoff data as it was outside the range of the VMI energy acceptance. This image is from the nanoparticle contributions of the 'wings' of the laser focus. This asymmetry helps to show that the AuNP samples are indeed clean in the particle jet.*

Near-field Enhancement

The field enhancement values used in Chapter 4 were found using a free-to-use software package called 'SPlaC v1.01 SERS and Plasmonics Codes package for Matlab' [162]. This is a Mie solver that was used to solve for the ratio of the scattered field outside a nanoparticle to the incident field strength, the so-called near-field enhancement. The maximum enhancement along with its spatial position relative to the nanoparticle can be calculated for any diameter spherical nanoparticle with its particular relative permittivity. The field enhancement as a function of nanoparticle diameter, composition, and wavelength is shown in Figure B.8. The enhancement factor for AuNPs has a much more diverse size response than for silica. The cutoff values shown in Figure 4.13 for size dependent SiO_2 are influenced by this near-field. Following the cutoff values and the near-field enhancement curve, there are definitely some similarities. For AuNPs, no reliable data was taken above 200nm, though according to the AuNP enhancement plot, one would expect a noticeable cutoff change at sizes larger than 300nm.

Also plotted is the angle of maximum field (blue line) which gives information as to where the largest enhancement is found for a nanoparticle of a given size and composition. The angle is defined relative to the nanoparticle poles (0°) and a shift away from this position is seen as an increase of this angle.

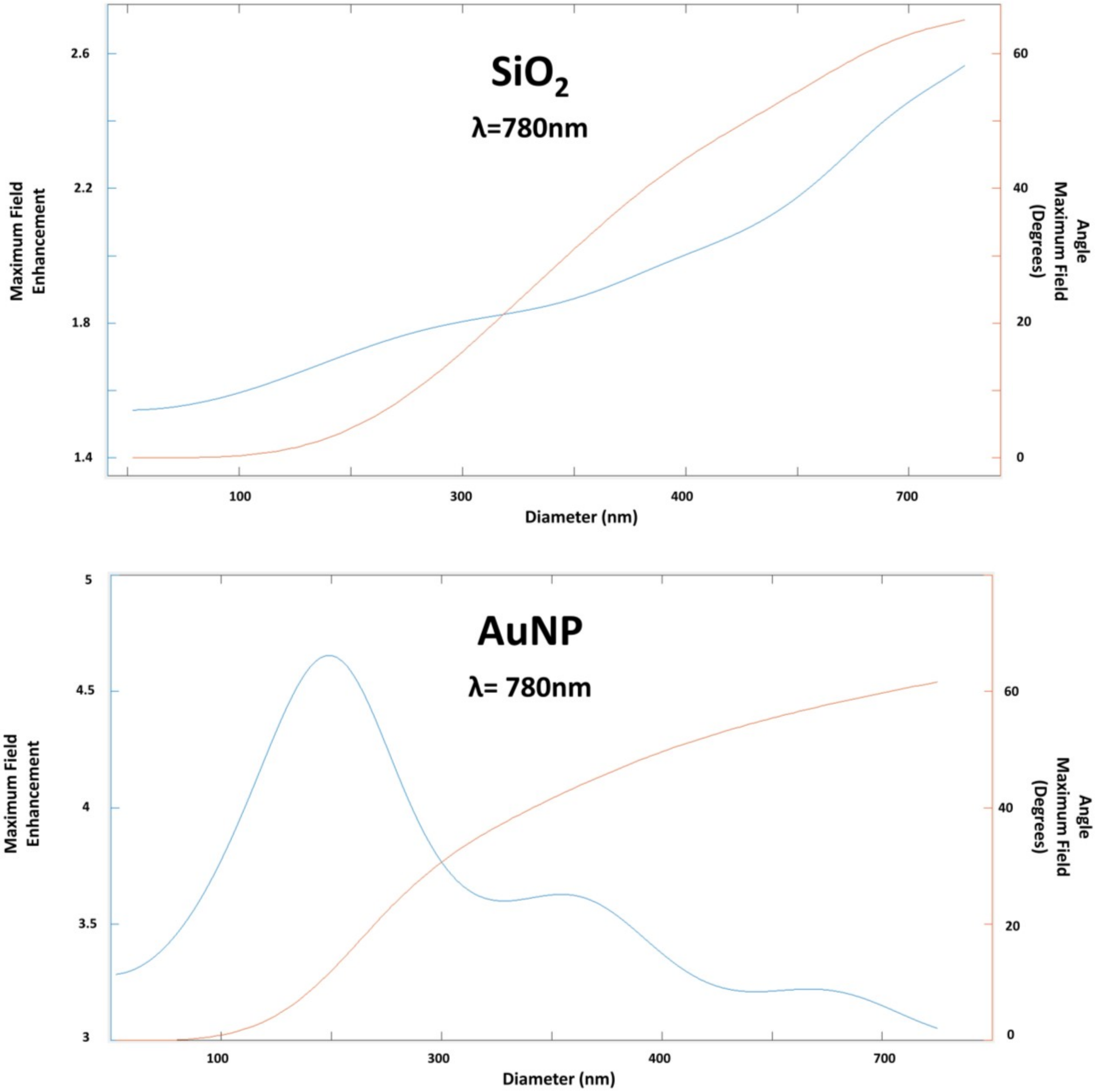

Figure B.8 *Near-field enhancement (blue) of* SiO_2 *and AuNP as a function of diameter at 780nm wavelength. Size range is from 5nm to 750nm. Blue line indicates the angle where the maximum enhancement occurs with respect to the vertical (poles) of the nanoparticle.*